UC-25
LBL-24552

Lawrence Berkeley Laboratory
UNIVERSITY OF CALIFORNIA

Materials & Chemical Sciences Division

RECEIVED
LAWRENCE
BERKELEY LABORATORY

MAR 4 1988

LIBRARY AND
DOCUMENTS SECTION

Microstructure and Magnetization Reversal of Iron/Rare Earth/Boron Permanent Magnets

R. Ramesh
(Ph.D. Thesis)

August 1987

For Reference

Not to be taken from this room

LBL-24552 c.1

Prepared for the U.S. Department of Energy under Contract DE-AC03-76SF00098

DISCLAIMER

This document was prepared as an account of work sponsored by the United States Government. While this document is believed to contain correct information, neither the United States Government nor any agency thereof, nor the Regents of the University of California, nor any of their employees, makes any warranty, express or implied, or assumes any legal responsibility for the accuracy, completeness, or usefulness of any information, apparatus, product, or process disclosed, or represents that its use would not infringe privately owned rights. Reference herein to any specific commercial product, process, or service by its trade name, trademark, manufacturer, or otherwise, does not necessarily constitute or imply its endorsement, recommendation, or favoring by the United States Government or any agency thereof, or the Regents of the University of California. The views and opinions of authors expressed herein do not necessarily state or reflect those of the United States Government or any agency thereof or the Regents of the University of California.

MICROSTRUCTURE AND MAGNETIZATION REVERSAL OF IRON/RARE EARTH/BORON PERMANENT MAGNETS

R. Ramesh

Ph.D. Thesis

Department of Materials Science and Mineral Engineering
University of California, Berkeley

and

Materials and Chemical Sciences Division
Lawrence Berkeley Laboratory
University of California
Berkeley, California 94720

August 1987

This work was supported by the U.S. Department of Energy
under contract Number DE-AC03-76SF00098

TABLE OF CONTENTS

ABSTRACT

ACKNOWLEDGMENT

I. INTRODUCTION 1
1. Historical prologue 1
2. Fundamentals of permanent magnets 3
3. The Fe-Nd-B alloy system 10
4. Aim, approach and scope of this investigation 24

II. EXPERIMENTAL DETAILS 26
1. Production of sintered Fe-RE-B magnets 26
2. Alloy compositions studied 27
3. X-Ray diffraction analysis 27
4. Scanning electron microscopy 28
5. Transmission electron microscopy 28
6. Auger electron spectroscopy and elemental mapping 29
7. Magnetic measurements 30

III. RESULTS AND DISCUSSION 31
1. Overall microstructure of sintered magnets with optimum properties 38
2. Dominant magnetization reversal mechanism of sintered magnets with optimum properties 36
3. Effect of post-sintering treatments on magnetic properties 44
4. Microstructure based magnetization reversal model 54
5. Lorentz microscopy:Microstructure-domain wall interactions 74
6. Alloy design implications 80

IV OVERALL SUMMARY 90

APPENDIX I 94

REFERENCES 95

FIGURE CAPTIONS 103

TABLES 117

FIGURES 123

MICROSTRUCTURE AND MAGNETIZATION REVERSAL OF IRON-RARE EARTH BORON PERMANENT MAGNETS

R.RAMESH
AUGUST 1987

Ph.D. Materials Science and Mineral Engineering

This work was supported by the Director, Office of Energy Research, Office of Basic Energy Sciences, Materials Science Division of the U.S. Department of Energy under contract No. DE-AC03-76SF00098.

ABSTRACT

An experimental investigation of the microstructure and details of magnetization reversal of the new class of permanent magnets, Fe-Nd-B, has been undertaken to understand the inter-relationship between the microstructure and magnetic properties of the magnets. The overall microstructure consists of almost defect free grains of the matrix $Nd_2Fe_{14}B$ surrounded by a Nd-rich, oxygen stabilized, fcc phase. This paramagnetic phase is observed, both at the triple grain junctions and as thin layers in the two-grain boundaries. A third phase, Fe_4NdB_4, along with the rare earth sesqui-oxide was infrequently observed as isolated grains. Through the examination of the virgin magnetization curve, the applied field dependence of the intrinsic coercivity and remanence it was conclusively shown that the magnet behaves as a nucleation controlled magnet, i.e., the magnetization reversal is controlled by the domain wall nucleation step. Since the interiors of the matrix grains are defect-free, domain wall

nucleation occurs due to defects at the grain boundaries and two-phase interfaces. One possible defect is oxygen which can be a possible cause for the large difference between the anisotropy field and the intrinsic coercivity, even in the case of a optimally treated magnet. The effect of post-sintering heat-treatments upon the intrinsic coercivity and energy product has been rationalized based upon the above observations. Increase in the cooling rate after sintering leads to a decrease in the intrinsic coercivity due to the effect of quenching stresses, caused by thermal expansion mismatch at the fcc phase-matrix interface. Thus, the combined effect of oxygen and the quenching stresses causes a large reduction in intrinsic coercivity and energy product. Based on the microstructural observations and the magnetic properties measured, a magnetization reversal model has been proposed, which incorporates the effect of quenching stresses also. The predictions of the model have been shown to be in close agreement with experimental observations of the effect of temperature and composition on the intrinsic coercivity and anisotropy field. The statistical nature of domain wall nucleation has also been emphasized by a detailed analysis of the effect of grain size on the intrinsic coercivity. Lorentz electron microscopic observations suggest that domain walls interact strongly with grain boundaries and the grain boundary fcc phase when they are parallel to the microstructural feature. Inclusions of size below 500Å have been observed to pin domain walls, thus suggesting a possible mechanism for improving the magnetic properties. Finally, it has been shown that further improvement in the intrinsic coercivity and energy product can come about only by selective engineering of the structure and composition of the grain boundaries and two-phase interfaces in order to make domain wall nucleation more difficult.

ACKNOWLEDGMENTS

I wish to gratefully acknowledge those who have been of assistance in the completion of this thesis. Thanks first of all goes to Professor Gareth Thomas who supported and supervised this research endeavor. He was not only a research supervisor but also a friend, philosopher and a guide. He is a great source of inspiration for me. I also wish to thank Professors Didier de Fontaine and Alan M. Portis for their support, time and guidance during this research, serving on my thesis committee and advising me. I wish to extend my gratitude to Professors R.O. Ritchie, R. Gronsky and J.W.Morris and Dr. R.M.Cannon, who were always willing to share their knowledge with me.

The samples used in this research were provided by two people, Professor M. Okada, Tohuku University and Mr. B.M.Ma, formerly of Crucible Research Center. My grateful thanks to both of them not only for the samples they provided, but also for their readiness to discuss any aspect of this research without any reservations. B.M.Ma, especially, provided me with samples with just two days notice. It was a great experience working with him. I was supported by an University of California Regent's Fellowship for one year of my stay at Berkeley and a James Monroe McDonald Fellowship supported me partially for another year. Furthermore, this work was supported by the Director, Office of Energy Research, Office of Basic Energy Sciences, Materials Sciences Division of the U.S. Department of Energy under contract No. DE-AC03-76SF00098.

I would also like to thank my fellow graduate students, especially those in the "G.T." group. First among them is K.Srikrishna, with whom I have had many stimulating discussions, not limited only to science. Dr. Tim Dinger guided me through the teething period at Berkeley with his great sense of humor and also shared his common sense and knowledge at every stage of his stay at Berkeley. Jimmy Chen was always willing to hear out my "brain-waves", however, inane they were. Simon Kwok, B.G.Demczyk and J.H.Ahn also helped me in the earlier part of my stay at Berkeley. I am grateful to them. Dr. K.M. Krishnan helped me a lot in the early stages of this research with some useful suggestions. Lai Hing Chan was one of my

best friends at Berkeley. I also wish to thank my other fellow graduate students, H.M.Ho, M.L.A.Dass, D.Callahan, T.Huynh, C. Carter, and undergraduate students H.Ng and F.Abhari who helped me carry out some of the experiments reported in this thesis. These people put up with me for upot four years. Need I say more ?

Thanks to Don Jurica for maintaining (or attempting to maintain) a state of equilibrium in and around the lab. He illuminated me on several aspects, not particularly related to materials science. Thanks also to Adrian Gronsky and Jean Zissler for their readiness to help out in a tight situation. Chuck Echer at the National Center for Electron Microscopy was a source of immense help in carrying out the analytical electron microscopy experiments. In addition, he was a great humorist and kept me humored during times of stress. Thanks also to John Holthuis and James Wu who helped me carry out the heat treatments. Ron Wilson and John Van Slyke were always willing to help me out on the SEM ; my thanks to them.

I gratefully acknowledge the support, both financial and emotional, of my parents during my whole educational career. They had faith in me all through. I would not be where I am but for them. I am also indebted to my wife, Sudha, for her patience, kindness and support ever since we were engaged. I would be lost without her. Thanks to my sister, Latha, for being a sister.

This work is dedicated to my family : my parents, my wife and my sister.

Finally, a big "THANK YOU" to the good lord who is there somewhere !

CHAPTER I
INTRODUCTION
1. HISTORICAL PROLOGUE

In the Intermag meeting of 1966, Hofer and Strnat[1] reported results of measurement of magnetocrystalline anisotropy of rare earth-cobalt alloys such as YCo_5, with the values of the first anisotropy constant K_1 reaching $5x10^7$ ergs/cm^3. This heralded the advent of a new class of hard magnetic materials based on compounds with large uniaxial magnetocrystalline anisotropy. One of the basic ideas behind the development of such materials was to combine elements with high magnetic moments such as Fe or Co with the high moments of the rare earths, while maintaining the high ferromagnetic ordering temperature of the 3d-metals. However, the total magnetization obtained depends upon the nature of the coupling between the rare earth atom and the 3d-atom[2]. The above selection criterion is not by itself sufficient to obtain the best permanent magnetic properties. Another guiding criterion is the presence of an easy or uniaxial magnetization direction, in the presence of a large magnetocrystalline anisotropy. This means that considerable energy must be expended to re-orient the magnetization from an easy direction to a non-easy or hard direction. The implications of this property in permanent magnet based applications are discussed in section I.3. One particular alloy in the rare earth-cobalt system which proved to be technically successful was Sm-Co. Specifically, two intermetallic compounds, $SmCo_5$ and Sm_2Co_{17}, possessed outstanding permanent magnetic characteristics and hence use in commercial applications followed.

The commercial development of Sm-Co based alloys depended very much upon the availability of Sm and Co. A significant portion (almost 50%) of the world's cobalt production comes from the African countries of Zaire (38%) and Zambia(12-15%)[3]. Thus, the western market was, to a large extent, controlled by the political health of these countries and their relationships with the western world. In 1978, the political situation in Zaire degraded rapidly. This led to frequent disruptions in cobalt supply and the price of cobalt in the western market rose sharply.

This, coupled with the rather strained political relations between these African countries and the western world, and the subsequent declaration of cobalt as a strategic element meant that : (1) commercial Sm-Co based magnet production would be stifled ; (2) other alternative alloys should be investigated.

While the Sm-Co system was being extensively investigated, other related systems, primarily, Fe-rare earth based systems were also being investigated. However, two main reasons prevented the development of Fe-rare earth based permanent magnets as a parallel to the Sm-Co based alloys. They were[4] : (1) In the Fe-rare earth system, the $Fe(RE)_5$ type compound could not be synthesised in a stable form (or even in a metastable form); (2) in the case of $Fe_{17}(RE)_2$ compounds, the following problems were encountered : (a) the hexagonal $Fe_{17}(RE)_2$ compound possessed a very low Curie temperature of 57°C compared to that of $SmCo_5$, which is about 730°C; (b) it did not exhibit uniaxial magnetocrystalline anisotropy but an easy plane of magnetization.
This led the search for ternary systems based on Fe-rare earths. Such studies were being carried out simultaneously in USA ,Japan, and in Europe. Several elements such as Si, Al, Ga, B, C, O, N were tried. Out of these systematic experiments, one compound, $Nd_2Fe_{14}B$ exhibited magnetic properties which were very suitable for permanent magnet applications[5,6]. These consisted of :
(1) A large saturation magnetization of 1.61Teslas(16.1kGauss) at room temperature.
(2) A high magnetocrystalline anisotropy, with the c-axis of the tetragonal $Nd_2Fe_{14}B$ as the easy axis.
(3) A relatively high Curie temperature of 312°C as compared to 57°C of Nd_2Fe_{17}.
(4) High thermal stability.

The discovery of this phase, almost simultaneously in Japan (Sumitomo Special Metals Co.) and in USA (General Motors Corpn.) has led to an explosion of research activity, in which the present author is also participating wholeheartedly, in an attempt to understand the evolution and details of the structure, microstructure and magnetic properties of Fe-RE-B magnets.

This dissertation details the results of the author's efforts in clarifying some of the microstructure related aspects of this exciting alloy system.

2. FUNDAMENTALS OF PERMANENT MAGNETS

The purpose of a permanent magnet is to provide a magnetic field in a particular volume in space(7). This can be achieved by an electro-magnet also, but a permanent magnet is a better choice since it provides a constant field without the continuous expenditure of power or the generation of heat. Thus, a permanent magnet is an energy storage device. Compared to electro-magnets permanent magnets offer the advantage of a larger ratio of the useful magnetic field volume to the volume of the magnet system. The usefulness of permanent magnets is especially apparent when a constant external field is required. To determine the material properties that are important for permanent magnet applications, it is essential to examine the conditions under which a permanent magnet operates. This depends upon the applications of the magnet.

Most of the essential magnetic data about a magnetic material (hard or soft) is contained in the hysteresis loop. Fig.I.1 is a typical hysteresis loop for a hard (permanent) magnet. In this figure, point "O" represents the thermally demagnetized equilibrium state of the magnet. In this state, each grain in the magnet consists of many "magnetic domains". When a field is applied to the magnet, the magnetization (induction) changes along the curve OL, which is called the virgin magnetization curve. The exact nature of the virgin curve will depend upon the microstructural state of the magnet. Point "L" represents the saturation point, wherein, the magnetization in all the grains (in a polycrystalline magnet) is along the applied field direction. Upon reversal of the applied field direction, the magnetization does not change along LO, but hysteresis is observed. The value of the magnetization at zero external field is called the remanence or remnant magnetization, B_r of the magnet. A large value of remanence is a prequisite for a good permanent magnet. As the applied field is increased further in the negative direction, the

magnetization drops to zero at a particular value of the applied field. This value of the applied field is called the intrinsic coercivity, iHc, of the magnet. A large value of iHc is another prequisite for a good permanent magnet. The extent to which a material will be suitable for permanent magnet applications depends on the amount of magnetic flux per unit area that can be generated and upon the maximum opposing field that can be tolerated without permanent loss of magnetization. This product (BH) of the flux density B and the associated opposing field H is called the energy product of the magnet. It is a very useful indicator of the performance of the magnet, since this is proportional to the potential energy provided by the magnet in an air gap. To determine the energy product of a magnet, information about the shape and size of the hysteresis loop, especially the second quadrant of the loop, is required. In the case of a permanent magnet under the influence of its own field, the opposing field will be the demagnetizing field. Under such conditions, the working point of the magnet is represented by a point in the second quadrant (or fourth quadrant) of the hysteresis loop. In the limiting cases of an infinitely long needle of a closed circuit (H=0) and an infinitely long plate (B=0), the energy product is zero. Between these two extremes, the energy product is a maximum for one particular combination of B and H. This is called the maximum energy product or $(BH)_{max}$. The three main quantities, namely, B_r, iHc, and $(BH)_{max}$ are simultaneously functions of the electronic structure dependent(i.e., inherent) properties as well as the microscopic (i.e., microstructural) parameters. In order to obtain a good permanent magnet, it is essential to optimise all the three parameters.

In addition to these fundamental properties, other attributes such as good corrosion resistance, low susceptibility to radiation damage (especially magnets used in electron beam wigglers, undulators and synchrotron sources), low temperature coefficients of iHc and B_r, good mechanical stability, easy machinability, etc. are also desirable.

The process of magnetization and hysteresis behaviour described above in the case of a technical permanent magnet involves the nucleation and movement of magnetic domain walls. A domain wall is a region of transition in magnetization, separating regions magnetized anti-parallel

to each other[8]. The process of movement of domain walls under the effect of applied field is shown schematically at the bottom in Fig.I.1. Thus, as the magnitude of the applied field is increased in one direction, the domain walls move so that the fraction of domains with magnetization direction parallel to the applied field direction is maximized. At saturation, ideally, there are no domain walls in the magnet and all the grains have their magnetization parallel to the field direction. On reversing the field direction, walls nucleate and traverse the grains to reverse their magnetization.

The saturation magnetization of a single crystal of a magnet is a fundamental property. It depends only upon the atomic species present and the nature of their electronic interactions. In the case of a polycrystalline magnet, the degree of mutual alignment of the grains will also play a role in determining the value of the saturation magnetization and consequently the remanence also.

A large value of iHc can be obtained, potentially, by two methods[9] : (1) if the material has a large shape anisotropy, i.e., it has a large aspect ratio, with the easy magnetization direction along the long axis of the particle. In this case, it is very difficult to reverse the magnetization direction, since the reversal process is opposed by large stray fields. A typical example is the case of Elongated Single Domain (ESD) magnets such as gamma-Fe_2O_3, AlNiCo, etc. ; (2) if the material has an easy magnetization direction coupled with a large magnetocrystalline anisotropy, characterized by a large value of the first magnetocrystalline anisotropy constant, K_1. This constant is obtained from the definition of the anisotropy energy as shown below :

$$E_{anisotropy} = K_0 + K_1.\sin^2\theta + \ldots\ldots\ldots$$

This equation describes the anisotropy energy, E, in terms of a series expansion of the direction cosines of the magnetization, relative to the crystal axes. Here, θ is the angle between the magnetization direction and the crystallographic direction, which, in the case of a uniaxial crystal, is the c-axis. K_0 is independent of θ and hence is ignored, since one is interested in the change in the energy when the magnetization vector rotates from the "easy" direction to a "hard" direction. K_1 is the first anisotropy constant and is generally the largest and the most important.

For a uniaxial crystal with the c-axis as the easy magnetization direction, K_1 is positive, so that the energy is the lowest for $\theta=0$. Typically, such crystals exhibit strong deviations from cubic crystal symmetry (such as hexagonal or tetragonal), with the c-axis being the easy axis of magnetization. The intrinsic coercivity in this case also will depend upon the microstructural condition of the magnet. The upper limit for the iHc obtainable is defined as the anisotropy field, H_A, of the magnet. This is the iHc of a magnet which undergoes magnetization reversal by a coherent rotation of the magnetization by 180°. (This derivation is presented in Appendix I). However, in technical magnets, such as the one described by the hysteresis loop in Fig.I.1, the reversal of magnetization occurs by the nucleation and movement of domain walls. Domain walls occur in such materials primarily because the demagnetizing fields are very high. Thus, above a particular grain size (the critical grain size) each grain prefers to exist in the multi-domain state in its lowest energy configuration, in the absence of any external field. Reversal by a domain wall mechanism means that the intrinsic coercivities obtained are much lower than the anisotropy field of the magnet. Thus, any attempt to improve the iHc of technical magnets must recognize the fact that domain walls exist and are the main cause for magnetization reversal. Consequently, the iHc can be increased if : (i) the nucleation of a domain wall is made difficult ; or (ii) the movement of the domain wall through the bulk of the grain is thwarted. This leads to a natural classification of the reversal behaviour of technical permanent magnets. In general, magnets in which the most difficult step is the nucleation step, are termed "nucleation controlled"[10]. On the other hand, if the movement of domain walls through the bulk of the grain is the most difficult step, the magnet is classified as a "pinning controlled" magnet, since the domain walls are pinned at certain sites and their movement prevented. Both processes occur to some extent in both types of magnets, but complete reversal is controlled by one of them. Thus, if the size of the grains is not below the critical size for single domain behaviour, the two main reversal mechanisms to contend with are the ones mentioned above. Consequently, any attempts to modify the structure and/or microstructure of the magnet must take advantage of either or both of these effects.

In general, since the particle (or grain) size is much larger than the critical size for single domain behaviour, only domain wall processes will be considered. Typical virgin curves and hysteresis loops of (i) a nucleation type magnet and (ii) a pinning type magnet are shown in Fig.I.2(a--i&ii)[9]. The corresponding microstructure is schematically illustrated in in Fig.I.2(b--i&ii) for the nucleation type and pinning type magnet respectively. On the other hand, when coherent rotation of magnetization is the mode of reversal, the iHc equals $H_A=2K_1/M_S$, where H_A is the anisotropy field of the magnetic phase, K_1 is the first anisotropy constant and M_S the saturation magnetization. The hysteresis loop in this case is rectangular, as shown in Fig.I.2(c). Nucleation of domain walls in technical permanent magnets occurs at regions of reduced magnetocrystalline anisotropy and /or regions of enhanced demagnetizing fields. The magnetocrystalline anisotropy of the matrix phase can be drastically altered at structural and chemical heterogeneities. Typical examples are grain boundaries, interphase interfaces, antiphase domain boundaries, dislocations.etc. Domain wall nucleation occurs at these regions because the domain wall energy, at least locally, is reduced to a value much lower than that in the matrix. The theory of nucleation fields has been reviewed by Aharoni and co-workers[11,12] who have concluded that for hard magnetic materials, for which $K_1 >> M_S^2$, the most probable cause for domain wall nucleation is a local reduction in the magnetocrystalline anisotropy. Localized irregularities, on the other hand can lead to demagnetizing fields of the order of $18M_S$[9], which, in turn, can be a source of lowered nucleation field. Typical examples of pinning sites are coherent precipitates parallel to the domain wall, antiphase domain boundaries, grain boundaries, etc. It should be pointed out that good nucleating sites can also act as good pinning sites.

Magnetization reversal in Particles: This aspect is being introduced here since many of the investigations of magnetization reversal mechanisms in permanent magnets have been carried out through a study of the reversal behaviour in single particles of these magnets. There have been numerous experiments carried out to understand the magnetization and reversal behaviour of both fine particles and

polycrystalline magnets in permanent magnetic systems such as Mn-Bi, ferrites, $SmCo_5$, etc[13-20]. An excellent review has recently been presented by Livingston[10]. These experiments have revealed abrupt reversal events which indicate that the iHc is controlled by either a nucleation or an unpinning event. The earliest classification came from Becker, who divided the nucleation and/or pinning sites into type I and type II[21]. Type I sites are those where a domain wall is pinned due to insufficient prior magnetizing field, and thus are associated with incomplete saturation of the grains. These pinned sites act as "embryos" for reversal on reversing the field direction. However, as the magnetizing field is increased, these "embryos" are progressively eliminated. Consequently, the nucleation field also increases, although not to a value close to the anisotropy field. This inability of the nucleation field to reach a value equal to the anisotropy field has been attributed by Becker to the presence of Type II nucleation sites. These sites are independent of the magnetizing field. They nucleate a wall at specific values of the applied field, depending upon their potency. The existence of such nucleation sites is supported by results on chemical polishing of the particles[22], which inevitably increases the iHc and the nucleation field. Such results suggest that surface defects can serve as nucleation sites, either due to the presence of low anisotropy regions or due to high demagnetizing field, as was mentioned earlier.

Becker[23] studied the temperature dependence of the nucleation fields of Co_5Sm particles and did note different temperature dependences for different particles reversing by different mechanisms. This was also confirmed by Gass et.al[24], who found that type II nucleation sites have a larger temperature dependence of the nucleation field than type I sites. They also correlated the change in the nucleation field to the temperature dependence of K_1 or $K_1^{1/2}$. Several workers have also studied the dependence of nucleation field on the angle between the applied field direction and the easy axis of the particle[25-28]. Type I sites appear to satisfy the Kondorsky relationship, i.e., the nucleation fields should increase as $1/(\cos\phi)$, where ϕ is the angle between the field direction and the easy axis. However, in most cases, the increase is somewhat slower than that predicted by this relationship.

Polycrystalline Magnets : The magnetization reversal behaviour of such magnets will be the focus of this dissertation. The main difference between single particles and polycrystalline magnets is the effect of particle interactions and the consequent changes in the demagnetizing field. Thus abrupt changes in the magnetization will be replaced by gradual changes, both due to the effect of a spectrum of nucleation fields as well as due to the effect of particle interactions(10). However, as an extension from the particle studies, it can be presumed that each grain in a nucleation type magnet has a defect controlled "nucleation field". But for the effect of particle interactions on the demagnetizing field, the reversal behaviour can still be considered as an isolated event for each grain. The local demagnetizing field, will, however, depend on the state of reversal of the neighbouring grains. Several experimental criteria have been used to identify the dominant reversal mechanism in such magnets, in which, as was described earlier, the main types are the nucleation and the pinning type magnets. These criteria are described along with experimental results in section III.4.

It is obvious that the intrinsic coercivity (and hence the energy product) of a permanent magnet is very sensitive to the microstructure, with a very complex dependence upon the microstructural parameters. The real structure of the magnet, consisting not only of the crystal structure of the magnetic phase in question, but also the shape , size and surface characteristics of the grains, contaminations, point, line and surface defects, and their distribution, precipitates and second phase particles, their magnetic properties relative to the matrix phase, their degree of coherency with the matrix phase, all contribute to the magnetic behaviour of the magnet. This is where the role of a materials scientist comes into play. Once the inter-dependence of structure-microstructure -processing-magnetic properties is established, further improvement of the magnetic properties to suit real life needs becomes easier. This is precisely the goal of this dissertation. Starting with a thorough research of the microstructural details of a typical Fe-Nd-B magnet, along with the knowledge of the magnetic properties, the dominant reversal mechanism will be established. This will consequently lead onto alloy design

considerations in order that the magnetic properties can be improved over that of existing magnets.

In the next section, the reader will be introduced to the Fe-Nd-B alloy system. Since the outstanding magnetic properties of this system accrues from the ideal structural and magnetic properties of the magnetic phase, $Nd_2Fe_{14}B$, in this alloy system, the next part of this introduction will be devoted to the structural and magnetic features of this phase.

3. THE Fe-Nd-B ALLOY SYSTEM

Before the discovery of hard magnetic properties in Fe-Nd-B based alloys, it was not a very commonly studied alloy system. However, since the discovery in 1983, there has been an explosion of research to elucidate the structural and magnetic intricacies of this system, specifically, the phase $Nd_2Fe_{14}B$, which is the main magnetic phase. Thus, beginning with the crystallography of this phase, the evolution of the magnetic properties will be detailed, followed by a discussion of the reasons for the success of this system and the major drawbacks. The effects of alloying substitutions in the $RE_2Fe_{14}B$ lattice on the magnetic properties and their alloy design implications will also be discussed.

Complex alloy structures, especially those occurring in transition metal alloys, are generally determined by the geometrical requirements of sphere packing, be they of the same size or different[29,30]. A prominent characteristic of such structures is that a structural unit seldom found in cubic or hexagonal structures, i.e., tetrahedral groupings of atoms, is found very frequently. Thus, the coordination polyhedra have only triangular faces, thereby achieving, albeit locally, Platonic-type solids. Thus, for 12-fold coordination of rigid equal sized spheres, it is neither the cub-octahedral coordination of the fcc structure nor the twinned cub-octahedral coordination of the hcp structure that is found in such alloy systems, but the icosahedral coordination. As has been succinctly described by Frank and Kasper[29,30], the presence of the icosahedral coordination has two consequences : (1) with slightly compressible mutually attracting spheres or with spheres of slightly different sizes,

the circumscribing sphere will be the least for the icosahedral coordination---hence the lowest energy. (2) The second consequence is that in icosahedrally coordinated compounds, simultaneous coordination requirements of the atoms which are not the central one, can be met by a slight deformation of the coordination sphere.

Kasper[31] recognized that there are only four types of triangulated coordination shells with 5- or 6-fold vertices, wherein no atom with 6-fold surface coordination was contiguous. These four types are the ones with 12, 14, 15 and 16 fold coordinations. These occur very frequently in transition metal alloys. These have been termed normal coordinations by Frank and Kasper[29,30]. One typical feature in structures with normal coordination is the occurrence of unbounded planar or almost planar layers. Two main types of layers occur : (1) In the first, called the primary layer, the arrays comprise of tessellations of triangles and hexagons. In this layer the connections correspond to interatomic distances. (2) The second type, called the secondary layer, consists of normal coordination, made up of tessellations of squares and triangles. A typical example of each is shown in Fig.I.3(a&b). These two basic nets are denominated by the numerical symbols, 3.6.3.6. and $3^2$4.3.4. These are known as Schlafli notations and represent the number and sequence of various polygons around each vertex. More details about the nature of such complex sphere packings can be found in the classic papers of Frank and Kasper.

$Nd_2Fe_{14}B$ is a classic example of how the ideas of sphere packing and primary and secondary layers can be used to describe the arrangement of atoms relative to each other in the unit cell. The next section will describe the crystallography of the phase $Nd_2Fe_{14}B$.

Crystallography of $Nd_2Fe_{14}B$: The crystal structure of $Nd_2Fe_{14}B$ is shown in Fig.I.4(a). The original structural determination was carried out by Herbst et.al[32] through neutron diffraction studies. Concurrently, several other structural determinations were being carried out by Shoemaker et.al[33], Givord et. al[34], Sagawa et.al[6], and Boller and Oesterreicher[35]. The unit cell of the tetragonal structure phase contains 68 atoms. The various atomic sites, their occupancies and

coordinates (in terms of the lattice constant a=8.9Å; c=12.18Å) are tabulated in Table I[36]. The compound belongs to the space group $P4_2/mnm$, with four formula units per unit cell. It can be described in terms of puckered nets perpendicular to the c-axis, which bears similarity to the sigma phase in Co-Cr, Fe-Cr alloys. The almost planar (puckered) structure is shown in Fig.I.5(a-c). In this figure, (a) represents the mirror plane at z=0 ; (b) represents atoms at z≈1/8 and z≈3/8 and at z≈1/4 ; (c) represents atoms in the mirror plane at z=1/2. There are triangular nets formed by Nd(1), Nd(2), Fe(1) and B in the mirror planes at z=0 and z=1/2 (Fig.I.5(a) and (c)). The dotted lines in these indicate distances that are longer than the bond distances. Between each pair of adjacent mirror planes are sandwiched two puckered sigma-phase main layer type nets (i.e., at z≈1/8 and z≈3/8) of only Fe atoms. At z≈1/4 there exists a sigma-phase subsidiary layer type net, also made up of Fe atoms. These primary and subsidiary layers are typical examples of the coordinations described by Frank and Kasper.

The spatial relationships among the several atomic "layers" is shown in Fig.I.5(a-c)[33]. The Nd atoms are near the centers of Fe hexagons, in the z≈1/8 and z≈3/8 layers. In the z=0 and z=1/2 planes, the semi-regular tessellation of $3^2.4.3.4$ is observed, Fig.I.5(a,c) (in dark lines). This net provides the closest packing of equal spheres (Nd in this case) in a plane in which there is 4-fold symmetry and every sphere has the same environment, apart from orientation. The coordinations of the different atoms are given in Table II[33]. It is noteworthy that all atoms except B have 12 or more coordinated shells, in the Frank and Kasper notation. Also, it should be pointed out that the Fe atoms at the j_2 sites have more than 12-fold coordination (14-fold coordination). This site has very unusual and large magnetic moments. The consequences of this will be discussed later in this section. The other Fe sites which are not in the z=0 and z=1/2 plane all have distorted icosahedral environments. The coordination polyhedron of the Fe(c) atoms, i.e., the Fe atoms in the z=0 and z=1/2 planes in Fig.I.4(a) is icosahedral, but distorted to allow for larger bonding distances to Nd atoms. In the vertical direction, there are infinite zig-zag rows of Fe-Nd-Fe-Nd atoms. The puckering of the hexagonal layers perpendicular to these rows is due to the relative

inclinations of the rows with respect to each other. The arrangement of triangular nets in this structure and in the sigma-phase nets above and below it resembles the arrangement of layers in the $CaCu_5$ ($D2_d$), the parent structure of $SmCo_5$. In the case of $SmCo_5$, the rare earth atom is surrounded by six transition metal atoms in the plane, six above and six below, in the form of planar "kagome" nets. In the case of $Nd_2Fe_{14}B$, there are the mirror planes at z=0 and at z=1/2 formed by the Nd atoms which are surrounded by B and Fe atoms in the plane. The sigma-phase type nets above and below this plane contain 3.6.3.6., 6^3 and $3^2.6^2$ tessellations, as shown in Fig.I.5(b). The bond angles in the $Nd_2Fe_{14}B$ triangular nets range from 57.9° to 66.7° except for those with a j_2 site at the vertex, which, due to the puckering, lie between 52.4° and 55.7°. The Fe-Fe bond lengths extend from 2.39Å to 2.8Å. It may be pointed out that for Fe-Fe bond distances lower than 2.5Å, the exchange interactions become negative (anti-parallel coupling).

The Boron coordination is shown in Fig.I.4(b)[32]. Boron atoms occupy the centers of trigonal prisms, formed by the three nearest iron atoms above and the three below the z=0 and z=1/2 plane. The prisms pucker the Fe nets(as was described above) since the Fe(e) and Fe(k_1) atoms(Fig.I.4(a)) in them are displaced significantly towards the boron containing plane, as compared to other Fe atoms in the nets. It appears that the prisms are strong structural units linking the Fe planes above and below those containing Nd and B. The prisms also coordinate all rare earth and boron atoms. Thus, three rare earth atoms are bonded to each boron through the rectangular prism faces. The fundamental nature of such trigonal prisms in many transition metal-metalloid (e.g., Fe-C and Fe-B systems) has been stressed by Gaskell[37].

Magnetic properties of the $RE_2Fe_{14}B$ compounds (R=Nd and other rare earths and Y): In this section, the origin of the excellent magnetic properties of this compound will be discussed. Since Nd is the most common rare earth element used in Fe-RE-B magnets, the discussion will be based upon the magnetic properties of the $RE_2Fe_{14}B$ compound of Nd. The short-comings in the magnetic properties of this phase will then form the background for a discussion of substitutions on Fe, Nd and B sites.

The relevant magnetic properties are summarized below, specifically for $Nd_2Fe_{14}B$:

(1) Saturation magnetization of 1.61Teslas(16.1KGauss) at room temperature.

(2) Curie temperature of 312°C.

(3) Anisotropy field of 71kOe at room temperature.

(4) First order anisotropy constant of 3.5MJ/m^3.

(5) Maximum possible energy product of 65.4MGOe.

To put these properties in perspective, they are compared with those of two other permanent magnet systems, namely, $SmCo_5$ and AlNiCo. These results are presented in Table III. Clearly, the magnetic properties are quite impressive. The origin of these properties is summarized below. Most of the details of the intrinsic magnetic properties are discussed in several of the magnetism conference proceedings.

(1) Saturation magnetization and remnant magnetization: The large value of saturation magnetization of $Nd_2Fe_{14}B$ is attributable to the following reasons :

(a) the almost full contribution of the iron moment of 2.1μ_B/Fe atom to the total magnetization, mainly due to large Fe-Fe 3d-exchange interactions; (b) parallel coupling of the Fe and Nd moments (since Nd is a light rare earth); (c) an induced component to the Fe moment due to the 3d-4f electron interactions. The moment coupling in $Nd_2Fe_{14}B$ (and in general $RE_2Fe_{14}B$) is similar to that observed in R-Fe and R-Co intermetallics, i.e., there is an anti-ferromagnetic coupling between Fe-spins and R-spins. Thus, for compounds with R= light rare earth (J=L-S), the total rare earth moment is coupled parallel to the Fe spins. On the other hand, in the case of heavy rare earths (J=L+S), the R moment is anti-parallel to the Fe moment. This difference in coupling should be evidenced in the temperature dependence of magnetization. In the case of the light rare earths(parallel coupling) the magnetization should increase with lowering of temperature, while the converse is true for the heavy rare earths. These features have been experimentally observed by several researchers. The Fe moments have been investigated in detail by Givord, Li, and Tasset[38], using Polarized Neutron Diffraction. The results are

summarized in Table IV. The difference in the moments of Fe in the six sub-lattices can be attributed to the differences in the local environments of the respective Fe atoms. Thus, a high Fe coordination for the Fe(4) site is associated with the large value of magnetic moment of Fe in this site. On the other hand, when the Fe atom has a large Nd coordinance, the moment is lower. Data on Fe-B alloys(39) indicate that the Fe moment is reduced by 2p-3d electron transfer. A similar effect is found in the case of the Fe(1) site, which exhibits a markedly lower moment. Bolzoni et.al expect strong hybridization between low lying p-states of Boron and the d-states of the rare earth atoms, from the high stability of rare earth-boron alloys(40). They attribute this as one of the reasons for the large 3d moment due to the indirect reductions of 3d-5d hybridization. The magnetic behaviour of the Fe sub-lattices have been determined by using non-magnetic rare earths such as Ce^{+4}, Lu^{+3} or Y^{+3} (41-48). The Fe sub-lattices exhibit anomalous temperature dependence of lattice parameters, indicating the possibility of magnetostrictive effects. The different iron moments have also been confirmed by several Mossbauer effect and neutron diffraction studies(49-52). The Mossbauer studies indicate that the internal magnetic fields scale as the Curie temperature, with the spectra being independent of the rare earth component. These results indicate that the electronic configurations of the iron atoms are nearly the same in all the compounds. The occurence of a large magnetic volume anomaly(i.e., an anomalous expansion below T_C) in the magnetically ordered state is similar to that in R_2Fe_{17} compounds. This is due to the minimization of magnetic energy at the expense of elastic energy. These effects suggest that the magnetic interactions exhibit a strong dependence on the Fe-Fe interatomic distances. Thus, depending upon the Fe-Fe distance, the coupling can vary from parallel to anti-parallel. The volume magnetostriction varies as the square of the magnetization.

Measurements of saturation magnetization on $Ce_2Fe_{14}B$ (in which Ce exists as Ce^{+4}) indicate that the Fe saturation magnetization is not very different from that of trivalent rare earth 2-14-1 compounds. This indicates that changes in the valence electron concentration do not have a strong effect on the magnitude of the Fe moment, thus suggesting a more

localized 3d moment. Measurements of the difference in moments between $Nd_2Fe_{14}B$ (where the rare earth is magnetic) and $Y_2Fe_{14}B$ (where it is non-magnetic) indicate that the Nd moment is about $3.3\mu_B$[42], which is approximately 92% of the free ion moment of Nd. This indicates little quenching of the Nd moment by crystal field interaction. The observation of the rare earth moments of almost the same magnitude as g.J, indicates that the influence of the exchange field experienced by the 4f moments is much greater than that of the crystal field although the crystal field splitting still determines the preferred direction of the 4f moments. Replacement of boron by carbon leads to a decline in the saturation magnetization, probably due to a reduction in the mean iron moments[53]. The saturation magnetization of several $RE_2Fe_{14}B$ compounds is tabulated in Table V. From this Table it is evident that one of the reasons for the success of Nd and Pr over other rare earth elements is the large room temperature saturation magnetization.

(2) Curie Temperature: The higher Curie temperature in $R_2Fe_{14}B$ compounds as compared to the R_2Fe_{17} compounds can be attributed to the Fe-Fe interatomic distances, which affects the Fe-Fe exchange interactions[36,38]. In addition, the coordinance of the Fe atoms in $R_2Fe_{14}B$ is higher than that in R_2Fe_{17} compounds. This can be observed in the crystal structures of $R_2Fe_{14}B$ and R_2Fe_{17} , which are depicted in Fig.I.4(a) and Fig.I.6. respectively. The higher T_c of the $R_2Fe_{14}B$ structure may be attributed to the presence of completed Fe-Fe triangular nets that are not interrupted, as in the case of the R_2Fe_{17} structure, by Nd atoms. The reduction in Curie temperature compared to pure Fe can be attributed to the short interatomic distances (< 2.5 Å) which occur for some of the Fe sublattices. For the rare earth series, Gd has the highest T_c of 650°K, while the tetravalent rare earths Ce^{+4} and Th^{+4} have a low T_c of 425°K and 480°K respectively.

The Curie temperatures are almost twice as large for the cobalt counterparts despite the smaller Co moment[54-58]. This can be directly associated with the Fe-Fe (or Co-Co) interatomic distances, an aspect which has been observed in other isostructural series of rare earth intermetallics. For Co substituted $RE_2Fe_{14}B$ compounds the increase in

T_c has been explained in terms of a preferential occupation of the k_2 and j_1 sites, which in the case of Fe are involved with negative interactions. The RE-TM exchange also appears to affect the Curie temperature, since the Gd compounds have a larger T_c compared to the La or Lu compounds. This is thought to be associated with changes in the local environments, specifically at the Fe(4c) site, which dictates the 3d-exchange interaction along the c-axis. The Curie temperatures have been expressed in the mean field approximation with good agreement for the heavy rare earths, although for the light rare earths the agreement is not so satisfactory[42]. This difference has been attributed by Givord et.al[46] and Sinnema et.al[42] to the different 4f-5d overlap for the heavy and light rare earths. The presence of boron also appears to be necessary for the high Curie temperature, since replacement of boron by carbon leads to a marked decrease in the Curie temperature.

(3) Magnetocrystalline anisotropy and anisotropy field: In the $Re_2Fe_{14}B$ system, crystal anisotropy arises due to two causes[40-47,59-63] : (1) a major portion (60-70%) arises from the large crystal field splitting induced anisotropy of the rare earth atom when it has a non-zero orbital moment ($L \neq 0$) ; (2) the second contribution, which is a significant one, to the anisotropy comes from the anisotropy of the Fe sub-lattice, which can be inferred from the substantial magnetic anisotropy in $RE_2Fe_{14}B$ compounds in which the rare earth atom has no orbital moment (Y & Gd). This anisotropy of the Fe sub-lattice is of the same order as that of a hypothetical hexagonal Fe. It is believed that anisotropic dipolar interaction between the magnetic moments is not the main cause for this large anisotropy. Thus, in essence, the magnetic anisotropy is due to the interplay of crystal electric field splitting of the rare earth atom and the exchange interactions with the Fe moments. The nature of the rare earth atom dictates the overall anisotropy. The anisotropy fields of several $RE_2Fe_{14}B$ compounds are tabulated in Table V[64].

In a tetragonal symmetry, the magnetocrystalline anisotropy energy can be expressed as : $E_a = K_1.\sin^2\theta + K_2.\sin^4\theta + K_3.\sin^4\theta.\cos 4\varphi$, where, K_1, K_2 and K_3 are the first, second and third order anisotropy constants ; $\theta=$

the zenithal angle between the magnetization direction and the c-axis and φ=the azimuthal angle from the a-axis. The anisotropy constants are measured from high field torque curves using a spherical single crystal sample. At 4.2K, $RE_2Fe_{14}B$ compounds with RE=Sm, Er and Tm have the magnetic easy axis along the [100] direction of the tetragonal structure, while the other rare earths have the easy axis along the [001] axis, except Nd and Ho, which have a canted spin behaviour. At room temperature, Sm, Er, Tm and Yb have an easy plane while the others have an easy axis of magnetization.

Crystal field and magnetic anisotropy : The crystal field at the rare earth sites creates local anisotropy which determines to a large extent the magnetic anisotropy of the non-s-state rare earth atoms (i.e., those which do have an orbital moment). There are two rare earth sub-lattices, 4f and 4g, and eight rare earth sites in each unit cell. Both the 4f and 4g sub-lattices have mm point group symmetry. The expression for the crystal field at each site can be expressed as : $H = \Sigma_{n=2,4,6} B_n^m . O_n^m$, where B_n^m are the crystal field parameters and O_n^m are called the Stevens operators(47). At low temperatures, the second, fourth and sixth order terms are all important and hence the magnetization, in some cases, can be quite exotic. However, upon raising the temperature to room temperature the fourth and sixth order parameters decline rapidly and hence around room temperature the second order term is most important. At very high temperatures the second order term also declines rapidly and hence the anisotropy is governed by that of the transition metal. The second order term can be represented in terms of the second order Stevens coefficient θ_2, whose sign determines whether the compound has uniaxial anisotropy or easy plane magnetization. Thus for RE= Pr, Nd, Dy, Ho θ_2 is negative and the compounds exhibit uniaxial magnetization along the c-axis while for Sm, Er, Tm, and Yb θ_2 is positive and the compounds exhibit an easy plane of magnetization. This behaviour is opposite to that observed in the case of $SmCo_5$ compounds and can be explained qualitatively in terms of a change in the local environment between the two related structures(47).

The temperature dependence of the anisotropy in $RE_2Fe_{14}B$ is anomalous(40,65). With the exception of Th, there is an increase of

anisotropy up to $T/T_C \approx 0.4$. This can be explained as a result of : (i) competing anisotropies for the different Fe sites ; (ii) the magneto-volume anomaly mentioned earlier, leading to a change in the lattice parameters with a corresponding change in the anisotropy. The temperature dependence of the anisotropy field can be classified into two categories : (a) those of compounds in which the rare earth atom has an orbital moment ; (b) those in which the rare earth atom has no moment. As was mentioned earlier, the strong temperature dependence of the rare earth anisotropy leads to the anisotropy being dominated by the Fe sub-lattice anisotropy at high temperatures. However, at low temperatures, the anisotropy is dominated by that of the rare earth atoms. In the case of S-state rare earth atom, the temperature dependence of anisotropy field is modest. In the case of these compounds, the anisotropy field decreases with decrease in temperature. This indicates that the different Fe sites have different contributions to the anisotropy and also that their temperature dependence may be different. Attempts have been made to explain the anisotropy of the compounds in terms of a single ion crystal field model. The results of such computations indicate that a simple point charge model (i.e., a Coulombian interaction) cannot be used. The exact cause for the Fe sub-lattice anisotropy, which is clearly demonstrated in the compounds with s-state rare earth elements, is still not well understood.

4. Substituent effects in $Nd_2Fe_{14}B$: $Nd_2Fe_{14}B$, although possessing most of the desirable magnetic properties for permanent magnet applications, suffers from certain important drawbacks. The first among them is the rather low T_C which produces an undesirably high reversible temperature coefficient of remanence. Thus, even at a temperature close to room temperature, T/T_C=0.56, significant variations in the magnetic properties due to thermal fluctuations are observed. Another undesirable property is the rapid fall in iHc with temperature. This allows normal demagnetizing fields to cause large irreversible losses in magnetization. Yet another drawback is the availability and cost of Nd. The main cost in Nd production is in the refining of the metal from other rare earths such as Ce, Pr and La, all of which are chemically

similar. Thus, improvement of the properties of this phase and broadening the range of applications will depend upon how these drawbacks can be overcome. In this section, the effect of alloying additions to overcome these problems will be discussed. The effect of one such additive, Dy, on the microstructure and magnetic properties of Fe-Nd-B magnet will be discussed in section III.6.

The low T_c of $Nd_2Fe_{14}B$ can be raised by addition of Co[54-58]. By progressively replacing Fe by Co, the Curie temperature can be raised from 589°K to 1004°K. This increase in the Curie temperature can be attrtibuted to the changes in the inter-atomic distances upon going from Fe to Co, leading to better exchange interactions. In partially Cobalt substituted compounds, the preferential occupation of the k_2 and j_1 sites by Co may explain the sharp rise in Curie temperature observed. In addition, in $Nd_2(Fe_{1-x}Co_x)_{14}B$, for $x<0.2$, there is an increase in the saturation magnetization, which can also be attributed to the above effect. Thus, the essence in improving the T_c is to preferentially replace the Fe atoms at the sites where the exchange interactions are negative. However, further increase in the cobalt content reduces the saturation magnetization due to the lower moment of Co. Since most of the contribution to the saturation magnetization comes from the Fe atoms (or in general from the 3d element), and replacement of Fe by Co is not useful beyond $x=0.2$ (as shown above), improvements in the saturation magnetization beyond that of $Nd_2(Fe_{1-x}Co_x)_{14}B$ may be difficult. In addition, replacement of Nd by other rare earth elements such as Dy, Ho or Gd, which have large moments, is not beneficial either, due to the anti-ferromagnetic interactions with the Fe spins. Thus, one is confronted with the limitation that improvements in the saturation magnetization (and hence the remanence) of compounds with the same crystal structure may not be feasible. This in turn, means that the energy product cannot be increased considerably above that of the Nd based compounds. Thus, summing up, significant improvements in the energy product can be made only if the iHc of the magnet is increased by suitable metallurgical manipulations, with the remanence and saturation magnetization maintained constant. Possible solutions to this difficult task are presented in section III.6.

Due to the chemical similarity of the rare earth elements, a large number of solid solutions with different properties can be made by systematically changing the nature of the rare earth element[47,53,55,66-70]. Thus, the rapid fall of iHc with temperature or the drop in anisotropy field can be offset by replacing part of the Nd by Dy or Tb. $Dy_2Fe_{14}B$ and $Tb_2Fe_{14}B$ have a very large anisotropy field compared to $Nd_2Fe_{14}B$, Table V. However, one disadvantage in adding Dy or Tb is that, due to the anti-ferromagnetic coupling of the Dy spins with the Fe spins, the saturation magnetization decreases. Thus, these elements have to be added in limited amounts. Al can also be added to improve the anisotropy field and thus the iHc, although not as dramatically as in the case of Dy or Tb[58,71]. In this case, Al replaces Fe and this also causes a drop in saturation magnetization and Curie temperature. It has also been shown that by judicious choice of the rare earths and their concentrations, the temperature coefficient of remanence, dM/dT, can be made zero. This has been accomplished by the addition of Ho, Er and Dy[72]. Bolzoni et. al have studied the replacement of Nd by Pr and Fe by Co[56]. They have found that while the anisotropy field of $Nd_2Co_{14}B$ is lower than the corresponding Fe compound, the reverse is true for the Pr compounds. In general, the anisotropy field for the Co compounds are much higher than that of the Fe compounds, due to the smaller saturation magnetization of the Cobalt compounds. The general behaviour of the Co system is similar to that of the Fe system. Replacement of Fe by Mn leads to a decrease in the Curie temperature and saturation magnetization[73]. The anisotropy field has been found to increase. Addition of Zr has been shown to increase the anisotropy field with a concomittant decrease in the saturation magnetization and Curie temperature[74]. In terms of alloy design implications, the role of Cobalt, Dy and Al are important. In this investigation, the effect of Dy will be described.. There have been several investigations of the simultaneous effect of Co and Al, and optimum compositions have been arrived at, in terms of permanent magnet properties[71,75-80]. However, systematic investigations of the effect of such additions on the microstructure and the correlation to the magnetic properties have just been initiated[81,82]. In terms of the economy of permanent magnet production, the addition of

Ce, Pr, La has been found to be beneficial[83-85]. If an alloy of Ce-Pr-Nd-La, usually termed as "mischmetal" is used instead of pure Nd, the magnetic properties are quite inferior to that of the ternary alloy. For example, the iHc of a magnet with significant Ce-Pr additions is only about 5-6 kOe and the energy product only 24-25 MGOe. However, the cost of the magnet is cut by a third.

Structure-Property Relationships: Several key features characterize the Fe-Nd-B system and its success story. The most prominent among these is the separation of the Fe and the Nd,B layers, Figs.I.4 and 5, which results from the formation of the trigonal Fe prisms having B at the centers. These prisms occur in many transition metal-metalloid systems. In this case it happens that this not only dictates the bonding arrangement of the Fe layers but also allows space for the rare earth atoms to fit in the prism mid-planes. Thus, this arrangement is sterically favourable, with the rare earth atom occupying a convenient and strain free location.

The major differences in magnetic properties between the $Nd_2Fe_{14}B$ structure and the related Nd_2Fe_{17} structure can be understood by studying the structure of the two compounds. The $Nd_2Fe_{14}B$ structure is depicted in Fig.I.4(a), while the structure of Nd_2Fe_{17} is shown in Fig.I.6. Two important features identify the $Nd_2Fe_{14}B$ structure from the Nd_2Fe_{17} structure. The first is the higher Curie temperature of 312°C compared to 57°C. The second is the easy axis of magnetization compared to the easy plane in Nd_2Fe_{17}. The origins of these differences can be found in the crystallography of the two compounds. In the case of Nd_2Fe_{17}, only half of the triangular network is occupied by the Fe(c) sites. For the other half layers, Nd atoms interrupt the Fe-Fe bonding. In contrast, there are no Nd atoms to interrupt the Fe-Fe exchange in $Nd_2Fe_{14}B$. This is responsible for the higher Curie temperature. The easy axis behaviour is linked to the highly anisotropic Fe sub-lattice and the crystal field of the rare earth ion. This is evidenced from the easy axis of $Y_2Fe_{14}B$, which does not have a rare earth anisotropy contribution. In the case of $Nd_2Fe_{14}B$, except for the Fe(c) site and the Fe(j_2) sites, there are more number of Fe atoms above a given Fe atom than below it. In

Nd_2Fe_{17} only the Fe(c) atom exhibits significant anisotropy in coordination. Much progress has been made in furthering the knowledge of the intrinsic properties of this fascinating system, although much more remains to be unravelled. The above summary of the intrinsic properties of this family of compounds is by no means exhaustive in detail, but does provide at least an overview of the complexity of the system and summarizes the state of knowledge of the intrinsic properties of this alloy system.

4. AIM, APPROACH AND SCOPE OF THIS INVESTIGATION

The broad aims of this investigation are the characterization of the microstructural and the details of magnetization reversal of a typical sintered Fe-Nd-B magnet with optimum permanent magnet properties. This will include the structural and microanalytical characterization of various phases observed in such magnets and the inter-relationship of each phase to each other. Concurrently, the magnetic properties will be characterized in order to understand the dominant mechanism of magnetization reversal. Using the information obtained about the microstructure and the magnetization reversal mechanism, the role of microstructure in causing magnetization reversal will be examined. With the resolution of this complex problem , a general magnetization reversal model, based upon the knowledge of the microstructural features and the magnetic properties, will be proposed. This will describe the reversal behaviour of a magnet with optimum magnetic properties. With this knowledge, the focal question of this investigation, i.e., the effect of post-sintering heat-treatments on the magnetic properties, will be be addressed. The effect of post-sintering heat-treatments will then be built into the model, based upon the results of microstructural examination and measurement of magnetic properties. The statistical aspects of magnetization reversal, an aspect that is very pertinent to polycrystalline magnets, will also be invoked to take account of the distribution in the structural and magnetic characteristics of real magnets. Examination of the interaction of domain walls with the microstructural features by Lorentz microscopy will be used to provide supporting evidence for the details of magnetization reversal.

The salient aspects of the model(s) proposed above will then dictate the direction of the second part of this investigation, which will deal with the alloy design aspects as related to the particular type of magnetization reversal in this alloy system. These experiments will aim at improving the magnetic properties of the

ternary Fe-Nd-B alloy through the knowledge of the details of the microstructure and the magnetization reversal process. Specifically, the effect of substitutions on the rare earth site to improve the intrinsic coercivity as well as the temperature dependence of magnetic properties of the magnets, will be considered. In addition, novel experiments, involving specific sintering additives, will be carried out to modify certain microstructural aspects of the magnet, which are considered to be important in governing the magnetization reversal behaviour of the magnet (as determined from the first part of this investigation).

The scope of this investigation is limited primarily to the study of the extrinsic properties of the magnets in relation to the microstructural and micro-analytical details of the magnet. However, existing knowledge about the intrinsic characteristics of the magnet, specifically the $RE_2Fe_{14}B$ phase and the effect of alloying on its intrinsic properties, will be made use of. This investigation will thus attempt to unravel the complexity of magnetization reversal, from the knowledge of the above. The guiding factor will be the extrinsic and microstructure dependent magnetic properties. Thus, this thesis deals with the microstructural and micro-chemical causes for magnetization reversal in a specific class of permanent magnets and attempts to rationalize the complex process of magnetization reversal in this new class of technologically important magnets, based primarily upon the microstructural observations.

CHAPTER II
EXPERIMENTAL DETAILS

1. PRODUCTION OF SINTERED Fe-RE-B MAGNETS

In this section, the overall route for the production of sintered magnets will be discussed. This route is adopted for the manufacture of fine particle permanent magnets(5). The same general sequence has been adopted to make all the magnets used in this study. Wherever relevant, the differences in the specific production conditions will be highlighted. The various steps involved are illustrated schematically in Fig.II.1. The alloy of required composition was induction melted in an alumina crucible under an Argon atmosphere. The ingots were then crushed in a nitrogen atmosphere to a particle size of about 1mm in a jaw crusher. Following this, the coarse powders were ground down to 100μm in a disk mill, then pulverized either dry or under trichloro-trifluoroethane to about 3μm in a jet mill or in a ball mill. The powders were then magnetically aligned, with a field of 10kG and pressed normal to the aligning direction with a pressure of 200MPa. The green compacts were then sintered at 1050-1100°C in an argon gas atmosphere/vacuum for a period of 1-3 hours and cooled to room temperature at the requisite cooling rate (i.e., quenching in water, oil, air or furnace cooling at 50°C/hour). The magnet with optimum properties was obtained by slow cooling at 50°C/hour from sintering temperature. For the step quenching experiments, the magnets were furnace cooled up to the quench temperature, at which temperature it was quenched into water. In the case of the water quenched samples, a post-quenching isochronal annealing was given to the magnet at various temperatures, with the optimum temperature range being 500-600°C. Since the alloy composition is, by design, richer in Nd compared to the stoichiometric composition $Nd_2Fe_{14}B$, all magnets contain excess Nd. Thus during sintering, the excess Nd liquifies and enhances densification by liquid phase sintering.

2. ALLOY COMPOSITIONS STUDIED

In this investigation, two different types of alloys were studied. It must be mentioned, that although the magnets are being classified into two types for the sake of descriptive convenience, they are magnets prepared by the same method and are comprised of the same overall microstructure. The first group of alloys were used to study the microstructure and magnetization reversal mechanism in a typical sintered Fe-RE-B magnet. These alloys were prepared by Professor M. Okada at Tohuku University, Sendai , Japan. They had the overall composition of Fe-32.5 wt.% RE-1 wt.% B, where the rare earth composition consisted of 80%Nd-15%Pr-5%Ce. This Ce-Pr-Nd alloy is termed as "didymium". This alloy behaves for all practical purposes as a ternary Fe-Nd-B magnet. An Fe-Nd-B magnet, obtained by courtesy of Mr.J.K.Chen was also examined to ascertain that the microstructural details of the alloys studied did not differ markedly from that of a ternary Fe-Nd-B magnet. This alloy had a composition of Fe-32 wt.% Nd-1.4 wt.%B. All the magnets used in the experiments described in section III.1-4 were of this composition. The samples used for the study of the effect of grain size on the iHc and the effect of alloying additions (i.e., addition of Dy to improve the iHc) were prepared by Dr.B.M.Ma, Crucible Research Center, Pittsburgh through a collaborative project. These magnets were of the same overall composition as the alloys used in the experiments described in section III.(1-4), although they were ternary Fe-Nd-B magnets. For the grain size effect experiments, different sieve fractions were used as the starting material to prepare the magnets.

3. X-RAY DIFFRACTION ANALYSIS(XRD)

X-ray diffraction spectra were obtained from metallographically prepared bulk magnets using a Siemens Diffractometer, using Cu K_α radiation at 30kV. The experimental conditions consisted of an angular scanning range of 10° to 80° in steps of 0.05^o, with an acquiring time of 2 seconds per step. The diffraction spectra were analysed with the

assistance of existing xray diffraction data on the $RE_2Fe_{14}B$ phase and transmission electron microscopy information.

4. SCANNING ELECTRON MICROSCOPY(SEM)

Scanning electron microscopy was carried out to try to establish the nature of the phases present in the magnets and also to measure the grain size and establish the grain size distribution. This was carried out using an ISI DS-30 SEM at an accelerating voltage of 25 kV. Samples for SEM were metallographically prepared by polishing progressively with finer SiC paper with a finish polish using 1μm diamond paste. The samples were etched with either 2% or 5% Nital to reveal the microstructure.

5. TRANSMISSION ELECTRON MICROSCOPY(TEM)

(a) Specimen preparation for TEM : Electron transparent specimens for TEM were prepared by Argon ion milling slices of the sample that had been mechanically thinned down to a thickness of about 50-75 micrometers. To reduce the volume of the magnet that was introduced into the microscope 3mm discs were not used. The slices were mounted onto a copper grid with silver epoxy glue. In some cases, the sample was dimpled to reduce ion milling time. Argon ion milling was carried out at 6kV accelerating voltage using a liquid nitrogen stage. A total gun current of 0.4mA was used, corresponding to a specimen current of 30-40 μA. The gun tilt angle was set at 22° at the start of ion milling and was reduced to about 17° in the closing stages. Milling was completed in about 12-15 hours.

Transmission electron microscopy and related microanalytical techniques have been used throughout this investigation. TEM imaging was carried out using a Philips 400TEM/STEM at an accelerating voltage of 100kV. The microdiffraction experiments were carried out on this microscope using a nominal probe size of 400Å. This probe size was obtained using an excited condenser lens configuration. Part of the analytical microscopy was carried out using a conventional Be window detector that is attached to the Philips 400 TEM/STEM and a 400Å probe

size to acquire microanalytical information from a localized region. Spectral quantification was carried out using the Kevex 7000 software. However, in order to detect elements such as oxygen, the JEOL 200CX STEM microscope, at the National Center for Electron Microscopy (NCEM) was used at 200kV. This microscope is fitted with an ultra-thin window EDX detector, thus enabling the detection and quantification of elements such as oxygen. On this microscope, EDX spectra were acquired in the STEM mode with a nominal probe size of about 400Å. Spectral deconvolution and quantification was carried out using a Kevex 8000 system software using theoretically generated thin foil k-factors. In the case of oxygen, however, experimentally determined k-factors were used. Care was taken to ensure statistical significance of the EDX data by acquiring at least 10^5 counts. Point microanalysis and line profiles were carried out at various regions in the same sample as well as in different samples to ensure the validity and reliability of the microanalysis data. High resolution electron microscopy (HREM) was carried out using a JEOL 200CX microscope at 200kV. This microscope is also located at the NCEM. Primarily, the interface between the matrix phase and the grain boundary phase was examined. Lattice fringe images were obtained from different regions to examine for differences from one region to another. Lorentz electron microscopy (LEM) was carried out using a Hitachi 650 high voltage microscope at 500kV. The use of the higher voltage enabled the examination of domains in thicker foils, which would be more representative of the bulk domain structure.

6. AUGER ELECTRON SPECTROSCOPY AND ELEMENTAL MAPPING

The presence of oxygen was checked by an independent experiment involving the examination of the Auger spectrum of an in-situ fracture surface of the magnet. Auger spectroscopy was carried out using a Phi-spectrometer. Standard in-situ fracture samples were prepared and fractured inside the spectrometer in a vacuum of 3×10^{-9} torr and examined immediately. In addition to point analyses, Auger electron maps were also generated, in order to examine the spatial distribution of elements such as oxygen, Nd and Fe. To study the depth distribution of the

elements, the surface was sputtered with Argon and the Auger peak-to-peak heights were recorded at regular intervals upto five minutes.

7. MAGNETIC MEASUREMENTS

Magnetic measurements were carried out using a B-H hysteresigraph, with a maximum applied field of 25kOe. To study the effect of applied field on the magnetic properties, the samples were exposed to progressively higher fields, with intermediate demagnetization. The hysteresis loops were traced out using a Hewlett-Packard recorder that was interfaced with the hysteresigraph. In general, 1cm x 1cm cylindrical magnets were used for the measurements, so that the aspect ratio of the magnets was maintained constant.

CHAPTER III
RESULTS AND DISCUSSION

1. OVERALL MICROSTRUCTURE OF SINTERED MAGNETS WITH OPTIMUM PROPERTIES

Since it is well known that the intrinsic coercivity is strongly influenced by the microstructural condition of the magnet, several research groups are actively engaged in the investigation of the microstructure of sintered as well as melt spun magnets, in order to correlate the microstructure to the magnetic properties and the changes due to thermal treatments. In this investigation , the methodology was to first understand the microstructural details of an optimally treated sintered magnet. With this achieved, the changes in the magnetic properties due to post-sintering thermal treatments could be understood by examining the changes in the microstructure that may be occurring during the treatments. Thus, the first experiments were carried out on a magnet which was slowly cooled (50°C/hour) to room temperature from the sintering temperature. This is considered as an optimally cooled magnet. The magnetic properties in this case were as follows : iHc = 8.9 kOe ; B_r = 12.5 kG ; $(BH)_{max}$ = 36 MGOe. In general, results on sintered magnets from different laboratories and magnet producers indicate that the magnetic properties depend upon the actual processing conditions, including the composition of the alloy chosen. Thus, iHc values in the optimum condition range from 9-13.5 kOe , B_r values range from 11-13 kG and $(BH)_{max}$ ranges from 36-45 MGOe. In this section of this study, since magnets from the same producer were used for each set of experiments, the systematic variations were minimized, or were at least maintained constant. Fig.III.1 is a typical xray diffractogram from the slow cooled sample. All the major peaks in this diffractogram can be indexed for the matrix $RE_2Fe_{14}B$ phase, with the aid of published xray powder diffraction data[6,35].

Fig.III.2 shows a scanning electron micrograph of the slow cooled sample. This shows, in addition to the large equiaxed grains of the matrix phase, a second phase at the grain boundaries. Thus ,the

microstructure consists of at least two phases. Transmission electron microscopy (TEM) was then carried out to take advantage of the higher spatial resolution as well as the diffraction and analytical capabilities. Figs.III.3(a & b) show electron micrographs of the second phase observed at the triple grain junctions in (a), and frequently in the two-grain boundaries in (b). For clarity, these microstructural features are depicted schematically in (c) and (d) respectively. The spatial extent of the triple junction region varies from 0.1 μm to 2-3 μm, while in the two-grain boundaries the width can be zero (a conventional grain boundary) to a few hundred angstroms. This phase is heavily defective, which may be inherent, or due to the mechanical polishing and/or ion milling. Since considerable controversy about the structure of this phase existed in the literature(86), the next step was to determine the structure of this phase, both at the triple junctions as well as in the two-grain boundaries.

The structure of the phase at the triple junctions was established by microdiffraction along with specimen tilting to access various low index crystallographic zone axes, to unequivocally determine the structure. This was carried out using a nominal probe size of 400Å in the TEM mode. Since all the low index zones were not accessible in a single region (since the maximum tilt available on the Philips 400 was ±45°) some of the zone axis patterns (for example the [111] zone axis pattern) were obtained from a nearby region. Fig.III.4, which shows the results of this tilting experiment, is a tableau of micro-diffraction patterns from the stereographic triangle. The [100] type (four -fold rotation symmetry) and the [111] (six-fold rotation symmetry) indicates that the structure could be fcc or bcc. However, the presence of the non-orthogonal [110] micro-diffraction pattern with two-fold rotation symmetry clearly proves that the structure could be only fcc and not bcc. In most cases, the fcc phase at the triple junctions exhibited a single crystal diffraction pattern, as is evidenced by the series of nanoprobe diffraction patterns (obtained using a nano-probe of about 100Å diameter) shown in Fig.III.5. The diffraction patterns from all the regions are in virtually the same orientation. In the case of the two-grain boundary region, since in general the spatial extent is not more than 200Å, nano-probe diffraction was used

to determine the structure. In this region also, the structure was found to be fcc, as is shown in Fig.III.6. In this figure,the bright field image shows the two-grain boundary phase extending from the triple junction. Nano-probe diffraction patterns were obtained from points 1, 2 and 3, as shown in the figure. The $[110]_{fcc}$ type symmetry of all the diffraction patterns conclusively proves that the grain boundary phase is fcc. The lattice parameter of this phase, as determined from the microdiffraction patterns is 5.24Å.

In order to determine the composition of this phase, microanalysis was carried out by Analytical Electron Microscopy (AEM). Fig.III.7 shows a typical EDX spectrum from the matrix phase, the stoichiometric composition of which was used to monitor consistency in the k-factors involved in the quantification of the EDX data. Preliminary analysis was carried out on the Philips 400 using a Be window EDX detector. In Fig.III.8 an EDX spectrum from the triple junction phase is shown along with an EDX spectrum from a two-grain boundary region,shown in the bright field image in Fig.III.9, which was wide enough to position a 400Å probe in order to acquire an EDX spectrum. Two features of the EDX spectra in Fig.III.8 are of importance : (a) the grain boundary phase is rich in Nd (and Ce and Pr), along with a small amount of Fe ; (b) the composition of the two-grain boundary region is the same (within experimental errors) as the triple junction region. The first inference, however, is inconsistent with the fact that the structure is fcc, since no fcc, Nd rich, Nd-Fe phase has been reported in the literature(87). It is, however, known that the rare earths are easily contaminated by elements such as N, C, O, etc., , due to their strong affinity for these elements. Thus, it is conceivable that the Nd-rich phase is indeed contaminated with oxygen during the processing of the magnet. Consequently, the grain boundary phase was examined using an ultra-thin window (UTW) EDX detector, which allows the detection and quantification of light elements such as oxygen, etc. Fig.III.10 (a) shows the EDX spectrum from the grain boundary phase, obtained using the UTW detector. While the Nd rich composition is still observed, an extra peak, that of oxygen, is now observed. This is shown more clearly in the low energy end of the EDX spectrum in Fig.III.10(b). Using system generated k-factors as well as experimentally determined

k-factors for oxygen, it was possible to quantify this spectrum. The results indicate that the fcc phase could contain upto 40 at.% of oxygen. However, these results of oxygen quantification should be regarded as only semi-quantitative, since quantification of a light element is fraught with difficulties such as absorption by the heavier Nd atoms, and foil thickness correction. If the foil thickness is known with some accuracy (foil thickness can be measured by convergent beam electron diffraction(CBED) techniques), and if the absorption coefficients and sample density are known,then corrections can be made for the effect of absorption. However, foil thickness measurement by CBED was not possible since the fcc phase is heavily deformed and hence the "pendullossung" fringes were not observed. Thus, an absorption correction could not be quantitatively carried out. However, it was clear that the fcc structure could be stabilized by the presence of oxygen in the grain boundary phase. To ascertain this fact, the presence of oxygen in the sample was examined by an independent experiment.

The presence of oxygen was definitely confirmed by Auger spectroscopy and elemental mapping. Fig.III.11(a) is the fracture surface of the in-situ fractured sample and shows a mixed trans-granular/inter-granular fracture. In Fig.III.12(a), the Auger spectrum from an inter-granular fracture region, point A, is displayed. The main feature of this spectrum is the large oxygen signal, in addition to the weaker Nd signal. Depth profiling using Argon sputtering enabled the determination of the depth of this oxygen-rich layer. This is shown in Fig.III.12(b). The oxygen peak-to-peak ratio is significant, even after five minutes of milling, which indicates that the oxygen signal observed was not a surface contamination due to the oxygen in the system vacuum (which was about 10^{-9} torr). The trans-granular fracture region, point B, also shows an oxygen edge,shown in Fig.III.13(a). This is clearly surface contamination, since the results of depth profiling experiments, Fig.III.13(b), indicate that the maximum depth of the oxygen is about 30Å. Since the matrix $RE_2Fe_{14}B$ phase does not contain any oxygen, the oxygen signal observed must be due to oxygen from the system. Using the spectrum from point A, an oxygen Auger map was generated, to examine the distribution of oxygen and also Nd. Figs.III.11(b &c) depict oxygen and

Nd Auger electron maps respectively, corresponding to the fracture surface in Fig.III.11(a). The maps clarify the following points : (1) significant oxygen Auger electron intensity is found for inter-granular fracture regions, as was also observed in the point analysis data in Fig.III.12; (2) regions with significant oxygen Auger electron intensity are accompanied by a significant Nd Auger elctron intensity, suggesting that oxygen rich regions are also rich in Nd. These results fully corroborate the EDX results presented earlier and hence the presence of oxygen along with Nd in the grain boundaries (both triple junctions as well as the two grain boundaries) was conclusively established.

To examine the spatial distribution of oxygen in the grain boundary phase, microanalytical line profiling was carried out across the triple junctions. Since the two-grain boundaries were not of sufficient width to obtain enough number of points on the line profile, this experiment was limited to only the triple junctions. The specific objective of this experiment was to examine for any specific segregation patterns, such as segregation to interphase interfaces or to grain boundaries (of oxygen or the other rare earths). This is of importance since micro-scale heterogeneities in composition can potentially lead to large changes in magnetic properties. Fig.III.14 shows schematically, how the line profiling experiment was carried out across the triple junction. In this case, the diameter of the spots correspond to the probe diameter used. Fig.III.15 is a typical line profile plot of all the elements present in the magnet across the matrix-fcc phase interface. This plot shows segregation of oxygen to the center of the triple junction, while Ce and Pr segregate to the interfaces. Similar line profile data were obtained in the case of a ternary Fe-Nd-B alloy, which was provided by courtesy of Mr.J.K.Chen. Fig.III.16 shows these data, wherein the oxygen concentration in the middle of the triple junction is higher than at the interfaces. These segregation patterns, however, have to be viewed with considerable caution for several reasons: (1) the quantification of one element is relative to the other and (2) the strong dependence of oxygen x-ray signal detected upon the foil thickness. It is conceivable that the changes in the oxygen content are due to local changes in foil thickness(due to non-uniform ion milling). Since the local foil thickness could not be

determined, the observed segregation pattern should be considered semi-quantitative. This also highlights the difficulties involved in the detection and quantification of light elements, when ideal defect-free samples cannot be achieved.

A third phase often found in sintered Fe-Nd-B magnets is a paramagnetic $NdFe_4B_4$ phase[5,6,88,89]. This phase is found as independent grains and does not play a significant role in the evolution of the magnetic properties. Fig.III.17 shows a bright field image of this phase along with the diffraction pattern. The sub-structural details of this phase have been determined by several workers. In addition to the above features, in sintered magnets, rare earth oxides are also found, primarily due to improper processing or due to impure starting raw materials. Fig.III.18 shows a bright field TEM image of an oxide inclusion, along with a selected area diffraction pattern, in the $[1123]_{hcp}$ orientation. The inset in this figure shows the EDX spectra from the oxide phase obtained using an UTW detector. The matrix spectrum is also shown for the sake of comparison.

DISCUSSION : In the results presented above, the details of the microstructure of an optimally treated sintered magnet have been described. The focus of this discussion will be the grain boundary fcc phase, since considerable controversy exists regarding its structure, composition and role in the magnetization reversal process. The fcc structure is stabilized by the presence of oxygen, a feature which is well documented in the case of rare earth elements. The strong electro-positive character of the rare earths is the main cause for the presence of oxygen in the grain boundary phase . Oxygen can enter the system during any of the various processing steps. Prime among them is the ball milling or jet milling stage, wherein the oxygen content varies almost linearly with the milling time and can reach about 1.4 wt.% for milling periods of about 4 hours[90]. This oxygen can dissolve in the Nd rich phase during sintering, thus stabilizing the fcc structure. The presence of oxygen is responsible for the absence of the eutectoid decomposition of the Nd rich phase. In the case of a binary Nd-Fe alloy which is rich in Nd, the eutectoid decomposition around 630°C leads to

the formation of dhcp ß-Nd and Nd_2Fe_{17}, which is ferromagnetic at room temperature[91]. If this reaction had occurred, the Nd_2Fe_{17} could act as sites for nucleation of reverse domain walls. The presence of oxygen is beneficial in this aspect. However, the strong interaction of oxygen with Nd can be responsible for the significant difference between the iHc of the optimum cooled sample and the anisotropy field of $Nd_2Fe_{14}B$, which is 71kOe at room temperature. This will be discussed in detail later in this chapter.

2. DOMINANT MAGNETIZATION REVERSAL MECHANISM OF SINTERED MAGNETS WITH OPTIMUM PROPERTIES

The next step in the characterization of the optimally treated sintered magnet was to determine the dominant reversal mechanism. As was mentioned in the Introduction to this thesis, in technical magnets, wherein the reversal of magnetization occurs by domain wall processes, the reversal process is controlled either by the nucleation of a domain wall or the unpinning of the domain wall from a pinning site(10). In all magnets, however, both components exist to some degree, although one dominates. The determination of the dominant mechanism is important, not only to understand the fundamental magnetic behaviour of the magnet but also in the design of better microstructures, since both the nucleation step as well as the pinning step are influenced by the microstructural condition. After a brief description of the methods used to identify the dominant reversal mechanism, the results of some of the experiments on the optimally treated magnet will be presented.

The nature of the virgin curve is one good indicator of the type of magnet(92). A large initial permeability (i.e., a steep slope of the virgin curve) indicates the absence of any significant domain wall pinning sites in the bulk of the magnet, and suggests that the magnet could behave as a nucleation type magnet. On the other hand, if pinning in the bulk of the magnet is significant, the virgin curve will exhibit a shallow slope until an applied field higher than the unpinning field of that type of pinning site is applied. If higher fields are applied, the virgin curve rises sharply to saturate the magnet. These features are schematically depicted in Fig.III.19 (a) for a nucleation type magnet and in (b) for a pinning type magnet. The virgin curve is shown in thick lines. Such a difference in magnetization behaviour is also evidenced in the nature of the hysteresis loops. This is also depicted in Figs.III.19(a & b). In the case of a nucleation type magnet, the second quadrant of the hysteresis loop is square (or slightly rounded in the case of polycrystalline aggregates), while in the case of a pinning type magnet, a definite kink in the loop at low reverse fields can be observed. This corresponds to the easy nucleation step, with a subsequent pinning of the wall at the site of

nucleation. Reversal finally occurs when the wall is unpinned from the pinning site.

In a series of pioneering experiments on Sm-Co alloys, Becker[13,14,21,23,26,28,93] showed that in addition to the nature of the virgin curve, the shape of hysteresis curves as a function of the externally applied field conveys much information about the magnetization reversal process. This can be used to make a sharp distinction between nucleation and pinning controlled magnets. The results of such experiments is schematically shown in Figs.III.20 (a-d). Two extreme types of behaviour can be envisioned. In the case of a single grain (or single particles with one grain per particle) of a nucleation dominated magnet, the hysteresis loops as a function of applied field are depicted in Fig.III.20(a). At low fields the loops are narrow and sheared to the extent of the magnet's demagnetizing factor. With increasing field intensity, the loops become increasingly wider and tend to become rectangular, Fig.III.20(a). For bulk wall pinning, the field required to move the wall is the same anywhere in the material. Hence the iHc remains the same, while the remanence increases with applied field. These details are shown in Fig.III.20(b). In the case of aggregates of particles (i.e., polycrystalline materials) the variations in the individual nucleation fields will smooth out the square loops and give curves such as those depicted in Fig.III.20(c). In real materials, however, due to some contribution from pinning, the behaviour may not be very as simplistic as this model, and hence such a dependence alone cannot be used to determine the dominant mechanism. For wall pinning the overall behaviour will depend upon the overall pinning structure and the sequence of hysteresis loops is similar to that shown in Fig.III.20(d). This functional dependence can be alternatively described in terms of the applied field dependence of the intrinsic coercivity and the remanence. In general, there is a strong dependence of the iHc on the applied field for nucleation type magnets, while for pinning type magnets there isn't. In addition, the temperature dependence of the nucleation field (or the iHc), along with the effect of temperature on the anisotropy field and magnetocrystalline anisotropy constants, can be used to determine the nature of nucleation sites and/or pinning sites. For example, in the case of a nucleation type magnet, iHc varies with

temperature in the same fashion as does the anisotropy field, while in the case of a pinning type magnet the temperature variation of iHc is related more to the temperature variation of the magnetic properties of the pinning sites, relative to those of the matrix. The dependence on the angle, Ø, of the applied field direction to the sample alignment direction can also be used to examine the reversal characteristics. In some cases, a 1/cosØ dependence is found.

Probably one of the best methods to identify the dominant reversal mechanism is to study the effect of average grain size and the grain size distribution on the iHc[93-99]. In the case of nucleation type magnets, wherein the main nucleation sites are structural and chemical inhomogeneities at grain boundaries and two-phase interfaces, a definite grain size dependence of the iHc can be found. Although, in general, a dependence on the inverse of grain size has been observed by some workers[94-99], a rigorous description, based on the specific nature of the nucleation sites, of how the nucleation field (or iHc) varies with grain size, has still not been put forward. However, the observation of an inverse dependence on the grain size indicates that the nucleation field and hence the reversal mechanism is dominated by the nucleation event. It is noteworthy that this dependence would be valid only if the grain size (or grain size distribution) is well above the critical domain size, which in the case of Fe-Nd-B magnets is about 0.3 micrometers. In the case of a pinning type magnet, on the other hand, since domain walls already exist in the magnet,the grain size itself is not of great significance. Thus, in contrast to nucleation controlled magnets, the unpinning field (which governs the reversal of pinning magnets) may increase with increase in grain size, since a larger grain size may represent a greater probability of finding the most potent pinning site. A systematic study of the nature of the B-H loops, the iHc values obtained as a function of grain size can not only help in identifying the dominant reversal mechanism, but also delineate the type of nucleation sites in the magnet under consideration. Results of such experiments are detailed in section III.6

Finally, direct examination of the microstructure of the magnet can give vital information about the nature of pinning sites, if any, and their spatial extent and distribution. The interaction of these microstructural

features with domain walls can be observed through Lorentz microscopy. Hence, by assimilating the information obtained from these experiments, the dominant reversal mechanism can be inferred. In what follows, the results of experiments on the magnet with optimum properties will be presented. The magnets examined here were the same as the ones used in section III.1.

Fig.III.21 shows a typical virgin magnetization curve along with the hysteresis loop, for the optimally cooled magnet, for a maximum applied field of 21 kOe. The sharp rise in the virgin curve (high initial permeability), indicates that the domain walls present in the thermally demagnetized condition can move very easily inside the grains, suggesting that bulk wall pinning is minimal. The effect of applied field on the shape of the hysteresis loops is shown in Figs.III.22(a-c). At a low field of 1kG, Fig.III.22(a), the loop is narrow and sheared, indicating that forward and backward motion of the domain wall is very easy and also that the applied field is not sufficient to saturate the grains. When the field is increased to 12.7 kG, the loop is wider, Fig.III.22(b), although it is still not square. This indicates that the grains are progressively being saturated. When the field is increased to 21 kG (the maximum attainable using the hysteresigraph available currently at Berkeley), the loop is almost square, Fig.III.22(c), and the iHc is very high. These results are shown in Fig.III.23, as a plot of iHc (and B_r) versus the applied field intensity. This plot shows a flat regime of low iHc upto fields of about 7-8 kG, after which the iHc rises sharply. The applied field at this stage corresponds to the overall internal demagnetizing field which has to be overcome by the applied field in order to saturate the grains. Almost complete saturation occurs at about 20kG, after which the changes in iHc are linear with applied field and not very large. The changes in iHc are accompanied by similar changes in the remanence, as shown in Fig.III.23. Until the demagnetizing field is overcome, the remanence is low since the domain walls relax into the demagnetized condition once the applied field is removed or reduced to zero. The remanence measured in this case is thus low. Once the applied field is above the demagnetizing field of a sizeable fraction of the grains, the remanence also increases, since the grains are saturated even if the applied field is reduced to zero and negative fields

are required to bring the remanence to zero. With further increase in the applied field, the remanence follows the trend in the fraction of grains being saturated. Similar results have been reported by several workers and confirm the general idea that the magnetization reversal of this class of magnets is controlled by the nucleation step[5,6,65,100-102].

High resolution TEM of the matrix phase, shown in Fig.III.24, shows no specific and regularly spaced pinning sites, such as second phase particles, inside the grains and supports the conclusions arrived at from the magnetic data. It should be pointed out that the rare earth sesqui-oxides observed infrequently in the magnets (both intra-granular and as discrete grains) are not a prominent source of wall pinning, although they could act as sites for wall nucleation, due to the large demagnetizing fields around them. Although the temperature dependence of iHc and anisotropy field could not be experimentally determined in our laboratory, temperature dependent effects will be discussed based upon existing published data, in section III.4. In summary, in this section, it has been shown that the magnetization reversal is typical of a nucleation type magnet.

In section III.4, the possible role of oxygen in the nucleation of magnetization reversal will be discussed through a model of the microstructure, particularly near the grain boundaries and two-phase interfaces. The interaction of the domain walls which are nucleated in the grains and move inside them, with the microstructural features such grain boundaries, the fcc phase, etc. will be presented in section III.5.

As was described in the introduction to this thesis, nucleation of a domain wall involves the formation of a nucleus of reverse magnetization in a grain, separated from the rest of the grain by a domain wall. In nucleation type magnets, the nucleation event has to occur in spite of the high magnetocrystalline anisotropy of the grain. Hence, the most potent nucleation sites are regions of lowered magnetocrystalline anisotropy or enhanced local demagnetizing fields. Such sites can occur in grain boundaries where the local disorder in the atomic configuration will lead to significantly lowered magnetocrystalline anisotropy, which depends strongly on the crystalline order and the degree of crystallographic anisotropy. Such sites can also occur at interphase interfaces, such as

the fcc phase-$RE_2Fe_{14}B$ phase interface, since the interface is a region where the magnetocrystalline anisotropy can be much lower than the bulk value. So also, the segregation of impurity elements or substituent elements to the grain boundaries and interphase interfaces can change the local magnetocrystalline anisotropy due to local change in composition. Easy nucleation can also occur at sharp corners, such as grain corners, wherein the local demagnetizing field can be very high. Localized strains at the sites of nucleation can also accentuate the nucleation process. Thus, if one or all of these parameters can be varied, the iHc can be altered. This, then leads to the focal point of this thesis : why and how do the magnetic properties, especially the iHc and consequently the $(BH)_{max}$ vary with post-sintering thermal treatment ? This again leads to the question as to how the composition, processing and microstructure, can be altered to optimize these properties. In what follows, the results of experiments to study the effects of post-sintering heat-treatment on the magnetic properties, will be presented. Such a study is of importance for the following reasons : (1) post-sintering heat-treatments have been shown to influence significantly, the room temperature magnetic properties, not only in Fe-Nd-B type magnets, but also in $SmCo_5$, which is another example of nucleation type magnets ; (2) there is no concensus on the nature of microstructural influence on these changes in magnetic properties ; (3) from a practical view point, i.e., in designing new alloys , it is essential to know the optimum microstructural condition along with the right combination of alloy composition and processing conditions.

3. EFFECT OF POST-SINTERING TREATMENTS ON MAGNETIC PROPERTIES

In the pioneering papers of Sagawa et. al[5,6], the slow cooling treatment, which was used to obtain the optimum properties and microstructure described in section III.1, was not used to produce the magnets. Instead, the samples were quenched from the sintering temperature into water and a post-sintering annealing was given to the magnets in order to achieve the optimum coercivity and energy product. The annealing treatments consisted of holding the magnet at various temperatures for one hour, followed by quenching into water. It was found that the optimum annealing temperature was in the range of 500-600°C, for one hour.

Several causes were put forward to explain the sharp increase in iHc due to such an annealing treatment. In the original work of Sagawa et. al it was proposed that in the quenched samples, the grain boundaries and two-phase interfaces were stressed and defected[5,6]. On annealing the stresses were assumed to be relieved, concomittant with a smoothing of the grain boundaries and two-phase interfaces, where wall nucleation occurs. It was also suggested that the optimum annealing temperature was close to the melting temperature of the grain boundary Nd-rich phase, hence suggesting that the liquification of the grain boundary phase was connected to the drastic improvement of the magnetic properties of the quenched sample, upon annealing. Hiraga et. al[103,104], through high resolution TEM, proposed that in the water quenched condition, the matrix $RE_2Fe_{14}B$ phase was penetrated by bcc platelets from the grain boundary regions. This phase was reported to have a Fe:Nd ratio similar to that of $Nd_2Fe_{14}B$, with a lattice parameter close to that of bcc Fe. Tokunaga et. al[105] also observed the bcc platelets, but observed no direct correlation of the iHc with the density of the platelets. Sagawa et. al[106] have produced, by melt spinning, an Fe-Nd phase that is equivalent to the bcc grain boundary phase, with a Curie temperature of 150°C. However, if this phase were to be involved in pinning of the domain walls, the pinning force should be expected to increase with increase in temperature, especially above 150°C. This is not observed. Livingston[107] has also countered the "bcc phase" mechanism with the argument that the dissolution of a

large atom such as Nd in Fe would be expected to produce significant lattice expansion. Stadelmaier et.al[108,109] proposed that the changes in magnetic properties were connected with the changes in the nature of the grain boundary phase. Specifically, they have proposed that the grain boundary phase, consisting of a dispersion of fine Fe crystals dispersed in a glassy oxide phase formed during cooling. This was, however, shown to be artefacts during Argon ion milling, used for sample preparation for TEM observations[110]. Zhou et. al[111] suggest that the changes upon annealing are due to changes in the concentration gradient in the two-phase boundaries. Thus it is clear that considerable doubt still exists about the microstructural details of reversal, although a variety of explanations have been put forward.

In this section, results of experiments carried out to resolve the questions regarding the effect of post-sintering treatments, will be presented. It will also be shown that some of the results published in the literature can be explained in terms of artefacts in specimen preparation for TEM. Fig.III.25 illustrates the effect of isochronal annealing at different temperatures, on the iHc of a water quenched magnet. The samples were quenched into water after the annealing treatment. The properties were measured at room temperature after applying the same field of 21kG in the forward and reverse directions. In the water quenched condition, the iHc is low (3.0 kOe). On annealing at temperatures up to 500°C, there is no improvement in the iHc. However, on annealing at 500°C for one hour, the iHc rises to about 2-3 times the as-quenched value. This high iHc value can be obtained by annealing in the temperature range of 500-600°C. For higher temperatures, there is a drop in the iHc after annealing. Since changes in the microstructure will affect the iHc of the magnet, the microstructure of the magnet in three different conditions was focussed upon. These were the as-water quenched, water quenched and annealed at 500°C for one hour and slowly cooled from sintering temperature(results for which were presented in section III.1).

Fig.III.26 (a &b) show bright field TEM micrographs of the grain boundary phase at the triple junctions and the two-grain boundary in a water quenched magnet. The structure of this phase is still fcc, both at the triple junctions and in the two-grain boundary in a water quenched

magnet. The phase is heavily defective. As in the case of the slow cooled sample, oxygen was found in the grain boundary phase, both by EDX spectroscopy as well as by Auger elemental mapping. Fig.III.27(a) shows the fracture surface of the in-situ fractured sample, while (b) and (c) depict oxygen and Nd elemental Auger mapping of the fracture surface in (a). As in the case of the slow cooled magnet,microanalytical line profile across the matrix-grain boundary phase interface did not indicate any significant difference in the three samples. In Fig.III.28(a-c) results of microanalysis across the interface is shown for the slow cooled, as-water quenched and water quenched and 500°C annealed samples respectively. In this case oxygen was not detected since a Be window detector was used. In the case of the slowly cooled sample, however, poly-granular structure of the fcc phase was frequently observed. Figs.III.29(a&b) illustrate this observation. However, it must be pointed out that this feature was not observed in the case of all triple junctions and two-grain boundaries and was not observed in the case of the water quenched sample at all. Thus, it is likely that in the case of the slow cooled sample, the grain boundary phase had enough time during cooling to recrystallize, thus relieving any strains that could have arisen due to thermal expansion mismatch or thermal shock.

It is noteworthy that both in the slow cooled sample as well as in the quenched sample, there was no indication of a bcc phase between the fcc phase and the matrix , as was proposed by Hiraga et. al[103,104]. This was clarified by high resolution lattice fringe imaging of the interface in both type of samples. Fig.III.30 shows one such image of the interface between the matrix and the grain boundary phase in the optimally cooled magnet. Clearly, no other phase is observed. So also, in the case of the water quenched sample, Fig.III.31, no bcc phase was observed. However, some disruption in the image can be observed at the interface (shown by the arrows). If these are localized lattice defects, they could be suitable sites for domain wall nucleation. Probable causes for the observation of a bcc phase will be presented in the discussion to this section.

From the above microstructural and microanalytical results for the water quenched, slowly cooled and water quenched and annealed magnets, it can be seen that, but for infrequent observation of recrystallized fcc

regions, there are no obvious differences. Changes in oxygen content at the matrix phase-fcc phase interface, if any, in the slowly cooled magnet and the water quenched magnet could not be detected with certainty, due to the problems mentioned earlier. However,the above observations do not rule out the possibility that the differences in iHc between the slow cooled sample and the water quenched sample (or between the as-water quenched sample and the water quenched and 500°C annealed sample) may be due to the strains due to quenching. This may be manifest at the interphase interfaces, which are also the most potent sites of domain wall nucleation. This suggests that the quenching process from the sintering temperature may itself be of significance and needs to be investigated. That is, if the cooling rate from the sintering temperature is varied by employing different quenching media, significant differences in the iHc should be found. Thus the next set of experiments were directed at understanding the effect of cooling rate from sintering temperature on the iHc.

Fig.III.32 shows the iHc and $(BH)_{max}$ plotted against the cooling rate(112). The cooling rate was assumed to be similar to those of alloy steels. As is evident, there is a definite influence of the cooling rate on both the iHc and $(BH)_{max}$. This trend in the iHc was observed repeatably, as was verified by an independent set of experiments, using Fe-Nd-B magnets, from a different producer. The results of this independent experiment, which was carried out for six different cooling rates, are shown in Fig.III.33. The remanence, however, is independent of the cooling rate, Fig.III.34, since it is fixed by the starting alloy composition. This strong dependence of the iHc on the quenching rate indicates that the quenching stresses, which also increase with the cooling rate, may play a significant role in aiding domain wall nucleation. So also, the partitioning and segregation behaviour of oxygen to the interfaces may be affected by the quenching rate from the sintering temperature. However, as was mentioned earlier, precise determination of oxygen concentrations is not possible without the availability of precise absorption parameters. The hysteresis curve and virgin magnetization plot for each of the cooling rates is presented in Figs.III.35(a-d), while Fig.III.35(e) shows the iHc as a function of the applied field for : (1) the slowly cooled magnet ; (2) the

water quenched and annealed (500°C, 1 hour) magnet ; (3) water quenched magnet. The steep rise in the virgin curve in all the cases indicates that the domain walls can move very easily at small applied fields. Although the shape of the hysteresis loops is still the same (rectangular, without any pronounced kinks) nucleation is occurring at progressively lower fields as the cooling rate is increased. This suggests that the magnetization reversal is still of the nucleation type, although at different fields, with easier nucleation occurring for faster cooling rates (accompanied by higher quenching stresses). The sharp increase in iHc around 10-12 kG (Fig.III.35(e)) in all the three samples indicates that the demagnetizing fields are not significantly different.

That quenching stresses do exist is well demonstrated by examining the surface of the magnets. Figs.III.36 (a &b) show SEM images of the polished surface of the water quenched and slow cooled magnets. While several quench cracks can be observed on the surface of the water quenched magnet (WQ), no cracks can be seen in the case of the furnace cooled sample(FC). Quench cracks were observed in the case of the oil quenched magnet also, while the air cooled sample did not exhibit any visible cracks. Examination of the nature of crack propagation, i.e., inter-granular or trans-granular can provide information about the location of stress concentrations during quenching. Hence, one of the cracks in a water quenched sample was opened up by gently applying pressure on either side. Figs.III.37 (a&b) show SEM images of the fracture surface. The fracture mode, which is completely inter-granular is clear in the high magnification image in Fig.III.37(b). This lends support to the idea that the grain boundaries (and two-phase interfaces) are weaker than the matrix during the quench and also that the quenching stresses manifest strongly along the grain boundaries and two-phase interfaces. This result along with the Auger elemental maps and EDX microanalysis, suggest strongly that one of the causes for grain boundary weakening may be oxygen. Such cases of embrittlement in ferrous and non-ferrous materials by elements such as hydrogen, oxygen, antimony, bismuth etc. is well documented[113]. So also, in the case of ceramics, intergranular fracture due to thermal expansion anisotropy (or mismatch) across the grain boundary or two-phase interface has been shown to be very

common[114]. Although the embrittlement itself is not of highest importance in this investigation, it suggests that the grain boundaries and two-phase interfaces can be subjected to severe quenching stresses, which, if higher than the fracture stress of the interface, manifest as quench cracks. This effect of quenching stresses, along with the assistance of oxygen, can be a prominent source of nucleation sites. Similar results have been obtained in the case of Sm-Co alloys by Doser and Smeggil[115]. They have observed that the iHc obtained after a 900°C annealing treatment depends upon the cooling rate and that the natural fracture mode is inter-granular. The stresses due to quenching can also lead to magnetostrictive effects, as will be discussed in section III.4.

DISCUSSION: Several mechanisms have been proposed to explain not only the low iHc of the water quenched magnet as compared to the optimally quenched magnet, but also the fact that the iHc of a water quenched magnet can be increased almost to that of the optimally cooled magnet by annealing at 500-600°C for an hour. Hiraga et. al[103,104] proposed that bcc platelets penetrate the matrix from the grain boundary region, which itself was suggested to be bcc. Fig.III.38 illustrates schematically the model proposed by Hiraga et.al. In this diagram, the microstructure of the magnet, close to the fcc phase-matrix interface is shown. The bcc platelets were supposed to extend into the matrix phase from a finely crystalline bcc region. However, this observation of a bcc phase, by TEM, can be explained as being caused by artefacts of ion milling, since bcc diffraction patterns were observed, not only at the grain boundaries, but also inside the matrix grains[110]. Fig.III.39 is a compound bright field image / dark field image / diffraction pattern of the two grain boundary region. The bright field image shows a mottled surface appearance, while the diffraction pattern shows the presence of a polycrystalline bcc phase, not only at the grain boundary region, but also inside the grains. Since it is well known that the $RE_2Fe_{14}B$ phase is very stoichiometric and does not undergo any phase transformation[5,6], the appearance of this polycrystalline bcc phase is surprising. The dark field image shows that the mottled structure exists inside the grain also. Thus it is conceivable that the conclusions of Hiraga et.al, based upon the

observation of bcc ring diffraction patterns, are in error. In addition, samples which were jet electro-polished did not exhibit any bcc ring pattern, Fig.III.40. In this image of the two-grain boundary, only an fcc ring diffraction pattern can be observed.

Fig.III.41 depicts schematically how a bcc phase can form on the surface of the ion milled thin foil. In (a), the slab of material (generally about 50-75 micrometers in thickness) is shown with the two grain boundary fcc phase along with the matrix on either side. In (b), the sample at an intermediate stage of ion milling is depicted. During the milling process, the matrix phase, which is rich in Fe, is progressively milled. The milling occurs by the impact of the Argon ions with the atoms of the sample, with the consequent removal of the atoms on the surface by momentum transfer. The Fe atoms which are removed from the surface are carried away by the Argon beam. However, if the concentration of Fe atoms in the vicinity of the sample is high, it is conceivable that the Fe redeposits on the surface of the sample being milled. This is depicted in (c), where a thin surface layer of the bcc Fe rich phase has formed. This bcc phase will not have any specific preference to a certain microstructural region, although, since the grain boundary fcc phase being softer, is milled away faster than the matrix, the" valleys" created by this differential ion milling can lead to the preferential deposition of the bcc "debris" in the grain boundary regions. Thus it is very improbable that a bcc phase exists in the grain boundary region, along with the fcc grain boundary phase. This conclusion is borne out by the results of high resolution TEM of the interfaces. Both in the optimally cooled magnet, Fig.III.30, and in the water quenched magnet, Fig.III.31, the interface is devoid of a third phase. Thus, some other mechanism needs to be invoked to explain the changes in iHc and $(BH)_{max}$ with thermal treatments, especially the effect of quench rate and the critical nature of the annealing temperature.

The strong influence of quenching rate from sintering temperature is clearly established from the results presented in Figs.III.32 and III.33. From the nature of the virgin curve and the hysteresis loops, Fig.III.35, it can be inferred that the overall magnetization reversal mechanism has not changed, although the reversal is occurring at progressively lower field

with increasing severity of quench. If quenching stresses are sufficient to cause cracking or micro-cracking, Fig.III.36(a&b), then it is possible that the demagnetizing fields at the cracked surfaces may be of importance. However, the effect of such a phenomenon appears to be minimal as shown by the results of two experiments. The first is the effect of annealing on the iHc of a water quenched magnet. As shown in Fig.III.25, if the magnet is annealed at 500-600°C, the iHc increases to about 2-3 times the water quenched value. However, if quench crack induced demagnetizing fields are the main cause for the drop in iHc, annealing should not produce any improvement in iHc, since the cracks will definitely exist after annealing. The second evidence which rules out the idea that demagnetizing fields at the cracked surfaces are the cause for easy reversal, is shown in Fig.III.35(e). As was described in section III.2, a strong applied field dependence of iHc is observed in the case of all the three samples, i.e., (1) the furnace cooled magnet ; (2) the water quenched and annealed (500°C, 1 hour) ; (3) water quenched magnet. The average demagnetizing field can be evaluated as that field at which the iHc is half way between the saturation value and the low iHc region. From Fig.III.35(e), it can be seen that this average demagnetizing field is not significantly different for the three different treatments, although the average iHc's are different. Thus, the role of demagnetizing fields at the cracked surfaces does not appear to be significant. The fact that even in the optimally cooled magnet the iHc is much lower than the anisotropy field means that the nature and effect of defects, especially at grain boundaries and two-phase interfaces must be examined in detail. One such defect is oxygen, which can be expected to alter the local magnetocrystalline anisotropy contribution of the Nd atoms significantly. In the case of the water quenched magnets, the effect of oxygen in reducing the iHc may be synergised by the effect of quenching stresses. Thus, the magnetization reversal mechanism must recognize these two aspects, especially in the case of the water quenched sample. Before examining the effect, if any, of quenching stresses on the magnetization reversal process, the causes for quenching stresses need to be examined. On quenching, stresses can arise due to two causes :

(1)Presence of thermal expansion anisotropies : this is especially

true in the case of a two-phase polycrystalline solid in which the phases have different thermal expansion coefficients or in a single phase polycrystalline sample with random orientation of anisotropic grains(114). In such a case, quenching leads to localized stresses across the two-phase interface. The magnitude of the local stresses depend upon the difference in coefficient of thermal expansions, the difference in temperature and the elastic properties of the solid (assuming that the solid does not undergo extensive plastic deformation to relieve the stresses). In addition, the magnitude of stresses due to localized thermal expansion are also functions of the average grain size and the cooling rate from sintering temperature. In the case of aligned grains (as in this case) it is more likely that the effect of difference in the thermal expansivities of the two phases may be more important.

(2) Thermal shock stresses : Brittle materials can also be stressed by quenching into a liquid medium, wherein the main form of heat transfer is by conduction(116). In this case the maximum stresses depend upon the overall thermal expansion, the Young's modulus and Poisson's ratio of the solid, the thermal conductivity, specific heat, and density of the quenching medium and the magnet.

In both the cases, the stresses are given by a similar functional dependence on the coefficient of thermal expansion of the solid, the Young's modulus and the Poisson's ratio along with the maximum temperature drop. In both the cases, the stresses increase with cooling rate. In the case of the quench rate dependence of the iHc, both these effects could be of importance, and need to be considered to evaluate the effect of quenching stresses on the ease of magnetization reversal.

Thus, in the next section, a microstructure based model for the nucleation field for the optimally cooled magnet will be presented. Following this, the effect of quenching stresses will be examined by first calculating the quenching stresses in the case of the typical example of a water quenched magnet. From the knowledge of the localized stresses, the contribution of stress anisotropy to the overall anisotropy constant will be calculated. This will provide an effective anisotropy field, in the presence of stresses. From this the effective anisotropy field will be determined. The iHc in the case of the water quenched magnet will then

be computed, using the same microstructural model as in the case of the optimally cooled magnet. These models and the calculations based on the models will not only throw light on the role of defects and quench rate on the iHc, but will also suggest alloy design criteria such as substitutions in the matrix phase or engineering of grain boundary structure and composition, and also optimum thermal treatments in order that the magnetic properties may be improved.

4. MICROSTRUCTURE BASED MAGNETIZATION REVERSAL MODEL

In this section, the information obtained on the microstructure and magnetic properties of the optimally cooled magnet (section III.1 and 2) will be used to propose a magnetization reversal mechanism. This mechanism is based upon similar observations made in the case of $SmCo_5$ magnets(117-120). In the case of $SmCo_5$ magnets, although the anisotropy field of $SmCo_5$ is very high (about 300-350kOe), the maximum observed iHc is never higher than 42kOe, a value obtainable only under very perfect conditions. Defects, especially at grain boundaries are thought to be the cause for the low iHc(121). The large oxygen affinity of the rare earths makes it especially attractive to examine whether the interaction of the rare earth atom with oxygen can be of significance in explaining the low iHc values obtained. This, if studied in conjunction with the temperature dependence of iHc and anisotropy field, will be useful in the understanding of the exact nature of the nucleation sites. The suggestion that oxygen is one of the defects does not preclude the possibility that structural defects at the grain boundary and two-phase interfaces, the inherent disorder of the grain boundary, etc. can aid nucleation of domain walls. However, it does recognize one significant aspect, i.e., the presence of oxygen in rare earth based magnets, such as Fe-Nd-B and Sm-Co, (due to the large affinity of the rare earths for oxygen), could significantly alter the magnetocrystalline anisotropy contribution of the rare earth atom to the local magnetocrystalline anisotropy of the crystal. This aspect has been completely overlooked in the literature. However, Jin et. al(122) have considered the effect of point defects in the $SmCo_5$ lattice, specifically, in the Sm sub-lattice in order to explain the difference between the intrinsic coercivity and anisotropy field. They do find that if one or more of the rare earth atoms are removed from the lattice, considerable reductions in the magnetocrystalline anisotropy can be brought about. In general, the rare earth Hamiltonian can be written in the form(123) :
$H = \lambda.\mathbf{L}.\mathbf{S} + H_C + 2.\mu_B.H_{ex}.\mathbf{S}$, where the first term is the spin-orbit coupling, the second is the crystal electric field term and the third is the exchange term. The crystal electric field term is the most important

term for the purpose of determining the magnetocrystalline anisotropy. It can be represented as : $B_l^m = \alpha_1 . \langle r^l \rangle . A_l^m$, where α_l are the Steven's coefficients that depend only upon the nature of the rare earth atom; r^l refers to the average radius of the 4f-shell ; A_l^m are terms that are determined by the electrostatic potential of the neighbouring ions and are dependent upon the nature of the neighbouring ions and the lattice parameters, the atomic charges of the neighbouring ions and their screening. Deryagin(123) has demonstrated that small changes in the lattice parameters can produce large changes in the anisotropy constants, due to the above dependence. Thus, if the presence of oxygen can accomplish this effect, then it is likely that considerable changes in the local magnetocrystalline anisotropy can be introduced.

Fig.III.42 schematically depicts the approach in this section. First the generalized model will be constructed, based upon the general microstructural features of the magnet. Then the effect of thermal treatments, specifically the different cooling rates, will be incorporated by estimating the stresses due primarily to the thermal expansion anisotropy at the matrix-fcc phase interface. This value of stress will then be used to calculate the effective anisotropy field and hence the iHc for different cooling rates. In addition, with the knowledge of the temperature dependence or the composition dependence of the anisotropy field and iHc it will be possible to experimentally verify the model. The temperature dependence will arise due to the specific characteristics of the nucleation sites and the temperature dependence of the activation barrier to nucleation, as was shown by Jin et.al(122) in the case of defects in $SmCo_5$.

Magnetization reversal model in optimally treated magnets :

The model depends upon the idea that the domain wall energy is a function of the location of the wall, with respect to the microstructural features of the magnet. This is the case especially when the wall is close to a grain boundary or to the fcc phase-matrix interface. The grain boundary, being a region of lattice disorder and possibly segregation of impurities such as oxygen can be expected to be a region of lowered magnetocrystalline anisotropy (and even exchange interaction, depending

upon the concentration of non-magnetic impurities). So also, the interface of the matrix with the fcc phase will be a region of lowered magnetocrystalline anisotropy since it is an incoherent interface with some disorder. In this model, however, the effect specifically, of oxygen in the fcc phase will be examined. Thus, stated in a different way, it suggests that oxygen in the grain boundary phase and at the interface reduces the magnetocrystalline anisotropy of the $Nd_2Fe_{14}B$ phase by its strong interaction with the Nd in the $Nd_2Fe_{14}B$ lattice. This is schematically described in Fig.III.43. In this figure, a unit cell of $Nd_2Fe_{14}B$ at the interface with the fcc phase is shown. In addition, oxygen atoms are shown near the Nd atoms to schematically describe the interaction of oxygen with the Nd atoms in the matrix phase.

The variation of domain wall energy with location of the wall is depicted schematically in Fig.III.44. Such a wall energy profile can be rationalized based upon the microstructural and microanalytical observations and with the knowledge that the rare earth rich oxygen stabilized fcc phase is paramagnetic at room temperature. Hence the wall energy is zero in this phase. Similarly, in the case of a grain boundary, the wall energy will decrease considerably from its matrix value of 35 mJ/m^2 (in the case of $Nd_2Fe_{14}B$)[100]. The wall width in this case is about 50Å[100]. Thus, over a small distance, the wall energy drops from its matrix value to zero (or close to zero). This drop in the wall energy can be thought to occur by a decrease in the magnetocrystalline anisotropy of the matrix phase, specifically due to the interaction with oxygen. Similar defect models have been developed by Aharoni[11], Abraham and Aharoni[12], Abraham[124], Hilzinger[125], based on micromagnetic theory, which was originally developed by Brown[126]. In this analysis an energy minimization approach will be adopted and the micromagnetic analysis will not be resorted to. Although this method is a simplification over the micromagnetic approach, it is useful in understanding the origin of the changes in the magnetic properties due to changes in the microstructure[117-120].

A grain in the polycrystalline magnet, is considered, which has been "technically" saturated in the positive direction, i.e., point "L" in Fig.III.45. In this condition, the grain is fully saturated, with no domain walls

remaining. Now let the reversing field act on the magnet, and specifically on the particular grain in question. Due to the finite activation required to nucleate a domain wall, the magnet will be in a metastable state when the field is reduced to zero, i.e., point M in Fig.III.45. The energy of the particle can be expressed in terms of the magnetization energy, the demagnetization energy and the domain wall energy. For a particle of diameter "d" this is given by :

$$E = -2.M_S.H_a.(x/d) + (1/2).D.(2x.M_S/d)^2 + F(x)/d \quad (1)$$

where : E = the total magnetic energy of the particle in question ; M_S= the saturation magnetization of the grain ; H_a = the applied field ; x= the instantaneous position of the domain wall (when it does exist) ; D= the particle demagnetization factor ; F(x) = the position dependent domain wall energy.

The first term in eqn.(1) is the magnetization energy, the second is the demagnetization energy and the third is the position dependent domain wall energy. The term "x/d" gives the instantaneous position of the domain wall as a fraction of the particle diameter. Minimizing the energy, with respect to the position parameter, x :

$$dE/dx = 0 = -2.(1/d).M_S.H_a + 4.D.M_S^2.x.1/d^2 + (1/d).\, dF(x)/dx \quad (2)$$

The instantaneous magnetization can be written as $m=x.M_S/d$. Thus, for example, when the domain wall traverses the width of the grain, x=-d and m=-M (since the direction of magnetization has been reversed).

At the minimum condition :

$$2(1/d).M_S.H_a = 4(1/d).D.M_S.m + dF(x)/dx \quad (3)$$

$$\text{i.e., } H_a = D.m + (1/2M_S).dF(x)/dx \quad (4)$$

At the condition of instability, when the domain wall moves instantaneously and reverses the magnetization of the grain, m=-M and

$$-D.M_S = H_a - (1/2M).dF(x)/dx \quad (5)$$

$$\text{i.e., } H_a + D.M_S = (1/2M_S).dF(x)/dx \quad (6)$$

At this condition of instability, H_a = iHc, the intrinsic coercivity, i.e., the value of the external field at which the reversal occurs. The left hand side of equation (6) is the total field on the grain at reversal, i.e., the nucleation field, which is defined as the value of total field on the grain at which reversal occurs. Here, dF(x)/dx is the gradient in the domain wall energy. For the sake of simplicity, a linear increase in the wall

energy will be assumed, as was the done by Aharoni[11]. Hence, in the first approximation, $dF(x)/dx \approx \Delta F/\Delta x$.
$\Delta F = F_{matrix} - F_{fcc}$, and since F_{fcc} is zero in this model (and very low in the case of grain boundary with oxygen impurities), $\Delta F = F_{matrix}$.
F_{matrix} can be written as $4(AK_1)^{1/2}$, where A is the exchange constant and K_1 is the first order magnetocrystalline anisotropy constant. (This relationship is derived in Appendix I).
Δx is the region over which the wall energy increases from almost zero to its value in the bulk. This can be expressed in terms of the wall width, $\partial = \pi(A/K_1)^{1/2}$. Thus the width Δx will be written as : $\Delta x = C.\partial$, where C is a constant, which is close to unity.

One aspect which emerges from this line of argument is that the nucleation field which has been derived in equation (6) is actually an unpinning field to push a domain wall from the grain boundary region or the fcc-matrix interface region, into the matrix. However, this cannot be considered a true pinning mechanism, since the pinning does not occur in the bulk of the magnet. In addition, this "unpinning" process cannot be distinguished experimentally from a true nucleation process, wherein a wall is nucleated in the grain boundary region. Alternatively, it can be considered that the wall does indeed nucleate at the grain boundary or two-phase interface, but soon gets pinned close to the interface. The nucleation field will then be the field required to push the wall from this position.
Therefore $\Delta x = C.\partial$ and $H_a + D.M_s = H_n = (1/2M_s).4(AK)^{1/2}/C.\pi.(A/K)^{1/2}$ (7)
This simplifies to H_n = nucleation field = $(2K/M_s)/C.\pi$ (8)
However, $2K_1/M_s$ = the anisotropy field for a uniaxial magnet (the derivation of this relationship is presented in Appendix I), when the contribution due to the second order magnetocrystalline anisotropy constant, K_2, is small enough to be neglected.
Therefore $H_n = H_a + D.M_s = H_A/C.\pi$, which for C= unity, reduces to
$H_a = iHc = H_A/\pi - D.M_s$. (9)

DISCUSSION : Before presenting the experimental results pertaining to this model, some aspects of this model will be elaborated. As was mentioned earlier, this model can be considered as an "unpinning" model

although this cannot be experimentally distinguished from a conventional nucleation process. Thus, such a model will be, for all practical purposes, equivalent to a nucleation model. The inherent simplicity of the model and its obvious likeness to the practically observed microstructure of the magnet makes the model appealing. The iHc calculated using this model (from equation (9)), is dependent upon the following parameters : (1) the nature of interaction between oxygen and Nd, or in general, the nature of the influence of the specific defect; (2) the anisotropy field of the matrix phase : any change in the anisotropy field of the matrix $RE_2Fe_{14}B$ phase, either by alloying , by heat treatment or by varying the temperature of measurement, will effect a change in the calculated value of this iHc ; (3) the demagnetizing field : This is dependent on the demagnetizing constant D, which is geometry dependent, and the value of the saturation magnetization, M_S. It may be pointed out that this is not a localized demagnetization factor but a bulk value. This may be determined by two methods : (a) from the slope of the virgin curve, the demagnetizing constant is determined and the product of this with the saturation magnetization gives the bulk demagnetizing field; (b) the demagnetizing field can also be determined from a plot of iHc versus $H_{applied}$ (such as in Fig.III.23), in which the demagnetizing field is the value of the applied field for a point half way to the top of the curve. Both the methods yield similar values of the demagnetizing field of about 12.5kGauss.

The model suggests that if the temperature dependence of the anisotropy field, iHc and the saturation magnetization are measured for the same magnet, then a linear relationship between the nucleation field (given as the sum of the iHc and M_S) and the anisotropy field (given by $2K_1/M_S$) should be observed, as per equation **(9)**. In addition, the slope of the straight line plot of nucleation field against anisotropy field must be equal to $1/\pi$ or about 0.32, within the limits of the assumptions made. So also, if the H_A of the matrix is varied by changing the composition, for example, by adding Dy to increase the anisotropy field, there should be a corresponding increase in the iHc. These two dependences were, thus, used to verify the model. The results are detailed below, for magnets with the same overall composition, i.e., the total rare earth content and the boron content of the alloy was kept the same. In addition, the grain

size of the alloys was also kept roughly the same. The magnets were given the same thermal treatment and the magnetic properties were measured for the same value of applied field.

The effect of temperature on the iHc and anisotropy field could not be experimentally measured due to equipmental limitations. Therefore, data published by Hirosawa et. al.(127) has been used. Fig.III.46 shows the plot of nucleation field versus anisotropy field, measured at different temperatures. Within the experimental errors, a linear fit is obtained, with a slope of 0.38. This value is very close to that predicted by the model (0.32). In another experiment, different amounts of Dy were added to the alloy during casting to obtain alloys with different amounts of Dy in the matrix phase. The anisotropy field of the matrix phase increases with increase in the amount of Dy in it. (Results of these experiments will be described in detail in section III.6). Fig.III.47 shows the effective anisotropy field plotted against the nucleation field. Again, a linear fit is obtained, with a slope of 0.38.

Thus, a reasonably good fit between the the experimental data (Fig.III.46 and Fig.III.47)and the prediction of the model is obtained, considering the approximations made. The slope of the straight line, 0.38, is an estimate of the nature of the nucleation sites. The value of this slope can be increased (as one would like to do to achieve higher intrinsic coercivities) if : (1) the oxygen content of the interface can be reduced--- a very arduous task, considering the strong affinity of the rare earth for oxygen; (2) structural defects can be reduced : this may indicate why the water quenched magnet has a lower iHc, since in this case more structural defects than the slow cooled magnet can be envisaged; (3) if the local composition, especially, the nature of the rare earth (e.g., replacing Nd by Dy or Tb) can be varied; (4) if the amount of the Nd in the alloy can be increased, thus providing better isolation of the magnetic grains through the non-magnetic grain boundary phase. Adler and Hamann(102) and also Herzer et.al(128) have developed similar equations based on empirical grounds. The value of the slope of the straight line in their case was 0.55, since the composition was richer in Nd. However, the significant point is the similarity in the nature of the relationships derived in this investigation and by other investigators.

The value of the slope is sensitive to overall changes in the microstructural and microanalytical details of the magnet. Thus, as will be shown later in this section, the grain size of the magnet can wield a marked influence upon the iHc of the magnet. So also, the total amount of Nd in the alloy will have a significant on the iHc and B_r, as was experimantally shown by Sagawa et.al[5]. Hence, comparisons of magnetic properties should be carried out at comparable average grain size of the polycrystalline magnet. The model suggests, indirectly, that it is not necessary to increase the bulk magnetocrystalline anisotropy of the matrix phase in order to improve the iHc of the magnet. (This is because, once nucleation occurs at the grain boundaries and interfaces, the wall traverses almost instantaneously across the grain, to reverse the magnetization.) Instead, it is sufficient if the magnetocrystalline anisotropy of a local region of about a few hundred angstroms, near the grain boundaries and two-phase interfaces, is increased by suitable alloying additions. Such a specific "doping" of the grain boundaries and two-phase interfaces is discussed in section III.6.

Although the nature of magnetization reversal can be examined by using any of the methods employed in section III.2, one of the most striking evidences of a nucleation type magnet is the effect of grain size and distribution on the iHc and the distribution in iHc. In the model described in section III.4, it was illustrated that domain wall nucleation occurs, in general, due to the existence of regions of lowered magnetocrystalline anisotropy and/or enhanced demagnetizing fields. Such regions exist, for example, at the interface of the matrix with the oxygen stabilized grain boundary phase. Here, the interaction of oxygen with the Nd atom in $Nd_2Fe_{14}B$ was assumed to cause the decrease of anisotropy of $Nd_2Fe_{14}B$, although the calculations have been carried out for a general defect. Thus, in general, defects exist all over the surface of the polyhedral grains. The larger the number of defects, the greater the probability that one such defect will nucleate a domain wall. Thus, in general, a definite influence of the grain size on the iHc (or nucleation field) should be found, especially for nucleation type magnets, since in general, the number of defects will increase with grain size.

In general, there is an inverse relationship between the average grain

size and the iHc, although the exact nature of the dependence is not clear. In the case of other permanent magnetic materials, attempts were made to correlate the average grain size to the iHc. The earliest efforts were made by Guillaud[129] who examined MnBi particles and showed that the iHc was inversely proportional to the size of the particle, although the relationship was not hyperbolic. A similar relationship was predicted by Carey et. al[98]. Brown[94] suggested that the dependence of iHc on the particle size could be related to the density of surface defects, which could act as nucleation sites for domain walls, thus leading to iHc being lower than the anisotropy field and the consequent particle size dependence (Brown's paradox). Brown[94] has also shown that if the density of surface defects has a Poisson distribution, then the number of defects will decrease rapidly with decrease in the particle diameter. McCurrie[96] demonstrated that in the case of Sm-Co magnets, iHc is inversely proportional to the particle size, with a sharp increase in iHc for particle sizes below about 45 micrometers. However, he did not find a simple relationship between the particle size and grain size distributions.

This strong dependence of iHc on the grain size is probably one of the best evidences for a nucleation magnet. This dependence can be qualitatively explained as being due to an increase in the number of defects at the grain boundaries and surfaces. This leads to a greater probability of domain wall nucleation. However, analytical correlation of the defect statistics to the iHc distribution has still eluded theorists. In powder processed permanent magnets, such as Fe-Nd-B, the grain size distribution follows a log-normal distribution with a positive skew (more fines than coarse particles), as was shown by the analysis of Kolmogoroff on comminution of brittle materials[130]. A typical grain size distribution plot is shown in Fig.III.48., illustrating the positively skewed nature of the distribution. This plot is for the optimally cooled Fe-Nd-Pr-Ce-B magnets examined in section III.1&2. Corresponding to this grain size distribution, there exists a coercivity distribution, which can be determined from the slope of the demagnetization curve. Fig.III.49 illustrates the iHc distribution for the sample with grain size distribution shown in Fig.III.48. This plot has been obtained by taking the slope of the demagnetizing curve, at each point on the curve. This method has been

suggested by McCurrie[96]. The plot indicates that the iHc distribution is almost a normal distribution. If the particle size distribution is narrow, the iHc distribution will also have a sharp peak and vice versa. On the other hand, if coarse grains and fine grains co-exist, such as a bi-modal grain size distribution, then discrete steps in the second quadrant of the hysteresis loops will be observed, corresponding to the iHc (or nucleation field) of the coarse grains[131]. Thus, in general, a one-to-one correspondence exists between the grain size (and its distribution)and the iHc(and its distribution). It is also true, in general, that if the average grain size of the magnet increases, the iHc will decrease, thus validating the inverse relationship between grain size and iHc. This functionality comes about because of the dependence of the number of defects on the size of the particles and the dependence of the nucleation field on the number of defects.

To establish a relationship between iHc and grain size distributions, the following steps have to be undertaken :

(1) The first step is to define the morphology of the grains: this can be accomplished by assuming a tetrakaidecahedral shape of the grains, in which case the surface area of the grain is given by $S=26.78 \times l^2$, where "l" is the edge length of the grain(i.e., the grain size measured from optical micrographs)[132].

(2) The second step is to establish the relationship between the total surface area of the grain and the number of defects on its surface, with no distinction as to the nature of the defects. This can be accomplished using the idea that the probability of finding one defect in an area ΔS is $L.\Delta S$, where L is a constant; the probability of finding more than one defect is of the order of (ΔS^2); the defects act independent of each other. Thus the probability that there are "n" defects is[94] :

$P(n/S)= e^{-L.S}.(L.S)^n/n!$ --- **(10)** ---a Poisson distribution. The average number of defects is $L.S = L.x.26.78.l^2$. Thus, for L being a constant, the average number of defects in a grain of length "l" is proportional to l^2.

(3) The next step is to determine the value of the constant L : this has been accomplished by the following method : the critical particle size for single domain behaviour in the case of $Nd_2Fe_{14}B$ is 0.3μm[100,133]. This suggests that the magnetization of a particle of this diameter will not

reverse by domain wall nucleation, but by coherent rotation. This further suggests that the probability of finding a defect, which can potentially nucleate a domain wall, is negligible. This probability, $e^{-L.S}$, has been arbitrarily assumed, as was by Brown[94], as 10^{-2} (i.e., 1% probability of finding a defect). Since S for a tetrakaidecahedral particle of this diameter is known ($26.78 \times l^2 = .6025 \mu m^2$) the value of "L" can be calculated. This is found to be 7.64 μm^{-2}. Thus, the average number of defects as a function of grain size can be determined. The assumption here is that the constant "L" is independent of grain size.

(4) The next step is to establish the relationship between the average number of defects and the nucleation field(or iHc) : this has been accomplished by adopting a modification of the model proposed by Brown[94]. The probability of finding "n" defects is, as was shown before, a Poisson distribution. That is : $P(n/S) = e^{-(L.S)}.(L.S)^n/n!$, (11)

where the notation P(A/B) denotes the probability of the occurrence of the event A, given the event B[95].

Let the nucleation field (or coercive field) be "X", with a distribution function denoted by F(X). In a sample with a distribution of nucleation fields, the event "at least one nucleation field less than X" is exclusive to the event "all nucleation fields greater than X". This means that nucleation of a domain wall will occur at the site with the lowest nucleation field required and also that once this nucleation event has occurred, the other potential nucleation sites will not activate. This can be represented as :

$P(X_i<X)=F(X)$ and $P(X_i>X)=1-F(X)$. (12)

For "n" nucleation sites : $P(\text{all } X_i>X/n)= \{1-F(X)\}^n$ (13)

and, $P(iHc<X/n) = 1-\{1-F(X)\}^n$ (14)

This is because reversal nucleates when the reverse field exceeds the lowest of the various nucleation fields.

If B_i are mutually exclusive events, then : $P(A) = \Sigma_i P(A/B_i).P(B_i)$ (15)

Hence : $P(iHc<X) = \Sigma_n P(iHc<X/n).P(n)$. This is the distribution function of iHc and is denoted as:

$\varnothing(X) = \Sigma[1-\{1-F(X)\}^n].\exp^{-L.S}.(L.S)^n/n! = 1-e^{-(L.S.F(X)}$ (16)

where F(X) is the distribution function of the nucleation field, X (or the intrinsic coercivity). The probability density function is given by

$\phi(X) = d(\varnothing(X)/dx$.

This function is characteristic of a sigmoidal distribution, which is common in nucleation and growth transformations. In the above equation , the unknown is the form of the function F(X) or F(iHc), as a function of the particle size, or in other words, the number of defects on the surface of the particle. This can be determined from the plot in Fig.III.49, which is actually the iHc distribution. The cumulative fraction versus iHc plot corresponding to Fig.III.49 is shown in Fig.III.50. This plot has a sigmoidal shape and corresponds to the distribution function $\varnothing(X)$. To determine the nature of the function F(X), the above distribution function can be re-written as follows:

$1-\varnothing(X) = e^{-L.S.F(X)}$ and hence $\ln(1-\varnothing(X) = -L.S.F(X)$. **(17)**

Upon taking logarithms again, after cancelling the negative signs which appear upon taking logarithms the first time, the following is obtained:

$\ln[\ln\{1-\varnothing(X)\}] = \ln(L.S) + \ln F(X)$. **(18)**

Thus a plot of $\ln[\ln\{1-\varnothing(X)\}]$ against $\ln F(X)$ should give a straight line with intercept of ln(L.S) and slope corresponding to the nature of the function F(X). In Fig.III.51, $\ln[\ln\{1-\varnothing(X)\}]$ is plotted against iHc. A straight line fit is obtained, with a regression coefficient of 0.99, although in the intermediate regions, the plot shows deviations from linearity. In spite of this, the linear fit is significant in that it gives an indication of the nature of the function F(X). From the above equation and the nature of the plot in Fig.III.51, it can be seen that $\ln F(iHc) = 0.3427(iHc)$. Therefore, $F(iHc) = [\exp(iHc)]^{0.3427}$ or to the first approximation, $F(iHc) \approx [\exp(iHc)]^{1/3}$. Thus, in this approximation, the distribution function of iHc (or nucleation field) is given by :

$\varnothing(X) = 1-\exp(-L.S.[\exp\{iHc\}]^{1/3})$ **(19)**

In the case of a polycrystalline magnet, the expected value of coercivity is given by the median value of the distribution of coercivities. This value is given by : $\int\phi(X).dx = 1/2$. Upon substituting this in equation (19), the following result is obtained : $F(iHc) = (\ln 2)/(L.S)$. Since the nature of F(iHc) is already known from Fig.III.51 as $F(iHc) = [\exp(iHc)]^{1/3}$ the relationship between iHc and the average number of defects, L.S. and hence the grain size, "l", can be established. From the above equation :

$[\exp(iHc)]^{1/3} = (\ln 2)/L.S$; i.e.,$[\exp(iHc)]^{1/3} = (\ln 2)/L.(26.78xl^2)$ **(20)**

Upon taking logarithms : $iHc/3 = \ln(\ln 2/L.S)$. **(21)**
Thus, a plot of iHc against ln(L.S) should be linear. That is, a plot of iHc versus $\ln[(\text{grain size})^2]$ must be linear.

In order to test this model, polycrystalline magnets with different average grain sizes were prepared by using starting particles from different sieve fractions. The iHc in this case corresponds to the median value, i.e., the value of applied field for which the effective magnetization is zero (i.e., when the demagnetization curve crosses the x-axis) and the grain sizes correspond to the average obtained from plots similar to that shown in Fig.III.48. In order to maintain other microstructural factors such as the amount of the fcc phase, the oxygen content, etc. constant, all the magnets were prepared under identical conditions, with the same overall composition of Fe-34.5 wt.%Nd-1 wt.% B, at the same sintering temperature of 1040°C. However, in the case of the large grain size magnets, especially above 100μm, the sintering temperature had to be raised to about 1080-1100°C in order to obtain densification. The magnetic properties were obtained under the same applied field conditions. Fig.III.52 shows the effect of grain size on iHc. In this plot, iHc is plotted against $\ln[(\text{grain size})^2]$, where the grain size is expressed in micrometers. The linear fit is reasonably good, considering the nature of the approximations made in the derivation of the inter-relationships.

DISCUSSION : The model presented here is simplistic in the following respects : (1) the physics has been simplified, ostensibly so, in order to highlight the statistical effects which are evidently important in considering the nucleation process. The dependence of the nucleation field (or iHc) on non-statistical factors, such as composition, heat-treatment, etc. have been minimized by adopting the same composition and heat-treatment. One of the main aspects here is the nature of the dependence of the intrinsic coercivity on the number of defects (and hence the grain size). The dependence of number of defects on the size of each particle has been established by assuming a Poisson distribution for the number of defects (i.e., no interaction of the defects with one another). However, the unknown physical relation between the number of defects and the resulting iHc has been evaluated using the iHc distribution

data for a typical magnet. The implicit assumption that this relationship obtained for a typical furnace cooled magnet is valid for magnets with different grain sizes is reasonable since the hysteresis loops of the magnets with the large grains as well as fine grains have the same shape. (2) The statistics of the problem has been simplified to a certain extent. However, one of the positive aspects of this model is that the nature of the function $F(X) = [\exp(iHc)]^{1/3}$ has been obtained by a linear fit to the experimental data, while Brown(94) had assumed the same functional dependence on purely intuitive grounds. On the other hand, McIntyre derived the same equation, but used a different functional form of F(X), which was equal to $(iHc/H_A)^2$, where H_A is the anisotropy field of the magnet. This form, however, has no theoretical or experimental justification.

Another positive feature of the model is that the inverse linear dependence of iHc on Ln [(grain size)^2], i.e., ln(number of defects), is intuitively and metallurgically pleasing. Thus, as the number of defects increase, either due to an increase in the grain size or due to thermal treatments such as water quenching, the iHc decreases as the logarithm of the (grain size)^2 or the logarithm of the number of defects. The fact that the iHc (or nucleation field) decreases with increase in grain size (and hence the number of defects), should be taken as an indicator that the larger the number of defects, the greater is the probability of finding a more potent defect, as compared to a grain with smaller number of defects. Finally, the results are quite significant since they suggest that the statistical aspects of nucleation need to be considered in addition to the physical causes for nucleation of domain walls. This is more so in the case of polycrystalline magnets that are processed by conventional powder processing methods, wherein surface defects can be readily introduced. These defects can be introduced not only due to the powdering process, but also by the thermal treatments which follow the sintering step. One typical example is the water quenching treatment, which lowers the iHc, presumably due to the introduction of defects on the surface of the grains or the two-phase interfaces. Thus, in the next section, the effect of stresses due to quenching (thereby introducing defects) will be examined.

Effect of post-sintering treatments:

"No part of our subject is more interesting than that which deals with the effects of mechanical stress in altering the susceptibility, the retentiveness and other qualities of the three magnetic metals"---J.A.Ewing (1900).

This statement cannot be more valid in any magnetic material than in Fe-Nd-B magnets. One of the most intriguing aspects of this investigation is the observation of a strong dependence of the intrinsic coercivity on the cooling rate from sintering temperature. As suggested in section III.3, this dependence could arise due to the effect of quenching rate on quenching stresses, which in turn could impose local elastic deformation, near the grain boundaries and two phase interfaces. This local deformation could in turn lower the magnetocrystalline anisotropy of the $Nd_2Fe_{14}B$ phase, locally.

Upon quenching, stresses could arise due to the following reasons : (1) random orientation of anisotropic grains leading to localized thermal expansion anisotropy across the interfaces --- in the case of Fe-Nd-B magnets, since the tetragonal $Nd_2Fe_{14}B$ grains are pre-aligned with the c-axis along the axis of the sample, stresses due to random orientation of the c-axis may be considered to be negligible. However, the thermal expansivity of $Nd_2Fe_{14}B$ itself is anisotropic along the a-axis and the c-axis. (2) presence of two phases with a difference in thermal expansivity, leading to localized stresses at the interface(114) ; (3) thermal shock due to thermal gradients in the solid(116). However, since the magnet is metallic and high thermal conductivity can be expected, stresses due to thremal shock are bound to be minimal, as compared to the stresses that can arise due to the different thermal expansivities of $Nd_2Fe_{14}B$ and the grain boundary fcc phase. The high cooling rate of a water quench exacerbates the situation by not permitting relaxation of the stresses by diffusive creep. Hence, in the following analysis, stresses due to the inability to accomodate constrained thermal expansions of the two phases will be considered to be the main cause for the lowering of the local magnetocrystalline anisotropy of $Nd_2Fe_{14}B$ near the grain boundaries and two-phase interfaces.

In elastic solids , the local stresses due to difference in thermal expansion differences is given by : $\Sigma = \Delta a.\Delta T/S_{eff}$[114], **(22)**
where Δa= the difference in thermal expansions of the two phases; ΔT=the temperature difference between the sintering temperature and room temperature; S_{eff}= the effective material compliance. In the case when the difference in thermal expansions is due to the grain boundary phase the stress, Σ becomes : $\Sigma = \Delta a.\Delta T/(S_a+S_{fcc})$, where S_a is the compliance of the matrix phase along the a-axis and S_{fcc} is the compliance of the fcc phase. The model is schematically illustrated in Fig.III.53. It shows the interface between the matrix and the grain boundary fcc phase. $Nd_2Fe_{14}B$ exhibits exhibits anisotropy in thermal expansions along the c-axis and the a-axis. According to published data of Andreev et. al[134], a_a=12.4 x $10^{-6}/^oK$, a_c= 9.3 x $10^{-6}/^oK$, while a_v= 34.1 x $10^{-6}/^oK$. There is no published data at the present time for the thermal expansion properties of the grain boundary fcc phase. However, room temperature thermal expansivity data for polycrystalline commercial purity Nd (with some oxygen impurity) is available[135]. Although this may not be an accurate value for the grain boundary phase, it will be used to obtain an estimate of the magnitude of the stresses due to quenching. The coefficient of linear thermal expansion of polycrystalline Nd is 9.6 x $10^{-6}/^oK$. Thus, in addition to the anisotropy in thermal expansion along the c-axis and a-axis of the $RE_2Fe_{14}B$, there is, concievably, a difference in thermal expansivity of the a-direction and that of the fcc phase. This difference can lead to tensile stresses at the interface, since the matrix contracts more than the fcc phase, on quenching. Hence for a sintering temperature of 1100°C, with a quench temperature of 25°C, ΔT = 1075°C. Δa= (12.4-9.6)x$10^{-6}/^oK$, along the a-direction. $1/S_{eff}$ is the effective Young's modulus of the magnet. This has been determined as a function of temperature for the sintered magnet of similar composition as in this investigation, by Yang et.al[136]. At room temperature, the Young's modulus is 15x10^{11}dynes/cm^2, while at the sintering temperature it is only 10.3x10^{11}dynes/cm^2. It was shown by Yang et.al[136] that there is a sharp rise in the Young's modulus around 500-600°C. In addition, the anisotropy in the Young's modulus(i.e., along the c-direction and normal to it) reaches a maximum of about 12% at the same temperature. These

observations suggest the following inferences : (1) the magnet is mechanically stiffer at room temperature than at a temperature higher than 600°C; (2) the largest increase in the Young's modulus is at the same temperature as the optimum annealing temperature, to obtain the highest iHc. This is indicative that the magnetic properties and the changes in the iHc due to quenching may be related to the changes in the mechanical properties, i.e., the ability of the material to deform elastically. This experimentally determined value of Young's modulus, has been used for determining S_a of the matrix, while for the grain boundary phase, S_{fcc}, has been assumed to be similar to that of commercial purity Nd, for which the stiffness constants are available in literature. From this, the maximum value of thermal stress, $\Delta\Sigma$, is calculated to be :

$$\Delta T.\Delta a.E/2 = 1075 \times 2.8 \times 10^{-6} \times 3.28 \times 10^{10}/ = 0.98 \times 10^{8} \text{ Pa.} \quad (24)$$

The contribution of stress to the overall anisotropy is then calculated by using the relation $K_\Sigma = (3/2.L_a.\Delta\Sigma)$, (25)

where L_a is the room temperature spontaneous magnetostriction constant along the a-axis for $Nd_2Fe_{14}B$. This value has been obtained from the paper of Andreev et.al(134) and is 7.5×10^{-3}. From the above relationship, $K_\Sigma = 1.11 \times 10^6$ Joules/m^3. This is a significant fraction of the room temperature magnetocrystalline anisotropy constant of $Nd_2Fe_{14}B$, which is 4.5×10^6 Joules/m^3 (100). Therefore, the effective anisotropy, in the presence of the above-mentioned stress, is $(4.5-1.11) \times 10^6$ Joules/m^3 at room temperature.

This value of effective anisotropy constant can now be substituted into equation **(9)** (i.e., using the same model as for the optimally cooled magnet) and the effective local anisotropy field can be arrived at. This can be calculated to be $2 \times (4.5-1.11) \times 10^6/1.61 = 52.64$kOe, where the saturation magnetization of the grain is taken to be 1.61Teslas at room temperature. The intrinsic coercivity calculated using equation (9) is $52.64/\pi - N_d.M_s$, where the second term is the demagnetizing field. The demagnetizing field has been assumed to be the same as in the earlier calculation, i.e., 12.5kG. The iHc calculated is thus equal to 4.25kOe.

DISCUSSION: In the above approximate calculation, the effect of water quenching has been considered. The main inference from such an

approximate calculation is that the effect of quenching stresses can be quite significant in reducing the magnetocrystalline anisotropy of the $RE_2Fe_{14}B$ phase. The main contributions to this are : (1) the presence of two phases with different thermal expansivities; (2) the large value of spontaneous magnetostriction constant of the matrix phase---this value is much higher than other magnetic materials. Andreev et. al[134] have attributed this large value to the isotropic "exchange" contribution of the Fe sub-lattices rather than to the anisotropic contribution of the rare earth sub-lattices ; (3) the high cooling rates during a water quench. It is also possible to include the effect of different cooling rates into the calculation. Such a model, incorporating the effect of cooling rate into the calculation of thermal expansion stresses, has been carried out for anisotropic ceramics such as Al_2O_3 by Blendell and Coble[114]. In their model, stress relaxation is accounted for by diffusional creep, a phenomenon which could very well occur in the Fe-Nd-B system. In their model, Al_2O_3 has been considered as a linear visco-elastic solid. The application of such a model to the Fe-Nd-B system must await knowledge of the deformation characteristics of the magnet. One of the conclusions of their investigation, which is of great relevance in this work is that there exists a critical temperature, T_R, below which a quenched sample cannot relax the stresses due to thermal expansion differences. This temperature is about 0.6-0.7 T_M, where T_M is the melting point of the sample (in their case Al_2O_3). This temperature is dependent upon the cooling rate and the grain size of the sample. Of greater importance is the deduction that stresses due to thermal expansion differences can be avoided if the sample is cooled slowly to below T_R, after which the cooling rate has no effect on the stress and thermal expansion anisotropy stresses will not develop to a significant extent. In general, in the case of metals and alloys, it is known that the minimum temperature to which a sample must be heated in order to effect stress relieving is about $0.6T_M$, where T_M is the melting point of the solid. In the case of $Nd_2Fe_{14}B$, with a melting point of 1180°C[5] (1453°K), $0.6T_M$is about 600°C. Thus, the temperature T_R corresponds to the temperature to which a sample must be heated after quenching in order to relieve the quenching stresses. On the other hand, T_R ($\approx 0.6T_M$) is the minimum temperature to

which a sample should be cooled slowly, in order to avoid stresses due to thermal expansion. As was shown in Fig.III.25, the annealing temperature corresponding to the highest iHc is also around 500-600°C.

The above observation that the sample must be cooled slowly to below T_R (which in the case of $Nd_2Fe_{14}B$ is around 600°C) in order to avoid the influence of thermal expansion stresses, is authenticated by the results of step quench experiments, which are presented below. In this experiment, the magnet was slowly cooled to a temperature T_Q, followed by rapidly quenching into water. This is schematically illustrated in Fig.III.54. In this figure, the cooling curve for the slow furnace cooled sample
(50°C/hour) is depicted, with the superimposition of the step quench treatments. The samples were Fe-Nd-Ce-Pr-B magnets of the same composition as the samples used in the quench rate experiments (section III.3). The various step quench temperatures were 1080°C (sintering temperature), 900°C, 700°C, 500°C and 300°C. Specifically, 700°C and 500°C were chosen in order that the critical temperature of 600°C could be straddled. Samples were quenched into water after slow cooling to the quench temperature. Based on the results presented above, it could be expected that in the case of samples quenched from above T_R(about 600°C), the iHc would be low, while in the case of all the samples quenched from below this temperature, the iHc would be high.

Fig.III.55 shows the iHc as a function of the quench temperature, T_Q. This figure shows exactly what would be expected from the inferences of the quenching stress argument. For samples which were quenched from a temperature higher than 600°C, the iHc is low, although in the case of the 700°C sample, the iHc already shows signs of increasing from that of the quenched sample. However, when the quench temperature is just 200°C lower, i.e., 500°C, the iHc jumps to a large value of 9.5kOe. So, in the case of samples quenched from a temperature higher than T_R(i.e., 600°C), quenching stresses due to the thermal expansion difference between $Nd_2Fe_{14}B$ and the grain boundary phase are indeed significant in reducing the iHc. Fig.III.56, which depicts virgin curves and hysteresis loops for the different step quenched samples, also confirms the above conclusion. It shows that the virgin curves in all the samples are similar. The

hysteresis loops, although of the same shape, widen as the quench temperature is lowered. This again, as in the case of the different cooling rate samples,(Figs.III.35(a-d)), indicates that the only difference is that nucleation of domain walls occurs at lower fields, as the quench temperature is increased. It must be pointed out that there are no significant differences in the microstructural and micro-analytical details of the magnet. Thus the overall microstructure is similar to that shown in Figs.III.3(a&b). Microanalytical line profiling did not show any differences in the different quench temperature samples. Figs.III.57(a-e) show typical line profiles across the matrix-triple junction fcc phase interface. The line profiles indicate no significant differences in the microanalytical details for the different step quench temperatures. Thus, the changes in iHc due to the step quench treatment can indeed be attributed to the effect of stresses caused by thermal expansion difference between the matrix and the grain boundary phase.

In summary, in this section, two different aspects of nucleation of domain walls have been examined. One of them is the physical causes for wall nucleation, i.e., the existence of regions with lowered magnetocrystalline anisotropy, leading to domain wall gradients in the magnet. The extent of lowering of the magnetocrystalline anisotropy can be influenced by the cooling rate from sintering temperature (i.e., thermal treatments following sintering), the composition of the alloy, especially, near grain boundaries and two-phase interfaces, which are the most potent sites for wall nucleation. The other aspect is the statistical nature of the nucleation sites and hence the statistical nature of wall nucleation. Specifically, the effect of the number of defects, through the effect of grain size, on the iHc has been demonstrated through an analytical model, which was also verified experimentally, with a reasonably good correlation of the experimental data to the theoretical prediction. In the next section, the results of interaction of domain walls with microstructural features will be presented. The results will highlight the effect of grain boundaries, grain boundary fcc phase and inclusions on the movement of domain walls.

5. LORENTZ MICROSCOPY : MICROSTRUCTURE-DOMAIN WALL INTERACTIONS

In the earlier sections the plausible mechanisms of domain wall nucleation have been discussed, in order to understand the causes for the low iHc, compared to the anisotropy field of the magnets. In addition, the effects of thermal treatments have also been discussed. However, in all the cases, nucleation of domain wall and its prevention was the only concern, at least in the case of Fe-Nd-B magnets. Thus, once the wall nucleates, it inevitably traverses the grain to reverse the magnetization of the grain. If the movement of the wall can be resisted by some method, the iHc and some of the temperature dependent properties could be improved. Thus, if the nature of interaction of domain walls with the microstructural features could be observed, the microstructure could be suitably altered to try to prevent the motion of the walls. This can be accomplished by several techniques. Domain walls can be observed by the Bitter technique, Kerr optical method, Faraday method, Lorentz electron microscopy (LEM), differential phase contrast LEM, or by holographic techniques(7). Of all these techniques, LEM has reasonably high resolution (about 50-100Å) and can be accomplished on conventional microscopes.

Thus the interaction of domain walls with microstructural features were examined by Lorentz microscopy. In this mode of TEM, the objective lens is defocussed to observe the contrast due to domain walls by using the Lorentz effect. Thus, alternate domain walls appear bright and dark respectively. Although it was not possible to directly observe nucleation of domain walls in a saturated magnet, these experiments were helpful in qualitatively understanding the effect of grain boundaries and second phase regions on the movement of domain walls. This was made possible by using the goniometer tilt stage. By tilting the sample, the in-plane magnetic field of the objective lens could be changed. This was sufficient to move the walls in samples with the walls in the plane of the foil. By this technique, it was possible to observe the interaction of walls with the above mentioned microstructural features. The results of such experiments must, however, be considered qualitative since : (1) the magnitude of the in-plane field could not be precisely evaluated ; (2) the

experiments were carried out using thin foils, whose domain structure will differ from that of a bulk magnet ; (3) the process of ion milling could modify the nature of the microstructure, which consequently could alter the nature of interaction. In spite of these limitations, useful qualitative information can be derived from these experiments. All the experiments were carried out on samples with the optimum thermal treatment.

Samples were examined with the c-axis in the plane of the foil, since in this orientation the walls could be easily moved. Figs.III.58(a-c) shows a sequence of images for the case of a domain wall normal to the grain boundary, indicated by arrows in the in-focus image in (a). The walls move rapidly along the grain boundary, upon tilting the foil. No pinning was observed in this case, as was expected, since the displacement of the wall from its original position does not involve an increase in energy. This can be explained by a model similar to that illustrated in Fig.III.43. In this model, the domain wall energy varies with the position of the wall. Thus, the wall tends to remain anchored at positions of low energy, i.e., regions of low magnetocrystalline anisotropy or low exchange interaction, since these are the two parameters that influence the wall energy. In the case of Fig.III.58, where the wall is normal to the heterogeneity, i.e., the grain boundary (close to which the wall energy would be lower due to the disorder of the grain boundary lowering the anisotropy), the displacement of the wall normal to its length does not place the wall in a higher or lower energy configuration, with respect to its original position. Thus, depending upon the overall energy of the magnetic thin foil and the direction of the field applied, the wall displaces to the right or left without any resistance. This appears to be valid even when the wall is at an angle to the grain boundary. Fig.III.59(b) shows two domain walls at an angle to the grain boundary, shown in the in-focus image in (a). The mutual mis-orientation between the grains is indicated in the diffraction pattern shown in (c). The walls in this case also can be moved easily by tilting the foil. Similar observations have been made by Lin et.al[137].

When the wall was parallel to the grain boundary or to the two-phase interface, strong interaction was observed. This is illustrated in the sequence of images in Figs.III.60(a-d). Fig.III.60(a) is the in-focus image

showing a triple junction fcc phase at the left top corner of the micrograph. This triple junction extends into the two-grain region to a certain extent. This is schematically represented in Fig.III.61. In the Fresnel image in (b) the domain wall can be observed (and is indicated by the arrows). Upon tilting the foil, the wall progressively moves toward the two-grain interface. However, the wall is not driven out of the crystal on continued tilting. On the other hand, the wall is stuck to the two-grain boundary , as can be seen from the micrograph in (d). This progressive movement of the domain wall with tilting is shown schematically in Fig.III.61. This may be indicative of the type I nucleation site described by Becker[21], wherein, due to insufficient saturation, pinned residual domains or "nuclei" already exist in the grain boundary or two-phase interface regions. On reversal of the field direction, these walls reverse the magnetization of the grains, as soon as the field is sufficient to un-pin the wall from this type I site. In the case of the example in Fig.III.60, tilting the sample in the opposite direction did not reversibly move the walls, indicating that the wall was pinned to the site. This behaviour of the domain wall can be explained using the same model that was used to explain the case of a domain wall normal to the grain boundary, i.e., Fig.III.43. In this case, as the domain wall comes very close to the grain boundary, its energy is lowered compared to that in the matrix, since the grain boundary (or the two -phase interface) is a region of lowered magnetocrystalline anisotropy and thus lowered wall energy.

A very interesting observation was made in one of the experiments, wherein the interaction of walls with the fcc phase was examined. In this experiment, the fcc phase at the two grain boundaries was tapered, with a maximum width of about 500Å and a minimum of about 50Å, before the fcc phase merged into a grain boundary. This tapering fcc phase is depicted in Fig.III.62(a) and also in Fig.III.63(a). Fig.III.63 is a continuation of the region depicted in Fig.III.62. In Fig.III.62(b-d) the domain wall, indicated by arrows, is progressively moved inwards by tilting the foil. It is noteworthy that the wall is not continuous across the fcc phase, i.e., the wall corresponding to that in the lower grain, is not observed. In Fig.III.63(b-d) the subsequent positions of the wall are depicted. The main feature in the images in Fig.III.63 is that at a particular stage, between

(b) and (c), the wall becomes continuous across the fcc phase. The thickness of the fcc phase at this point is about 50-100Å. Beyond this, the wall is continuous across the interface. These observations are schematically illustrated in Fig.III.64. It thus appears that a particular critical thickness of the fcc phase is required so that the walls do not interact across the interface. Below this critical thickness of the inter-granular fcc phase, it is possible that there is significant interaction between the two adjacent grains, leading to nucleation of a wall in one grain due to the presence of a wall in the neighbouring grain. This may also explain the increase in iHc with Nd content above that of the stoichiometry of $Nd_2Fe_{14}B$. A higher Nd content means that the number of grain boundaries that are "laced" with the Nd-rich fcc phase will increase. So also, the width of the fcc phase at the boundaries will increase with Nd content.

Domain walls were found to interact strongly with inclusions whose size was within an order of magnitude of the wall width. It has been shown that the most effective wall pinning can be achieved when the extent of the pinning site is of the order of the wall width. However, significant wall pinning can be observed even if the size of the pinning site is within an order of magnitude of the wall width. In Fig.III.65(a-d) a sequence of images is shown, showing the different positions of the wall for different angles of foil tilt. This sequence shows the interaction of the wall with an oxide inclusion, whose diameter is about 500Å. The wall width is about 50-60Å. The strong interaction of the wall with the particle can be observed in (c), where a sharp deflection of the wall near the particle can be seen. The wall did not move out of this "pinned" configuration until the foil is tilted by about 25° from the original position. Similar observations were made in the case of other similar sized inclusions. However, if the inclusion size was much larger than the wall width, no such pinning was observed. This "pinning" suggests that if non-magnetic particles(or even magnetic particles such as γ-Fe_2O_3) of this size are uniformly dispersed throughout the matrix, the domain walls can be effectively pinned. Consequently, this may be one of the methods by which the temperature dependence of iHc and B_r could be improved.

DISCUSSION : The results presented in this section, although qualitative, suggest the following : (1) grain boundaries are weak pinning sites for domain walls, when the wall is non-parallel to the boundary. When the wall is parallel to the grain boundary, the pinning strength appears to be enhanced, an observation which has been verified in the case of other magnets. Otherwise, in the matrix phase the walls are very mobile, an observation that corroborates the large permeabilities observed in the virgin curves of the magnets. This is so in the case of the quenched magnets also. It must be pointed out that although the tilting experiments were carried out on the quenched magnets also, no significant difference was observable. This does not indicate that there are no differences in the reversal behaviour between the quenched magnet and the slow cooled magnet, but only indicates that the difference may lie in the nucleation behaviour, an aspect that could not be examined by these experiments. (2) Another observation has been that of strong pinning of walls by small inclusions. This also has to be qualified by the fact that the observations are on a thin foil, in which the interaction of walls with the microstructural features may be very different from that in bulk magnets. Thus, observation of pinning must be corroborated by supporting observations of the nature of the hysteresis loop and the virgin curve. Notwithstanding this qualification, this observation suggests that a dispersion of fine inclusions could cause domain wall pinning. Thus, if, in addition to "strengthening" the grain boundaries and two-phase interfaces against wall nucleation, either by alloying additions or by suitable heat-treatments, such pinning sites are introduced in the matrix phase, the overall behaviour of the magnet could be improved. This would be especially true of the temperature dependence of iHc and B_r.

Recapitulation: In this chapter, so far, various aspects of the microstructure and magnetization reversal of Fe-Nd-B magnets was discussed. It was shown that the magnetization reversal is controlled by the nucleation of domain walls at grain boundaries and two-phase interfaces. Nucleation was shown to be easier in magnets which were quenched into water, compared to slowly cooled magnets. The role of oxygen in the grain boundary fcc phase was highlighted in explaining the

physical aspects of initiation of magnetization reversal. In the case of the quenched magnets, it was shown that the thermal expansion stresses are the main reason for lowering the overall magnetocrystalline anisotropy, at least locally. The importance of the statistical aspects of nucleation was also emphasised by developing a model which could explain the grain size dependence of iHc. It was also briefly illustrated that domain walls are very mobile inside the grains and interact with grain boundaries only when they are parallel to the boundaries. It was also indicated that the walls could potentially be pinned by fine inclusions.

The next section will describe how the results and inferences of the earlier five sections have been used to suitably modify the composition of the ternary Fe-Nd-B alloy in order to achieve certain combinations of magnetic properties. These results and inferences have been augmented by the knowledge of existing data on the effect of alloying substitutions on the magnetic properties of the $RE_2Fe_{14}B$ phase, which was discussed in section I.4.

6. ALLOY DESIGN IMPLICATIONS

In section I.4, the effects of various additions on the magnetic properties of $Nd_2Fe_{14}B$ were outlined. The salient aspects will be summarized here to put this section in perspective. Alloying elements are added with the following in mind : (1) improve the overall performance of the magnet, i.e., increase the iHc and/or the B_r, which consequently will increase the $(BH)_{max}$ of the magnet. This would mean that for a given volume of the magnet, the energy provided to the external circuit will be larger. A higher iHc also means that the magnet will resist larger demagnetizing fields. Conversely, a higher $(BH)_{max}$ will also mean that for the same amount of external energy required, a smaller volume of the magnet will be sufficient. This will, in turn, lead to a reduction in the size of the final product.

(2) The second and more pressing reason for examining the effect of alloying additions to Fe-Nd-B is that the temperature dependence of iHc for the ternary Fe-Nd-B magnet is very high[107]. This rapid fall of iHc with temperature allows normal demagnetizing fields to produce substantial irreversible losses of magnetization. The low Curie temperature of $Nd_2Fe_{14}B$ produces an undesirably high reversible temperature coefficient of remanence. The adverse effect of a high temperature coefficient of iHc can be substantially offset by additions of Dy or Tb, both of which increase the overall anisotropy field and thus the overall iHc[66-70]. However, both of them lower the remanence due to their anti-parallel coupling to the Fe sub-lattice spins. The major approach to improve the Curie temperature is by adding Co, which, however, decreases the iHc[54-58,75-80]. Full compensation of the reversible temperature coefficient of remanence can be achieved by alloying with Ho[72]. On the other hand if the economy of the process is of importance, Nd can be partially or fully replaced by mischmetal (an alloy of La-Ce-Pr-Nd), which, however, has inferior magnetic properties compared to Nd[83-85].

A totally different, although still untried method, is that of pinning the domain walls. Since magnetization reversal occurs by wall nucleation and movement, the iHc and its temperature dependence can be favourably

altered by introducing inclusions (magnetic or non-magnetic) which can hinder the movement of the walls[138]. This idea is further augmented by the Lorentz microscopy results presented in section III.5. Since the $RE_2Fe_{14}B$ phase tolerates no deviations from stoichiometry and is also very resistant to solid state phase transformations, introduction of second phase particles by a solid state transformation is not feasible. Thus, second phase particles have to be deliberately included in the matrix. There have been,a few attempts to execute this idea experimentally. However, this aspect will not be addressed in this investigation.

From the magnetization reversal model presented in section III.4 it was inferred that any changes in the anisotropy field of the matrix phase will affect the nucleation field of the magnet. This, however, may lead to certain disadvantages, as will be discussed for the case of Dy additions. It was also suggested that large changes in the iHc (or nucleation field) could be potentially brought about by modifying the composition locally, near the grain boundaries and two-phase interfaces, where wall nucleation is most likely to occur. Another important inference was that if the oxygen content around the grain boundaries and at the two-phase interfaces could be reduced or avoided altogether, significant increases in iHc could be produced. However, considering the strong interaction of the rare earths with oxygen and the difficulty in maintaining high vacuum conditions at high temperatures, this has not been attempted. It has already been shown, both theoretically and experimentally,in section III.4, that from the statistical point of view of wall nucleation, higher iHc values can be obtained if the grain size is refined. Refining the grain size leads to a reduction in the number of structural defects. Thus, in this section, attention will be focussed on two aspects. The first is the effect of Dy additions to the matrix on the magnetic properties and microstructure of the magnets. In this set of experiments, Dy was added to the alloy in the ingot casting stage. Results of these experiments will be presented and will be discussed in terms of the model presented in section III.4. The drawbacks of such an addition will then be discussed which will lead to the second aspect, i.e., a brief discussion of other methods of alloying additions to improve, primarily, the iHc.

Effect of Dy additions : It is well established that addition of Dy (either as Dy or as Dy_2O_3) to Fe-Nd-B magnets can increase the iHc of the sintered magnets[81,105,139-141]. Intuitively this has been attributed to the large anisotropy of Dy (anisotropy field of $Dy_2Fe_{14}B$ is ≈155kOe compared to that of $Nd_2Fe_{14}B$, which is 71kOe). However, it has not been shown whether this increase in iHc was due to the preferential partitioning of Dy to the $Re_2Fe_{14}B$ phase or due to segregation to the interfaces and grain boundaries. As was shown earlier, both these mechanisms could increase the iHc. Thus, in order to clarify this and understand the role of Dy in the evolution of the magnetic properties, increasing amounts of Dy were added to a ternary Fe-Nd-B alloy, keeping the total rare earth content of the alloy constant. So also, the grain size and post-sintering treatments were maintained the same. The magnetic properties were measured under the same conditions.

Fig.III.66 shows the remanence plotted against the Dy content of the alloy, which is expressed as a fraction of the total rare earth content of 35.1 wt.%. The linear decrease in remanence can be explained in terms of the ferrimagnetic coupling of the Dy spins to the Fe spins. The intrinsic coercivity, on the other hand, increases sharply for small additions of Dy, Fig.III.67. However, for Dy contents greater than 10% of the rare earth content (about 3.5 wt.%), the rate of increase in iHc drops, although the iHc still increases. Thus, for a 12 wt.% Dy addition, the iHc can be raised to about 25kOe although the remanence is quite low. This leads to a low energy product. Since the anisotropy field of the $RE_2Fe_{14}B$ phase also increases with Dy content. a correlation between the effective anisotropy field of the $RE_2Fe_{14}B$ phase and the iHc could be expected. The effective anisotropy field has been calculated using a linear rule of mixtures method: $H_A(eff) = X_{Nd}.H_A^{Nd} + X_{Dy}.H_A^{Dy}$, where X_{Nd} and X_{Dy} are the relative atom fractions of Nd and Dy in a total rare earth content of 35.1 Wt.% ; H_A^{Nd} and H_A^{Dy} are the room temperature anisotropy fields of $Nd_2Fe_{14}B$ and $Dy_2Fe_{14}B$ respectively. In Fig.III.68, the iHc is plotted against the effective anisotropy field, calculated using the above equation. For low Dy contents, the relationship is linear, as was observed by Hirosawa et. al.[127], but for Dy contents above about 3-4 wt.% the

plot is non-linear. Since the assumption behind this plot was that Dy enters the $RE_2Fe_{14}B$ lattice and homogeneously replaces Nd, this non-linearity may indicate that some changes in the microstructure may be occurring, leading to the non-linearity. Thus microstructural and microanalytical analyses of the magnets were carried out to understand the cause of this non-linearity.

Microstructure and Microanalysis : The general microstructure of the magnets does not differ significantly from that described in section III.1. A typical bright field TEM micrograph is shown in Fig.III.69, consisting of the matrix phase with the grain boundary fcc phase. In the case of the high Dy content magnets, however, spherical inclusions were observed inside the matrix grains, Fig.III.70 Microanalysis was carried out with two main objectives : (1) examination of partitioning of Dy between the $RE_2Fe_{14}B$ phase and the fcc phase ; (2) determination of whether the inclusions observed in the high Dy content magnets were rich in Dy. Specifically, a correlation between the appearance of the inclusions and the deviation from linearity in Fig.68 was sought. Hence xray microanalysis was carried out for magnets marked A and B (Fig.III.67). For Dy compositions below that of B, detection and quantification becomes practically impossible. The distribution of Dy was examined by line-profiling, Fig.III.14, which is illustrated in Fig.III.71, for the reader's convenience. Fig.III.72(a) shows a typical profile from sample (A). For clarity, the Dy profile is shown in Fig.III.72(b) which shows that, within the limits of EDXS analysis there is no partitioning of Dy to the grain boundary phase, although one might expect Dy, as with the other rare earth elements, to be associated with the oxygen stabilized rare earth rich grain boundary phase. It is also clear that there is no segregation of Dy to the interfaces. This means that the increase in iHc is mainly due to the Dy content of the matrix, which raises the effective anisotropy field of the $RE_2Fe_{14}B$ phase. However, in sample (A) the Dy content of the matrix (3.7-4.0 at.%) was consistently found to be lower than the nominal alloy composition, i.e., 5 at.%. This indicated that some of the Dy could exist in the inclusions found in these high-Dy magnets. Indeed, the inclusions did contain significant amount of Dy, as indicated by the EDX

microanalysis from one such inclusion. Quantification yielded a composition of 59 at.% Nd and 41 at.%Dy. Since the spectrum was obtained using a Be window detector, the possible presence of oxygen in the inclusions was not revealed. However, it is very likely that they are oxides. The presence of such Dy-rich inclusions justifies the drop in iHc observed in the case of sample (A), since it not only reduces the Dy available for the matrix (thereby reducing the effective anisotropy field) but also provides sites for the nucleation of reverse domains, due to the demagnetizing field around the inclusion. In Fig.III.73(a &b), microanalytical line profile for sample (B) is plotted. As in the case of the higher Dy content magnet, in this magnet also Dy partitions almost fully into the matrix phase, without any segregation to the interfaces. Thus, if Dy is added to the alloy in the induction melting stage itself, it partitions almost completely into the matrix.

One of the interesting aspects of the microanalysis data is that in the case of sample (A), the Dy content of the matrix is only about 3.7-4.0 at.%, while the nominal content in the alloy is 5 at.%. Thus, if the effective anisotropy field is calculated with this experimentally determined Dy content, it is lower than that calculated from the nominal composition. In Fig.III.74, the iHc is plotted against the effective anisotropy field calculated from the experimental determination (EDXS) of Dy content of the matrix. In this case, a linear fit can be easily obtained. It is noteworthy that the slope of this linear fit is 0.38, a value which is very close to that predicted by the theoretical model in section III.4 (i.e., $1/\pi$). This again strongly supports the physical basis of the model outlined in section III.4.

DISCUSSION : In this section, it has been illustrated that the iHc of Fe-Nd-B magnets can be increased by small additions of Dy, as has been shown by other workers also. If the Dy addition is made in the induction melting stage, Dy partitions almost fully into the $RE_2Fe_{14}B$ phase. This causes an increase in the effective anisotropy field of the matrix, leading to the increase in iHc. However, one of the main drawbacks of this method is that the remanence drops monotonically with increasing Dy content, Fig.III.66. Consequently, the $(BH)_{max}$ also drops sharply. For instance, the

$(BH)_{max}$ for the highest Dy content magnet is only about 15MGOe, as compared to that of the ternary Fe-Nd-B alloy of the same rare earth content, which is about 36MGOe. This can be a serious drawback, since, in this case, a magnet of twice the volume is required to produce the same field as produced by the Fe-Nd-B magnet. Thus, the main problem in the case of Dy addition is that it is distributed uniformly in the $RE_2Fe_{14}B$ phase, leading to a reduction in the saturation magnetization, remanence and $(BH)_{max}$. However, as was suggested by the results in section III.4, it is not necessary to uniformly increase the magnetocrystalline anisotropy of the $RE_2Fe_{14}B$ phase in order to achieve high iHc and improve the magnetic properties of the magnet. Large iHc values can be obtained if the composition close to the grain boundaries and two-phase interfaces can be modified, such as segregating Dy to these interfaces. This idea is shown schematically in Fig.III.75, in which a hypothetical composition profile across the matrix-fcc phase interface is illustrated. The plot shows the strong segregation of an alloying element close to the interfaces, with the concentration of the added element dropping to zero (or to a very low value) after a short distance into the matrix. The depth to which this "doping" is required can be very small, since the primary motive in this type of "doping" is to make wall nucleation more difficult than in the case of the "undoped" magnet. The purpose in adding the "dopant", which for example could be Dy, Tb or Al,(all of which enhance the anisotropy field of $RE_2Fe_{14}B$), is to locally enhance the anisotropy field so that the effective anisotropy field that is used in equation (9) in section III.4, i.e., $iHc = H_A(eff)/\pi - D.M_S$, is higher. By this method, the bulk of the magnet is still made up of $Nd_2Fe_{14}B$, with a thin shell at the interfaces that is enriched in a high anisotropy species. In essence, the grain boundaries and inter-phase interfaces can be suitably engineered to obtain the right combination of particle surface properties and bulk characteristics. However, to obtain this type of microstructure can be an arduous task. The first step is to device a method by which magnets could be processed to obtain such a microstructure. If such a method is available, then the next step is to control the depth of penetration of the "dopant".

One of the possible methods is to use the "dopant" in the form of a liquid phase, during sintering. Thus, during sintering, if the additive

liquified and redistributed by grain boundary diffusion as is likely to occur, it might be possible to achieve the desired composition profile. Another method of achieving this composition profile could be by vapour deposition of the required "dopant" onto the surface of the particles before aligning, pressing and sintering. In this case, by controlling the vapour pressure and time of deposition, the amount of the dopant"(or the thickness of the layer) can be controlled. However, such experiments have not been reported in the literature. In what follows, the effect of one such typical liquid phase sintering additive will be briefly discussed. The results of pilot experiments presented here are not exhaustive in detail, but do indicate that such sintering additives can be used to successfully achieve selective modification of the composition around grain boundaries and two-phase interfaces.

The main purpose behind the addition of the sintering additive was to improve the iHc of the magnets, without debilitating the remanence or the energy product. As was shown in the earlier part of this section, improvement in the iHc would require the addition of Dy and/or Al to increase the anisotropy field, either locally or throughout the matrix. Thus, low melting, Dy-based compounds were searched for. The main condition was that this additive compound must melt during the sintering of the magnet, thus enabling it to diffuse rapidly along the grain boundaries rather than by bulk diffusion. Examination of the phase diagram of Dy-based alloys indicated that in the case of Dy-Al alloys, an eutectic composition of 20 at.% Al (about 4 wt.% Al) exists. The eutectic melting temperature was around 930°C, ensuring the full melting of the sintering additive during sintering. Thus, a base Fe-33 wt.% Nd-1 wt.% B alloy was made up and 2μm powders were mixed with different amounts of the Dy-Al alloy, which was also in the form of powders (1.6-4μm). The magnets were sintered under conditions identical to that used in the earlier sections of this chapter. The samples were given a post-sintering anneal at 625°C for three hours.

Fig.III.76 shows the effect of different amounts of Dy-Al on the B_r, iHc and $(BH)_{max}$ of the magnets. As expected, the remanence decreases with increasing amounts of the sintering additive, but not significantly enough that the energy product should be low. As can be seen, the energy product

for the magnet with 8 wt.% of Dy-Al is still high enough(≈27MGOe), that the magnet can be used for most applications. However, the enormous iHc of this magnet, >25kOe, means that even at higher temperatures with the drop in iHc with temperature, it will be high enough to resist serious irreversible magnetization losses due to demagnetization effects.

Scanning electron microscopy was carried out on the 8wt.% Dy-Al magnet to examine the general distribution of Dy and Al. Fig.III.77(a) is a secondary electron image of the polished and etched surface of the magnet, and shows grains of the $RE_2Fe_{14}B$ phase typically of about 10-15μm grain size. The back-scattered electron image shown in (b) is interesting. It shows bright regions around the grain boundaries. Since contrast in the back-scattered image arises due to a difference in atomic numbers, this contrast observed in Fig.III.77(b) can be interpreted in terms of segregation of a high atomic number element, which, for example, could be Dy, to the grain boundaries. TEM and AEM were carried out to examine the microstructural features as well as the distribution of the sintering additives in the matrix phase. The focus of the microanalysis experiments was on the interface between the grain boundary fcc phase and the matrix phase, in order to examine for segregation of Dy and/or Al to these interfaces as well as the grain boundaries, as was suggested by the back-scattered SEM image in Fig.III.77(b).

The overall microstructure of the magnets was found to be similar to that of the ternary alloys described earlier in this chapter. Dy-rich inclusions were observed infrequently. Microanalytical line profile across the fcc phase-matrix interface proved to be interesting. Fig.III.78(a) shows a typical profile, obtained by using a line profiling computer program to carry out the STEM line profiling automatically. The concentration profiles for Fe and Nd are as expected. In the case of Dy there appears to be a small amount of segregation to the interface, although Dy appears to partition preferentially to the matrix. However, the most interesting aspect is the Al- line profile, shown for clarity in Fig.III.78(b). A well defined segregation profile can be observed, with the peak value much higher than the statistical fluctuation in the value in the matrix of in the fcc phase. Subsequently, Al segregation was detected in

almost all the interfaces from which microanalytical information was collected. Average compositions of the matrix, the fcc grain boundary phase, the interface between the two phases, as well as grain boundaries is tabulated in Table VI. This segregation of Al to the interface is uniform along the length of the interface as seen clearly from the x-ray map in Fig.III.79. In this figure, x-ray maps corresponding to Fe, Nd, Dy and Al are presented for a region including the grain boundary fcc phase as well as the two interfaces between the matrix and the fcc phase. As is presented in Table VI, grain boundaries also exhibit small amounts of Al segregation compared to the matrix. In the case of the two grain boundary fcc phase also Al segregation was definitely observed. This was determined by microanalysis at various points along the two-grain boundary fcc region using a STEM probe of 300Å. Results of this experiment are presented in Fig.III.80. The bright field image at the top of this figure depicts the triple junction region tapering into a thin two-grain boundary region of about 200Å width. Microanalysis was carried out at five points denoted as Points 1-5. Data for point 1 was acquired from a very thin region, with the 300Å probe consequently overlapping a considerable portion of the matrix on either side. The analysis reflects this. However, what is more important is the significantly higher Al concentration in this region compared to the matrix, point 5. On the other hand, point 3, which is well within the fcc phase, contains no Al and very little of Dy. Thus, it appears that Al segregates preferentially to the interfaces. Dy, on the other hand, tends to partition preferentially to the matrix, thus explaining, at least in part, the large iHc values obtained for this magnet.

These preliminary results suggest that it is indeed possible to achieve preferential segregation of one or more alloying elements to the two phase interfaces and grain boundaries by a suitable modification of the standard processing route. Although the preliminary results indicate insignificant Dy segregation to the two phase interfaces, it should be pointed out that these are but results of the first such experiments carried out to attempt to achieve the concentration profile shown in Fig.III.75. Thus upon optimization of the amount of the sintering additive, the processing conditions, the relative particle size distributions, it is

quite likely that the required concentration profile will be achieved. That it has already been achieved, to a certain extent in the case of Al must be taken as a sign of encouragement to try and further optimize the processing parameters.

CHAPTER IV
OVERALL SUMMARY

During the course of this thesis, the microstructural and microanalytical details of sintered Fe-RE-B magnets have been established. In addition to the matrix $Nd_2Fe_{14}B$ phase, several other phases have been observed. Main among them and the most important is a grain boundary Nd-rich, oxygen stabilized fcc phase. This phase is generally found at the triple junctions of the matrix grains, but frequently extends into the two-grain boundaries. This provides adequate magnetic isolation of the $Nd_2Fe_{14}B$ grains. More importantly, the oxygen in the grain boundary phase has been shown to be of significance in aiding the nucleation of domain walls at the two-phase interfaces and grain boundaries. Although defects, in general, have been attributed to be the cause for the nucleation of domain walls in high anisotropy magnets such as Sm-Co and Fe-Nd-B, the role of oxygen and its strong interaction with the rare earths has not been considered as a possible cause for wall nucleation. In this thesis, this aspect has been identified as one of the most plausible causes for wall nucleation. The main evidences for such a conclusion have been derived from the microanalytical experiments. Based on the microstructural observations, a magnetization reversal model has been developed, that has been used to calculate the iHc in the case of the optimally quenched magnet. This model predicts that the nucleation field, made up of the iHc and the demagnetizing field is linearly related to the anisotropy field. The slope of the linear plot was predicted to be $1/\pi = 0.32$. The validity of the model has been checked by two methods, both of which support the inferences of the model vey well. As a first check for the validity of the model, data on the temperature dependence of the nucleation field and anisotropy field, available in the literature, has been used. A linear relationship between the nucleation field and anisotropy field was shown to exist experimentally, with the slope of the linear plot being 0.38. This value is quite close to that predicted by the model, indicating that the model is valid, within the limits of the assumptions made. To counter-check the validity of the model, the effect of changes in the room temperature anisotropy field on

the nucleation field has been examined by varying the composition of the matrix phase. In this case also, within statistical limits, a linear fit was observed, with a slope of 0.38, thus providing sound experimental backing for the model.

The effect of post-sintering heat-treatments has also been investigated in detail. This has been a point of controversy in the literature. It has been shown that the easy reversal in water quenched magnets as compared to the slowly cooled (optimally cooled) magnet, is not due to the presence of soft-magnetic bcc platelets in side the matrix phase. The main cause for the decrease in iHc, upon water quenching, has been shown to be the thermal expansion stresses at the matrix -fcc phase interface, during quenching from sintering temperature. The quench rate dependence arises directly from the effect of quench rate on the thermal stresses. The presence of such quenching stresses is also related to the ideal post-water-quench annealing temperature of 500-600°C. In the case of $Nd_2Fe_{14}B$, the minimum temperature ($T_c/T_{melting} \approx 0.6$) for recovery of stresses is about 600°C. Thus the ideal annealing temperature is that at which stress relief occurs. Starting from an approximate model for estimating the stresses, the change in anisotropy due to the stresses and the consequent decrease in iHc have been calculated. This model, although approximate, does provide insight into the causes for the stresses and the corresponding decrease in iHc. The changes in the anisotropy due to quenching have been incorporated into the magnetization reversal model to compute an effective anisotropy field in the presence of stresses. It has been demonstrated that the iHc so obtained is close to that obtained experimentally for a water quenched magnet. The fact that the same magnetization reversal model, that was proposed for the optimally quenched magnets, is valid for the water quenched magnets lends additional support for the generality of the model. These results are also supported by the fact that the hysteresis loops for the magnets with different quenching treatments are similar in shape and only differ in their width. This indicates that the only difference is that nucleation occurs at different overall fields.

The statistical aspects of wall nucleation have also been analysed, to provide support for the wall nucleation mechanism. The defect model

proposed by Brown[94] has been used to examine the effect of grain size on the intrinsic coercivity of magnets prepared under identical conditions. Using the model and experimental results of iHc distributions observed in the magnets under study, an inverse dependence of iHc on ln[(average grain size)^2] was predicted. This dependence was experimentally verified to be valid, in the case of sintered Fe-Nd-B magnets.

Using the inferences derived from the microstructural investigation as well as the magnetization reversal model, alloying modifications were proposed and experimental magnets were prepared based on these ideas. It was shown that controlled additions of Dy to the matrix could raise the iHc by increasing the anisotropy field of the matrix phase. It was also shown that this led to a decrease in the remanence and energy product of the magnet due to the anti-ferromagnetic coupling of the Dy spins with the Fe spins. To overcome this problem, it was suggested that a Dy-Al liquid phase sintering addditive be added to a ternary Fe-Nd-B magnet to enhance the nucleation field by preferential segregation of either Dy or Al to the two-phase interfaces and grain boundaries. Results of preliminary experiments indicate that magnets with iHc greater than 25 kOe and energy products of about 28 MGOe can be prepared by this approach. The results of preliminary microanalytical experiments on the magnets suggest that there is significant Al segregation to the fcc phase-matrix interface, while Dy appears to partition preferentially into the matrix $RE_2Fe_{14}B$ phase. Although it would have been preferable to have Dy segregate to the two phase interfaces and grain boundaries, it must be pointed out that the above results have been obtained from pilot experiments. Hence there is much scope for improving the concentration profile (and the magnetic properties) by further modifications in the processing conditions.

Although considerable research has already been carried out on this alloy system, several aspects are still unanswered. For example, the phase diagram of the Fe-Nd-B alloy system is not well understood. Thus, it is quite likely that a systematic investigation of the ternary phase diagram will lead to the discovery of other phases of interest as potential permanent magnet materials. Novel processing routes such as vapour deposition of thin multi-layered films have not been fully examined.

Vapour phase coating of the Fe-Nd-B particles with Dy or Al prior to sintering could be another method by which the composition of the particles could be altered specifically near the grain boundaries and interfaces. It is clear that one of the main goals of further research in this system should be to improve the temperature dependence of the magnetic properties, especially iHc and B_r. Thus consideration should be given to methods by which the domain walls can be pinned. Since the $RE_2Fe_{14}B$ phase is thermally stable and stoichiometric, decomposition of this phase appears to be out of question. However, it is quite possible that pinning sites can be introduced artificially inside the matrix phase. Such pinning sites could be magnetic or non-magnetic second phase particles, an example of which was presented in Fig.III.65. If the cost of the product is of prime concern, then one can resort to additions of elements such as Ce, Pr, La or an alloy of all of them, which is easier to obtain than the pure elements. Thus, there are several aspects of the system that require further investigation in order to improve the properties. In addition, it must be pointed out that not much work has been carried out to elucidate the details of phase equilibria in this system. This is another area of focus for future research. It is very likely that a thorough investigation of the phase equilibria in this ternary alloy system could lead to the discovery of new and magnetically interesting phases.

APPENDIX I

COERCIVITY FOR MAGNETIZATION REVERSAL BY COHERENT ROTATION

In the case when magnetization reversal does not occur by wall nucleation but by a coherent rotation of the magnetization vectors, the intrinsic coercivity is given by the anisotropy field. The derivation of the anisotropy field is given below.

Consider a single crystal sphere of a material with uniaxial magnetic anisotropy, uniformly magnetized to saturation parallel to the easy axis of magnetization. For such a magnet the anisotropy energy is given by :

$$W_K = K_1.\sin^2\theta \qquad \textbf{(A.1)}$$

where θ is the angle between the easy axis and the magnetization direction and K_1 is the first anisotropy constant.

In the presence of a field H along the easy axis, the magnetization direction is rotated by an angle θ. In this state the total energy of the system is given by : $W = 1/6M_S^2 + K_1\sin^2\theta + H.M_S(1-\cos\theta)$ **(A.2)**

The first term is the magnetostatic term for the magnetized sphere with a demagnetizing factor of 1/3, the second term is the anisotropy energy and the third is the magnetic energy. For a minimum of energy W corresponding to the stable position of the magnetization direction :

$dW/d\theta = 0$ and $d^2W/d\theta^2 > 0$. **(A.3)**

Hence, $\theta=0$ is a stable position of the magnetization M_S when $H > -2K_1/M_S$. This value of H is the coercivity of the magnet and is called the anisotropy field of the magnet. In the case when reversal does not occur by wall processes, the magnetization becomes unstable when the absolute value of H is more than $2K_1/M_S$ and the magnetization reverses discontinuously from $\theta=0$ to $\theta=\pi$. The anisotropy field is the upper limit of the coercivity attainable in any magnet. The hysteresis loop, in the case when magnetization reversal does occur by coherent rotation, is rectangular, as shown in Fig.I.2(c).

REFERENCES

(1) G.Hoffer and K.J.Strnat, IEEE Trans. on Magnetics, Mag.-2(1966),p487.

(2) H.R.Kirchmayr and C.A.Poldy in Handbook on the Physics and Chemistry of Rare Earths, Edited by K.A.Gschneidner and L.Eyring, Chapter 2 of Volume 2, North-Holland Publishing Co.,(1979).

(3) R.M.Garvey and C.A.Montano, in Proc. of Eighth International Workshop on Rare Earth Magnets and their applications, Ed.K.J.Strnat, University of Dayton Press(1985), pp397-406.

(4) W.E.Wallace, Rare Earth Intermetallics, Academic Press(1973).

(5) M.Sagawa, S.Fujimura, N.Togawa, H.Yamamoto and Y.Matsuura, Jl.of Appl.Phys., Vol.55(1984), pp2083-2087.

(6) M.Sagawa, S.Fujimura, H.Yamamoto, Y.Matsuura and K.Hiraga, IEEE.Trans. on Magnetics, Mag.-20(1984), pp1584-1589.

(7) B.D.Cullity, Introduction to Magnetic Materials, Addison-Wesley Publishing Co., (1972).

(8) C.Kittel, Introduction to Solid State Physics, Wiley Interscience Publishing Co., (1983).

(9) H.Zijlstra, Chapter 2 of Volume 3 in Ferromagnetic Materials, Ed. E.P.Wohlfarth, North-Holland Publishing Co., (1982), pp37-106.

(10) J.D.Livingston, Paper No.AC-06, Intermag-87, Tokyo, Japan, April 1987.

(11) A.Aharoni, Phys. Rev., Vol.119(1960), pp 127-131.

(12) C.Abraham and A.Aharoni, Phys. Rev., Vol.120(1960), pp1576-1579.

(13) J.J.Becker, IEEE Trans. on Magnetics, Mag.-5(1969), pp211-214.

(14) J.J.Becker, IEEE Trans. on Magnetics, Mag.-7(1971), pp644-647.

(15) Ya.Shur, A.A.Glazer and V.G.Gass, Sov. Phys. Solid State, Vol17(1975), p627.

(16) H.Zijlstra, Jl. of Appl. Phys., Vol.41(1970), pp4881-4885.

(17) H.Zijlstra, Jl. of Appl. Phys., Vol.42(1971), pp1510-1515.

(18) A.S.Yermolenko, A.V.Korolev, V.I.Lagunova and Ye.V.Scherbakova, Phys. of Metals and Metallography, Vol.38(1974), pp1001-1011.

(19) V.G.Gass, A.A.Glazer and Ya.S.Shur, Phys. of Metals and Metallography, Vol.49(1980), pp191-194.

(20) A.S.Yermolenko and A.V.Korolev, Phys. of Metals and Metallography, Vol.36(1973), pp252-59.

(21) J.J.Becker, IEEE Trans. on Magnetics, Mag.-9(1973), pp161-164.

(22) C.W.Searle, W.G.D.Fredrick and H.J.Garrett, IEEE Trans, on Magnetics, Mag.-9(1973), 164-167.

(23) J.J.Becker, IEEE Trans. on Magnetics, Mag.-8(1972), pp520-522.

(24) V.G.Gass, Ya.S.Shur, A.A.Glazer and B.N.Filipov, Phys. of Metals and Metallography, Vol.43(1977), p191.

(25) Ya.S.Shur, A.V.Deryagin, T.V.Sysolina and G.S.Kandaurova, Phys. of Metals and Metallography, Vol.30(1970), p12.

(26) J.J.Becker, AIP Conf. Proc. No.5(1972).

(27) H.Nagel, H.P. Klein and A.Menth, IEEE Trans. on Magnetics, Mag.-11(1975), p1426.

(28) J.J.Becker, Jl. of Appl. Phys., Vol.38(1967), pp1015-1017.

(29) F.C.Frank and J.S.Kasper, Acta Cryst., Vol.11(1958), pp184-190 ; MSE 202, Department of Materials Science and Mineral Engineering, University of California, Berkeley, Spring 1984.

(30) F.C.Frank and J.S.Kasper, Acta Cryst., Vol.12(1959), pp483-499 ; MSE 202, Department of Materials Science and Mineral Engineering, University of California, Berkeley, Spring 1984.

(31) J.S.Kasper, in Theory of Alloy Phases, American Society of Metals Symposium(1956), p269.

(32) J.F.Herbst, J.J.Croat, F.E.Pinkerton and W.B.Yelon, Phys. Rev., B,Vol.29(1984), pp4176-4178.

(33) C.B.Shoemaker, D.P.Shoemaker and R.Fruchart, Acta Cryst., Vol.40C(1984), pp1665-1668.

(34) D.Givord, H.S.Li and J.M.Moreau, Solid State Comm., Vol.50(1984), pp497-499.

(35) H.Boller and H.Oesterreicher, Jl. of Less Common Metals, Vol.103(1984), L5-7.

(36) J.F.Herbst, J.J.Croat and W.B.Yelon, Jl. of Appl. Phys., Vol.57(1985), pp4086-4090.

(37) P.H.Gaskell, Nature, Vol.289(1981), p474.

(38) D.Givord, H.S.Li and F.Tasset, Jl. of Appl. Phys., Vol.57(1985), pp4100-4102.

(39) R.Hasegawa and R.Ray, Jl. of Appl. Phys., Vol.49(1978), p4174.
(40) F.Bolzoni, J.P.Gavigan, D.Givord, H.S.Li, O.Moze and L.Pareti, Jl. of Magn. and Mag. Matls., Vol.66(1987), pp158-162.
(41) D.Givord, H.S.Li and R.Perrier de la Bathie, Solid State Comm., Vol.51(1984), pp857-860.
(42) S.Sinnema, R.J.Radwanski, J.J.M. Franse, D.B.deMooij and K.H.J.Buschow, Jl. of Magn. and Mag. Matls., Vol.44(1984), pp333-341.
(43) N.C.Koon, B.N.Das, M.Rubinstein and J.Tyson, Jl. of Appl. Phys., Vol.57(1985), pp4091-4093.
(44) M.Sagawa, S.Fujimura, H.Yamamoto, Y.Matsuura and S.Hirosawa, Jl. of Appl. Phys., Vol.57(1985), pp4094-4096.
(45) X.K.Sun, R.Grossinger, R.Eibler and H.R.Kirchmayr, Physica 130B(1985), pp300-304.
(46) D.Givord, H.S.Li, J.M.Moreau, R.Perrier de la Bathie and E.de T.de Lacheisserie, Physica 130B(1985), pp323-326.
(47) J.M.D.Coey, Jl. of Less Common Metals, Vol.126(1986), pp21-34.
(48) F.E. Pinkerton and W.R.Dunham, Appl. Phys. Lett., Vol.45(1984), pp1248-1250.
(49) F.E.Pinkerton and W.R.Dunham, Jl. of Aopl. Phys., Vol.57(1985), pp4121-4123.
(50) H.M.van Noort, D.B.de Mooij and K.H.J.Buschow, Jl.of Appl. Phys., Vol.57(1985), pp5414-5419.
(51) M.Rosenberg, P.Deppe and M.Wojcik and H.Stadelmaier, Jl. of Appl. Phys. Vol. 57(1985), pp4124-4126.
(52) E.Potenziani, Jl. of Appl. Phys., Vol.58(1985), pp2764-2766.
(53) A.T.Pedziwiatr and W.E.Wallace, Jl. of Less Common Metals, Vol.126(1986), pp41-52.
(54) K.H.J.Buschow, D.B.de Mooij, S.Sinnema, R.J.Radwanski and J.J.M.Franse, Jl. of MAgn. and Mag. Matls., Vol.51(1985), pp211-217.
(55) H.Fujii, W.E.Wallace and E.B.Boltich, Jl. of Magn. and Mag. Matls., Vol.61(1986), pp251-256.
(56) F.Bolzoni, J.M.D.Coey, J.Gavigan, D.Givord, O.Moze, L.Pareti and T.Viadieu, Jl. of Magn. and Mag. Matls., Vol.65(1987),pp123-127.
(57) A.T.Pedziwiatr and W.E.Wallace, Jl. of Magn. and Mag. Matls.,

Vol.66(1987), pp63-68.

(58) E.Burzo, A.T.Pedziwiatr and W.E.Wallace, Solid State Comm., Vol. 61(1987), pp57-59.

(59) R.Grossinger, P.Obitsch, X.K.Sun, R.Eibler, H.R.Kirchmayr, F.Rothwarf and H.Sassik, Materials Letters, Vol.2(1984), pp539-543.

(60) Y.C.Yang, H.Y.Chen, Z.X.Liu, B.Liao, X.Feng and W.W.Ho, Jl. of Appl. Phys., Vol.57(1985), pp4115-4117.

(61) C.Abache and H.Oesterreicher, Jl. of Appl. Phys., Vol.57(1985), pp4112-4114.

(62) M.Q.Huang, E.Oswald, E.Boltich, S.Hirosawa, W.E.Wallace and E.Schwab, Physica 130B(1985), pp319-322.

(63) Y.Otani, H.Miyajima ans S.Chikazumi, paper No. BP-03 the the 31st Annual Conf. on Magnetism and Magnetic Materials, Baltimore, Maryland, Nov.17-20, 1986.

(64) E.B.Boltich, E.Oswald, M.Q.Huang, S.Hirosawa and W.E.Wallace, Jl. of Appl. Phys., Vol.57(1985), pp4106-4108.

(65) R.Grossinger, X.K.Sun, R.Eibler, K.H.J.Buschow and H.R.Hirchmayr, Jl. of Magn. and Mag. Matls., Vol.58(1986), pp55-60.

(66) X.J.Lu, X.Lou, G.L.Yang, Z.H.Ru, in Proc. Eighth Int. Workshop on Rare Earth magnets and their applications, Ed. K.J.Strnat, University of Dayton Press, (1985), pp683-692.

(67) M.C.Zhang, D.Ma, X.Jiang and S.Liu, in Proc. Eighth Int. Workshop on Rare Earth Magnets and their applications, Ed.K.J.Strnat, University of Dayton Press, (1985), pp541-552.

(68) R.Grossinger, X.K.Sun, R.Eibler and H.R.Kirchmayr, in Proc. Eighth Int. Workshop on Rare Earth magnets and their applications, Ed. K.J.Strnat, University of Dayton Press, (1985), pp553-564.

(69) E.B.Boltich and W.E.Wallace, Jl. of Less Common Metals, Vol. 126(1986), pp35-40.

(70) S.Y.Jiang, F.Pourarian, E.B.Boltich and W.E.Wallace, Paper No. DC-07 in Intermag-87, Tokyo, Japan, April 1987.

(71) Y.C.Yang, W.J.James, X.Li, H.Chen and L.Xu, IEEE TRans. on Magnetics, Mag.-22(1986), pp757-759.

(72) B.M.Ma, K.S.V.L.Narasimhan and J.C.Hurt, IEEE Trans. on Magnetics, Mag.-22(1986), pp1081-1083.

(73) M.Jurczyk and W.E.Wallace, IEEE Trans. on Magnetics, Mag.-2291986), pp755-756.

(74) M.Jurczyk and W.E.Wallace, Jl. of Magn. and Mag. Matls., Vol.59(1986), L182-184.

(75) B.M.Ma and K.S.V.L. Narasimhan, IEEE Trans. on mganetics, Mag.-22(1986), pp916-918.

(76) T. Mizoguchi, T.Sakai, H.Niu and K. Inomata, IEEE Trans. on Magnetics, Mag.-22(1986), pp919-921.

(77) M.Tokunaga, H.Kogure, M.Endoh and H.Harada, Paper No.BC-03, Intermag-87, Tokyo, Japan, April 1987.

(78) Y.Xiao, K.J.Strnat, H.F.Mildrum and A.E.ray, Paper No.BC-05, Intermag-87, Tokyo, Japan, April 1987.

(79) C.Lin, Z.Liu, X.Xu, Paper No. BC-06, Intermag-87, Tokyo, Japan, April 1987.

(80) S.Arai, T.Shibata, N.Koshizuka and M.Nakagura, Paper No. BC-07, Intermag-87, Tokyo, Japan, April 1987.

(81) R.Ramesh, G.Thomas and B.M.Ma. Paper No.F3.4, Materials Research Society Symposium on Permanent Magnet Materials, Symposium F, Anaheim, Ca, April 1987.

(82) J.K.Chen and G.Thomas, Paper No.F3.5, Materials Research Society Symposium on Permanent Magnet Materials, Symposium F, Anaheim, Ca, April 1987.

(83) M.Okada, S.Sugimoto, C.Ishizaka, T.Tanaka and M.Homma, Jl. of Appl. Phys., Vol.57(1985), pp4146-4148.

(84) M.Okada and M.Homma, in Proc. Eighth Int. Workshop on Rare Earth Permanent Magnets and their applications, Ed. K.J. Strnat, University of Dayton Press,(1985), pp507-524.

(85) C.R.Paik, H.Miho, M.Okada and M.Homma, Paper No.CC-03, Intermag-87, Tokyo, Japan, April 1987.

(86) For example, Panel Discussion, Intermag-86, Phoenix, Arizona, April 1986.

(87) K.A.Gschneidner, Rare Earth Alloys, Van Nostrand Publishing Co., (1961).

(88) A.Bezinge, H.F.Braun, J.Muller and K.Yvon, Solid State Comm., Vol.55(1985), pp131-135.

(89) D.Givord, J.M.Moreau and P.Tenaud, Solid State Comm., Vol.55(1985), pp303-306.

(90) J.Ormerod, Jl. of Less Common Metals, Vol.111(1985), pp49-69.

(91) W.G.Moffatt, Handbook of Binary Phase Diagrams, Vol.3, General Electric Co., (1978).

(92) J.J.Becker, IEEE Trans. on Magnetics, Mag.-12(1976), pp965-967.

(93) J.J.Becker, Jl. of Appl. Phys., Vol.39(1968), pp1270-1271.

(94) W.F.Brown, Jl. of Appl. Phys., Vol.33(1962), pp3022-3025.

(95) D.A.McIntyre, J. of Physics, Vol.3D(1970), pp1430-1432.

(96) R.A.McCurrie, Phil. Mag., Vol.22(1970), pp1013-1023.

(97) R.A.McCurrie and G.P.Carswell, Phil. Mag., Vol.23(1971), pp333-343.

(98) R.Carey, J.E.Coleman and I.V.F.Viney, Proc. Royal Soc. of London, Vol.328 A(1972), pp143-151.

(99) G.S.Kandaurova, A.V.Deryagin and A.E.Lagutin, Phys. Stat. Sol., Vol.27A(1975), pp429-440.

(100) M.Sagawa, S.Fujimura, H.Yamamoto, Y.Matsuura, S.Hirosawa and K.Hiraga, in Proc. Eighth Int. Workshop on Rare Earth Permanent Magnets and their applications, Ed.K.J.Strnat, University of Dayton Press, (1985), pp587-612.

(101) K.D.Durst and H.Kronmuller, in Proc. Eighth Int. Workshop on Rare Earth Permanent Magnets and their applications, Ed. K.J.Strnat, University of Dayton Press, (1985), pp725-736.

(102) E.Adler and P.Hamann, in Proc. Eighth Int. Workshop on Rare Earth Permanent Magnets and their applications, Ed. K.J.Strnat, University of Dayton Press, (1985), pp747-760.

(103) K.Hiraga, M.Hirabayashi, M.Sagawa and Y.Matsuura, Jap. Jl. of Appl. Phys., Vol.24(1985), ppL-30-32.

(104) K.Hiraga, M.Hirabayashi, M.Sagawa and Y.Matsuura, Jap. Jl. of Appl. Phys., Vol.24(1985), pp699-703.

(105) M.Tokunaga, M.Tobise, N.Meguro and H.Harada, IEEE Trans. on Magnetics, Mag.-22(1986), pp904-909.

(106) M.Sagawa, S.Hirosawa, H.Yamamoto, Y.Matsuura, S.Fujimura, H.Tokuhara and K.Hiraga, IEEE Trans. on Magnetics, Mag.-22(1986), pp910-912.

(107) J.D.Livingston, in Proc. of ASM Symposium on Soft and Hard

Magnetic Materials, Eds. J.A.Salsgiver, et.al., Florida(1986), pp71-79.

(108) N.A.El-Masry and H.H.Stadelmaier, Materials Letters, Vol.3(1985), pp405-408.

(109) H.H.Stadelmaier and N.A.El-Masry, in Proc. of Eighth Int. Workshop on Rare Earth Permanent Magnets and their applications, Ed. K.J.Strnat, University of Dayton Press, (1985), pp613-634.

(110) R.Ramesh, J.K.Chen and G.Thomas, Jl. of Appl. Phys., Vol.61(1987), pp2993-2998.

(111) S.Zhou, L.Lin, L.Zhang and Q.Hu, Paper No.4G4, International Conference on Magnetism, San Fransisco, (1985).

(112) R.Ramesh, G.Thomas, M.Okada and M.Homma, Paper No.AC-07, Intermag-87, Tokyo, Japan, April 1987.

(113) M.Guttmann and D.McLean, in Interfacial Segregation, Proc. American Society for Metals SeminarEd. W.C.Johnson and J.M.Blakely, (1977), pp261-350.

(114) J.E.Blendell and R.L.Coble, Jl. of American Cer. Soc., Vol.65(1982), pp174-178.

(115) M.Doser and J.G.Smeggil, IEEE Trans. on Magnetics, Mag.-9(1973), pp168-171.

(116) D.P.H.Hasselman, Materials Science and Engineering, Vol.71(1985), pp251-264.

(117) C.W.Searle, Appl. Phys. Lett., Vol.24(1974), pp30-32.

(118) C.W.Searle, Jl. of Appl. Phys., Vol.45(1974), 4581-4585.

(119) C.W.Searle and H.J.Garrett, Jl. of Appl. Phys., Vol.45(1974), pp5037-5042.

(120) C.W.Searle and I.Maartense, Jl. of Appl. Phys., Vol.50(1979), pp1039-1042.

(121) J.D.Livingston, Proc. AIP Conf. No.10(1973), p643.

(122) H.M.Jin, H.N.Chen, D.S.Tang, J.F.Han and Y.Shi, in Proc. Sixth Int. Workshop on Rare Earth Permanent Magnets and their applications, Ed. J.Fidler, Technical University, Vienna, Austria(1982), p549.

(123) A.V.Deryagin, Jl. of Physics, Vol.40(1979), pC5.

(124) C.Abraham, Phys. Rev., Vol.135A(1964), p1269.

(125) H.R.Hilzinger, Applied Physics, Vol.12(1977), pp253-260.

(126) W.F.Brown, Micromagnetics, Interscience Publishers, (1963).
(127) S.Hirosawa, K.Tokuhara, Y.Matsuura, H.Yamamoto, S.Fujimura and M.Sagawa, Jl. of Magn. and Mag. Matls., Vol.61(1986), pp363-369.
(128) G.Herzer, W.Fernengel and E.Adler, Jl. of Magn. and Mag. Matls., Vol.58(1986), pp48-54.
(129) C.Guillaud, Jl. of Rech. C.N.R.S., Vol.2(1949), pp267-278. (This paper
is in French and the reference has been obtained from refs.(97&98).
(130) A.N.Kolmogoroff, Dokl. Acad. Nauk. SSSR, Vol.31(1941), p99.
(131) R.Ramesh, Continuing research, UC Berkeley, 1987.
(132) R.M.German, The Int. Jl. of Powder Met., Vol.22(1986), pp31-38.
(133) J.D.Livingston, in Proc. Eighth Int. Workshop on Rare Earth Permanent Magnets and their applications, Ed. K.J.Strnat, University of Dayton Press, (1985), pp423-443.
(134) A.V.Andreev, A.V.Deryagin, S.M.Zadvorkin and S.V.Terent'ev, Soviet Phys. Solid State, Vol.27(1985), pp987-989.
(135) B.J.Beaudry and K.A.Gschneidner, in Handbook on the Physics and Chemistry of Rare Earths, Vol.1, Ch.2, North-Holland Publishing Co., (1978), pp173-232.
(136) L.Yang and Z.Nin, Paper No.GH-04, Intermag-87, Tokyo, Japan, April, 1987.
(137) I.N.Lin, R.K.Mishra and G.Thomas, IEEE Trans. on Magnetics, Mag.-20(1984), pp134-139.
(138) S.F.H.Parker, P.J.Grundy and J.Fidler, Jl. of Magn. and Mag. Matls., Vol.66(1987), pp74-78.
(139) W.Rodewald, Jl. of Less Common Metals, Vol.111(1985), pp77-81.
(140) W.Li, L.Jiang, D.Wang, T.Sun, J.Zhu, Jl. of Less Common Metals, Vol.126(1986), pp95-100.
(141) M.Ghandehari, Appl. Phys. Lett., Vol.48(1986), pp548-550.

FIGURE CAPTIONS

Figure I.1 : A typical virgin curve and hysteresis loop for a permanent magnet showing various features of practical interest.. At the bottom of the figure the magnetization and demagnetization by domain wall processes is also illustrated.

Figure I.2(a) : (i) Typical virgin curve and hysteresis loop of a nucleation controlled permanent magnet depicting the steep rise in the virgin curve (high initial permeability) and the square second quadrant loop ; (ii) typical virgin curve and hysteresis loop of a pinning controlled magnet depicting the low initial permeability and the step in the second quadrant loop.

Figure I.2(b) : (i) Typical microstructure of a nucleation controlled magnet depicting the absence of any significant bulk pinning sites ; (ii) typical microstructure of a pinning controlled magnet illustrating the uniform dispersion of pinning sites.

Figure I.2(c) : Schematic model for magnetization reversal by coherent rotation of the magnetic moments along with the corresponding hysteresis loop of a magnet reversing by coherent rotation.

Figure I.3 : Schematic representation of the two main types of layers found in transition metal alloys. (a) the primary layer, comprising of tessellations of triangles and hexagons (3.6.3.6); (b) the secondary layer comprising of tessellations of squares and triangles(3^2.4.3.4).

Figure I.4: (a) Schematic representation of the crystal structure of the phase $Nd_2Fe_{14}B$; (b) the boron coordination in this structure.

Figure I.5 : Spatial relationships among the several layers in the $Nd_2Fe_{14}B$ structure. (a) the mirror plane at z=0, depicting the triangular nets formed by the Nd(1), Nd(2), Fe(1) and B atoms ; (b) atoms in the planes z=1/8, 3/8 and 1/4, depicting the 3.6.3.6, $6^2.3^2$ and 3^2.4.3.4. tessellations of the iron atoms ; (c) the mirror plane at z=1/2.

Figure I.6 : Schematic illustration of the crystal structure of Nd_2Fe_{17}, to compare and contrast the structure with that of $Nd_2Fe_{14}B$.

Figure II.1 : Schematic illustration of the various steps involved in the production of sintered Fe-Nd-B magnets.

Figure III.1 : A typical xray diffraction spectra from a sintered and optimally treated Fe-Nd-Pr-Ce-B magnet, showing the prominent peaks for the matrix $RE_2Fe_{14}B$ phase. Note that the presence of other phases is not indicated.

Figure III.2 : A secondary electron scanning electron micrograph of a metallographically polished section of the sintered magnet with optimum properties, depicting the matrix grains as well as a second phase at the grain boundaries.

Figure III.3 : (a) Bright field transmission electron micrograph of the triple junction region showing the presence of a second phase in bright contrast ; this is schematically illustrated in (c) ; (b) bright field TEM image of the two grain boundary showing the presence of a thin layer of the second phase, schematically depicted in (d). The sample is one with the optimum treatment and the best properties.

Figure III.4 : A tableau of microdiffraction patterns from the stereographic triangle, obtained from the triple junction grain boundary phase in the magnet with optimum treatment. The presence of the [100], [110] and [111] microdiffraction patterns proves that the structure is fcc.

Figure III.5 : Nano-probe (100Å) diffraction patterns from different points in the same triple junction region, showing that the structure and orientation is the same.

Figure III.6 : Bright field image of a thin two-grain boundary region along with nano-probe diffraction patterns obtained from points 1,2 and 3. The

$[110]_{fcc}$ type diffraction patterns illustrate that the two grain boundary region is also fcc.

Figure III.7 : A typical EDX spectrum from the matrix phase obtained using the Be-window EDX detector fitted onto the Philips 400. A TEM probe of diameter of 400Å was used to acquire the spectrum. The spectrum was obtained from the magnet with the optimum treatment.

Figure III.8 : EDX spectra from the triple junction and two-grain boundary fcc phase, in the magnet with optimum treatment, obtained with a probe of 400Å and a Be window EDX detector. Note the similarity in the two spectra. Quantification yielded the same composition, within the limits of the errors of quantitative microanalysis.

Figure III.9 : A bright field TEM image of a rather wide two-grain boundary region in a magnet that was optimally treated and possessed the best properties,from which the EDX spectrum shown in Fig.III.8 was obtained.

Figure III.10 : (a) A typical EDX spectrum obtained from the grain boundary phase, in the magnet with the best properties, using an ultra-thin window EDX detector ; (b) the low energy end of the above spectrum, showing the presence of oxygen in the phase.

Figure III.11 : (a) Fractograph of an in-situ fractured Auger sample, showing a mixed trans-granular and inter-granular fracture ; (b) Oxygen Auger map from the region depicted in (a), showing regions of enhanced oxygen concentration and regions of almost no oxygen concentration ; (c) Nd Auger map from the same region as in (a) showing the good correspondence between regions of enhanced oxygen content and enhanced Nd content. The sample in this case is also the optimally treated magnet.

Figure III.12 : (a) Auger spectrum from a inter-granular fractured region, depicting the large oxygen peak-to-peak height ; (b) depth profiling of the region from which the spectrum in (a) was obtained, showing that the

oxygen is not superficial but exists for sputtering times upto five minutes. This indicates that the oxygen is inherent to the system. The sample used was one with the optimum treatment and properties, i.e., slowly cooled from sintering temperature.

Figure III.13 : (a) Auger spectrum from a trans-granular region of the fracture surface shown in Fig.III.11, showing the Fe signal in addition to the oxygen signal ; (b) depth profiling of the above trans-granular region showing that the oxygen detected is only superficial (from the system).

Figure III.14 : Schematic illustration of microanalytical line profiling across the matrix-fcc phase interface. The diameter of the spots corresponds approximately to the diameter of the probe.

Figure III.15 : A typical microanalytical line profile obtained from the Fe-Nd-Pr-Ce-B magnet, across the matrix-fcc phase interface in a slowly cooled magnet. The experimental conditions consisted of a probe size of 700Å ; 200kV accelerating voltage (JEOL 200CX); ultra-thin window(UTW) EDX detector.

Figure III.16 : A typical microanalytical line profile from a ternary Fe-Nd-B magnet obtained using the UTW detector, showing the similarity between the ternary magnet and the Ce-Pr-Nd magnet that was used extensively in this study. This magnet was also slowly cooled from sintering temperature.

Figure III.17 : Bright field image of the $Fe_4Nd_{1+x}B_4$ phase along with the diffraction pattern. This phase is observed only to a very small extent in all magnets with the overall composition of $Fe_{77}Nd_{15}B_8$.

Figure III.18 : Bright field image of a rare earth sesqui-oxide that is observed in sintered magnet due to defective processing. The insets show the EDX spectra from this phase as well as from the matrix phase and also the diffraction pattern from this hexagonal oxide.

Figure III.19 : (a) A schematic hysteresis loop for a typical nucleation controlled magnet ; (b) a schematic hysteresis loop for a typical pinning controlled magnet showing the kink in the second quadrant of the loop.

Figure III.20 : (a) Applied field dependence of the nature of hysteresis loops in a single particle of a nucleation controlled magnet. The progressive increase in iHc with applied field is to be noted ; (b) applied field dependence of the nature of the hysteresis loops in a single particle of a pinning controlled magnet. The progressive increase in remanence with applied field is to be noted ; (c) and (d) depict the applied field dependence of the nature of the hysteresis loops in polycrystalline nucleation and pinning controlled magnets respectively. These results of the pioneering work of Becker can be used to identify the dominant reversal mechanism.

Figure III.21 : A typical virgin magnetization curve for the optimally treated magnet used in this study. The virgin curve shows a steep rise in low fields, indicating high initial permeability and thus easy wall movement in the bulk of the magnet. This indicates that there are no significant pinning sites in the bulk of the magnet.

Figure III.22 : Applied field dependence of the shape of hysteresis loops in the slowly cooled, sintered Fe-RE-B magnets used in this study. (a) sheared loops at low fields indicating easy wall mobility at low fields and absence of saturation at such low fields ; (b) opening up of the loop at intermediate fields, with a significant increase in iHc and remanence ; (c) high field loop (21kG) showing the square second quadrant and high iHc and remanence. The magnet is still not fully saturated, although it is close to saturation.

Figure III.23 : Applied field dependence of iHc and and remanence for a magnet that was slowly cooled from sintering temperature. The iHc and remanence are low until the applied field is at least higher than the demagnetizing fields of a small fraction of the grains. When the applied field is higher than the demagnetizing field of the magnet, significant

increases in the iHc and remanence can be observed.

Figure III.24 : High resolution lattice fringe image of the matrix grains in a slowly cooled magnet, showing that there are no specific pinning sites inside the matrix. The misalignment of the c-axis in the two adjacent grains can be observed in this image. This image was obtained using the Philips 400 at 100kV.

Figure III.25 : Effect of isochronal annealing at different temperatures, on the iHc of a water quenched magnet. The sharp increase in iHc upon annealing in the temperature range of 500-600°C can be observed.

Figure III.26 : (a) Bright field TEM image of the triple junction phase in the water quenched magnet. The large spherical grain at the top right corner is a rare earth oxide ; (b) bright field image of the two-grain boundary phase in the water quenched magnet along with the microdiffraction pattern showing that the structure is still fcc.

Figure III.27 : (a) Fractograph of the in-situ fracture surface of a water quenched magnet showing mixed trans-granular and inter-granular fracture ; (b) oxygen Auger map from the region depicted in (a) ; (c) Nd Auger map from the region in (a). The inferences are similar to those arrived at in the case of FigIII.11.

Figure III.28 : Microanalytical line profile data across the fcc phase-matrix interface. (a) in a furnace cooled magnet ; (b) in a water quenched magnet ; (c) in a water quenched and annealed magnet. The plots indicate that there is no significant difference between the different treatments, although the magnetic properties are different.

Figure III.29 : (a) Bright field TEM image of the triple junction fcc phase in a furnace cooled magnet showing recrystallized grains ; (b) recrystallized grains in the two-grain boundary fcc phase in a furnace cooled magnet.

Figure III.30 : High resolution lattice fringe image of the interface between the fcc triple junction phase and the matrix in the slowly cooled magnet, showing the absence of bcc platelets near the interface. This image was obtained using the JEOL 200Cx at 200kV.

Figure III.31 : High resolution lattice fringe image of the interface between the triple junction phase and the matrix in a water quenched magnet, showing the absence of a third phase or platelets near the interface. This image was obtained using the JEOL 200Cx at 200kV.

Figure III.32 : Effect of post-sintering cooling rate in the iHc and $(BH)_{max}$ of the Fe-RE-B magnet used in this study. The coolong rate was assumed to be similar to that of alloy steels and are approximate values.

Figure III.33 : Effect of post-sintering cooling rate on the iHc, verified using magnets prepared by a different producer. This was a ternary Fe-Nd-B magnet. The cooling rate was varied by using different cooling media as well as a computer controlled furnace wherein the cooling rate could be controlled accurately over certain ranges of cooling rates.

Figure III.34 : Remanence of the sintered Fe-RE-B magnet used in this study as a function of cooling rate. The invariance of the remanence for different cooling rates is because the remanence is dependent only upon the composition and the degree of alignment of the individual grains.

Figure III.35 : Virgin magnetization curve and hysteresis loops for magnets with different cooling rates. (a) furnace cooled ; (b) air cooled ; (c) water quenched ; (d) oil quenched . (e) the effect of applied field on the iHc of the water quenched, water quenched and annealed (500°C, 1 hour), and the furnace cooled magnets. The absence of any significant variation in the value of the applied field at which the iHc starts to rise indicates that the demagnetizing fields (average) is the same in all the cases.

Figure III.36 : Seconday electron SEM images of the polished surfaces of

(a) the water quenched magnet and (b) the furnace cooled magnet. While the water quenched magnet shows the presence of several quench cracks, no such cracks are visible in the case of the furnace cooled magnet.

Figure III.37 : (a)Secondary electron SEM images of the fracture surface of the water quenched magnet showing totally inter-granular fracture, which is clearly illustrated in the high magnification image in (b).

Figure III.38 : A schematic model of the microstructure of the magnet near the two-grain boundary as proposed by Hiraga et.al. This shows , in addition to the fcc phase, a bcc phase, along with the intrusion of bcc platelets into the matrix phase.

Figure III.39 : A compound figure comprising of the bright field image, the diffraction pattern and the dark field image from the grain boundary region in a typical ion milled magnet showing the presence of surface ion milling artefacts.

Figure III.40 : Bright field image and diffraction pattern from the grain boundary region in a sample that was jet electro-polished. This shows that the bcc phase observed is an artefact of ion milling and is not observed in a jet polished sample.

Figure III.41 : A schematic model to elucidate the mechanism by which bcc phase can form by ion milling. (a) this shows the grain boundary region in a thin slab that is used for ion milling, before ion milling ; (b) the same slab after some time of ion milling, with the fcc phase being thinner than the matrix due to preferential thinning ; (c) the final thin foil in which the grain boundary region is thinner than the matrix (thus forming a valley), with the deposit of bcc Fe due to the back-sputtering of the Fe milled away.

Figure III.42 : Schematic block diagram of the approach to section III.4.

Figure III.43 : Schematic illustration of the possible interaction of the

oxygen in the grain boundary phase with the Nd in $Nd_2Fe_{14}B$. The figure shows a unit cell of $Nd_2Fe_{14}B$ at the interface with the fcc phase, along with the oxygen atoms close to the Nd atoms.

Figure III.44 : Schematic diagram of the variation of the domain wall energy with position in the sintered magnet. The wall energy, in the extreme case is zero at the interface, while in the case of a grain boundary it could attain a value much lower than that in the matrix given by γ_{matrix}.

Figure III.45 : Schematic hysteresis loop along with magnetization and demagnetization by wall processes in a typical permanent magnet. This figure is the same as Figure I.1 and is reproduced for the sake of the reader's convenience.

Figure III.46 : Plot of effective anisotropy field against nucleation field for a typical $Fe_{77}Nd_{15}B_8$ (a composition similar to that used in this study) magnet. The data points have been obtained for different temperatures. The plot is from a paper by Hirosawa et.al.

Figure III.47 : A plot of effective anisotropy field against nucleation field for Dy substituted magnets. The data points have been obtained at room temperature. The slope of the linear fit is the same as in the case of the plot in Fig.III.46.

Figure III.48 : A typical grain size distribution plotfor powder processed sintered magnets. The plot exhibits a positive skew due to the fact that during the powdering process, there are more fines produced than coarse particles. The overall distribution is similar in the case of all the magnets studied.

Figure III.49 : The iHc distribution for the sample with grain size distribution shown in Fig.III.48. The distribution was determined by obtaining the slope of the demagnetizing curve at each point and converting it into a percentage.

Figure III.50 : Cumulative fraction of particles with iHc less than or equal to a particular value plotted against that value of iHc. Thus, this plot is the integral of the plot in Fig.III.49.

Figure III.51 : A plot of ln[ln{1-cumulative fraction)}] versus the corresponding value of iHc. The fit is linear although in the intermediate regions it shows deviations from linearity.

Figure III.52 : Effect of grain size on the iHc of Fe-Nd-B magnets. In the figure, the iHc is plotted against ln[(grain size)^2]. The average grain size was determined by plotting a grain size distribution similar to that shown in Fig.III.48. The linear fit obtained is consistent with the prediction of the model.

Figure III.53 : A schematic illustration of the model to explain the presence of thermal expansion stresses at the matrix-fcc phase interface. The figure also shows the anisotropy in thermal expansions along the c-axis and a-axis of the $Nd_2Fe_{14}B$ structure.

Figure III.54 : A diagrammatic representation of the step quenching treatment given to study the effect of thermal expansion stresses. The quenching treatment was carried out from different temperatures along a furnace cooling route.

Figure III.55 : Effect of water quench temperature on the iHc of the magnets under study. The sharp rise in iHc for quenching temperatures below 600°C can be clearly observed.

Figure III.56 : Virgin curves and hysteresis loops for magnets quenched from different temperatures T_Q : (a) 1080°C ; (b) 700°C ; (c) 500°C ; (d) 300°C. The similarity in the shape of the hysteresis loops to that of the samples with different cooling rates can be observed here. The only difference between the four samples is the field at which nucleation occurs.

Figure III.57 : Microanalytical line profiles across the fcc phase-matrix interface for the magnets with different water quench temperatures. (a) 1080°C ; (b) 900°C ; (c) 700°C ; (d) 500°C ; (e) 300°C. The similarity in the plots demonstrates that there are no significant differences in the microanalytical details in the magnets with the five different quench temperatures, although the magnetic properties are quite different. The microanalysis was carried out using a Be-window EDX detector on a Philips 400 at 100kV.

Figure III.58 : Interaction of magnetic domain walls with a grain boundary when the wall is normal to it in a sample with the c-axis in the plane of the foil. (a) the in-focus image depicting the grain boundary ; (b) the Fresnel defocus image showing domain walls in bright contrast ; (c) position of the wall after the foil was tilted . The walls could move very easily upon tilting.

Figure III.59 : (a) in-focus bright field image of a grain boundary in a sample with the c-axis in the plane of the foil ; (b) Fresnel image showing the domain wall in bright contrast, at an angle to the grain boundary ; (c) the corresponding diffraction pattern , showing the misorientation between the two grains. In this case also, the wall moved very easily upon tilting the foil, indicating no wall pinning.

Figure III.60 : Interaction of domain walls with grain boundary or two phase interface when the wall is parallel to the interface : (a) in-focus bright field TEM image showing the triple junction region at top left corner and extending into the two-grain boundary region, across the image in (a) ; (b) Fresnel image showing a domain wall (indicated by arrow) ; (c) position of domain wall after the foil was tilted by a small amount ; (d) position of the wall that has become pinned to the interface.

Figure III.61 : Schematic illustration of the progressive movement of the wall for different values of foil tilt and also illustrating the pinned configuration of the wall.

Figure III.62 : Interaction of domain wall with grain boundary fcc phase : (a) in-focus bright field image depicting a tapered fcc phase whose maximum width was about 500Å and minimum about 50Å ; (b) Fresnel image depicting a domain wall at the end of the foil ; (c) and (d) depict positions of the wall upon progressively tilting the foil. The wall is existent only on one of the grains.

Figure III.63 : Continuation of Figure III.62. (a) the in-focus image ; (b) position of the wall after the foil was tilted from the position in Fig.III.62(d) ; (b), (c) and (d) depict the positions of the wall for subsequent tilting. For a tilt value between (b) and (c) another wall is nucleated in the upper grain, corresponding to the wall in the lower grain. This occurs for a thickness of the fcc phase of about 50-100Å.

Figure III.64 : Schematic illustration of the events described in Figs.III.62 and 63.

Figure III.65 : Pinning of domain walls by inclusions. (a) in focus image of inclusions of about 500Å diameter ; (b) Fresnel image of the wall at a distance from the inclusion ; (c) domain wall pinned strongly at the inclusion (note the sharp bending of the wall close to the particle) ; (d) position of the wall after further tilting.

Figure III.66 : Effect of Dy addition on the remanence of FNd-B magnet. The total rare earth composition was kept constant at 35.1 wt.% and the grain size of the magnet was also kept approximately constant at about 10 μm. The magnets were all given the same sequence of heat-treatments.

Figure III.67 : Effect of Dy additions on the iHc of Fe-Nd-B magnets. The magnets were propared under the same conditions as described in Fig.III.66.

Figure III.68 : A plot of iHc against effective anisotropy field for the Dy

substituted magnets. The effective anisotropy field was calculated using the overall composition of the alloy.

Figure III.69 : General microstructure of the Dy substituted magnets. The overall microstructural features of the Dy substituted magnets are similar to each other and also to the Fe-RE-B magnets used in the study of post-sintering heat-treatments.

Figure III.70 : Bright field TEM image of inclusions found in the 5 at.% Dy magnet, which also exhibited the strongest deviation from linearity (Fig.III.68).

Figure III.71 : Schematic illustration of line profiling across the fcc phase-matrix interface.

Figure III.72 : (a)Microanalytical line profile across the fcc phase-matrix interface in sample A (Fig.III.67), showing almost complete partitioning of Dy to the matrix phase, shown clearly in (b). No segregation of Dy to the interfaces was observed.

Figure III.73 : Microanalytical line profile across the fcc phase-matrix interface for sample B (Fig.III.67). As in the case of sample A, Dy partitions almost completely into the matrix.

Figure III.74 : Intrinsic coercivity versus effective anisotropy field, with the effective anisotropy field calculated from the EDX data for samples A and B only. The strong deviation from linearity is not observed in this case and a linear fit is obtained, with a slope of 0.38.

Figure III.75 : A hypothetical composition profile across the fcc phase-matrix interface, wherein the substitutional element segregated strongly to the interfaces. It is conceivable that high intrinsic coercivity can be obtained if such a concentration profile can be obtained for an element such as Dy.

Figure III.76 : Effect of Dy-Al sintering additive on the (a) the remenence ; (b) the iHc ; (c) the $(BH)_{max}$ of Fe-Nd-B magnets.

Figure III.77 : (a) Secondary electron SEM image of the metallographically polished section of an Fe-Nd-B magnet with 8 wt.% of Dy-Al added as sintering additive ; (b) back-scattered image corresponding to the image in (a), indicating possible segregation of an element with atomic number different from that of the matrix.

Figure III.78 : Microanalytical line profile across the fcc phase-matrix interface in the 8 wt.% Dy-Al sample obtained by using a computer program to carry out automatic STEM line profiling. (a) concentration profiles for Fe,Nd,Dy and Al ; (b) concentration profile for Al showing significant Al segregation to the interface.

Figure III.79 : Fe, Nd, Dy, and Al x-ray maps illustrating the uniform segregation of Al to the interfaces. The intensity in the map corresponds to the concentration of a particular element. The map was acquired on the JEOL 200CX using a STEM probe of 300Å.

Figure III.80 : (a) Bright field TEM image of a triple junction fcc phase penetrating into grain boundaries as a tapering region ; (b) point microanalysis data from the points marked 1-5 in the bright field image.

TABLE I

ATOMIC SITES, OCCUPANCIES AND COORDINATES

ATOM	SITES	OCCUPANCIES	X	Y	Z
Nd	4f	4	0.2679	0.2679	0.0000
Nd	4g	4	0.1403	-0.1403	0.0000
Fe	$16k_1$	16	0.2234	0.5673	0.1274
Fe	$16k_2$	16	0.0375	0.3598	0.1758
Fe	$8j_1$	8	0.0979	0.0979	0.2045
Fe	$8j_2$	8	0.3167	0.3167	0.2464
Fe	4e	4	0.5000	0.5000	0.1139
Fe	4c	4	0.0000	0.5000	0.0000
B	4g	4	0.3711	-0.3711	0.0000

* The coordinates are given as fractions of the lattice parameters of :

a = 8.88Å and c = 12.18Å at room temperature.

TABLE II

COORDINATIONS OF ATOMS IN THE $Nd_2Fe_{14}B$ UNIT CELL

ATOM	SITE	COORDINATION NUMBER	COORDINATION POLYGON
Nd	4f	18+2B	hexagonal prism + 8
Nd	4g	20	hexagonal prism + 8
Fe	$16k_1$	12	icosahedron
Fe	$16k_2$	12	icosahedron
Fe	$8j_1$	12	icosahedron
Fe	$8j_2$	14	sigma phase type
Fe	4e	12 + 1Fe(6)	icosahedron + 1
Fe	4c	12	icosahedron
B	4g	7+2	trigonal prism + 1 + 2

TABLE III

MAGNETIC PROPERTIES OF SOME PERMANENT MAGNETS

ALLOY SYSTEM	INTRINSIC COERCIVITY	REMANENCE	ENERGY PRODUCT
Fe-Nd-B	9-13	12-13	35-40
Sm_2Co_{17}	10-15	10-11	22-28
AlNiCo	0.5-1.0	5-7	1-5

TABLE IV

MOMENTS OF DIFFERENT SITES IN $Nd_2Fe_{14}B$ AT 4.2°K

ATOM	SITE	MOMENT, μ_B
Nd	4f	2.30
Nd	4g	2.25
Fe	4e	2.10
Fe	4c	2.75
Fe	$8j_1$	2.30
Fe	$8j_2$	2.85
Fe	$16k_1$	2.60
Fe	$16k_2$	2.60

TABLE V

SATURATION MAGNETIZATION AND ANISOTROPY FIELD FOR VARIOUS $RE_2Fe_{14}B$ COMPOUNDS AT ROOM TEMPERATURE

RARE EARTH ATOM	SATURATION MAGNETIZATION, μ_B	ANISOTROPY FIELD, H_A, kOe
Y	27.5	27.3
La	27.4	27.0
Ce	24.0	37.1
Pr	31.0	79.3
Nd	36.2	71.0
Sm	28.6	-
Gd	17.3	28.6
Tb	12.2	>139.0
Dy	14.1	>158.0
Ho	13.9	71.0
Er	19.6	-
Tm	-	-
Lu	15.7	26.0

TABLE VI

MICROANALYSIS DATA FOR 8 wt.% DY-Al MAGNET

LOCATION	At.% Fe	At.%Nd	At.%Dy	At.%Al
$RE_2Fe_{14}B$	84.92	9.68	4.61	0.79
fcc phase	10.41	88.97	0.61	0.00
interface	64.39	29.24	2.42	3.65
grain boundary	83.86	10.54	4.23	1.37

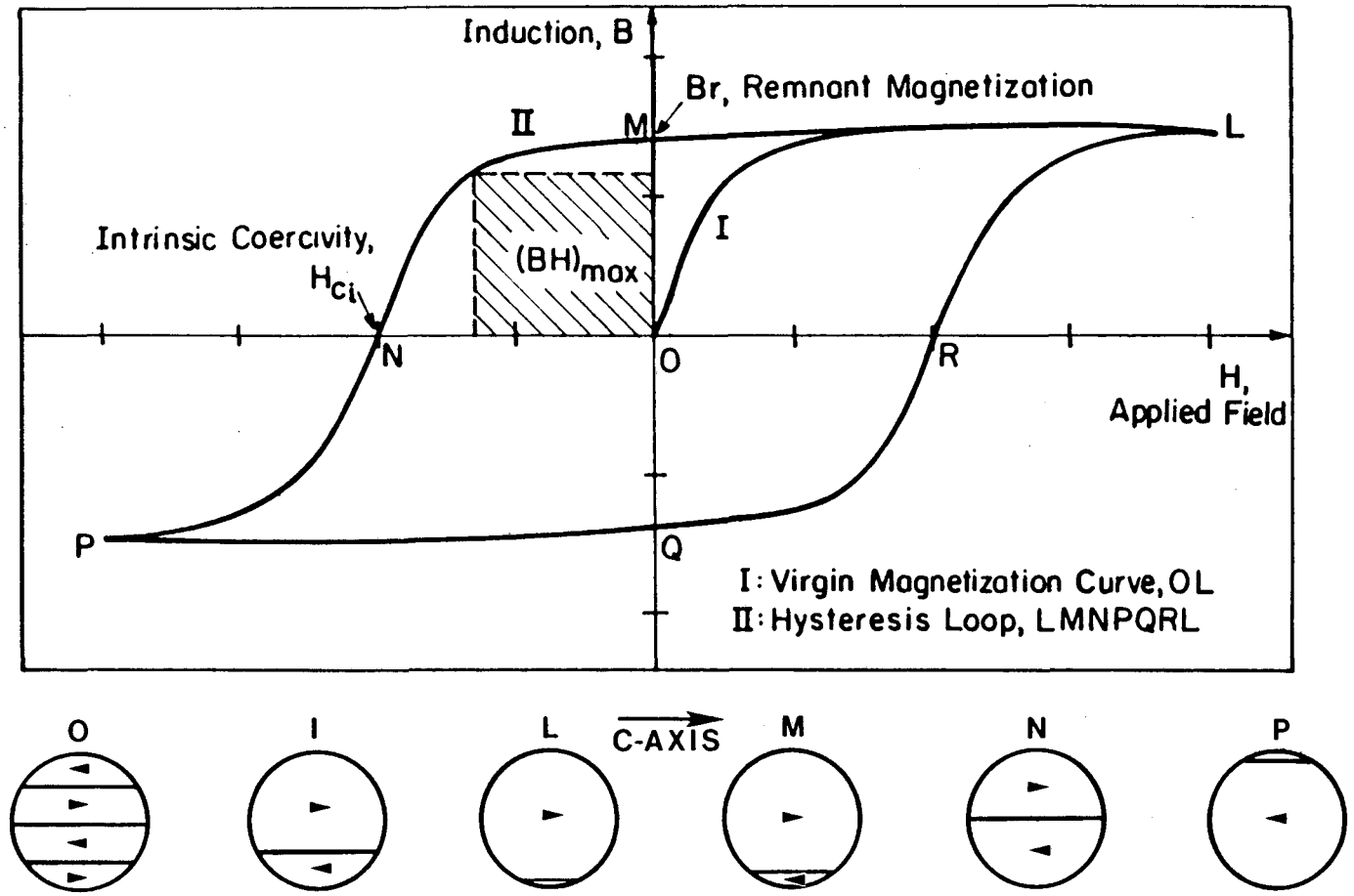

XBL 862-640

Fig.I.1

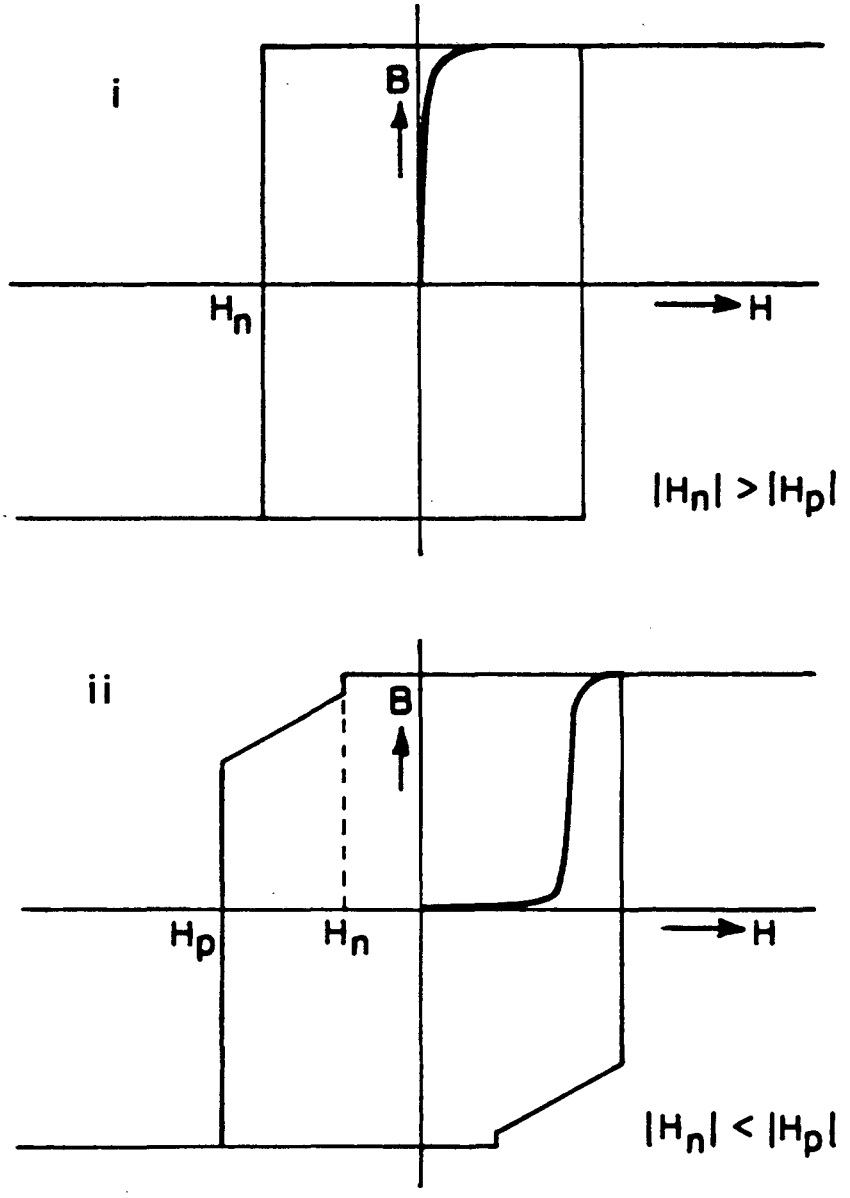

XBL 8512-6876

Fig.I.2(a)

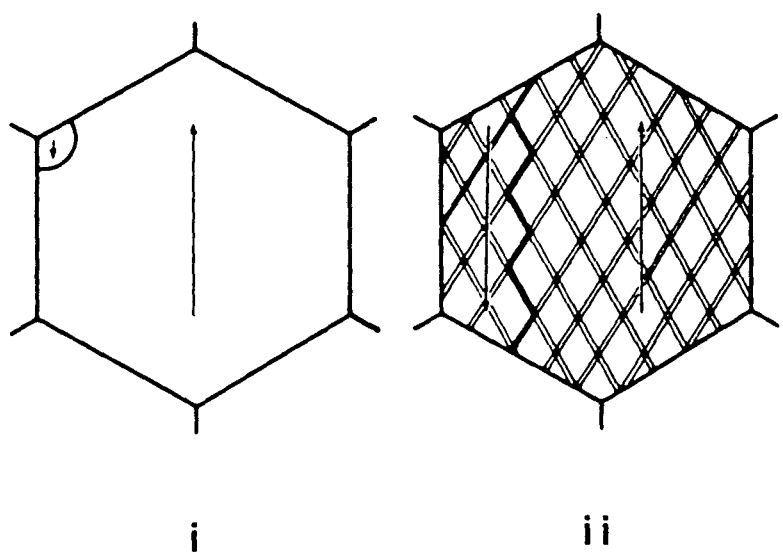

Fig.I.2(b)

XBL 874 1531

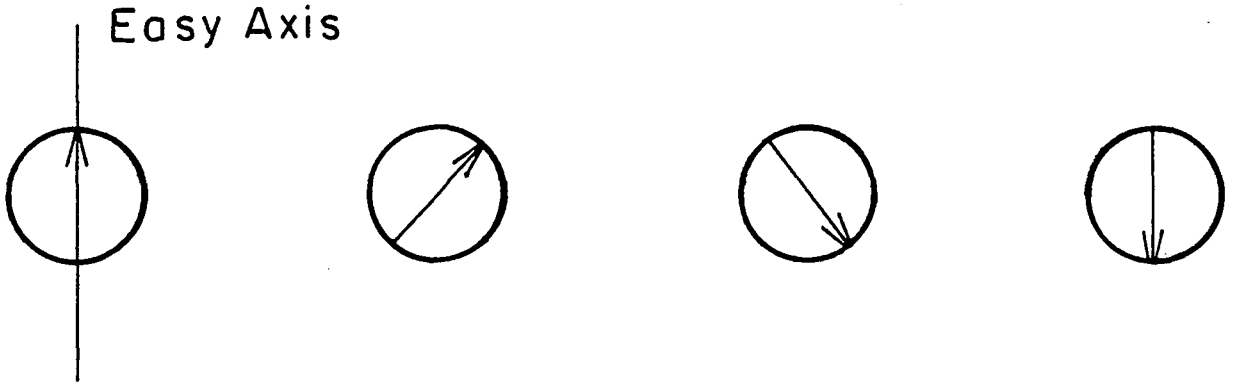

$$H_{c_i} = H_A = 2K/M_s$$

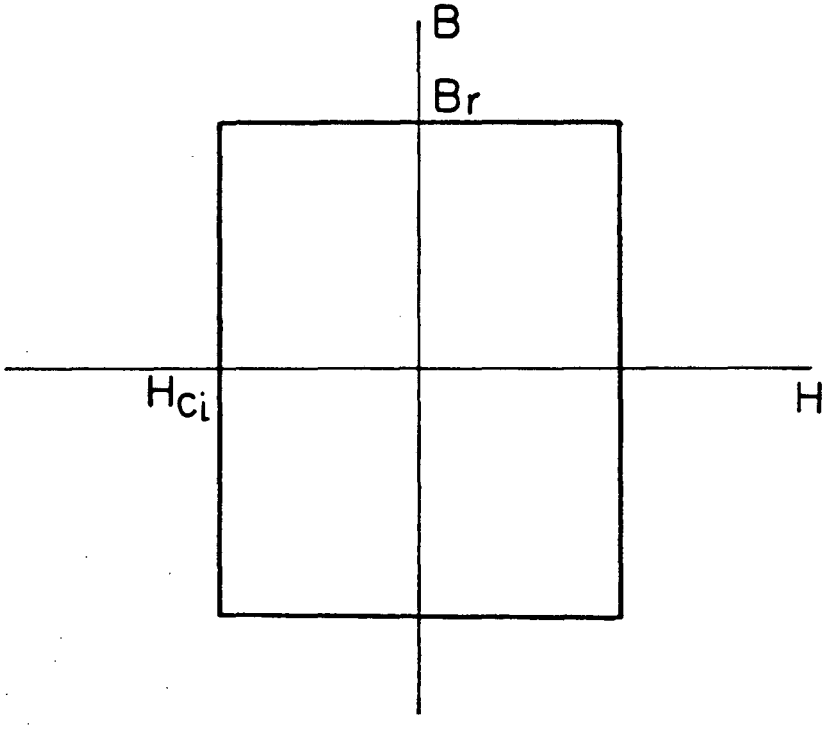

XBL8512-6869

Fig.I.2(c)

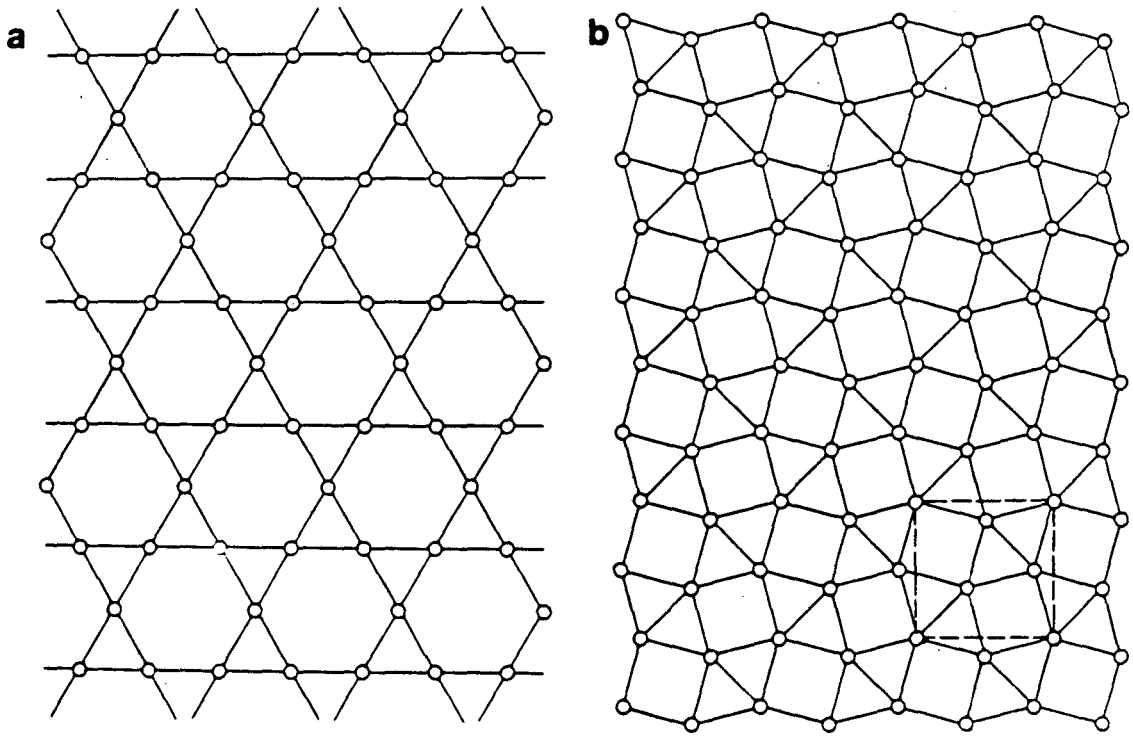

XBL 877-3356

Fig.I.3

a

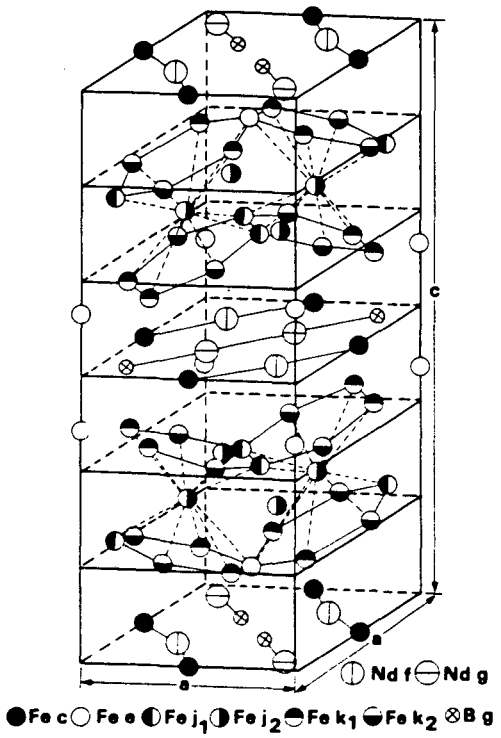

COMPOSITION : $Nd_2Fe_{14}B$

STRUCTURE : TETRAGONAL

SPACE GROUP : $P4_2/mnm$

ATOMS /UNIT CELL : 68

LATTICE PARAMETERS:

c= 12.20 A

a= 8.80 A

b

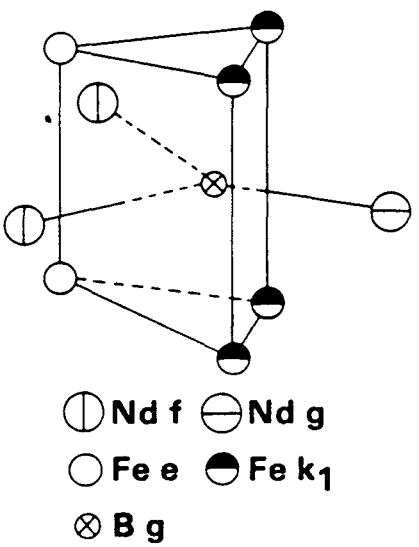

XBL 862-632

Fig.I.4

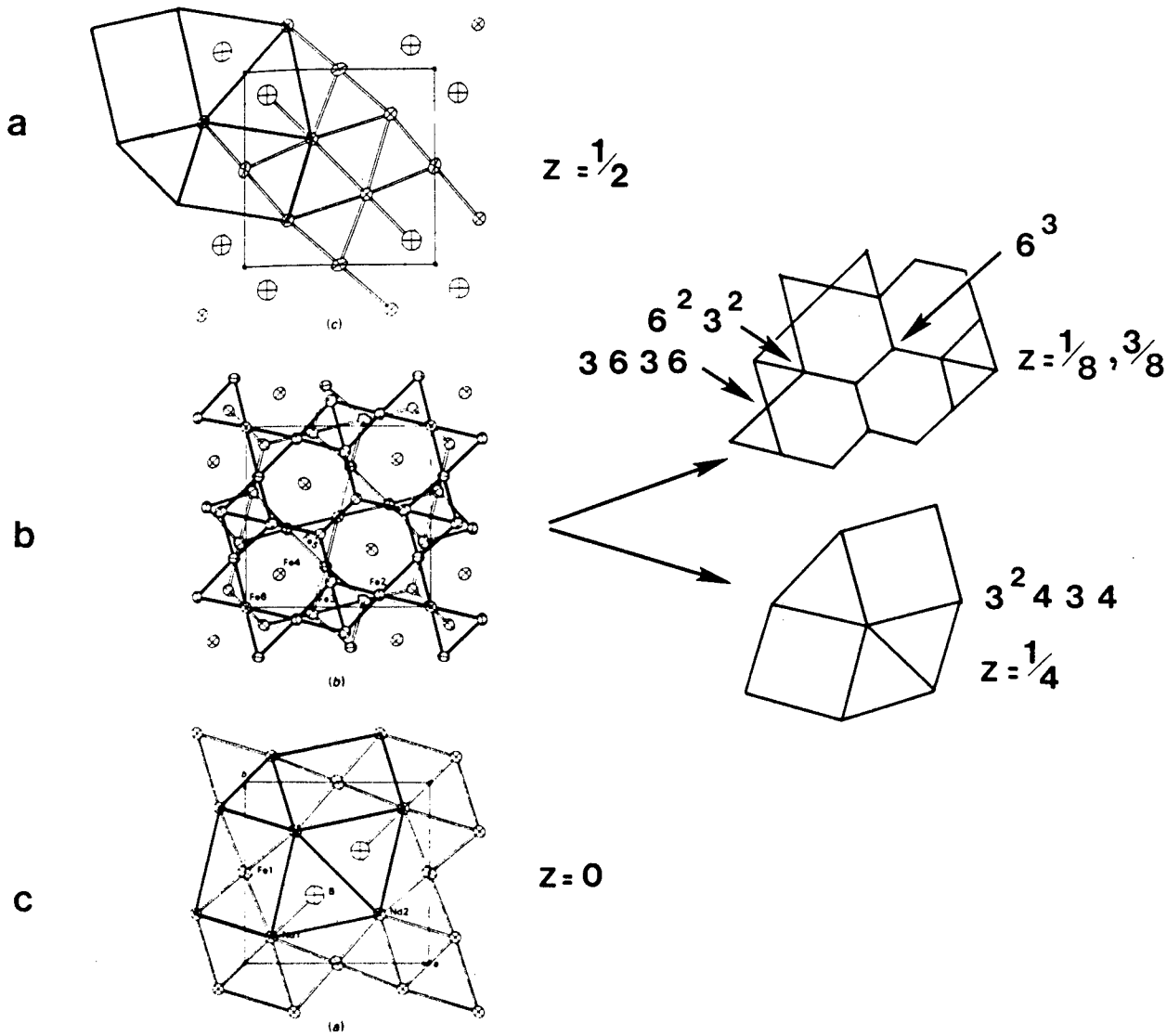

XBL 862-639

Fig.I.5

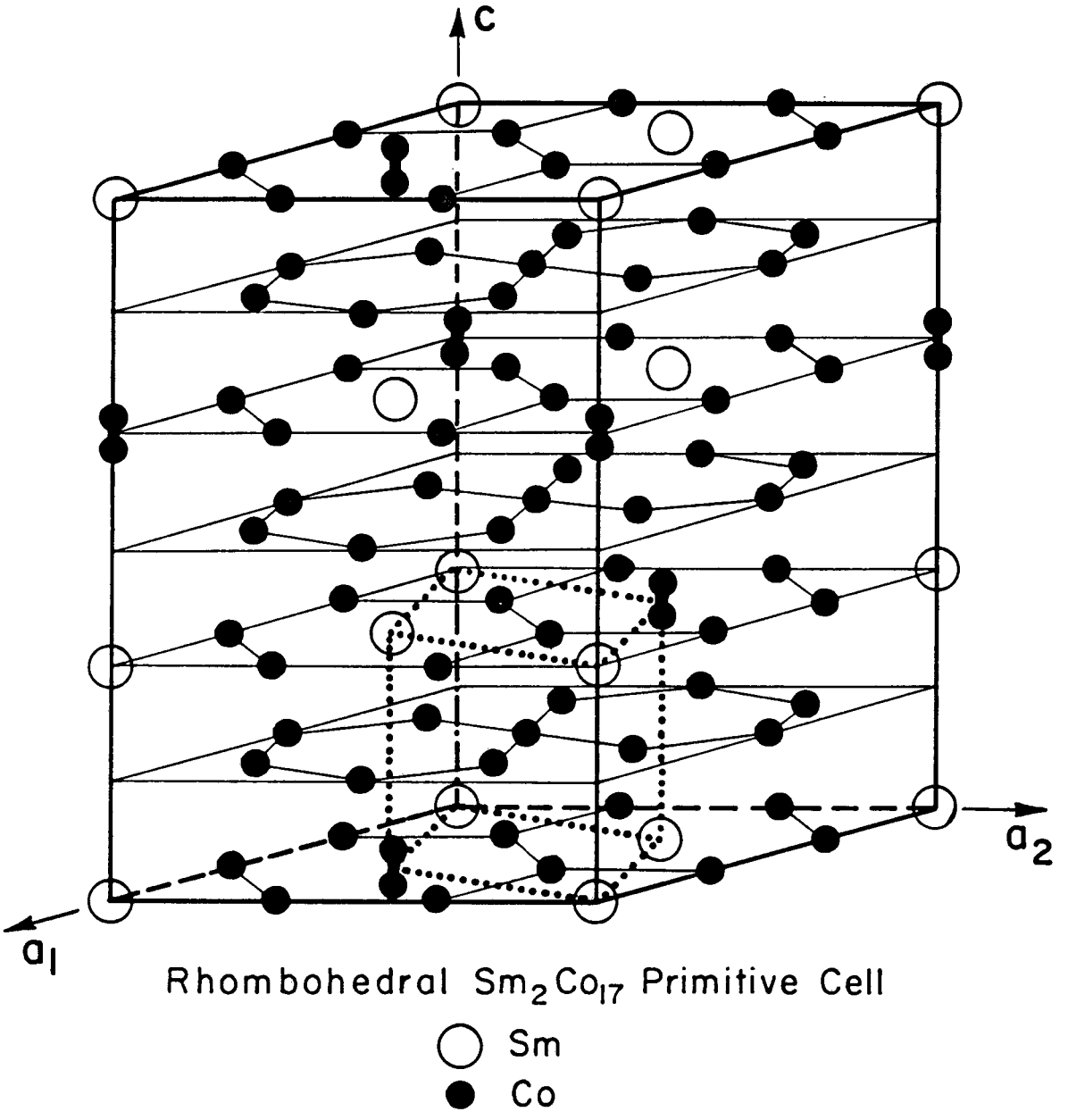

XBL 831-5007

Fig.I.6

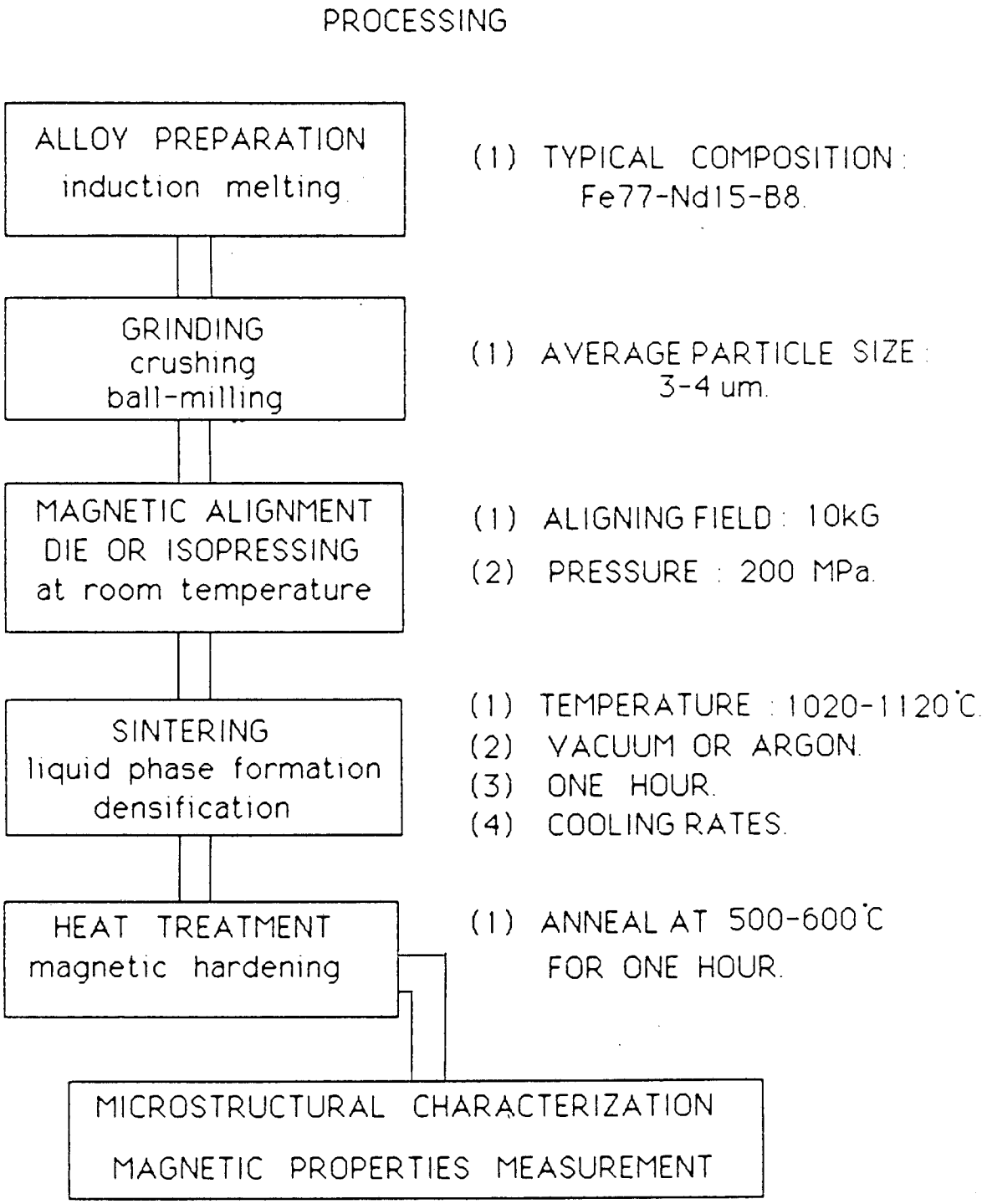

XBL 862-635

Fig.II.1

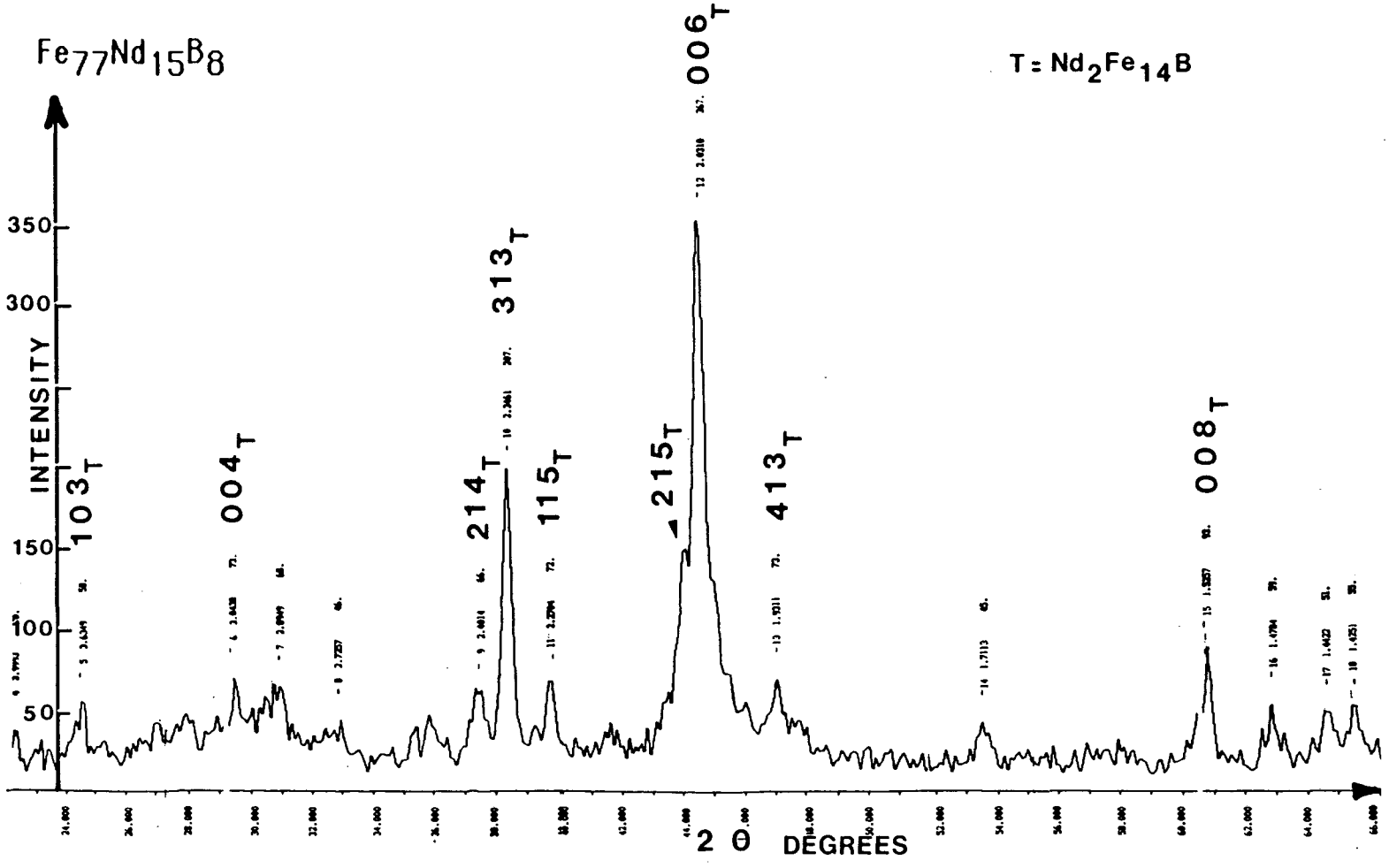

XBL 862-637

Fig.III.1

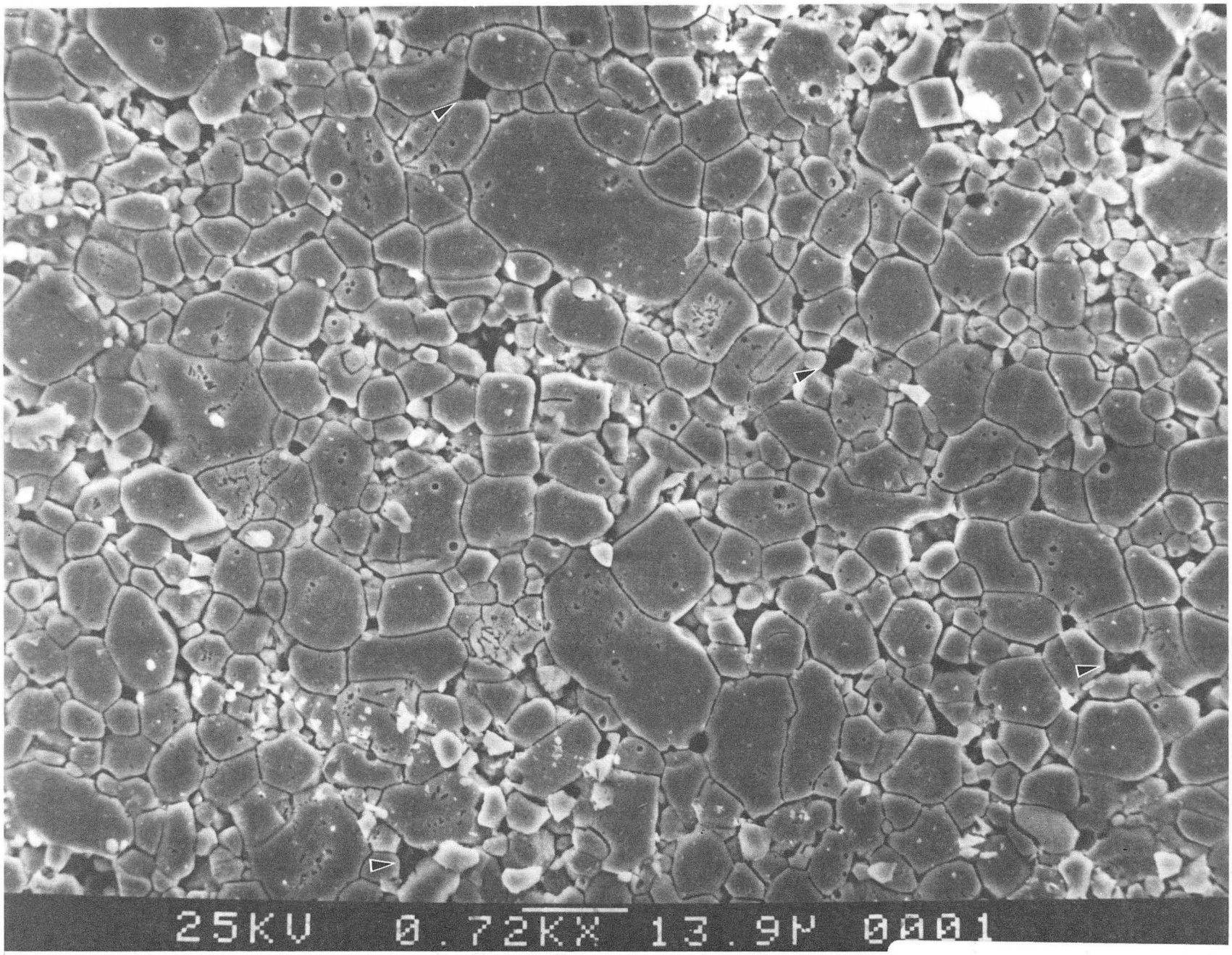

CH. 111, Fig. 2 XBB877-6161

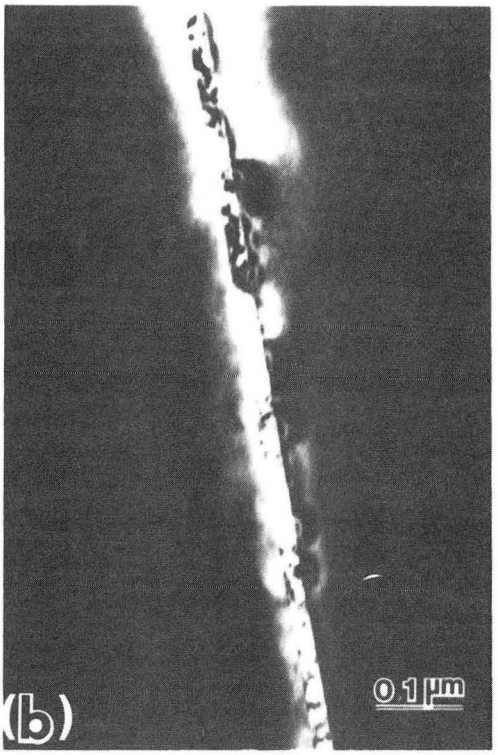

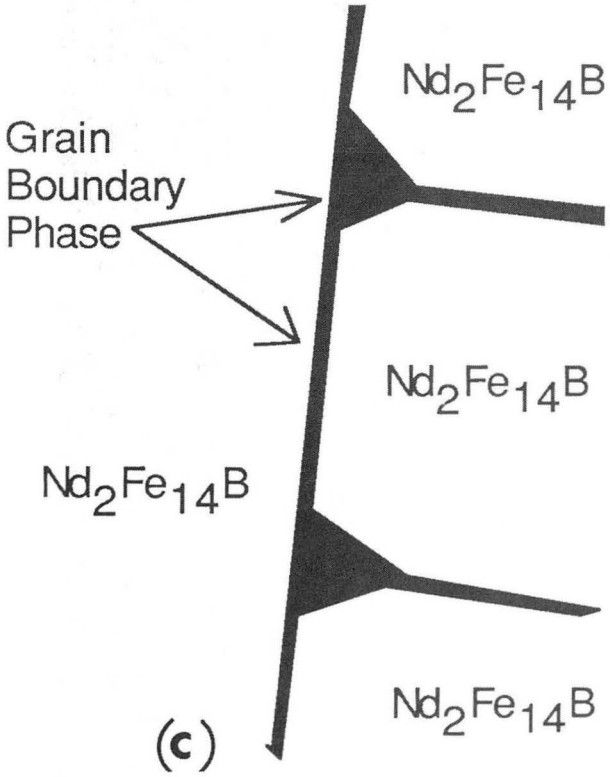

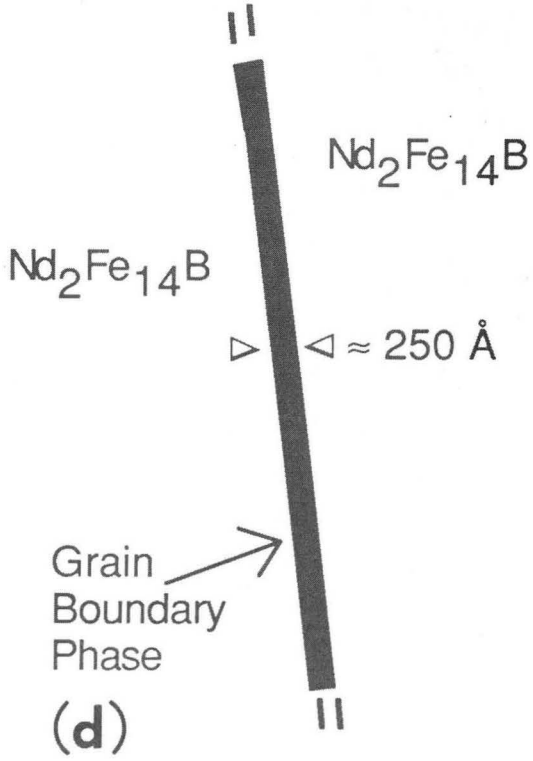

CH.111, Fig. 3 XBB 862-1270

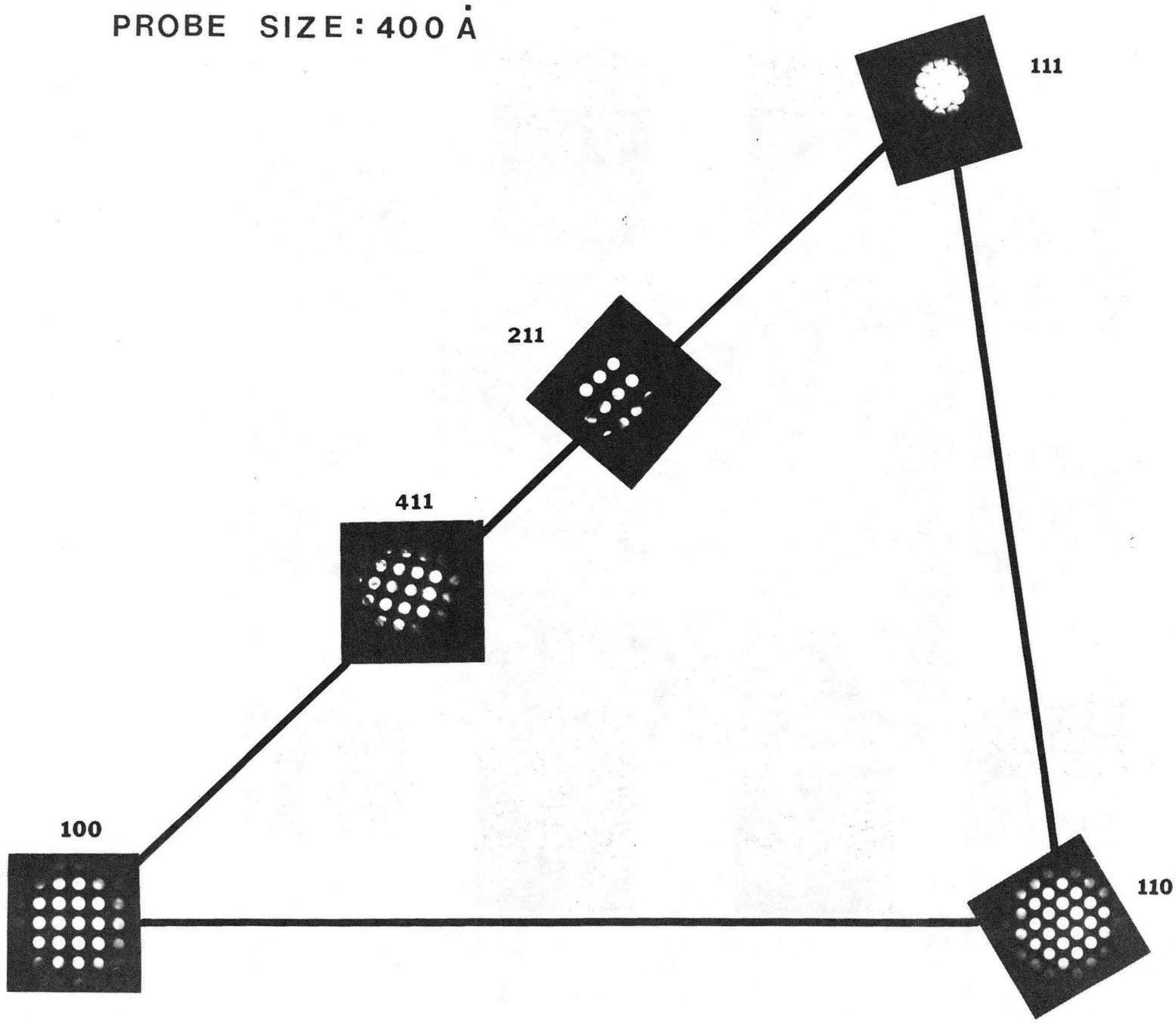

CH. 111, Fig. 4 XBB856-4526

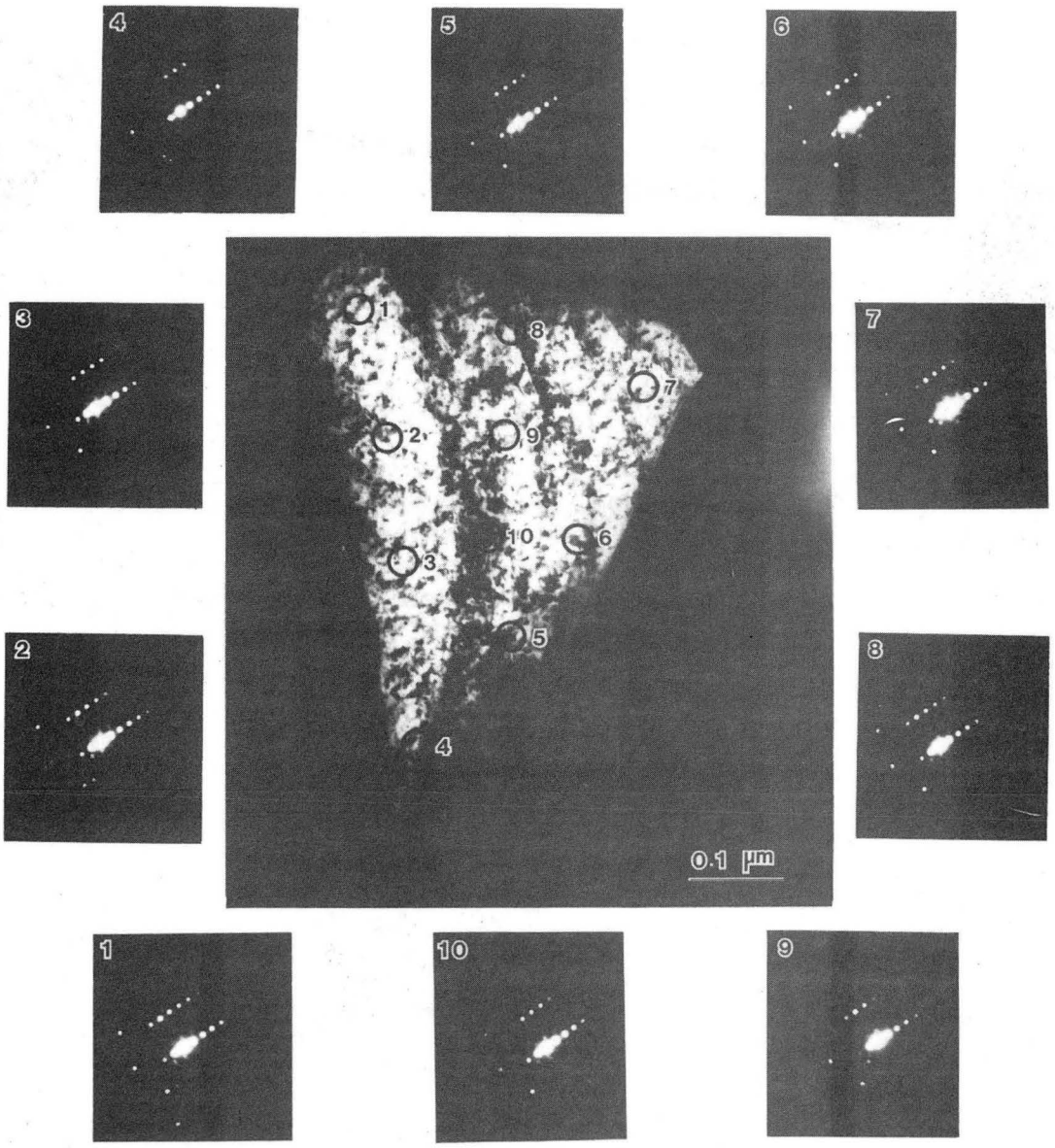

CH. 111, Fig. 5 XBB865-3637

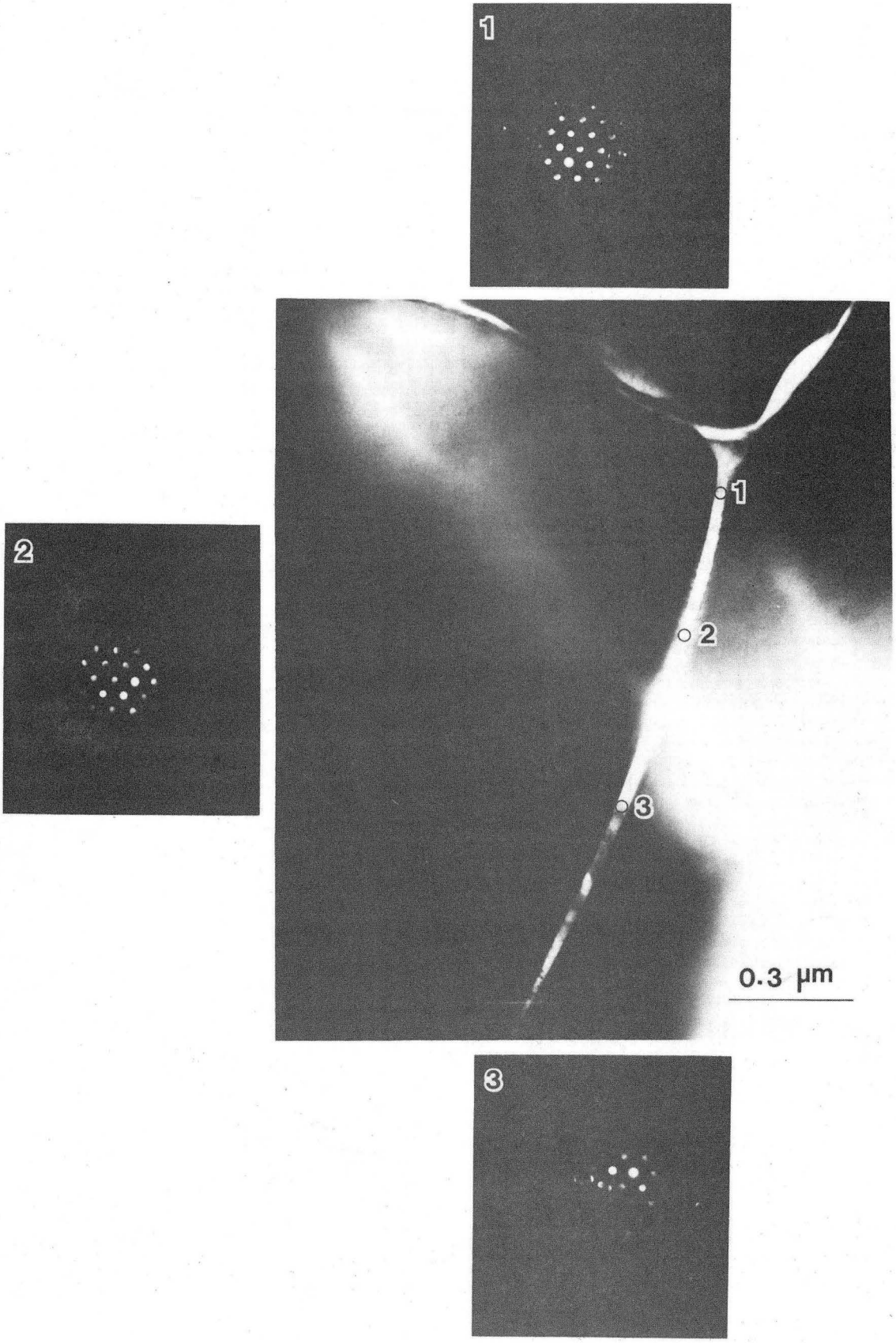

CH. 111. Fig. 6 XBB865-3634

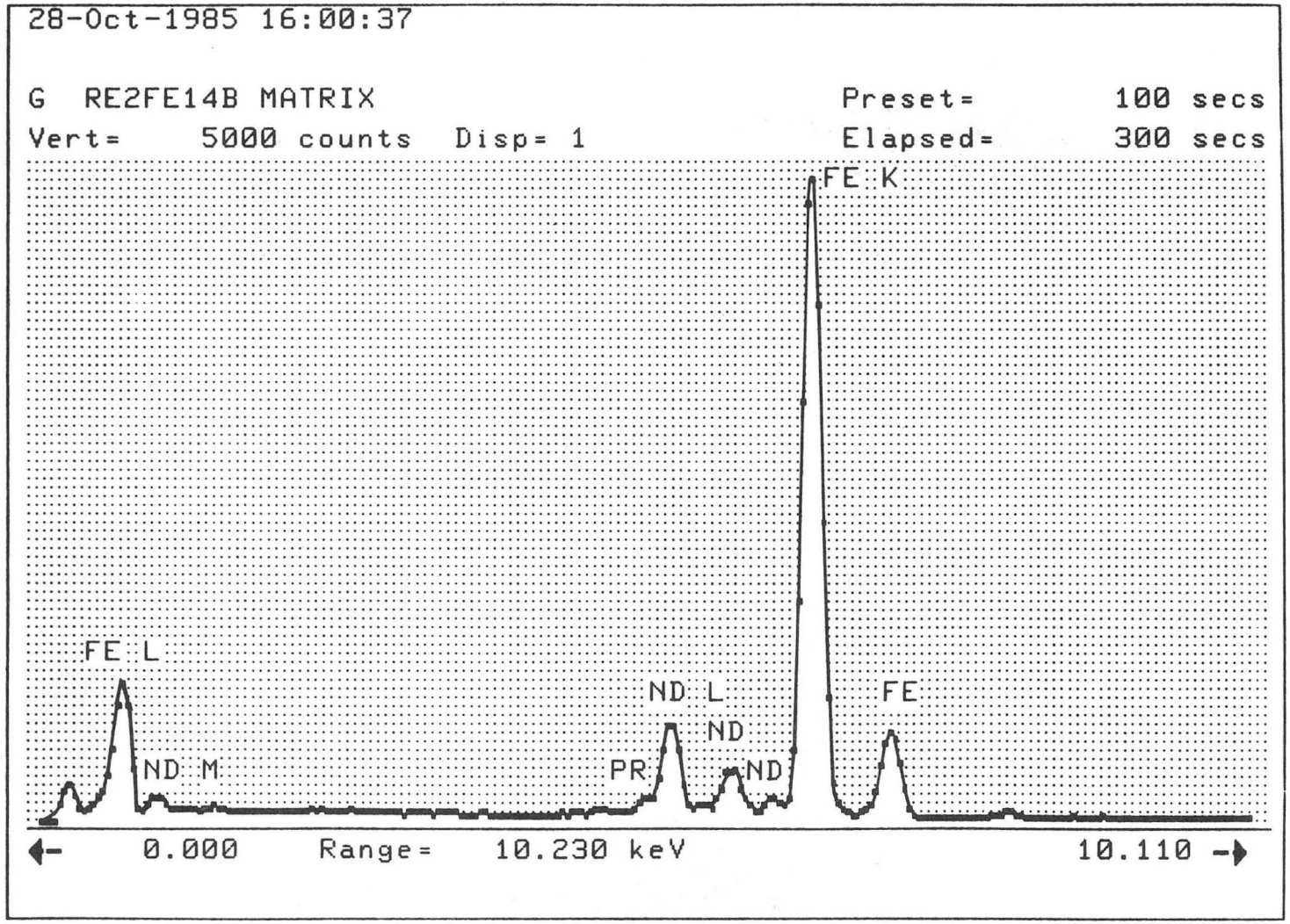

XBL 862-633

Fig.III.7

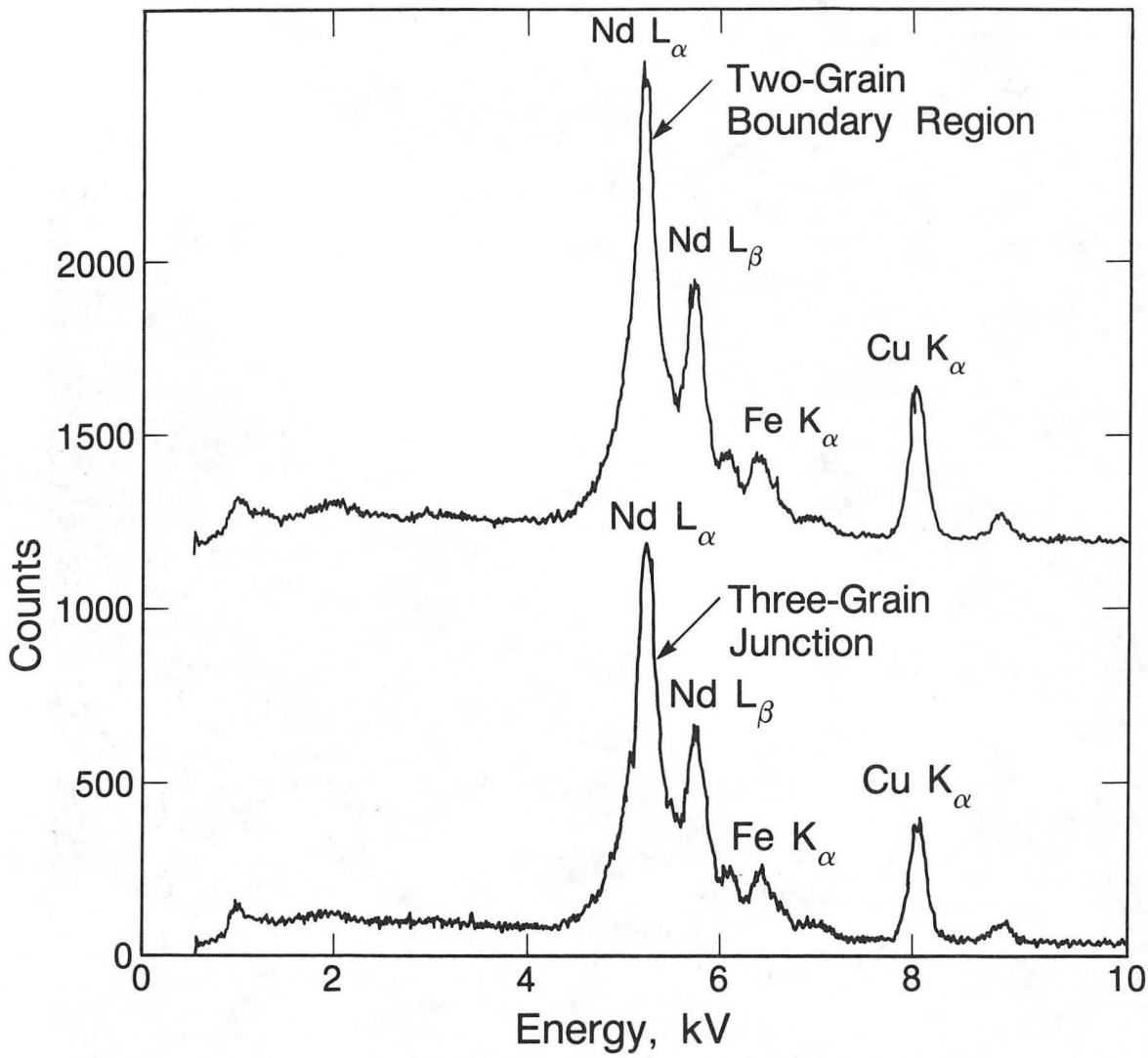

XBL 8611-9025

Fig.III.8

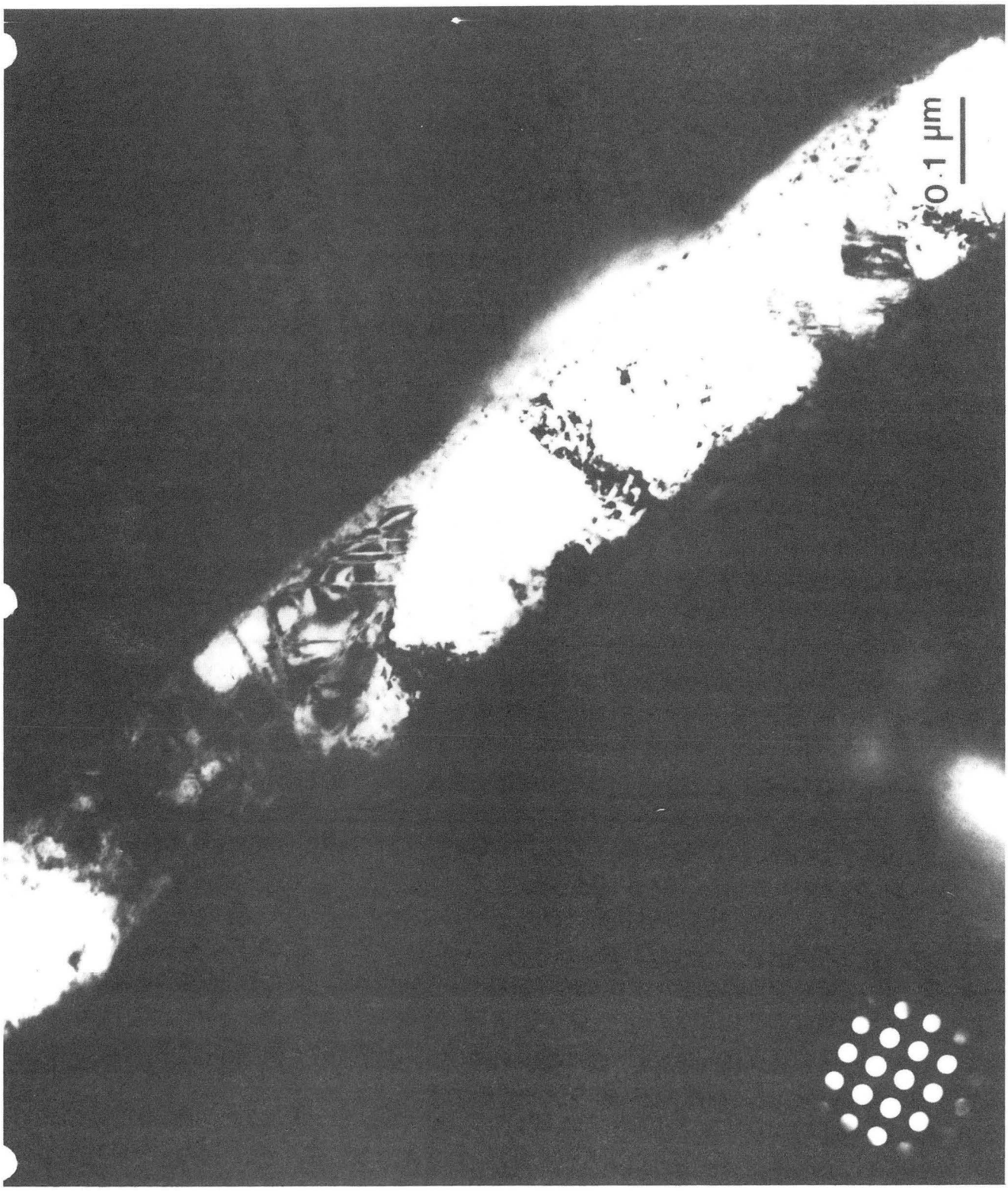

CH. 111, Fig. 9, XBB853-2444

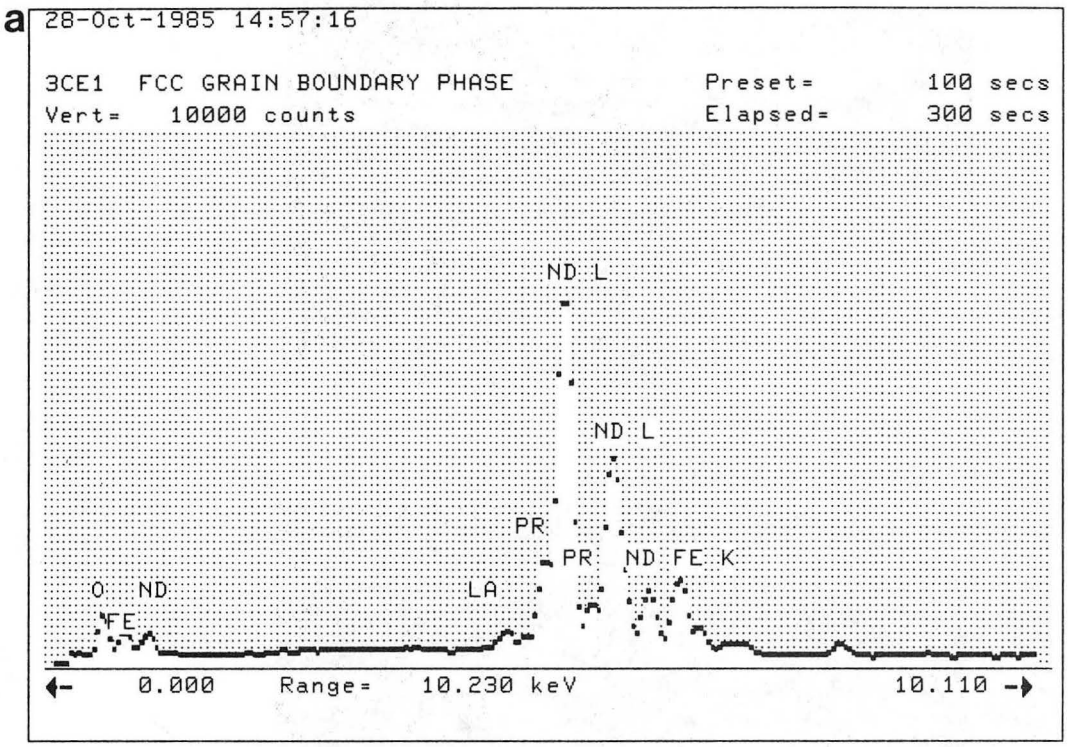

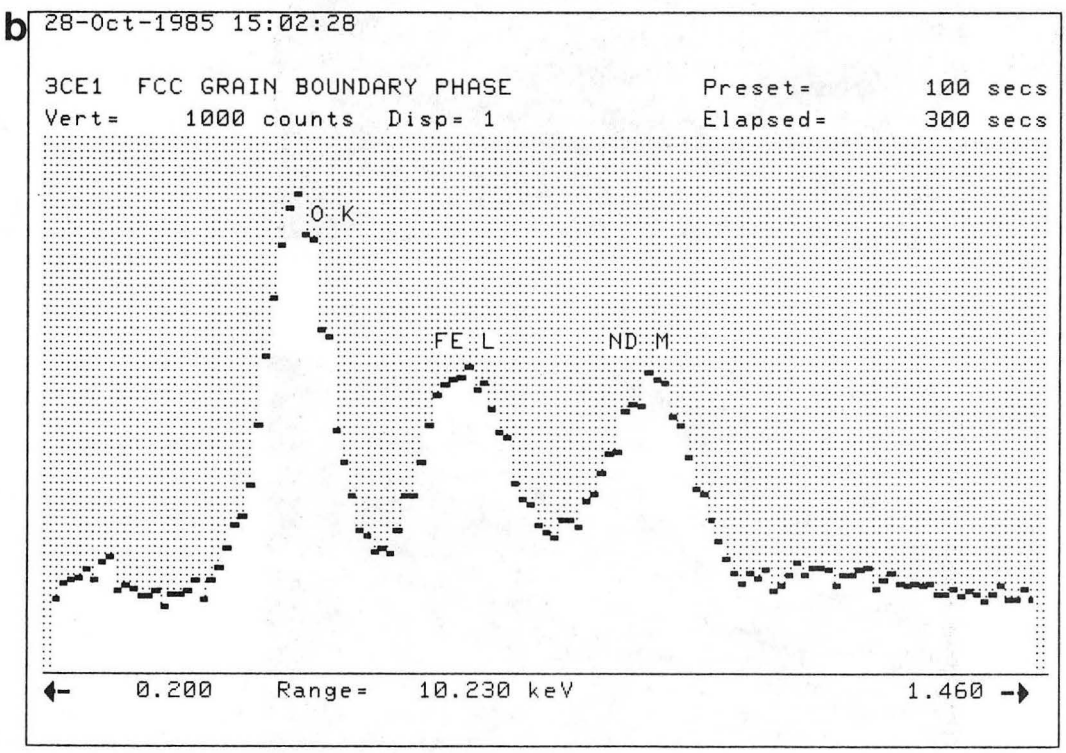

XBL 875-2254

Fig.III.10

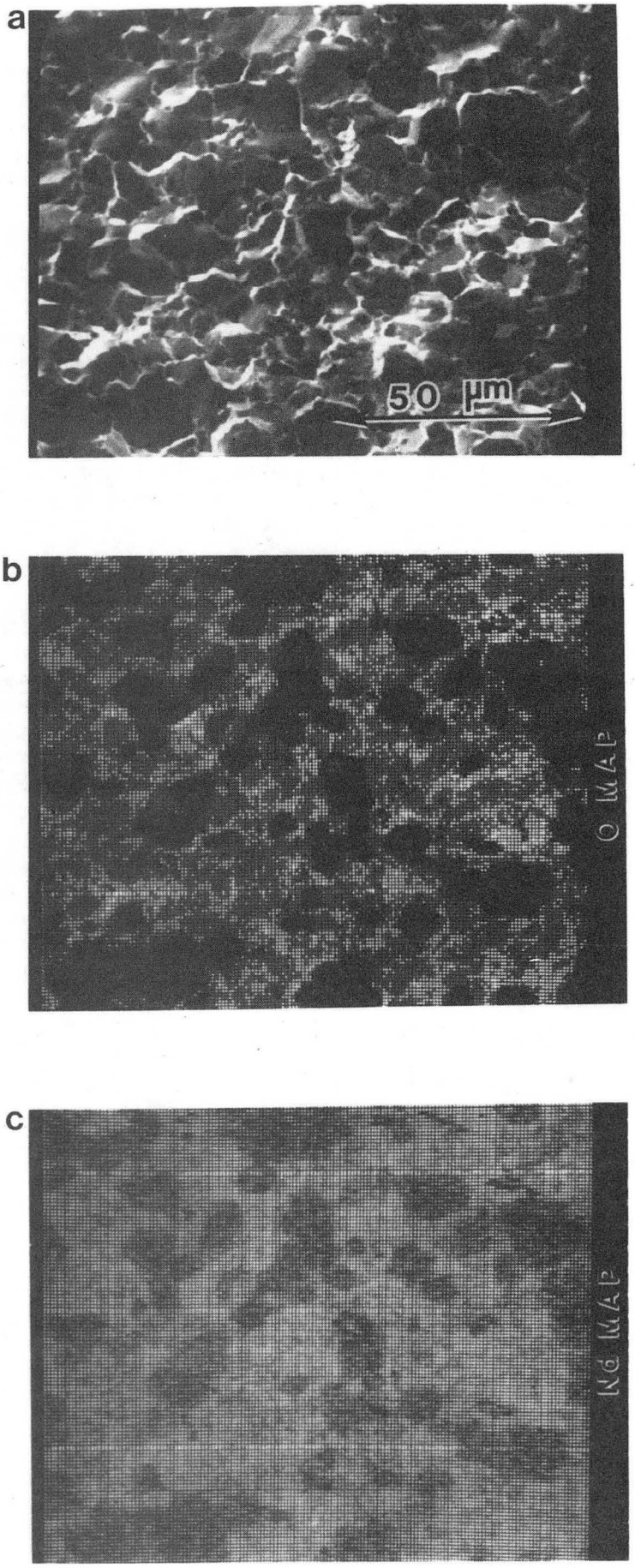

CH. 111, Fig. 11, XBB 850-10300

a

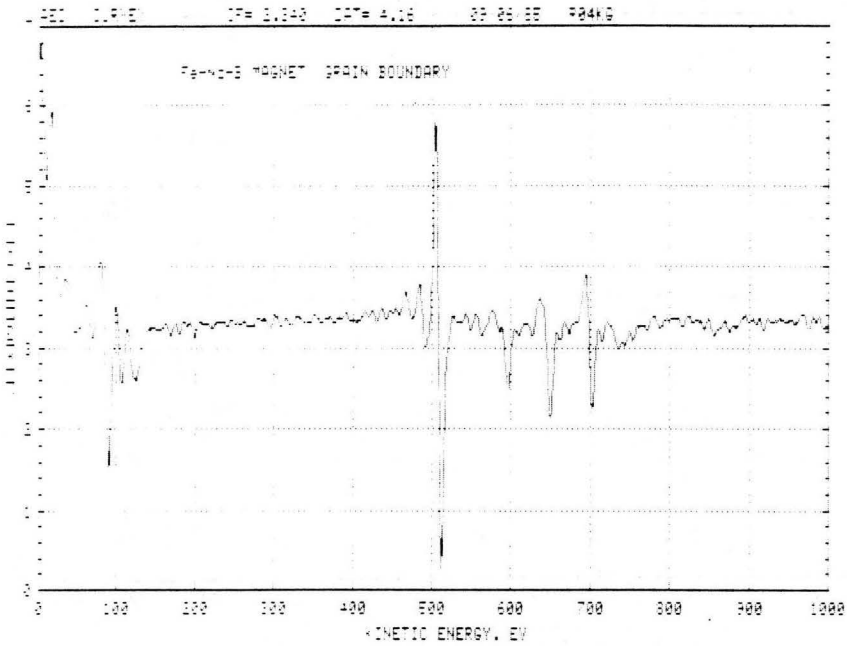

b

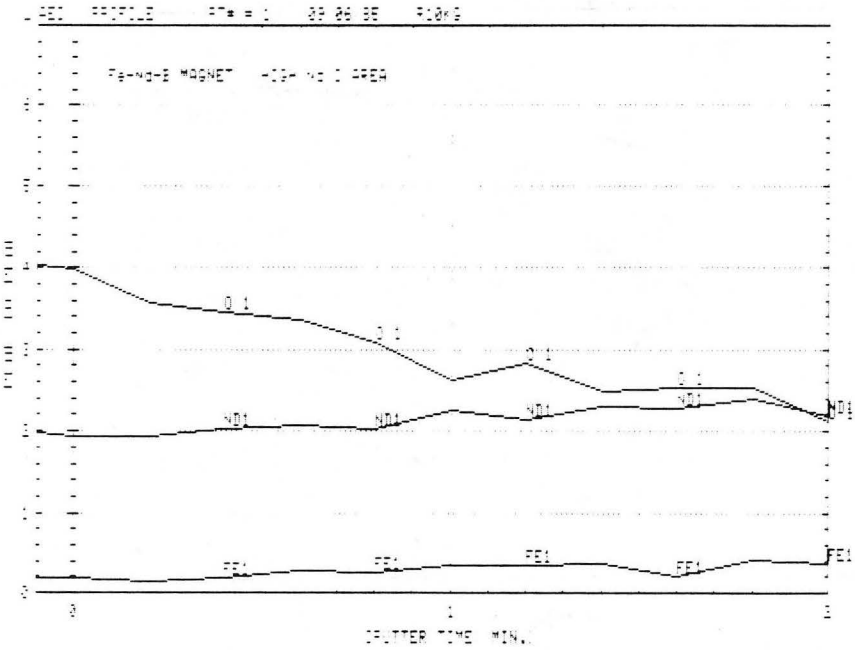

XBL 877-3217

Fig.III.12

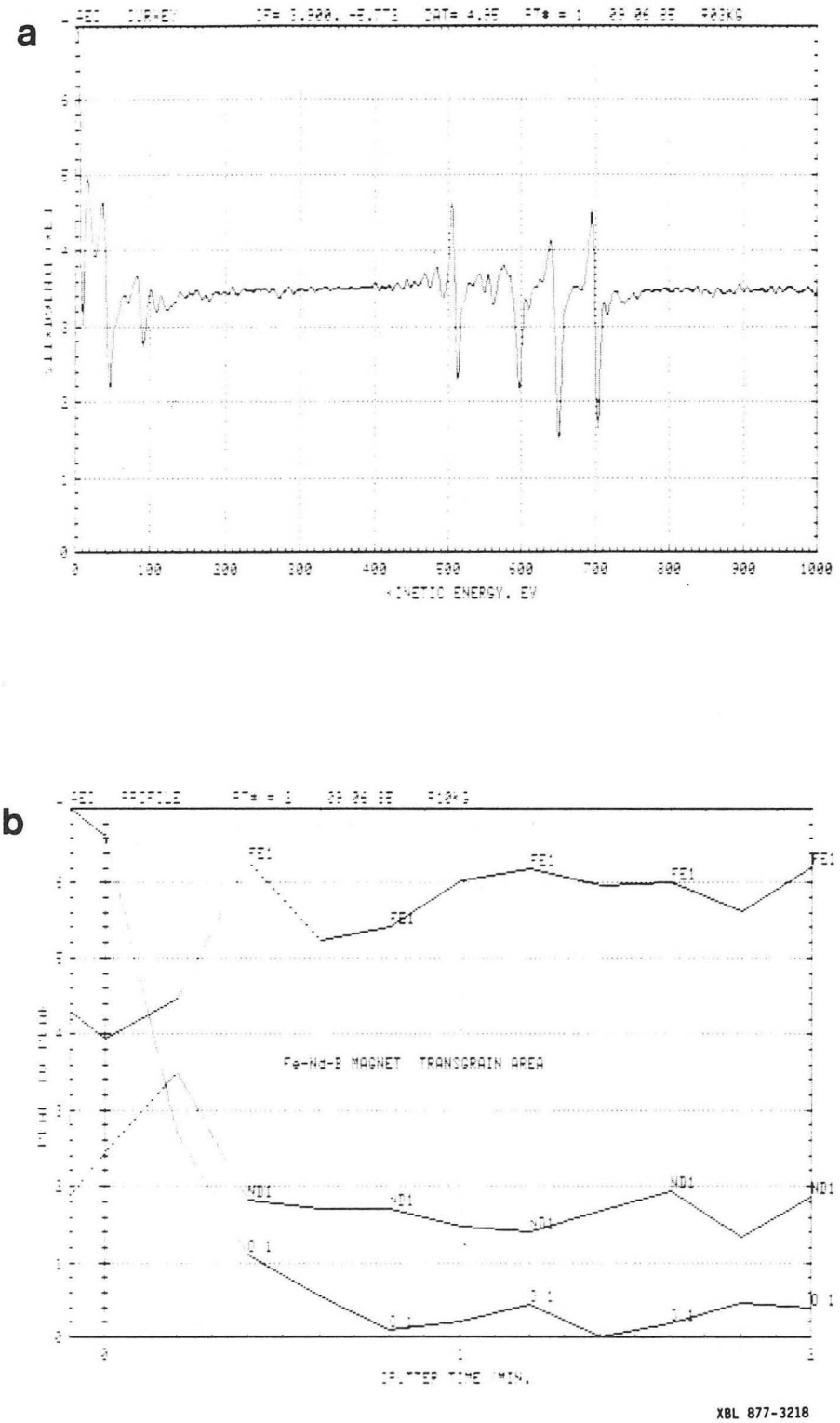
a
0
100
200
300
400
500
600
700
800
900
1000
KINETIC ENERGY, EV
b
FE1
ND1
Fe-Nd-B MAGNET TRANSGRAIN AREA
XBL 877-3218

Fig.III.13

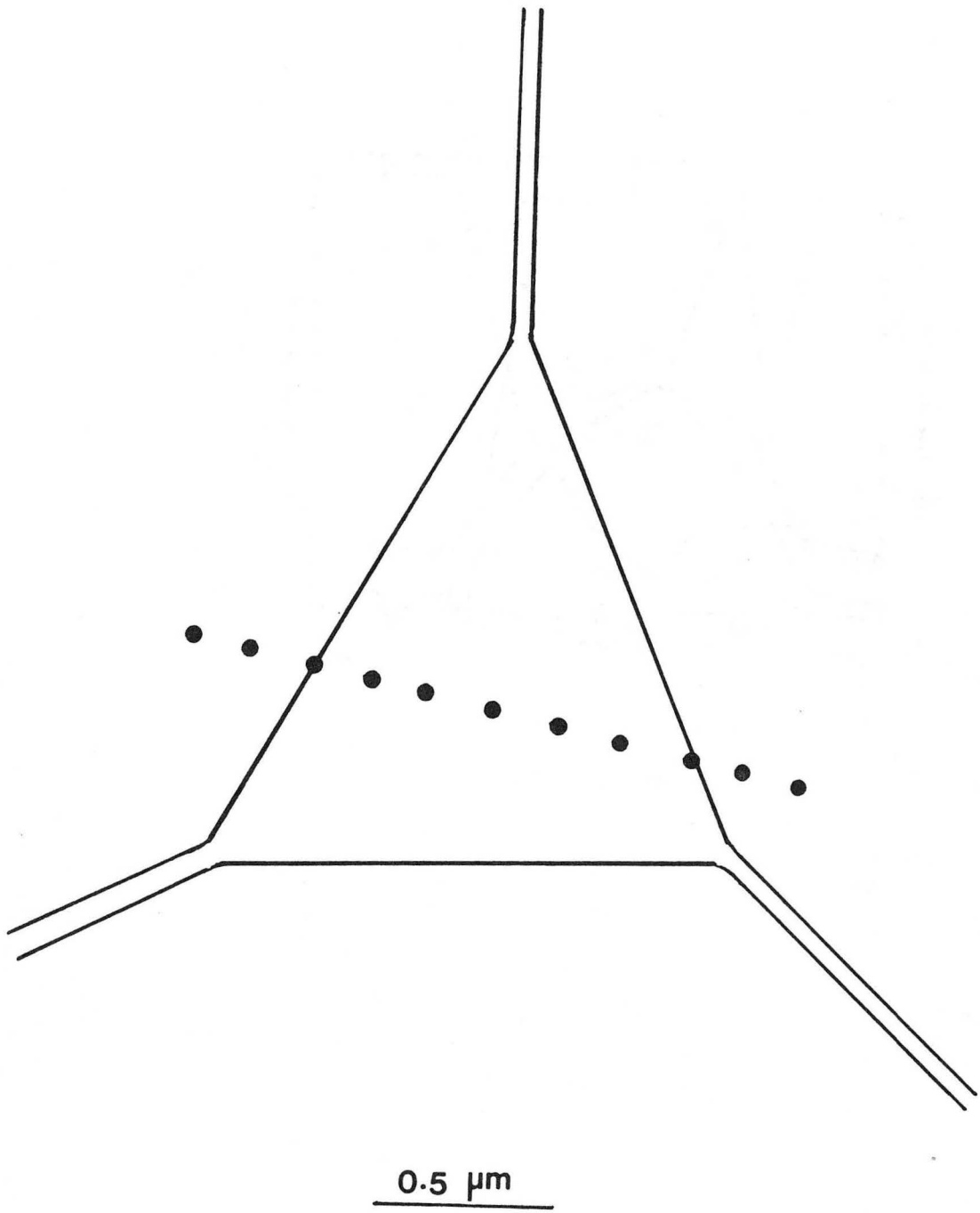

XBL 868-2980

Fig.III.14

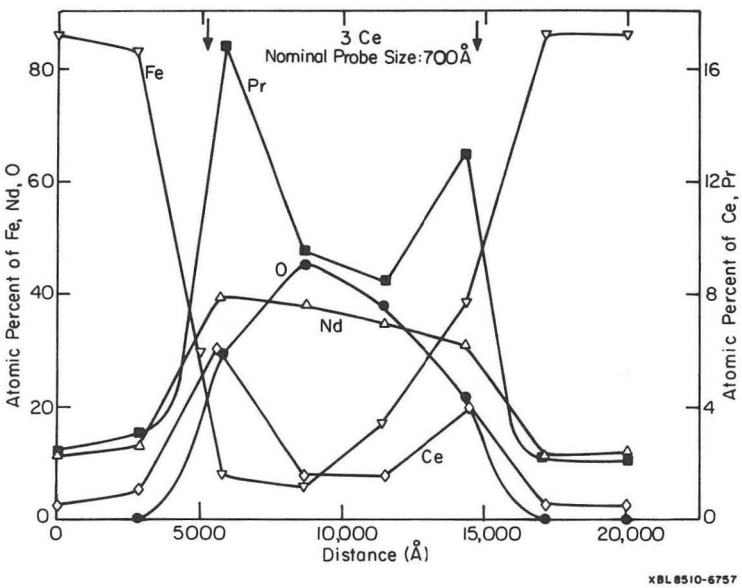
3 Ce
Nominal Probe Size: 700Å
Fe
Pr
O
Nd
Ce
Atomic Percent of Fe, Nd, O
Atomic Percent of Ce, Pr
Distance (Å)
0
5000
10,000
15,000
20,000
0
20
40
60
80
4
8
12
16
XBL 8510-6757

Fig.III.15

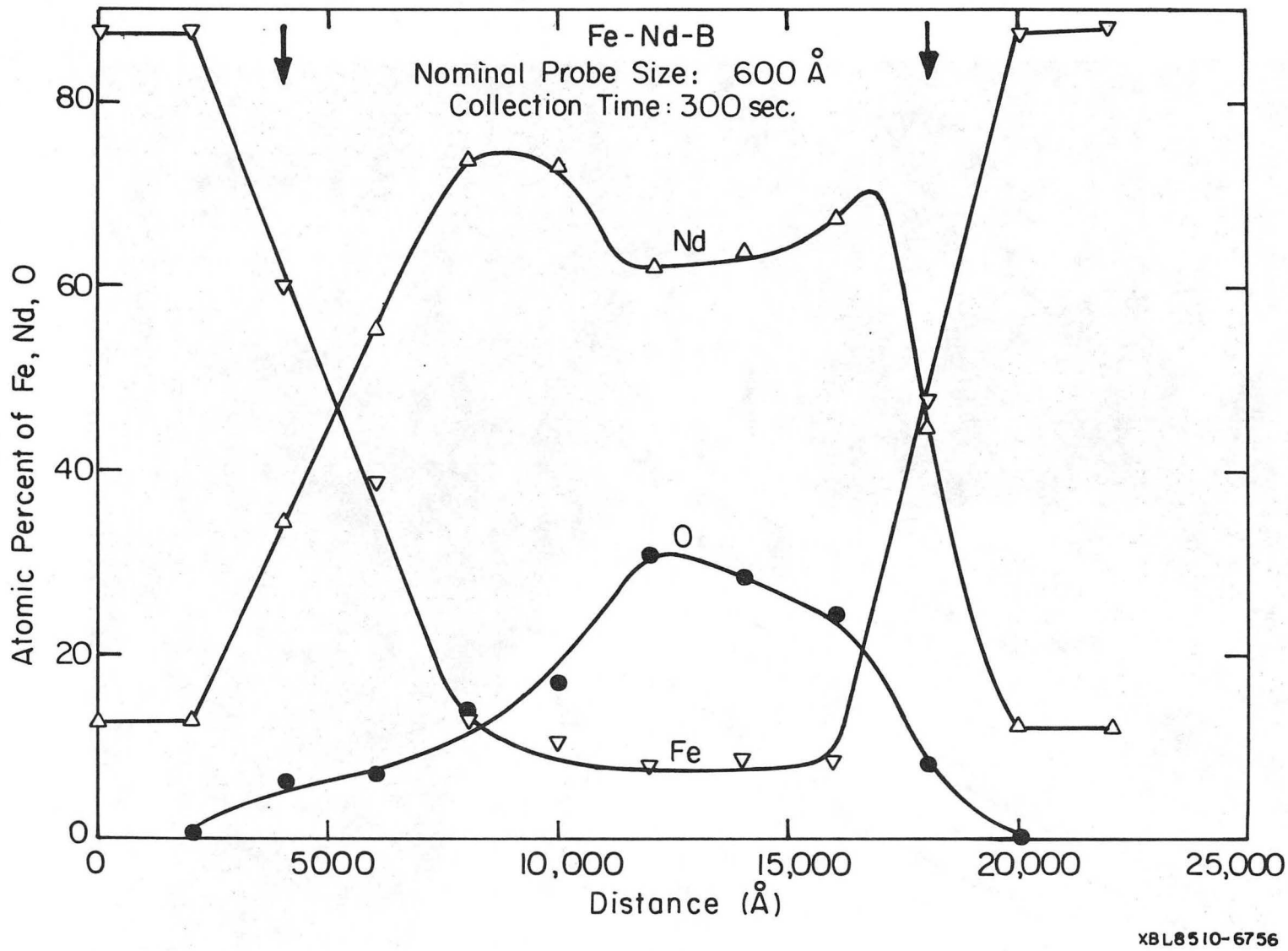
Fe-Nd-B
Nominal Probe Size: 600 Å
Collection Time: 300 sec.
Nd
O
Fe
Atomic Percent of Fe, Nd, O
0
20
40
60
80
0
5000
10,000
15,000
20,000
25,000
Distance (Å)
XBL8510-6756

Fig.III.16

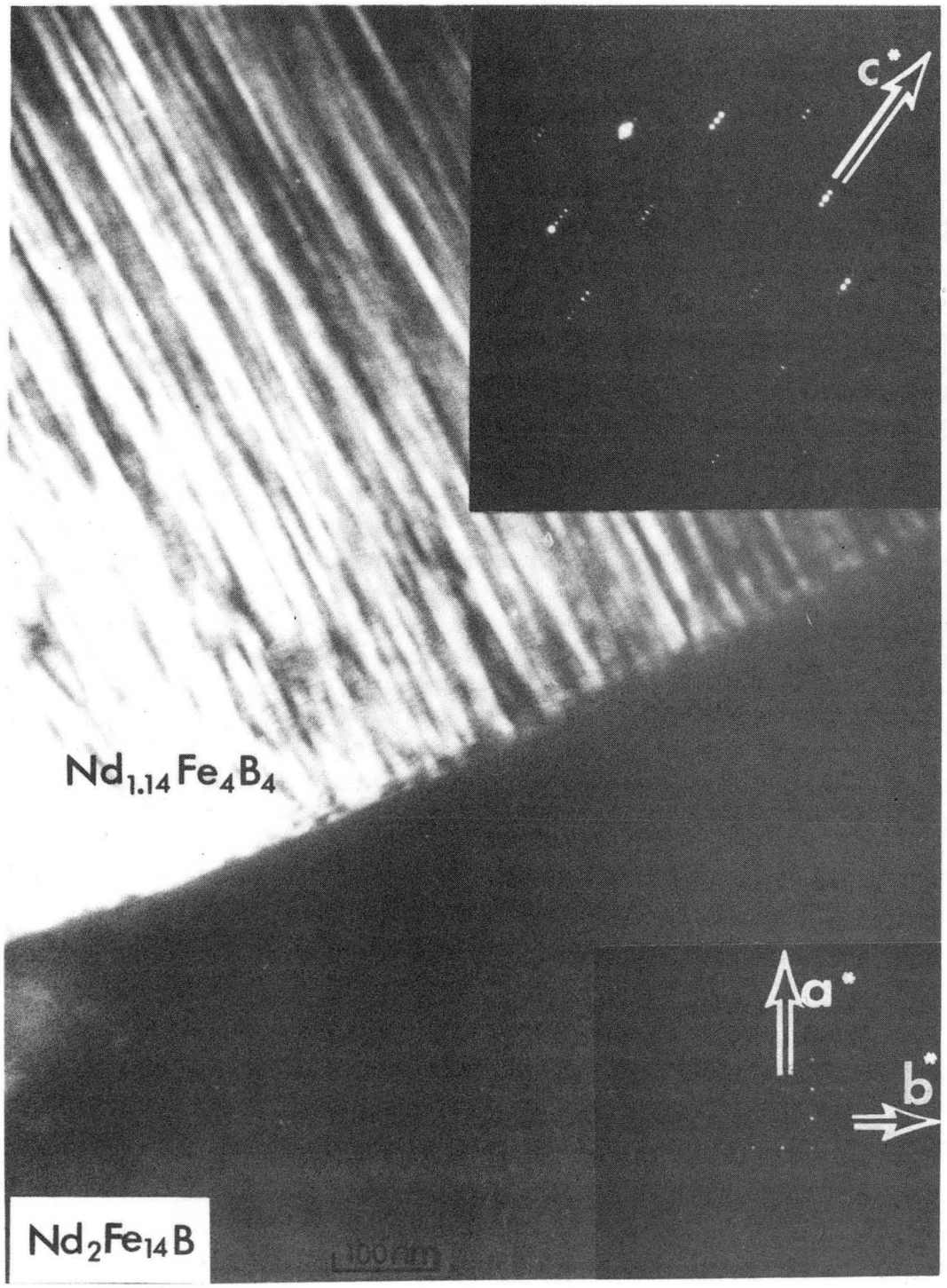

CH. 111, Fig. 17, XBB856-4860

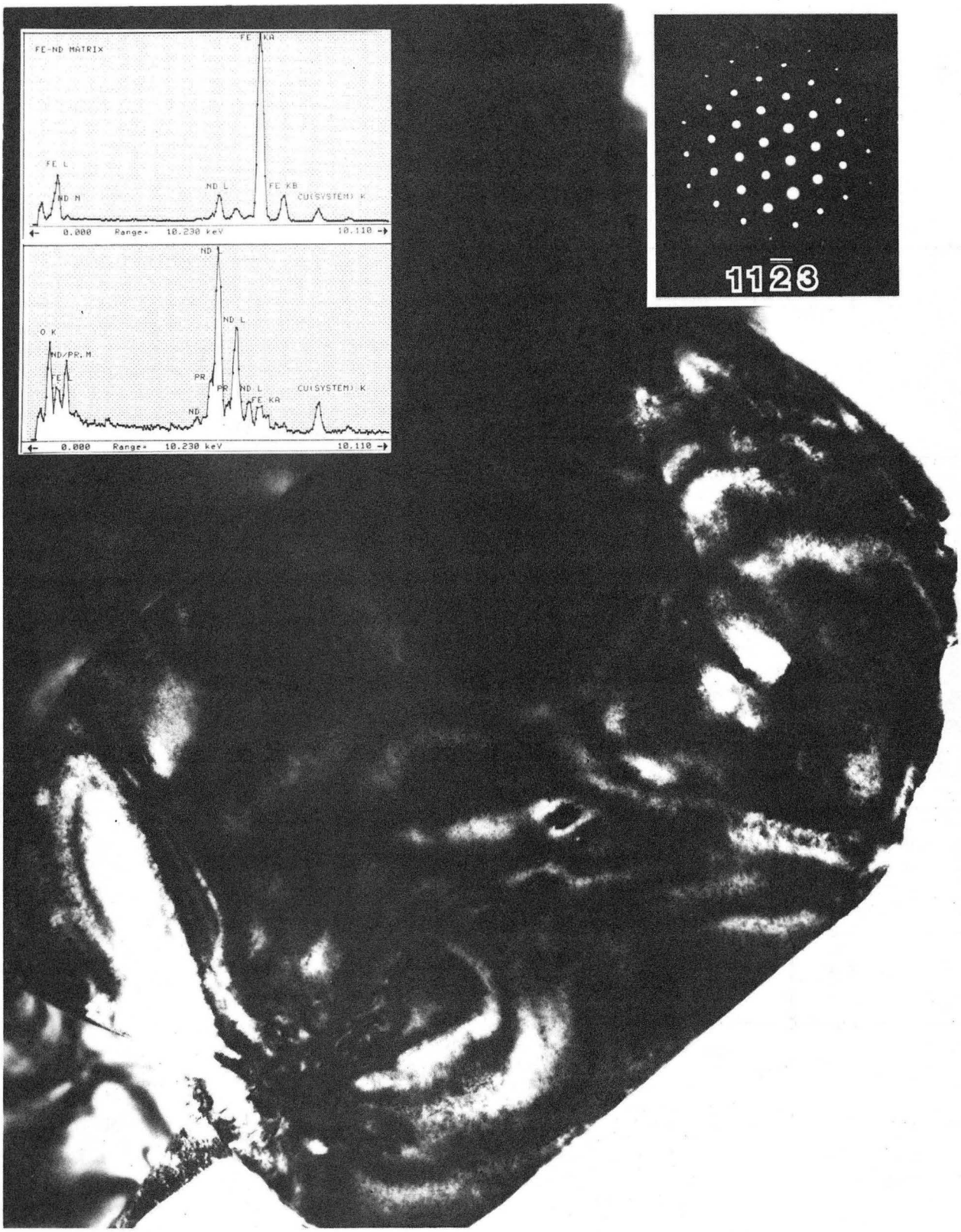

CH. 111, Fig. 18, XBB856-4525A

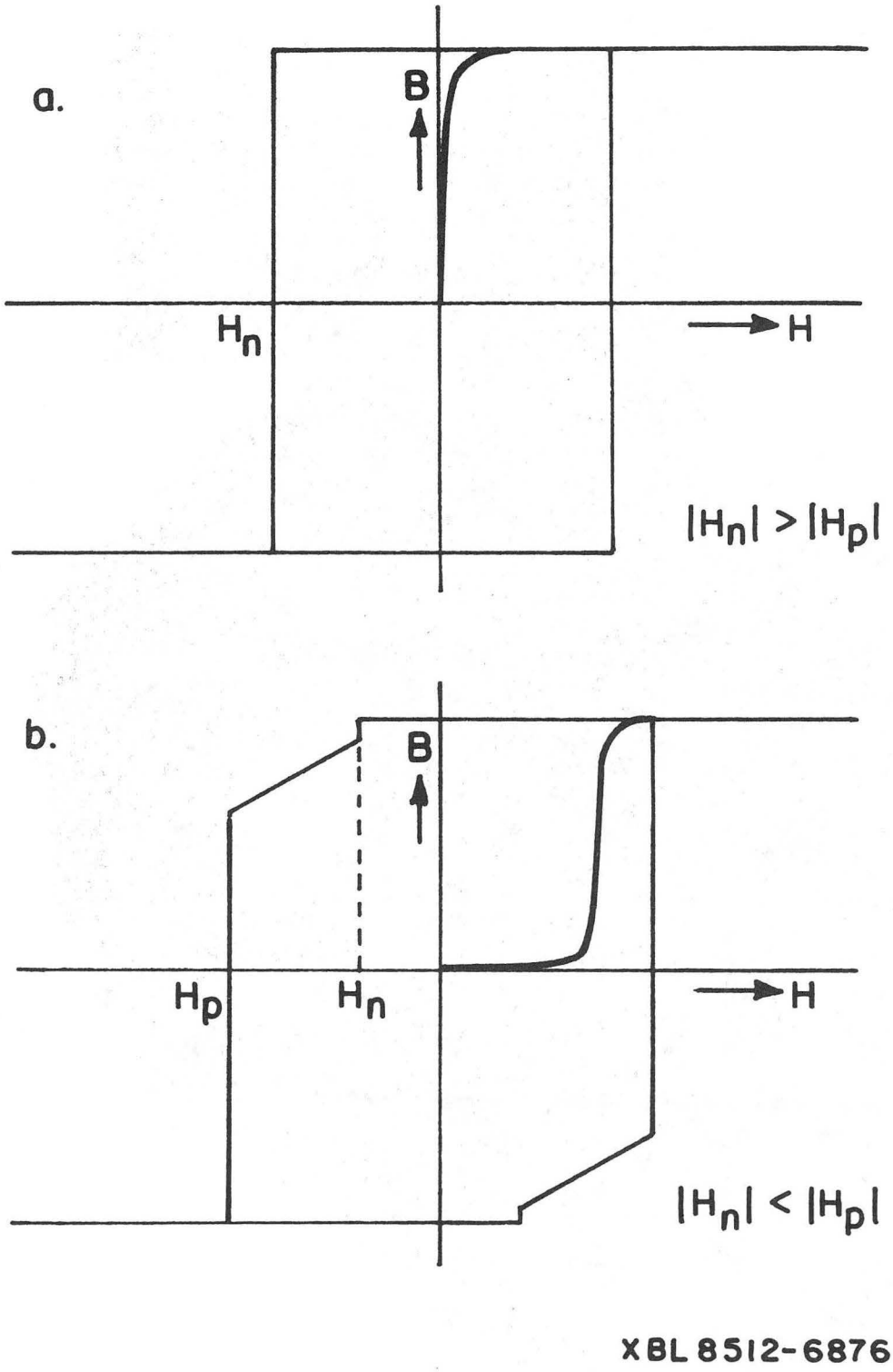

Fig.III.19

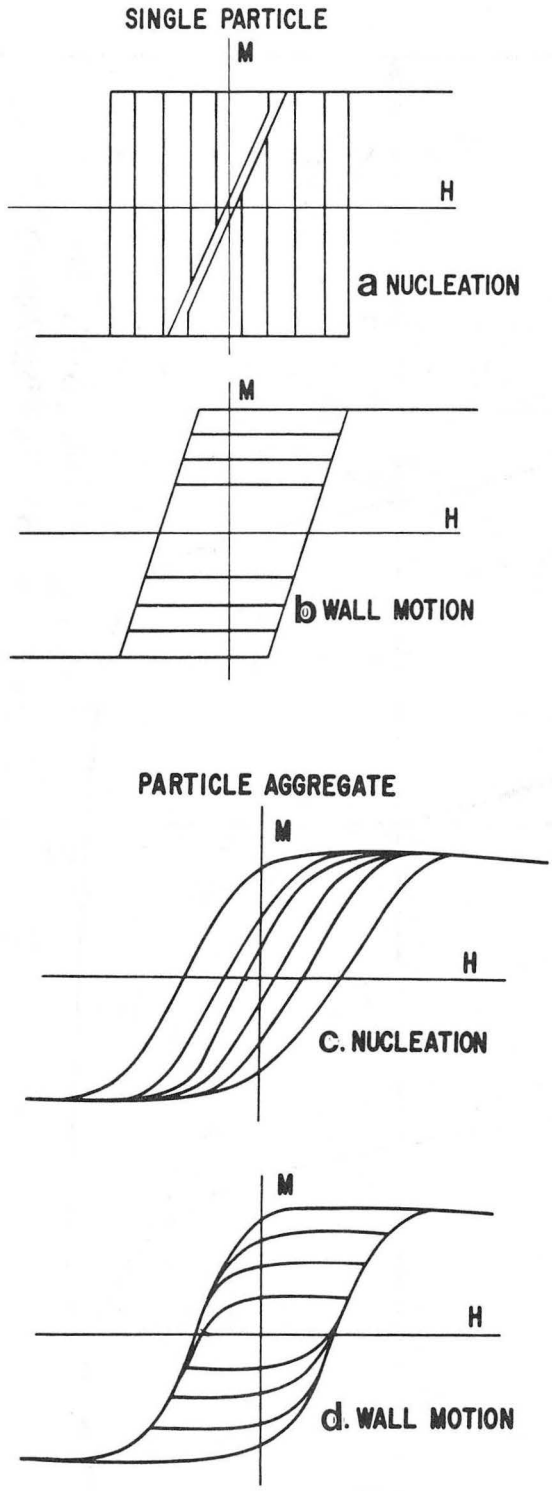

XBL 863-776

Fig.III.20

VIRGIN MAGNETIZATION CURVE MEASUREMENT

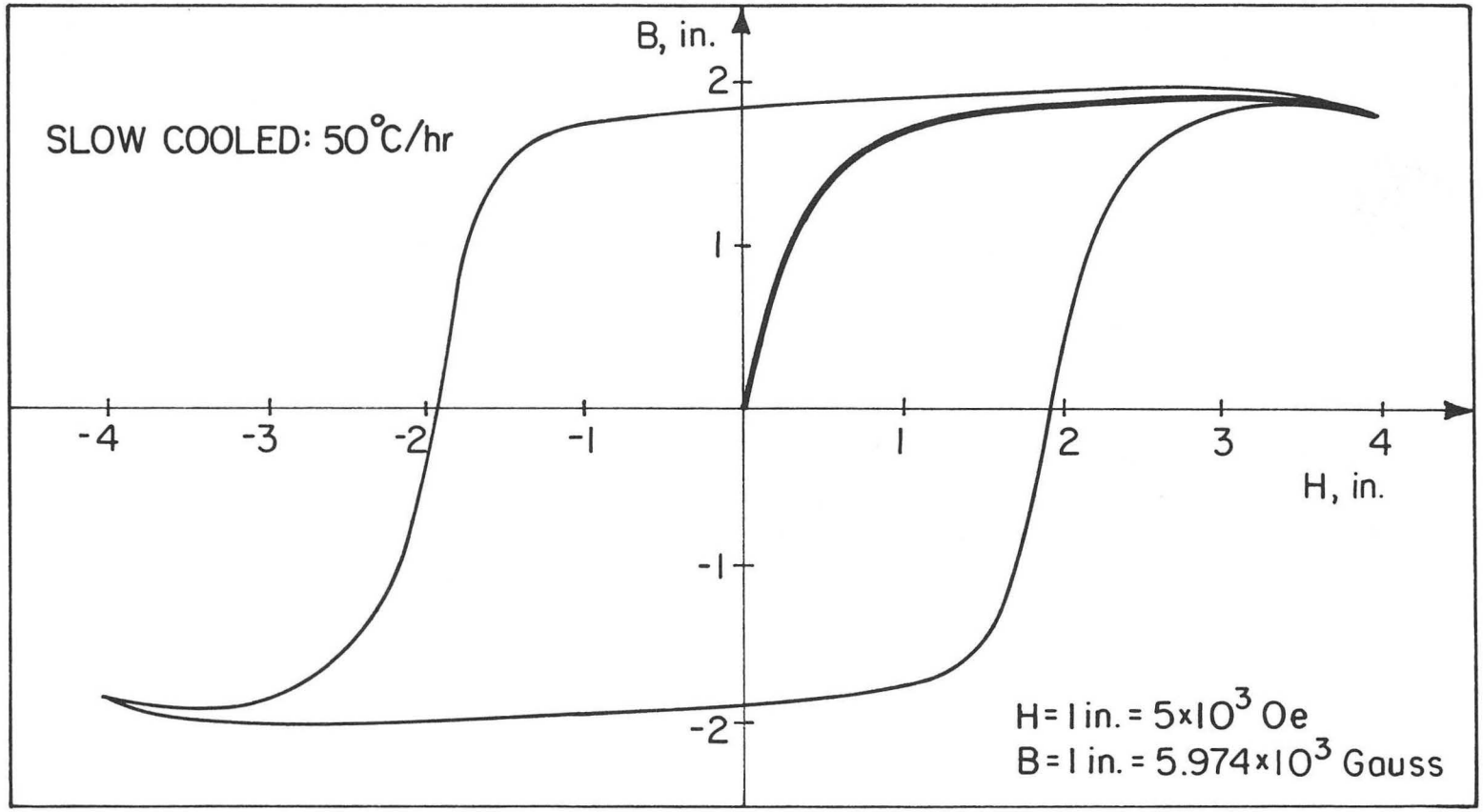

INFERENCE: Steep rise in virgin magnetization curve ⟹ easy movement of domain walls inside the grains ⟶ no significant pinning sites

XBL 861-7404 A

Fig.III.21

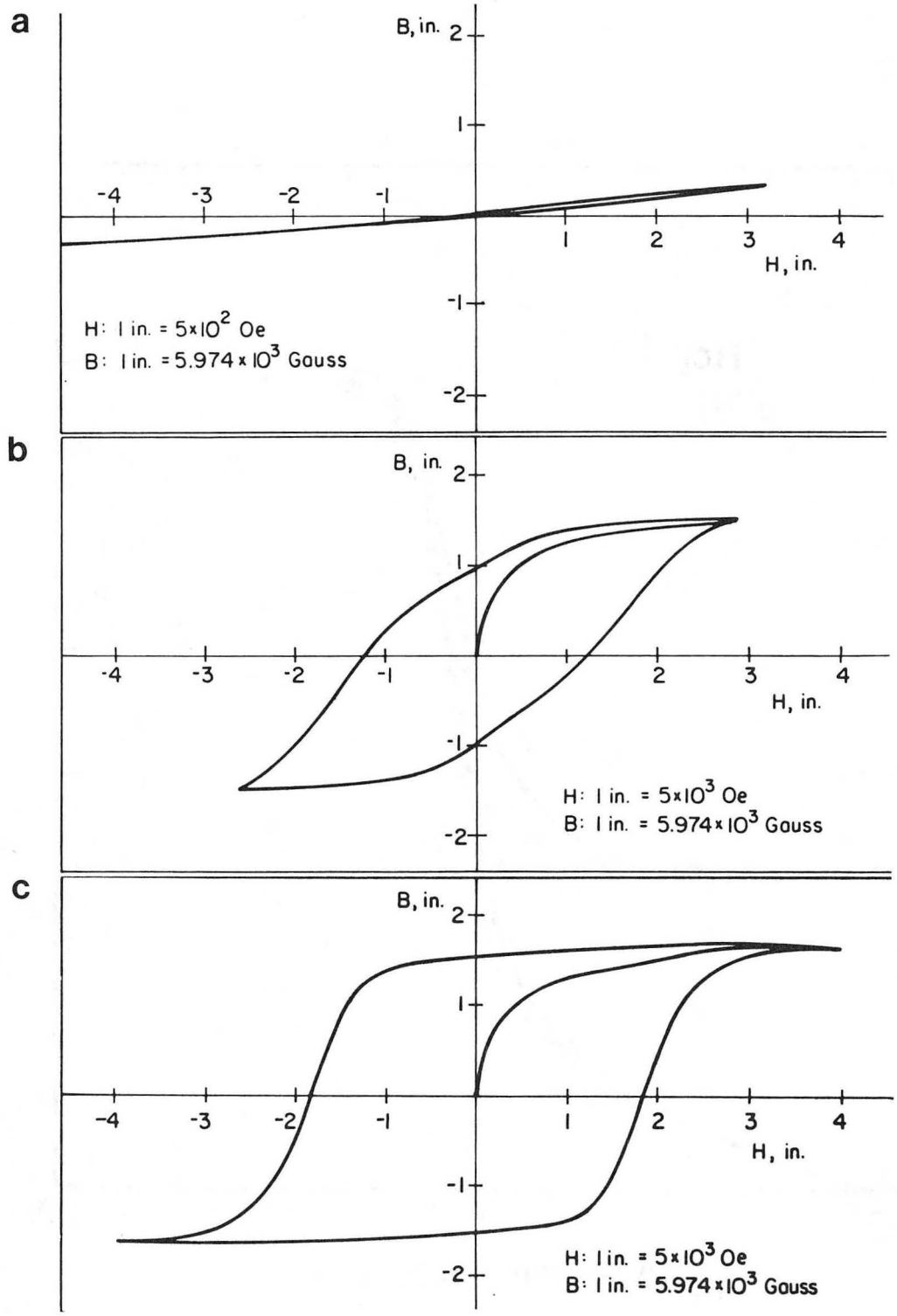

XBL 862-636

Fig.III.22

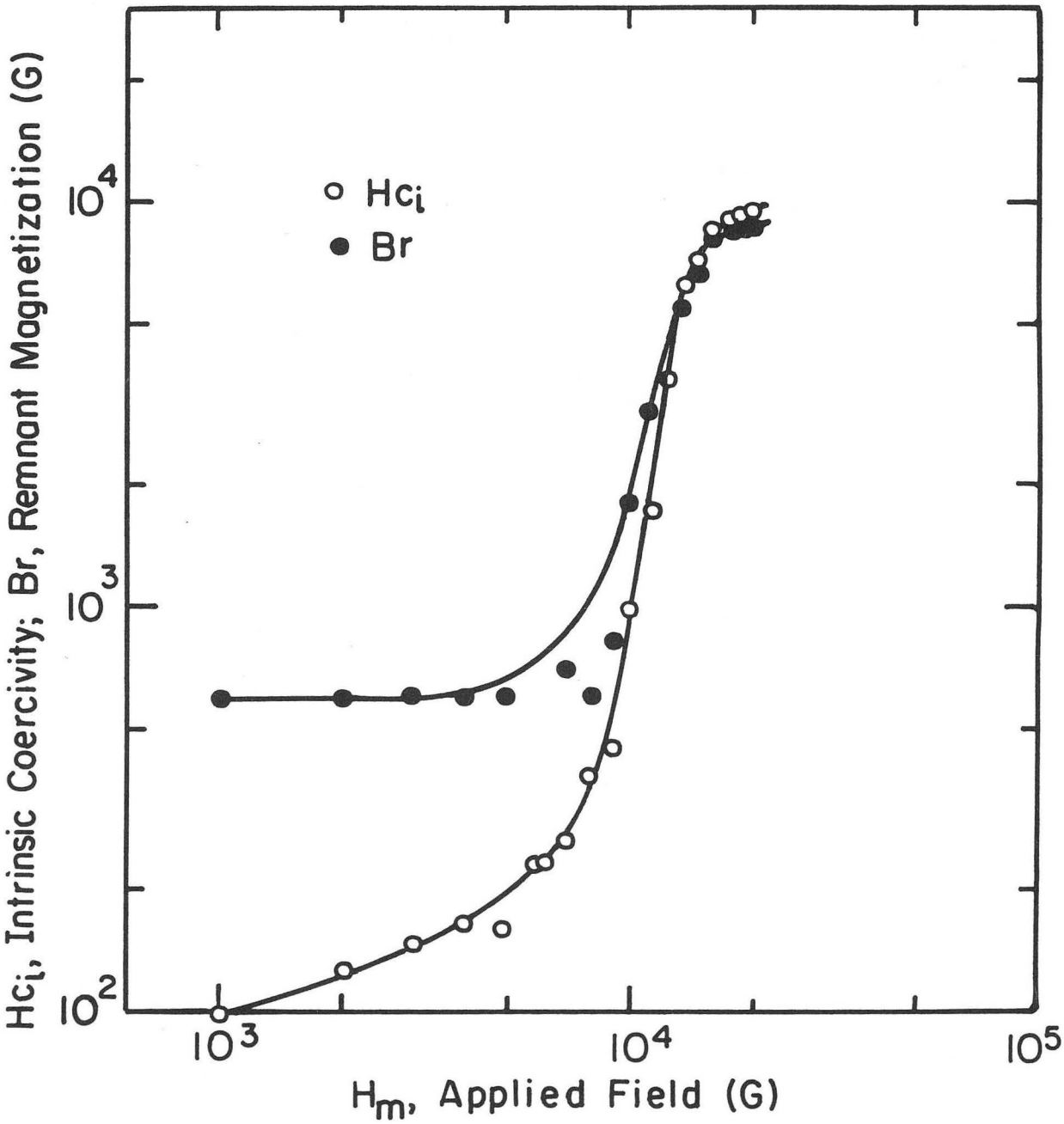

XBL 8510-6653

Fig.III.23

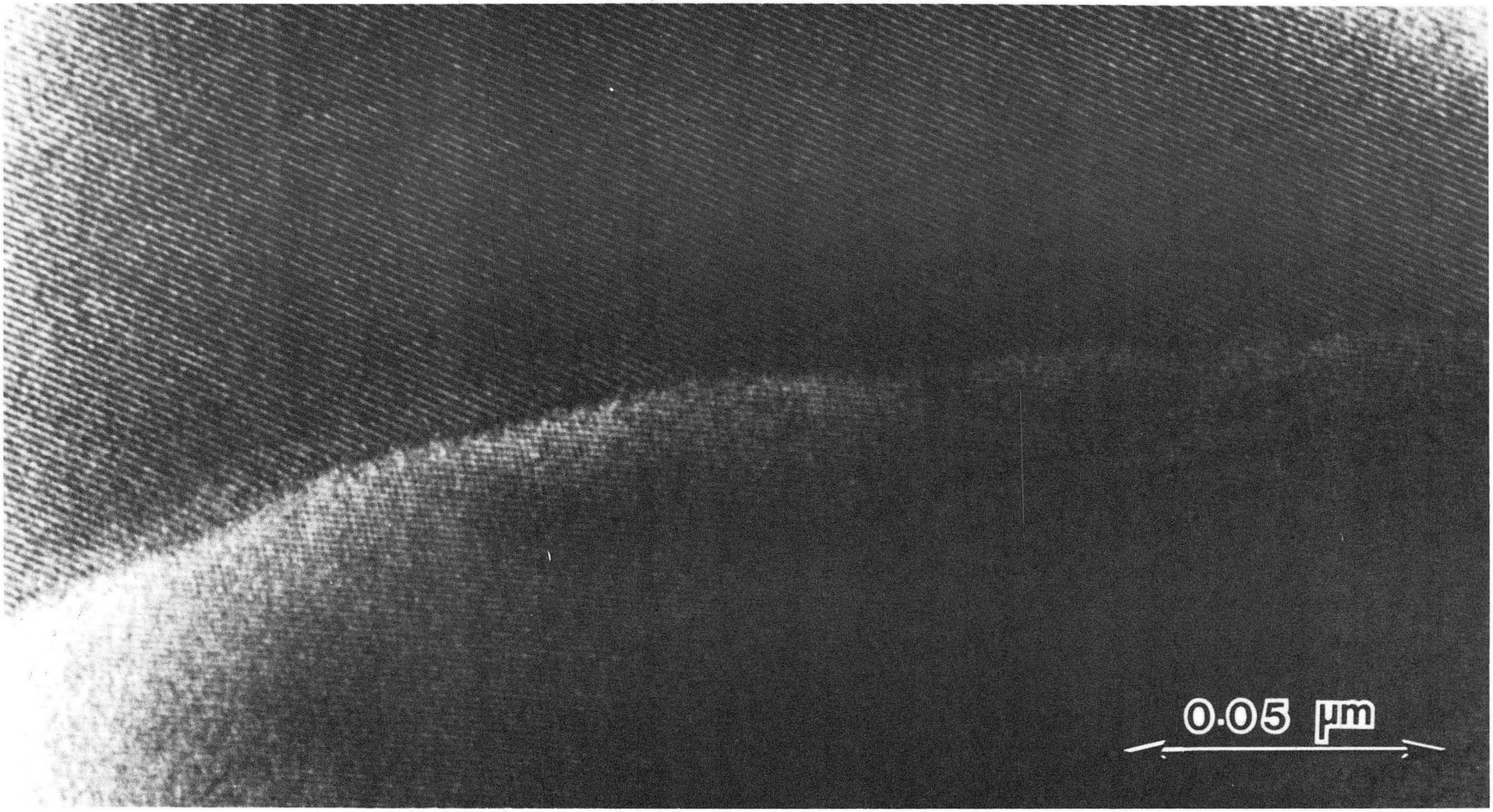

CH. 111, Fig. 24, XBB862-1266

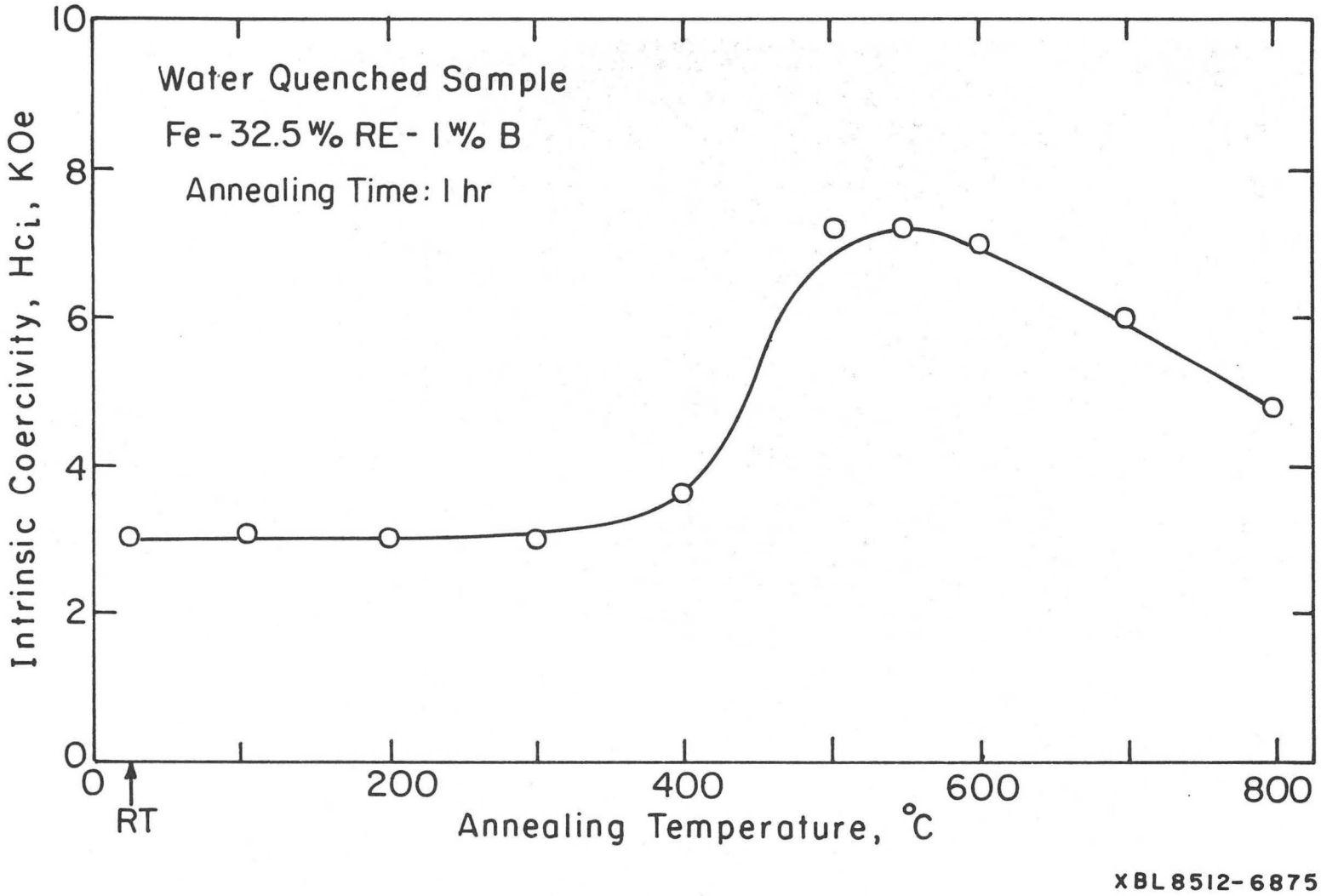
Water Quenched Sample
Fe - 32.5 w/o RE - 1 w/o B
Annealing Time: 1 hr
Intrinsic Coercivity, Hci, KOe
0
2
4
6
8
10
0
RT
200
400
600
800
Annealing Temperature, °C
XBL8512-6875

Fig.III.25

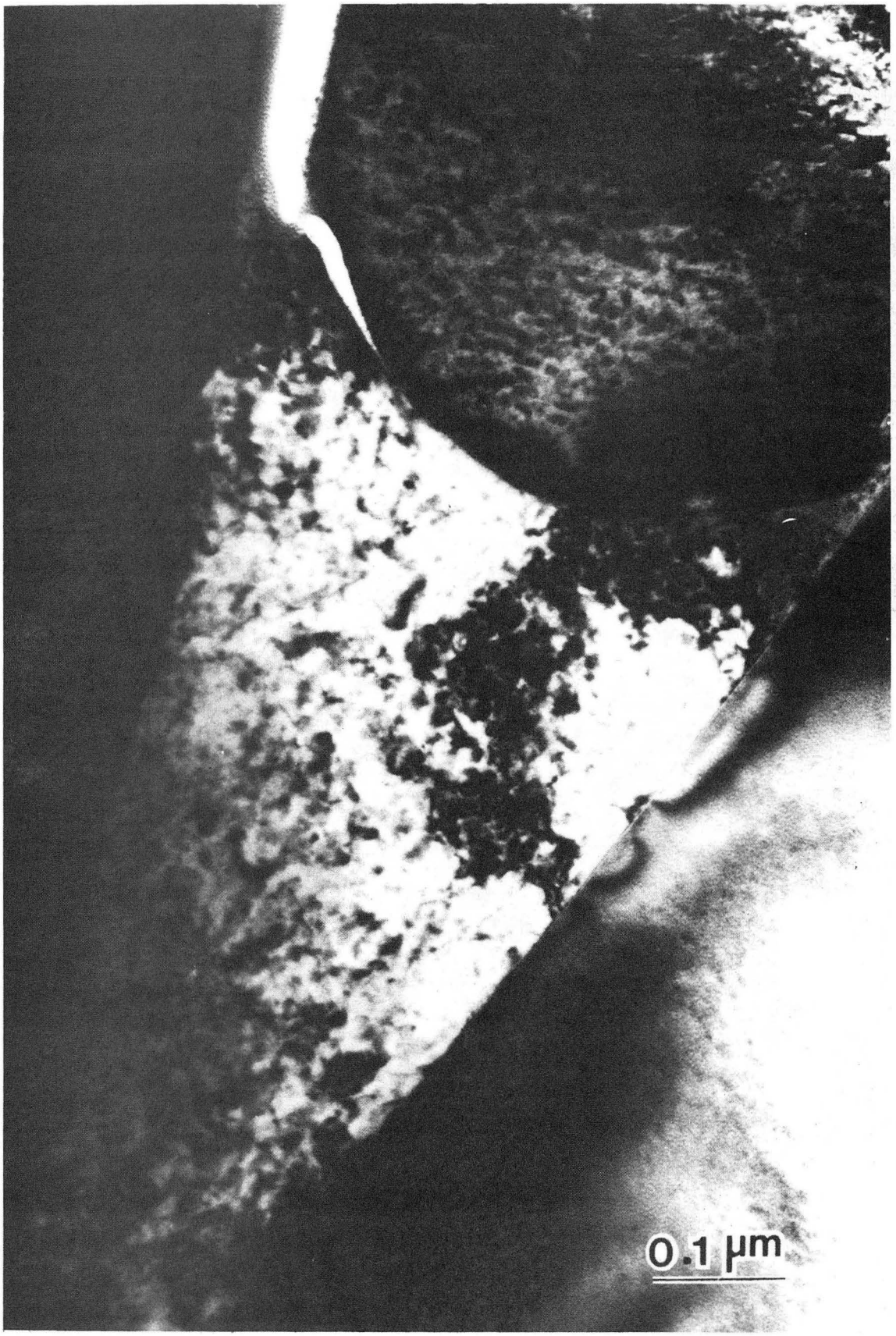

CH. 111, Fig. 26(a) XBB862-1134

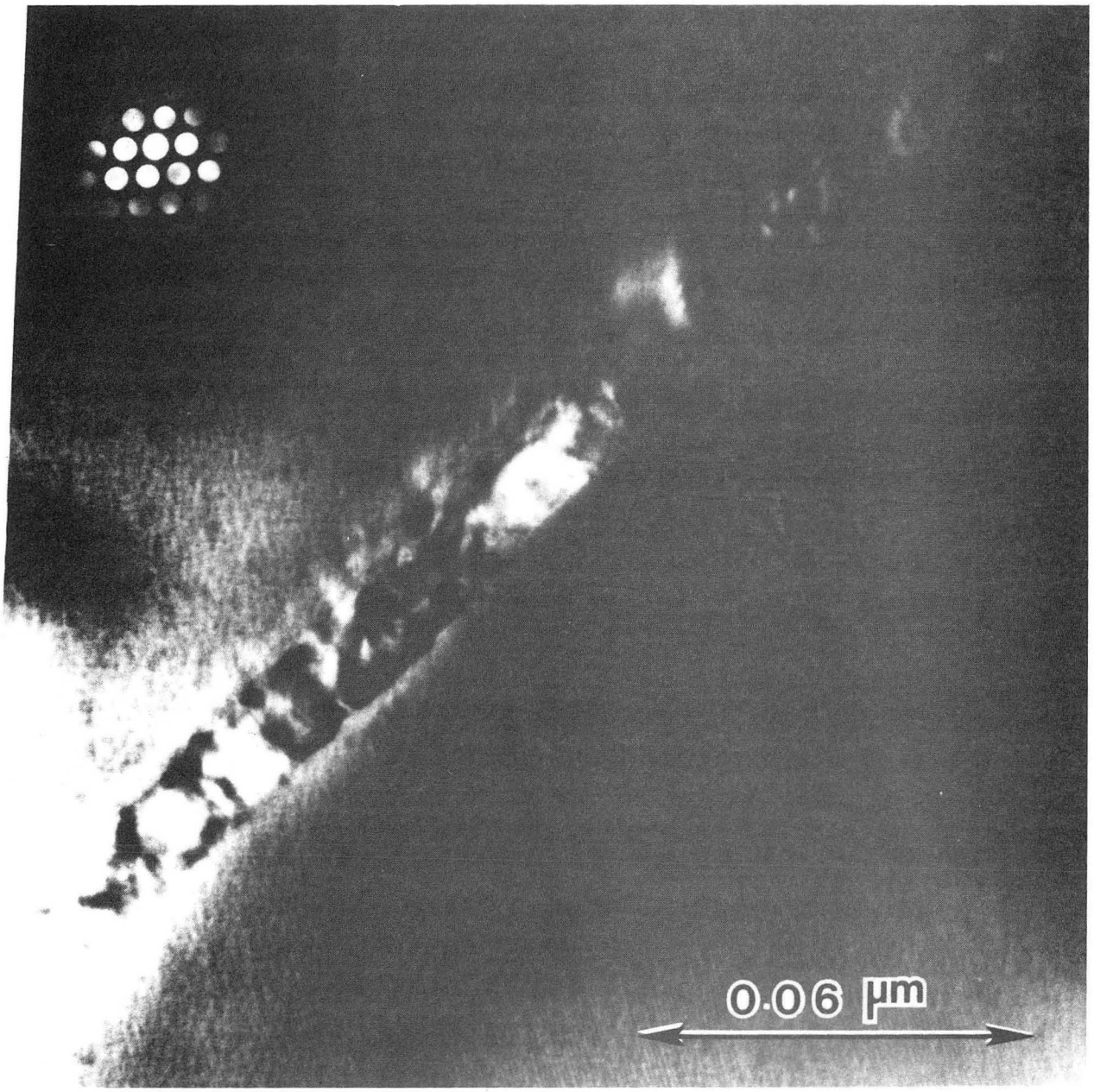

CH. 111, Fig. 26(b), XBB862-1269

a

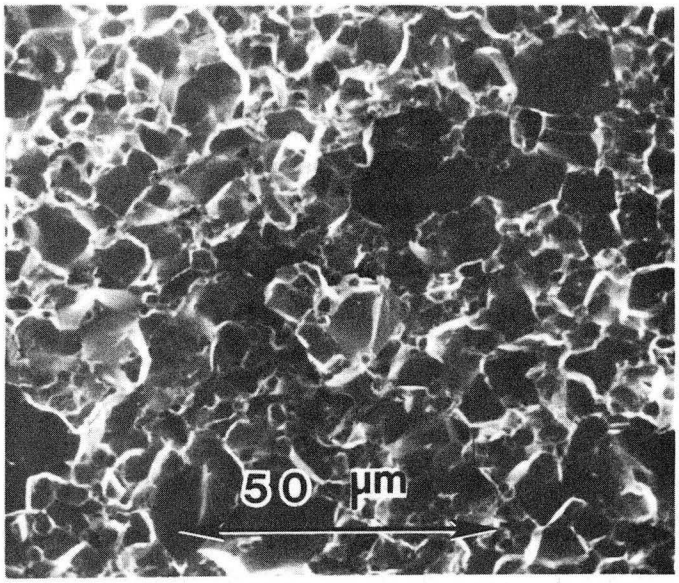

b

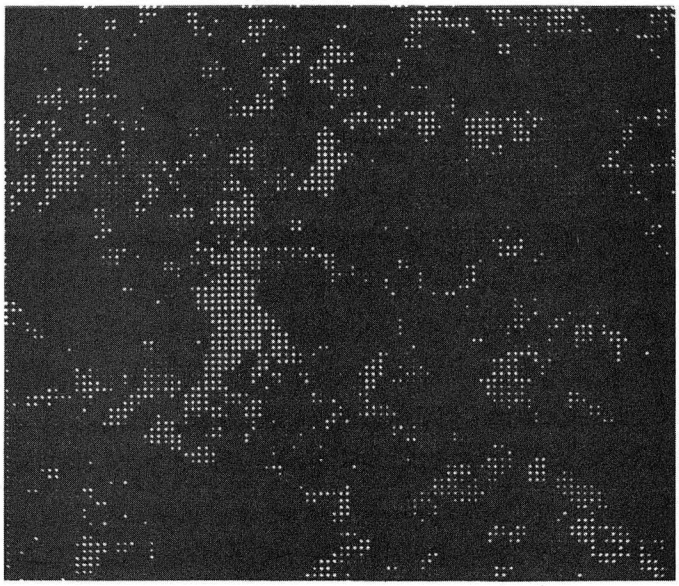

c

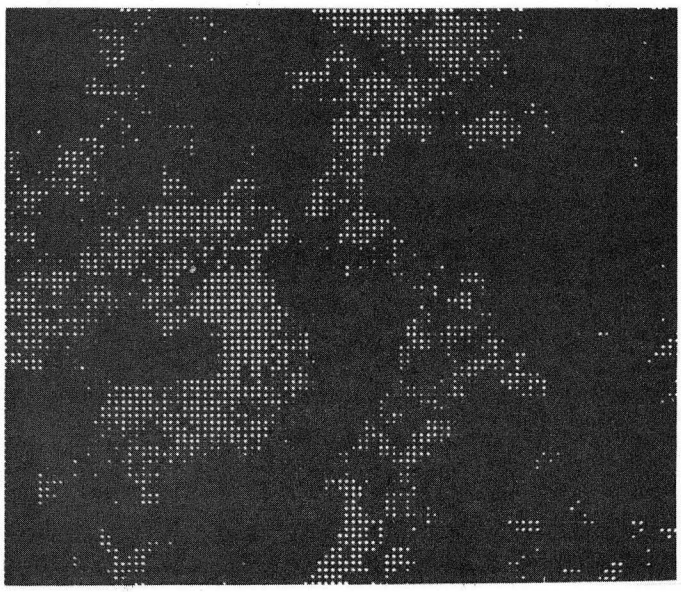

CH. 111, Fig. 27, XBB877-5710

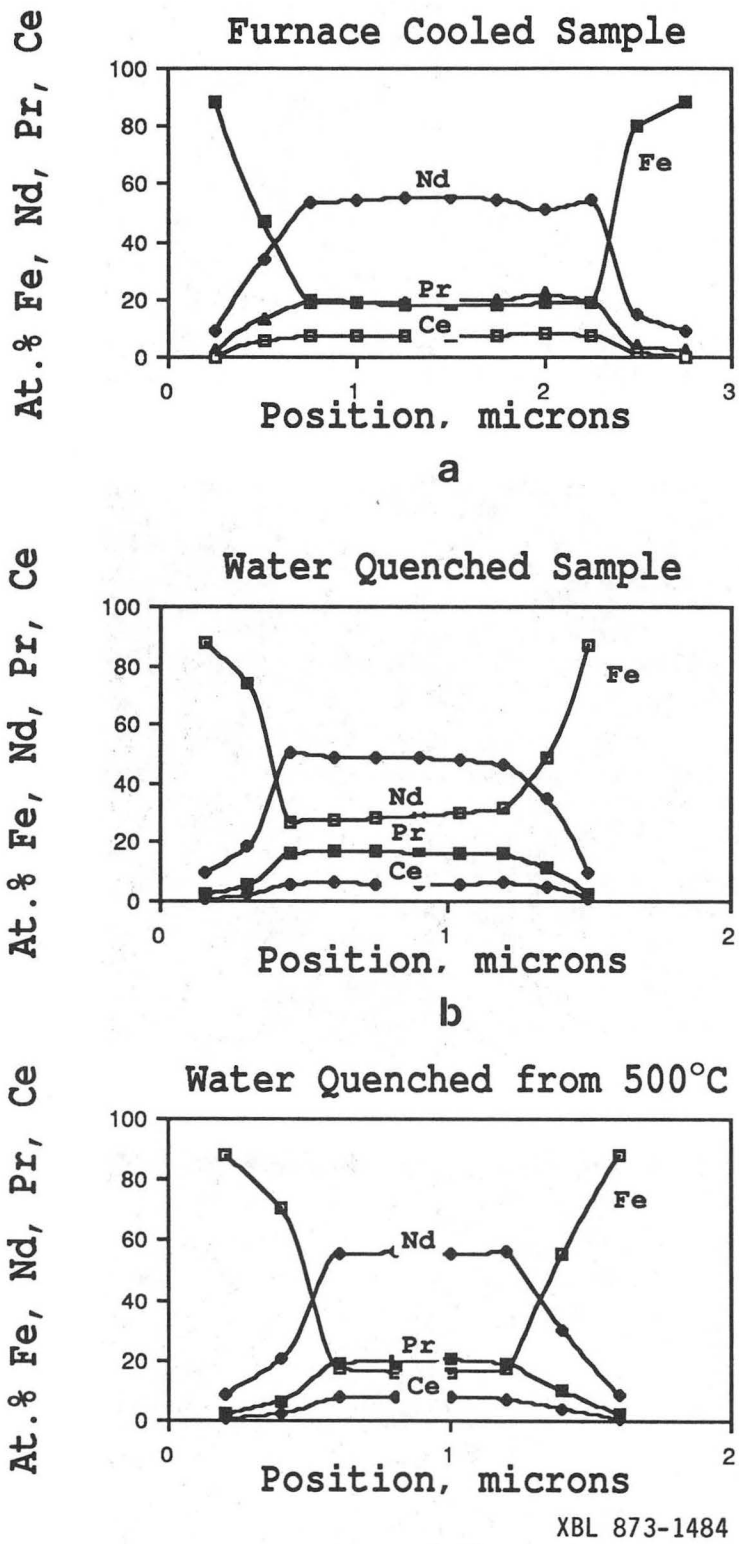
Furnace Cooled Sample
At.% Fe, Nd, Pr, Ce
100
80
60
40
20
0
0
1
2
3
Position, microns
Nd
Fe
Pr
Ce
a
Water Quenched Sample
At.% Fe, Nd, Pr, Ce
100
80
60
40
20
0
0
1
2
Position, microns
Fe
Nd
Pr
Ce
b
Water Quenched from 500°C
At.% Fe, Nd, Pr, Ce
100
80
60
40
20
0
0
1
2
Position, microns
Fe
Nd
Pr
Ce
XBL 873-1484
c

Fig.III.28

CH 111, Fig. 29(a) XBB874-2618

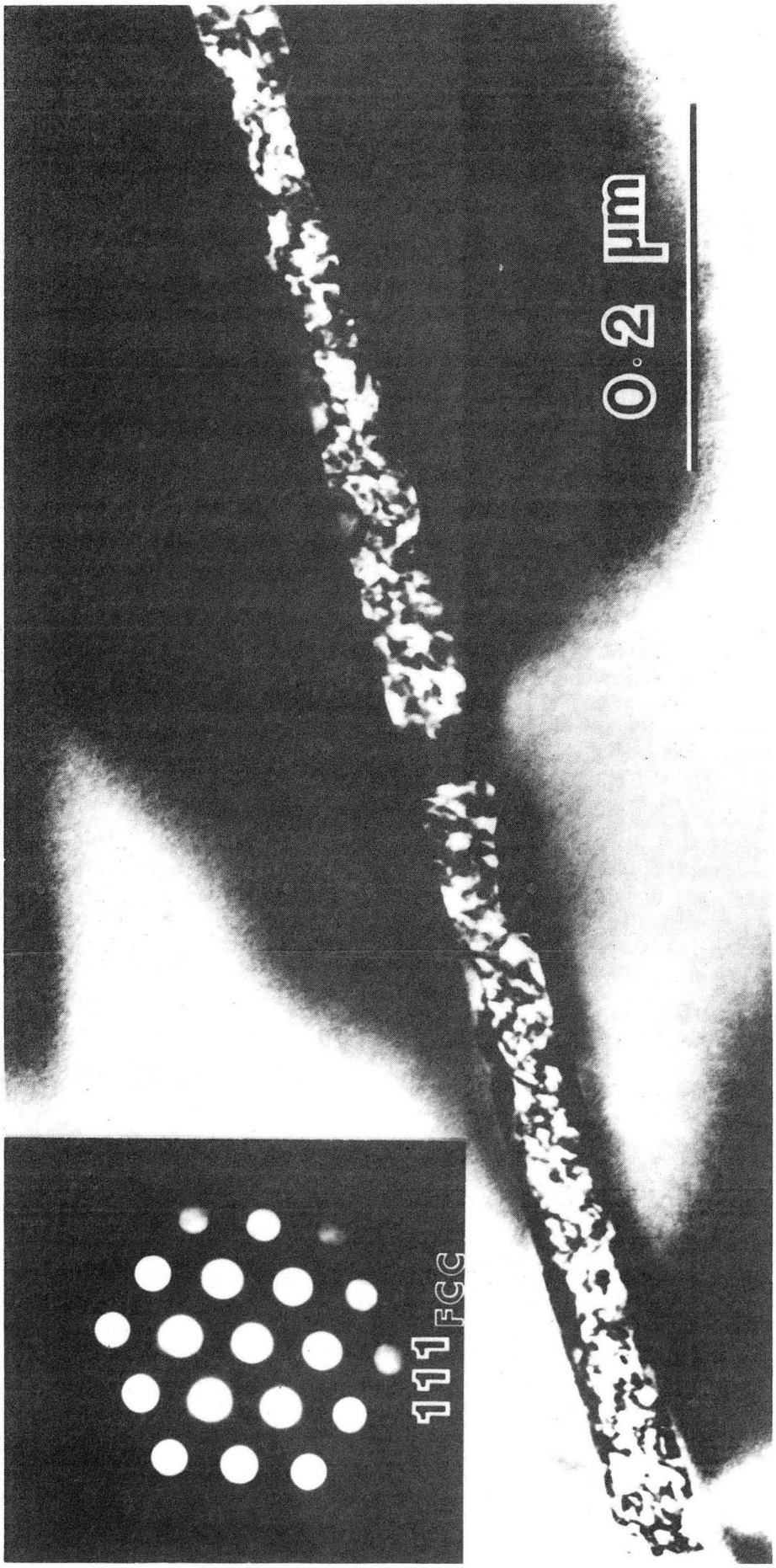

CH. 111, Fig. 29(b), XBB874-2621

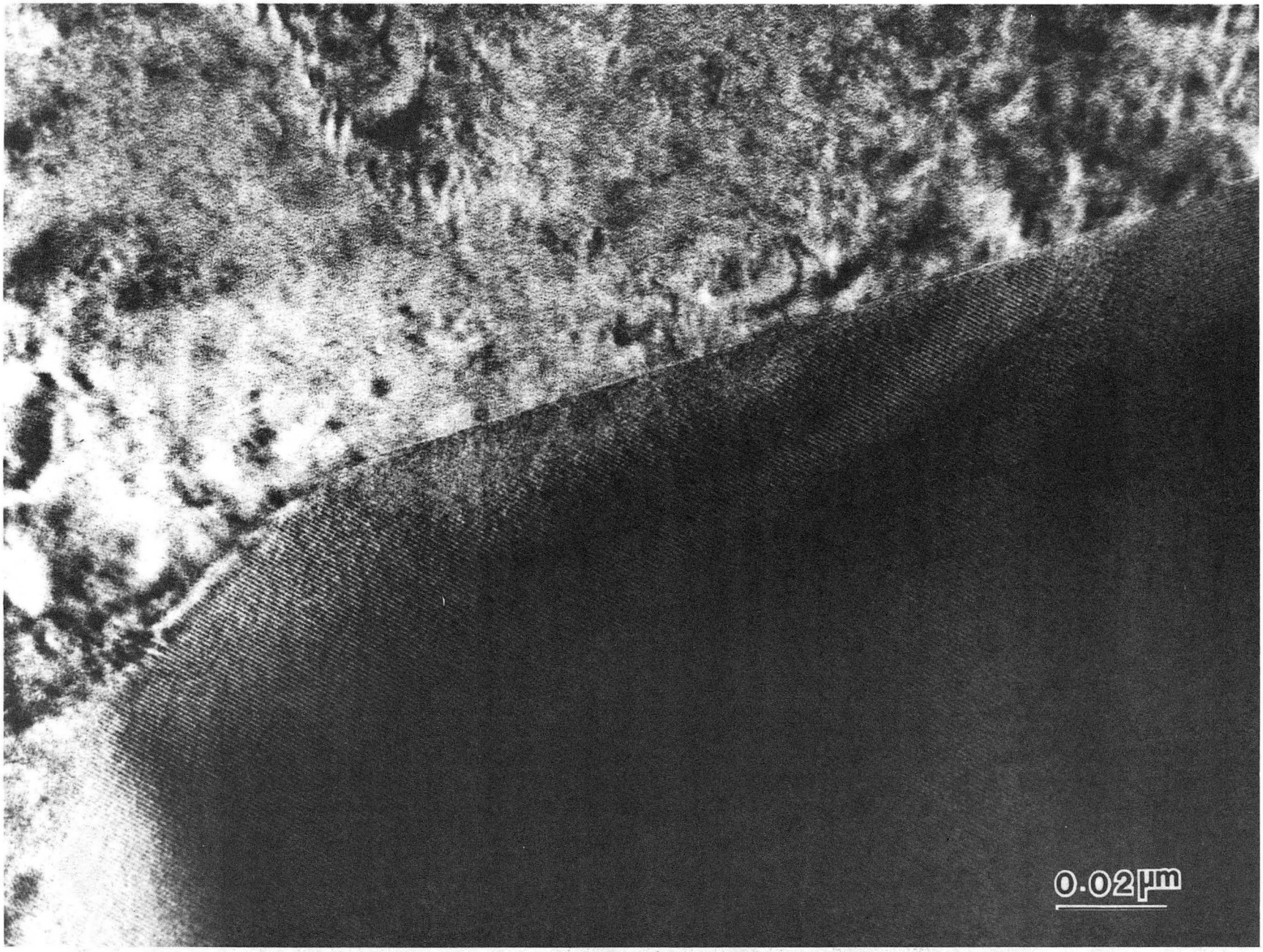

CH. 111, Fig. 30, XBB862-1436

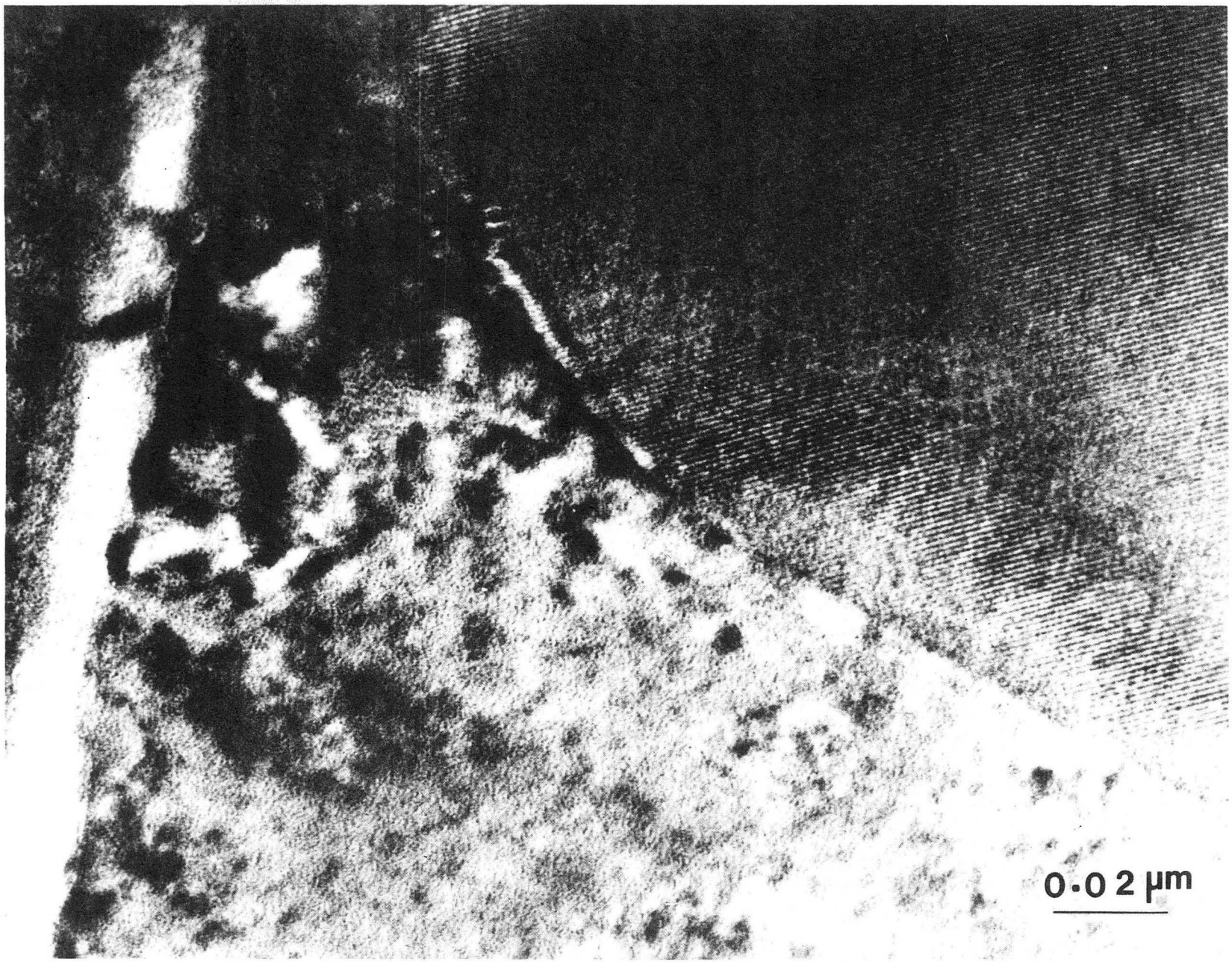

CH. 111, Fig. 31, XBB 862-1435

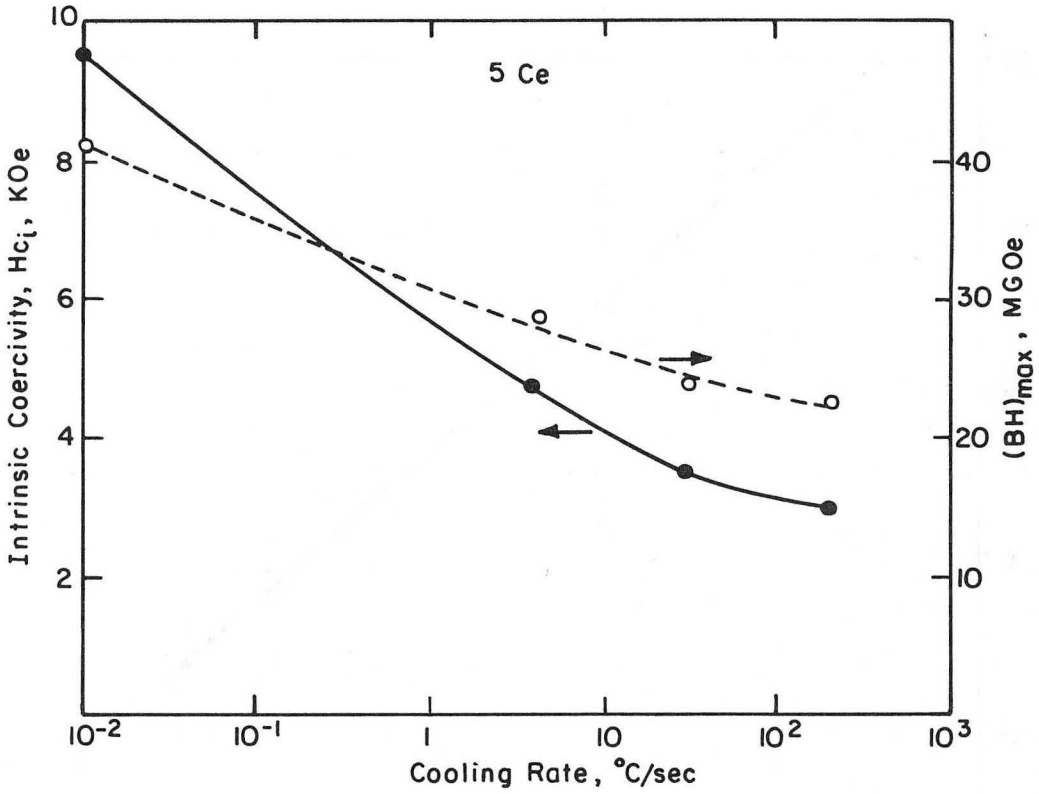

XBL 8510-6759 A

Fig.III.32

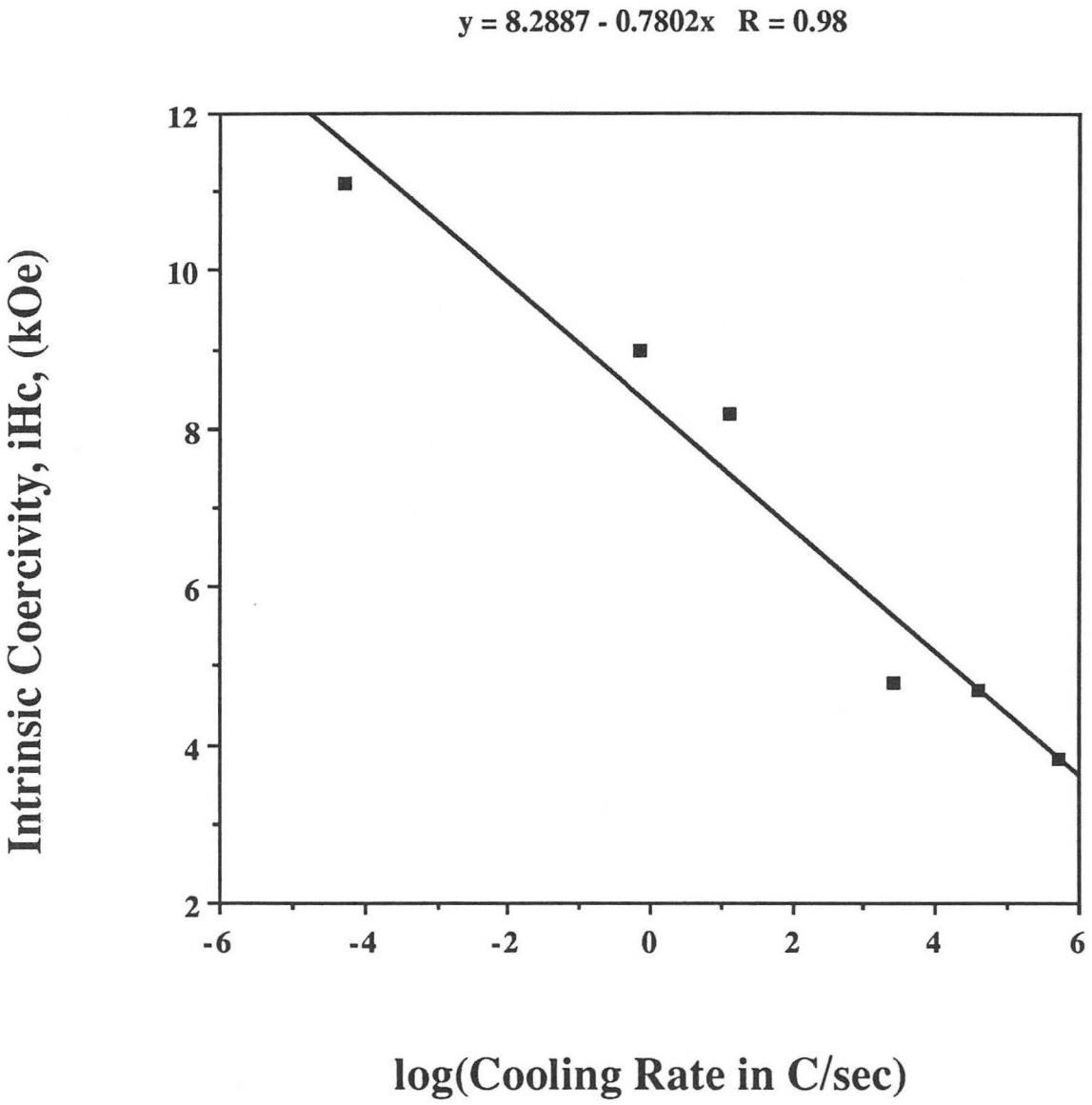

XBL 877-3357

Fig.III.33

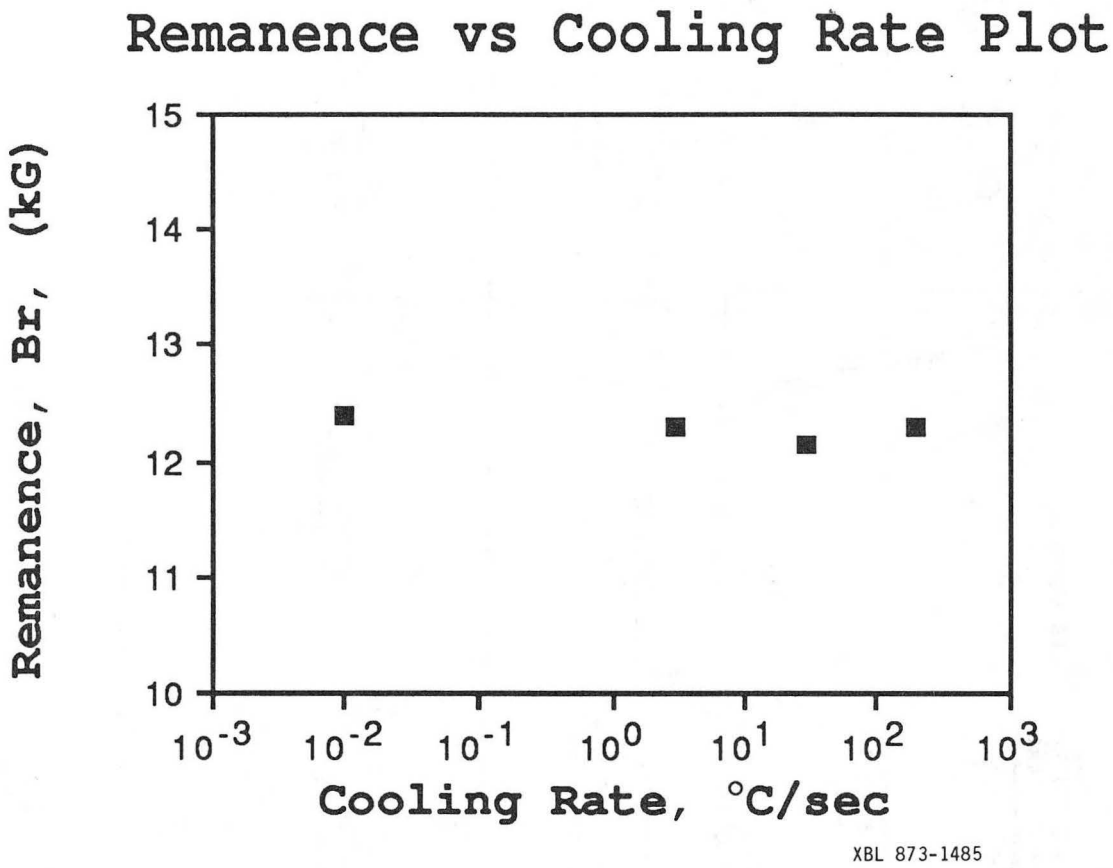
Remanence vs Cooling Rate Plot
Remanence, Br, (kG)
15
14
13
12
11
10
10-3
10-2
10-1
100
101
102
103
Cooling Rate, °C/sec
XBL 873-1485

Fig.III.34

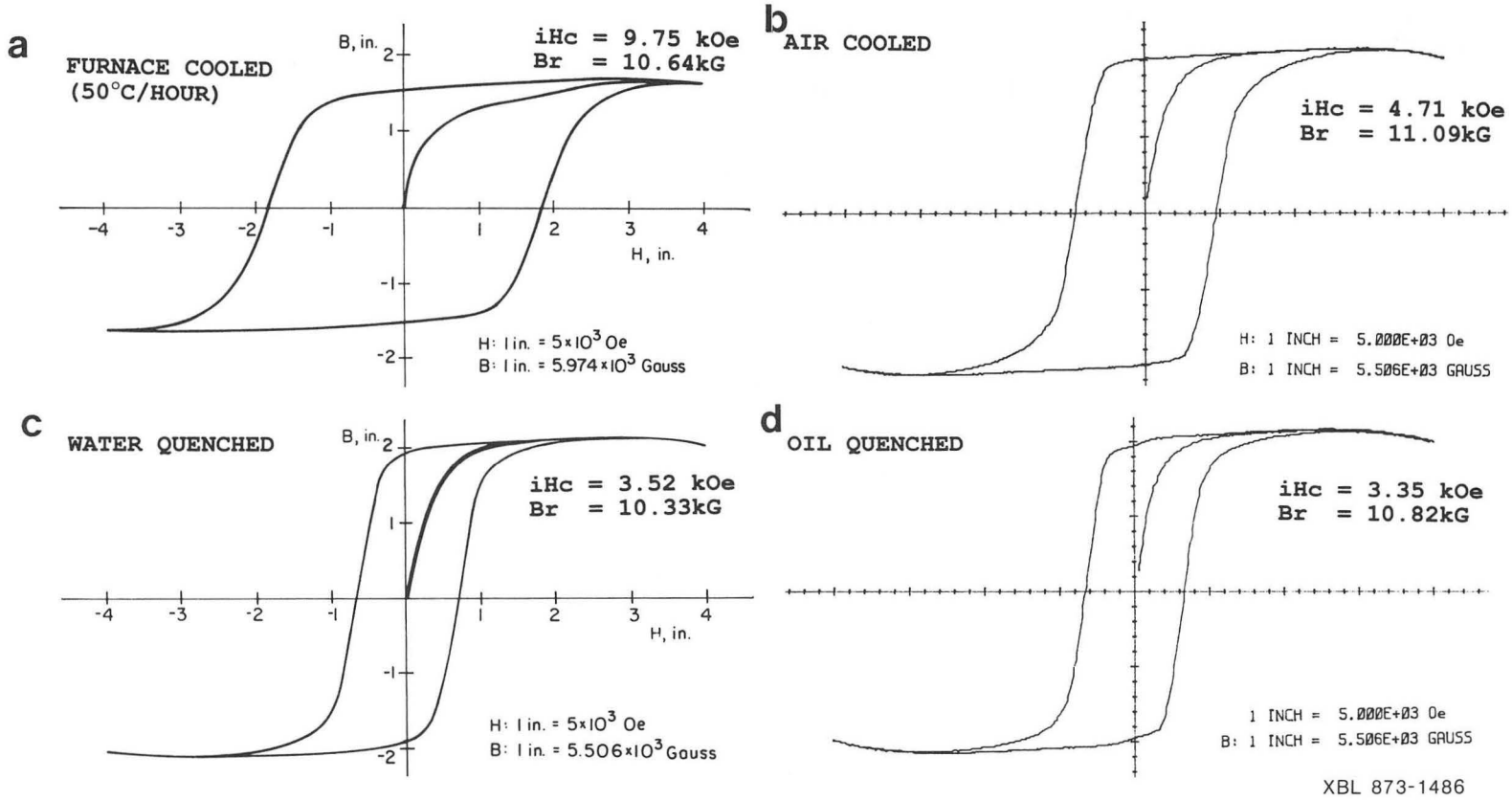
a
FURNACE COOLED
(50°C/HOUR)
B, in.
iHc = 9.75 kOe
Br = 10.64kG
H, in.
H: 1 in. = 5×10³ Oe
B: 1 in. = 5.974×10³ Gauss
b
AIR COOLED
iHc = 4.71 kOe
Br = 11.09kG
H: 1 INCH = 5.000E+03 Oe
B: 1 INCH = 5.506E+03 GAUSS
c
WATER QUENCHED
B, in.
iHc = 3.52 kOe
Br = 10.33kG
H, in.
H: 1 in. = 5×10³ Oe
B: 1 in. = 5.506×10³ Gauss
d
OIL QUENCHED
iHc = 3.35 kOe
Br = 10.82kG
1 INCH = 5.000E+03 Oe
B: 1 INCH = 5.506E+03 GAUSS
XBL 873-1486

Fig.III.35

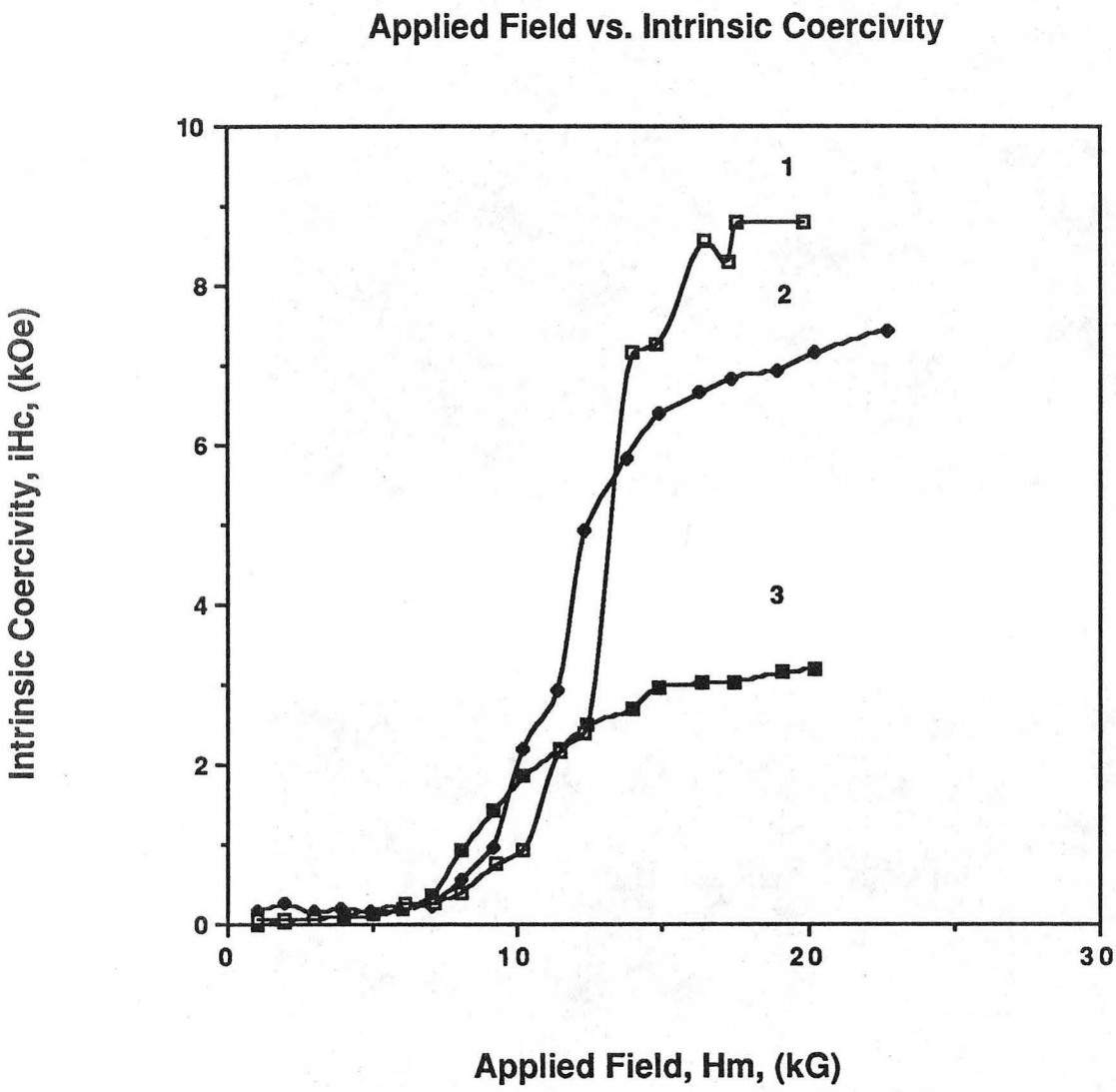

Fig.III.35(e)

— XBL 877-3392

a

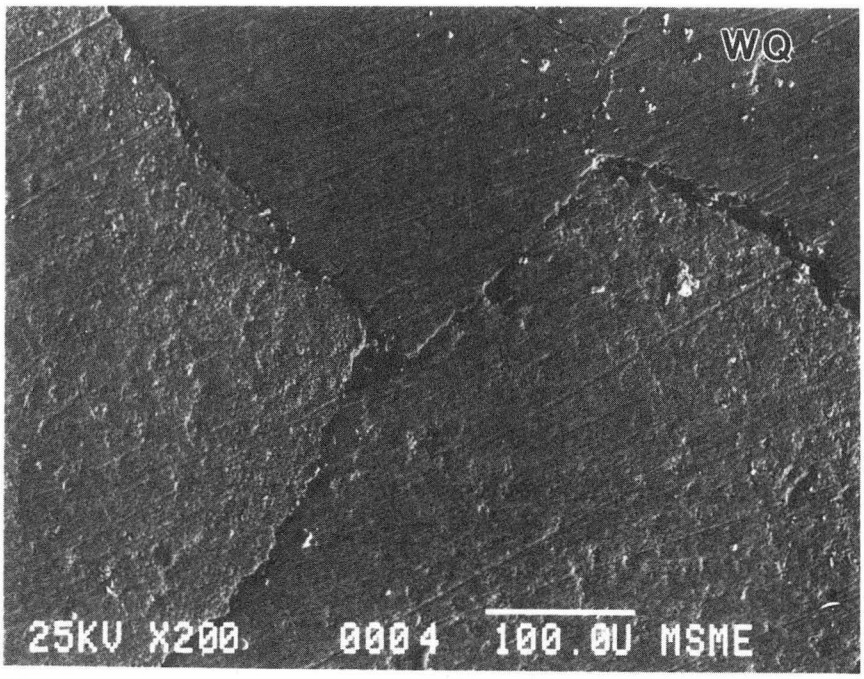

b

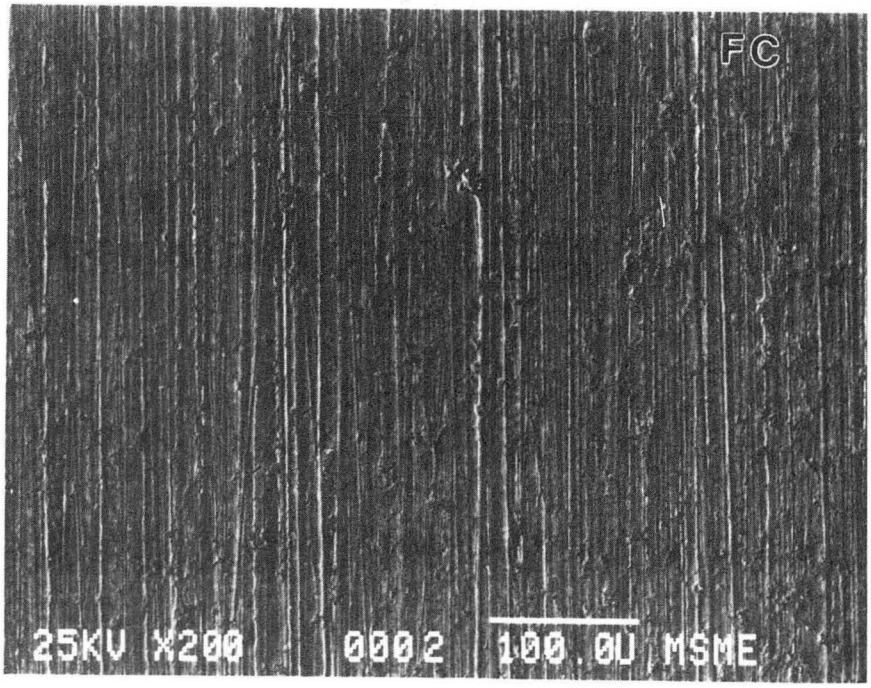

CH. 111, Fig. 36, XBB 874-2629

a

b

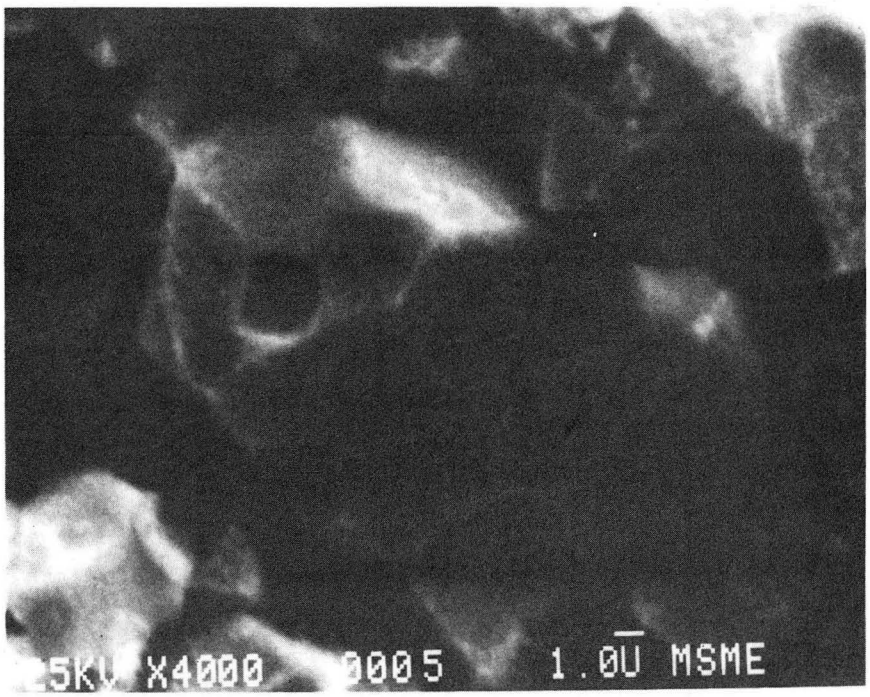

CH. 111, Fig. 37, XBB876-4484

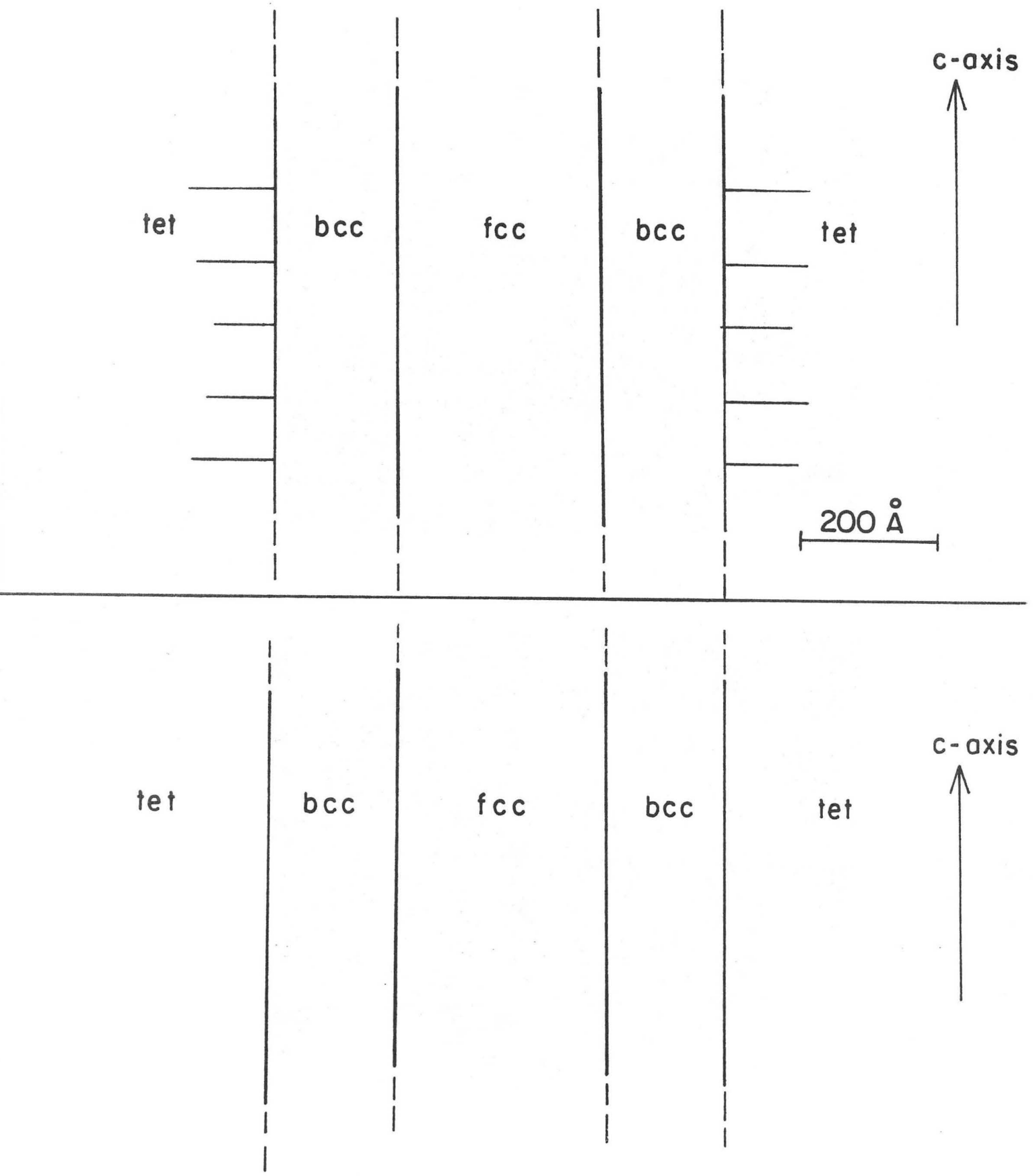

Fig.III.38

XBL8512-6868

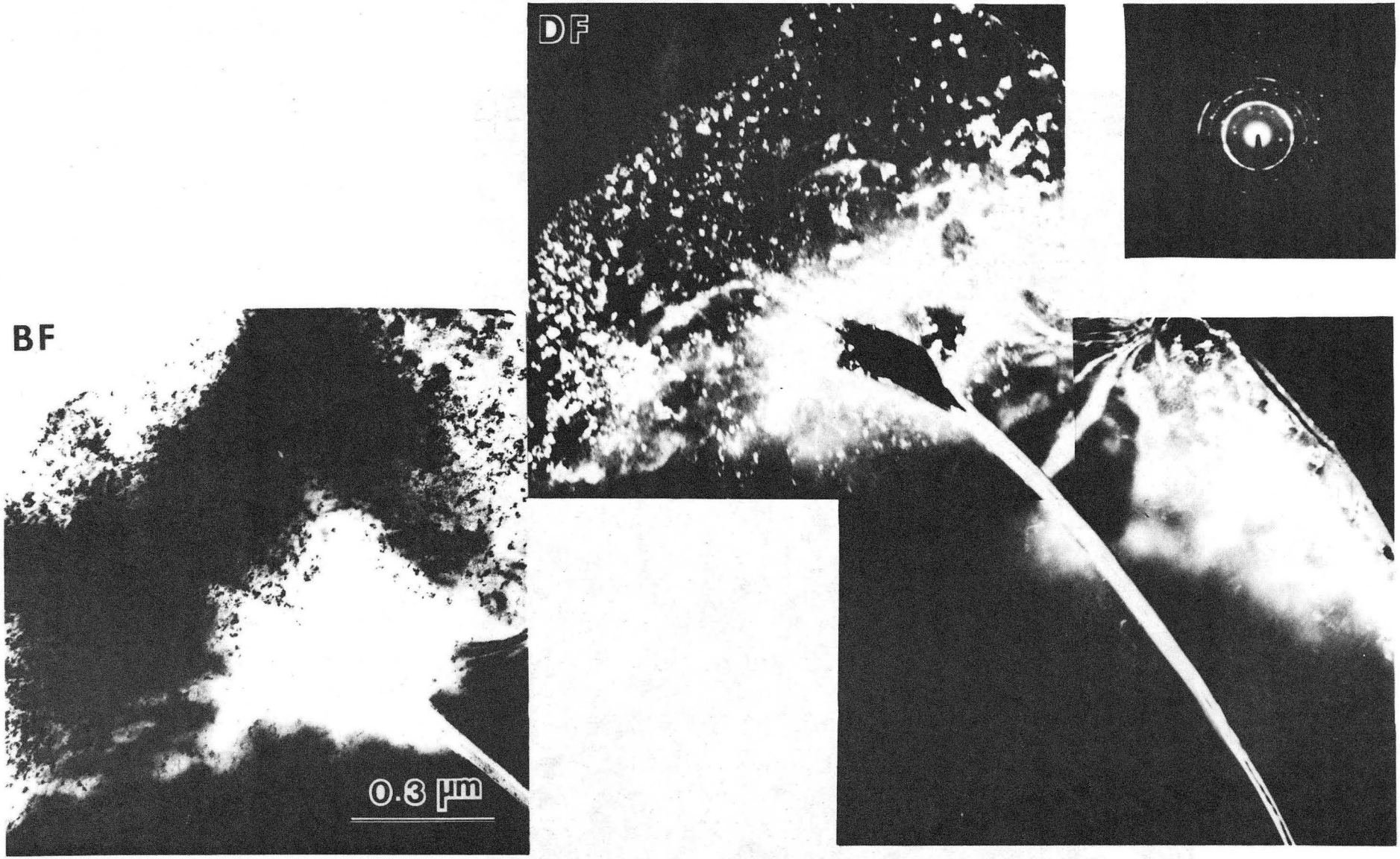

CH. 111, Fig. 39, XBB 876-4485

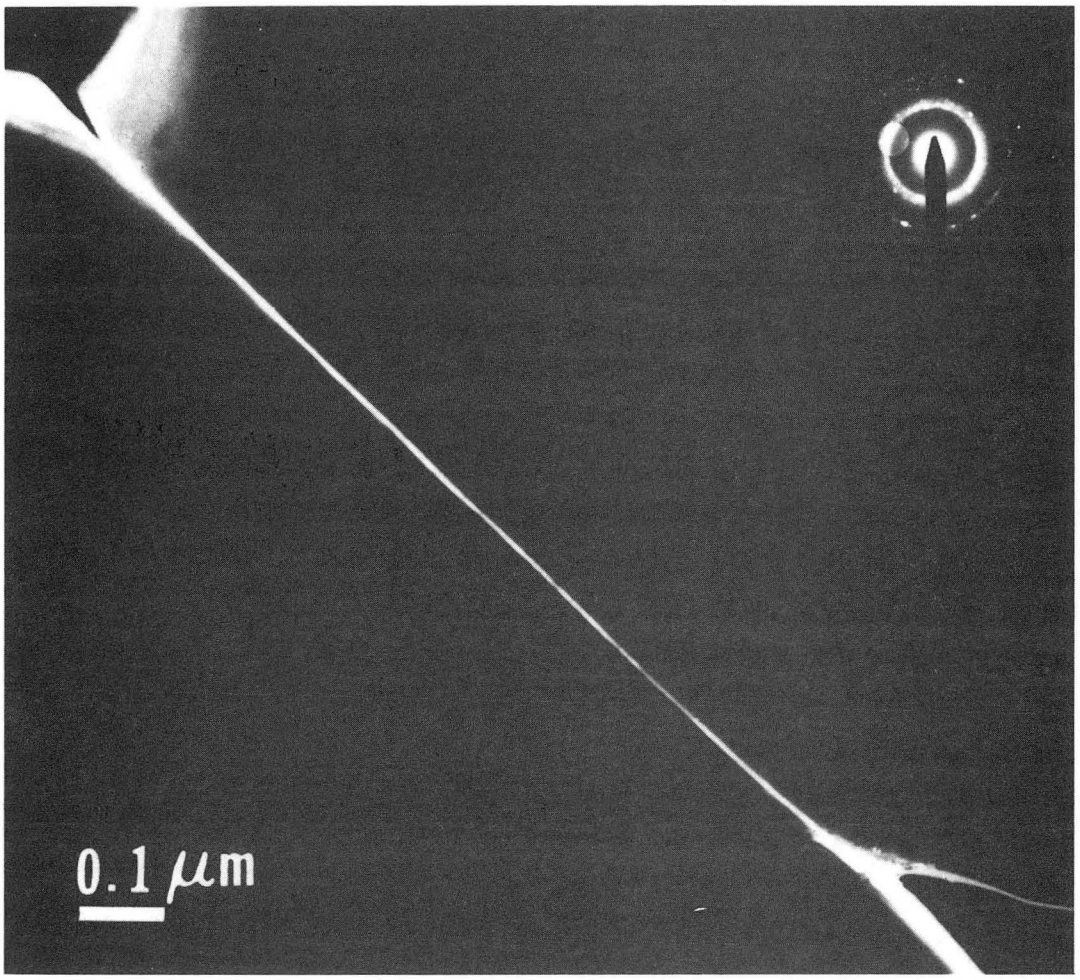

CH. 111, Fig. 40, XBB865-4343

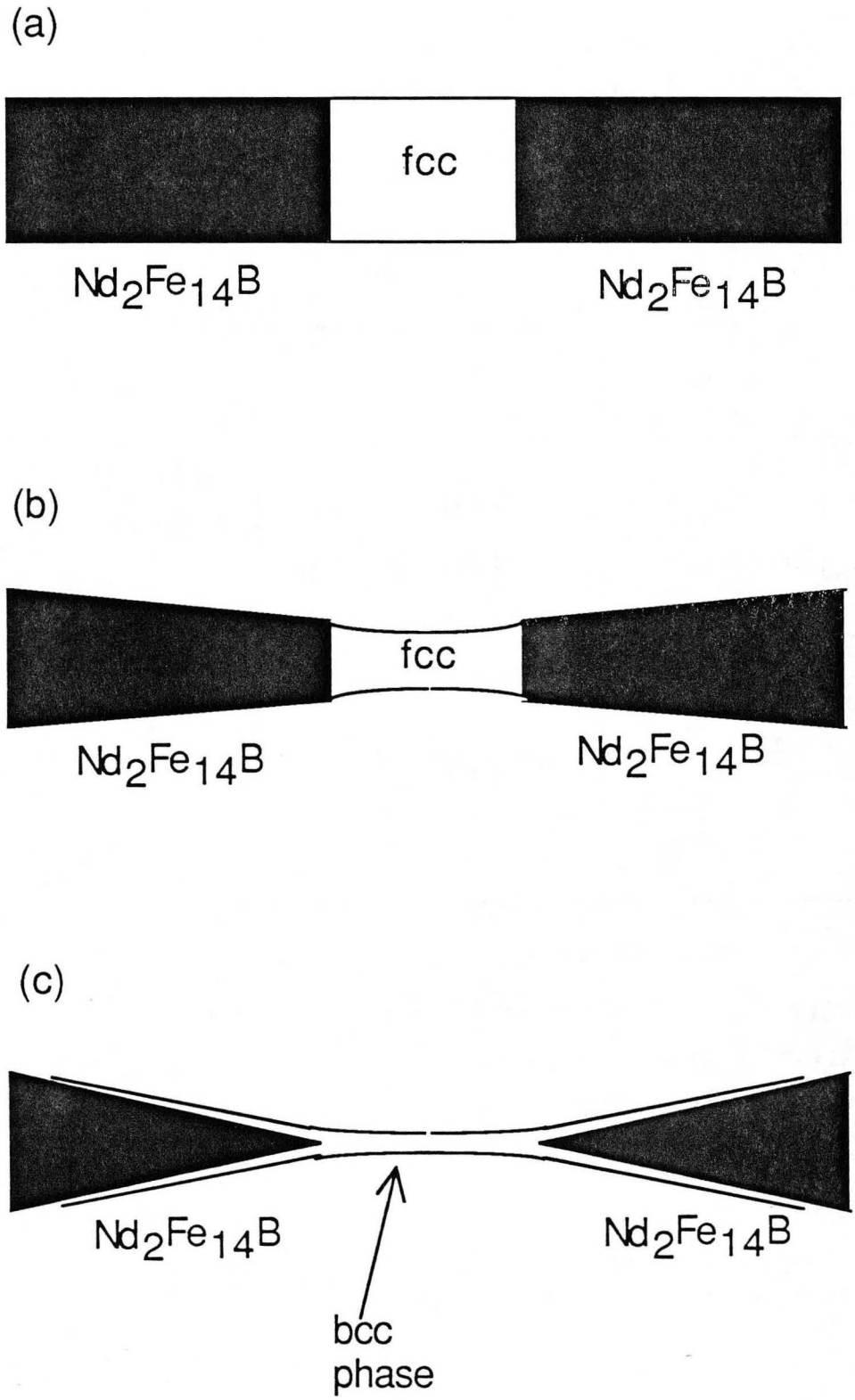

XBL 868-3206

Fig.III.41

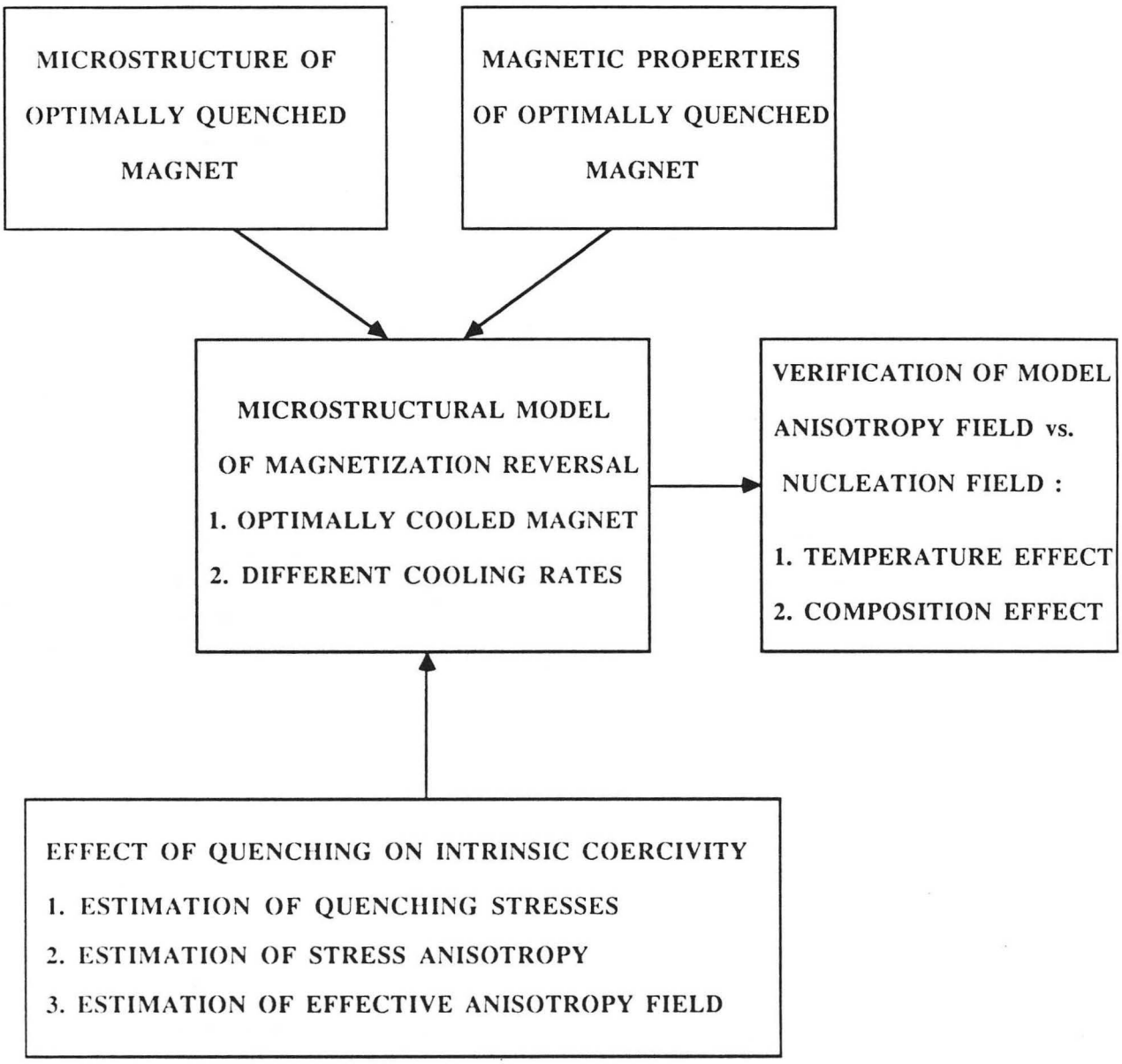

Fig.III.42

XBL 877-3387

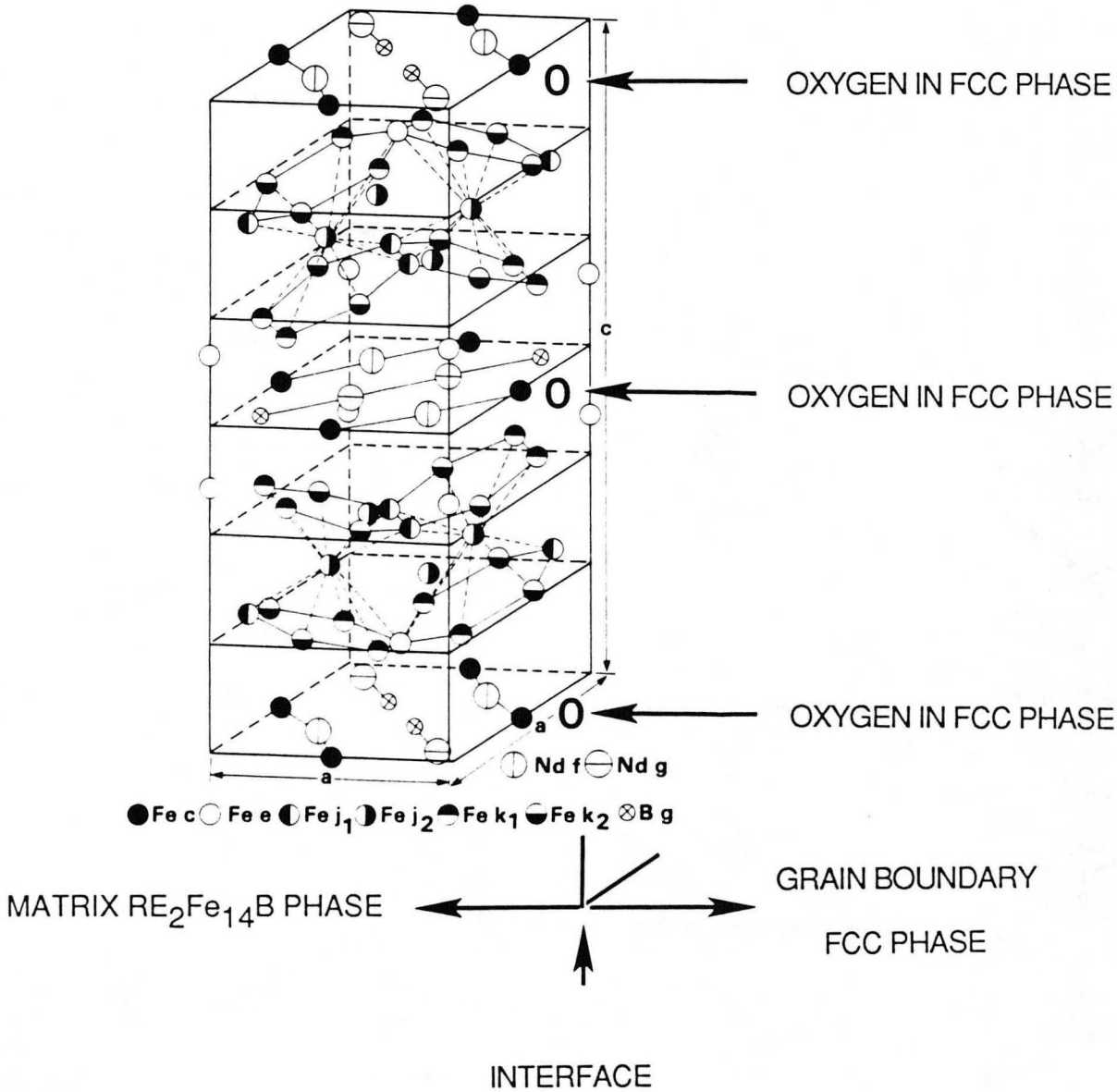

XBL 877-3362

Fig.III.43

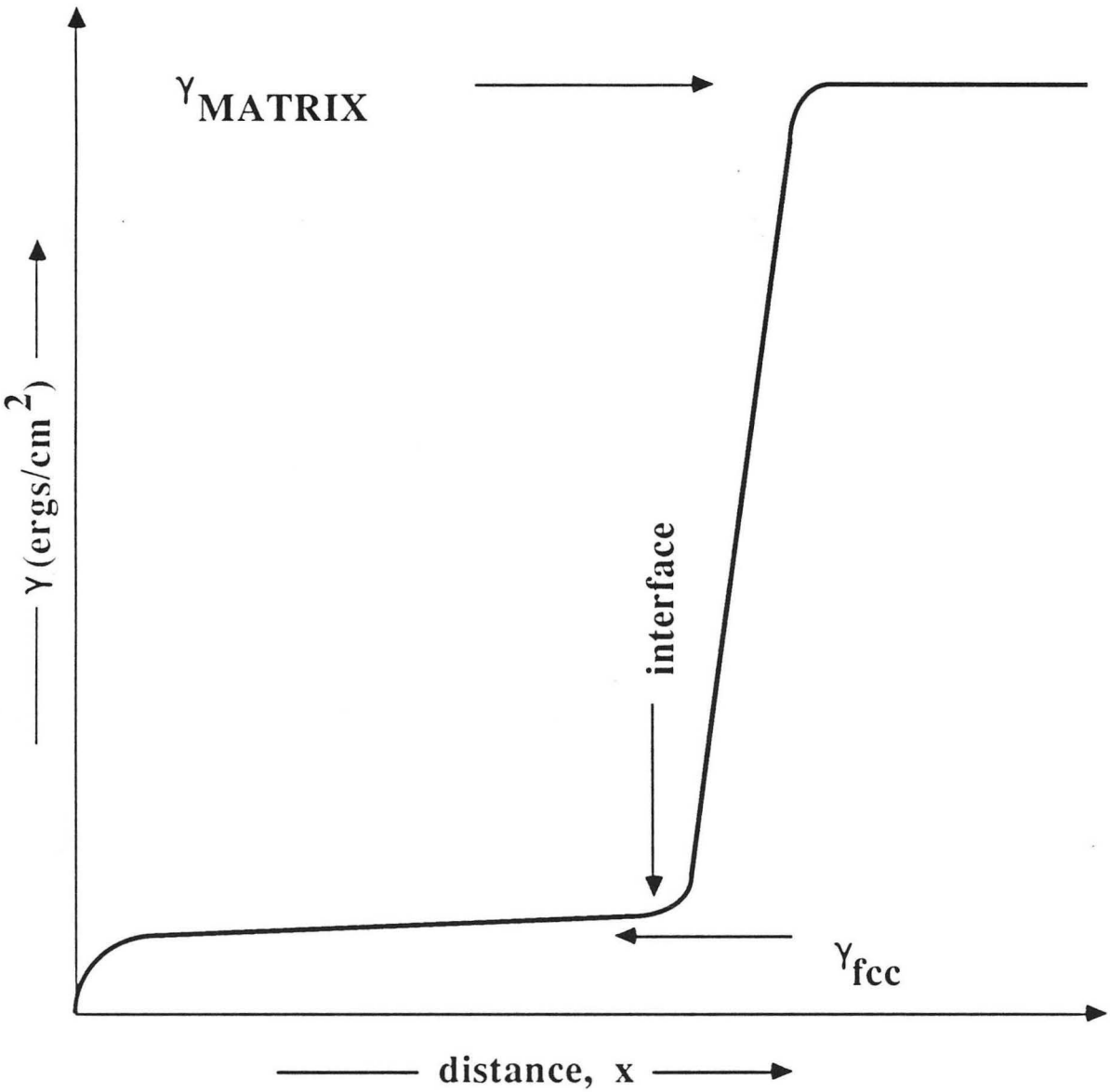

XBL 877-3384

Fig.III.44

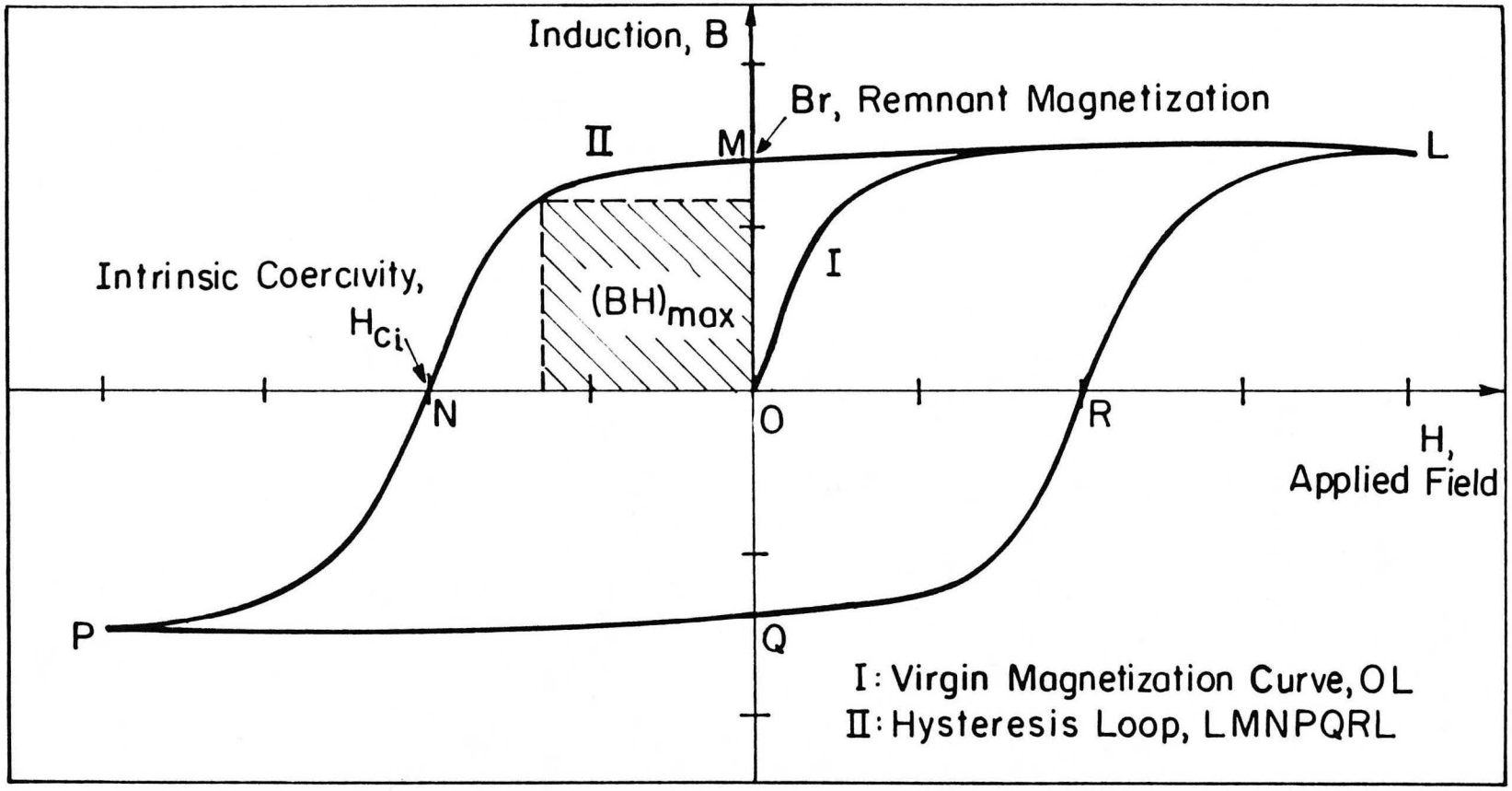

XBL8512-6870

Fig.III.45

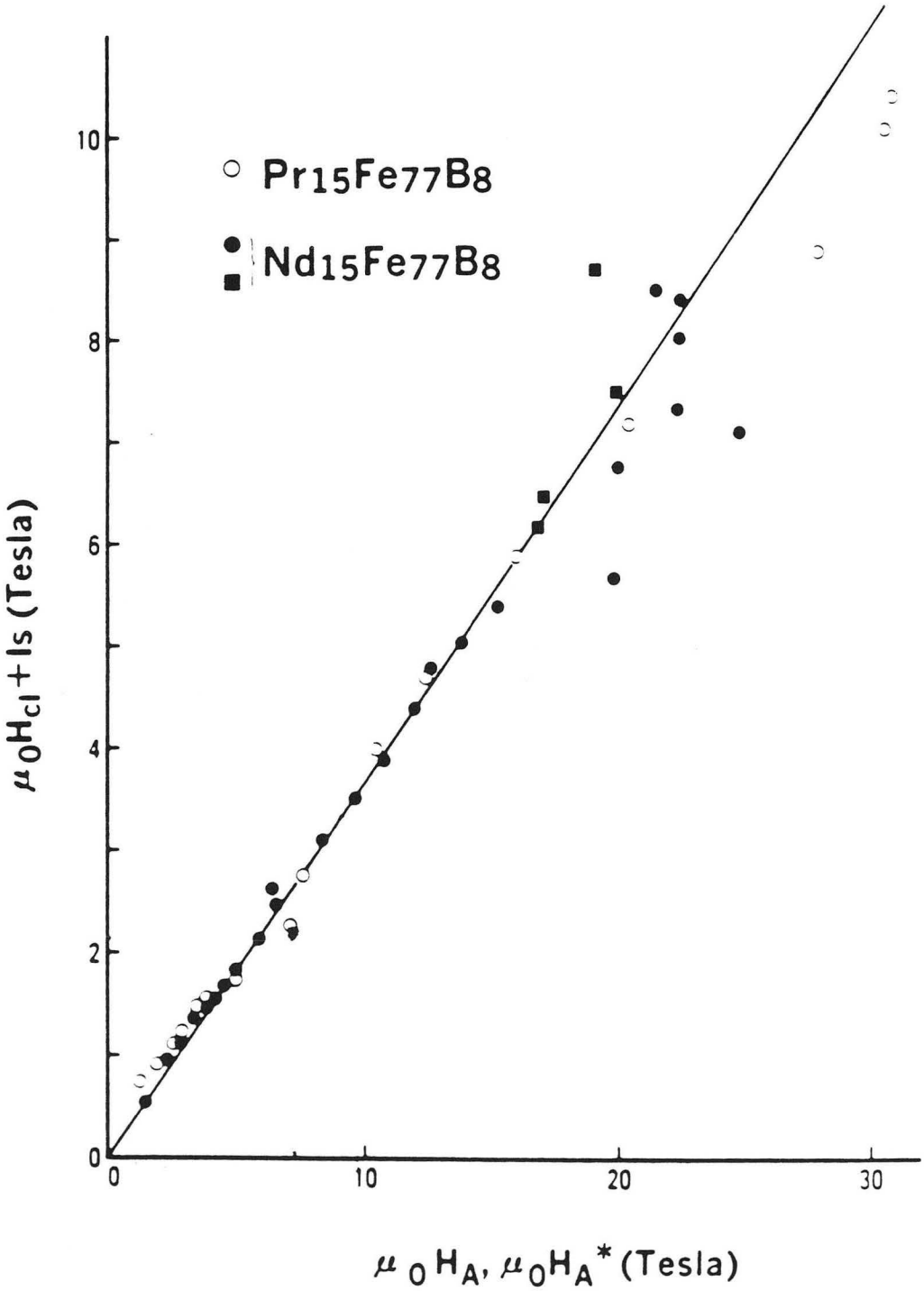

XBL 877-3222

Fig.III.46

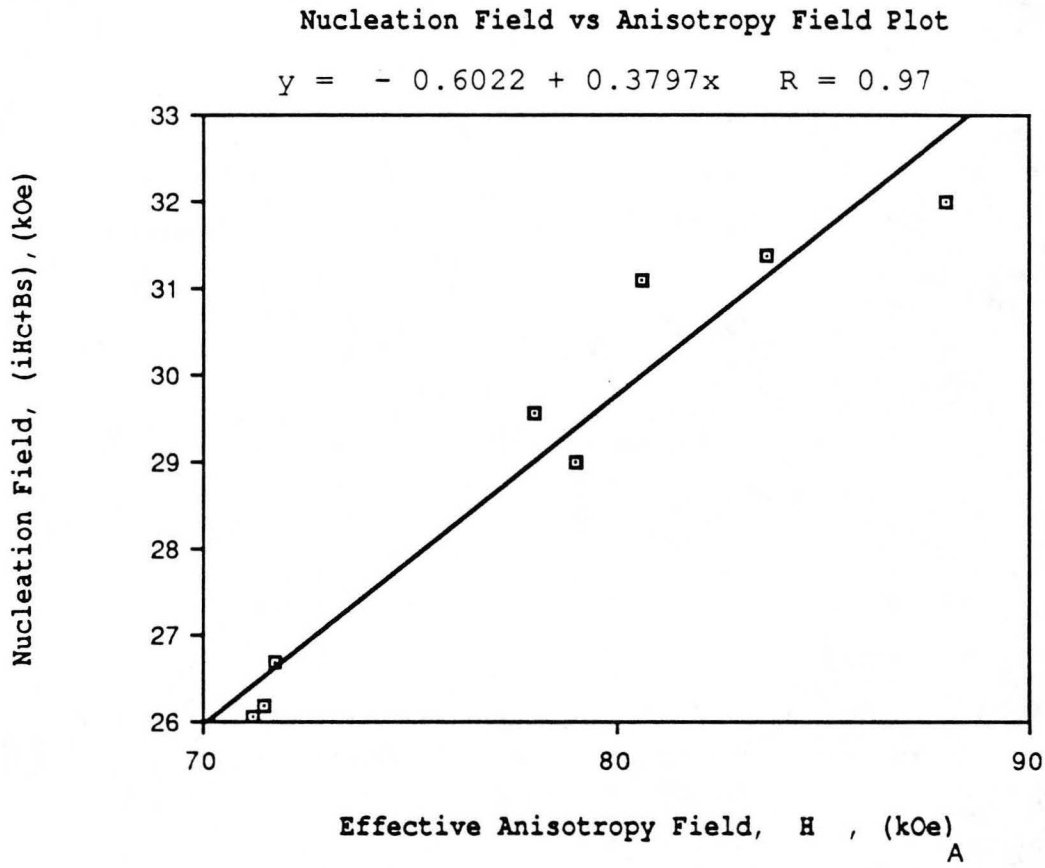

XBL 873-1413

Fig.III.47

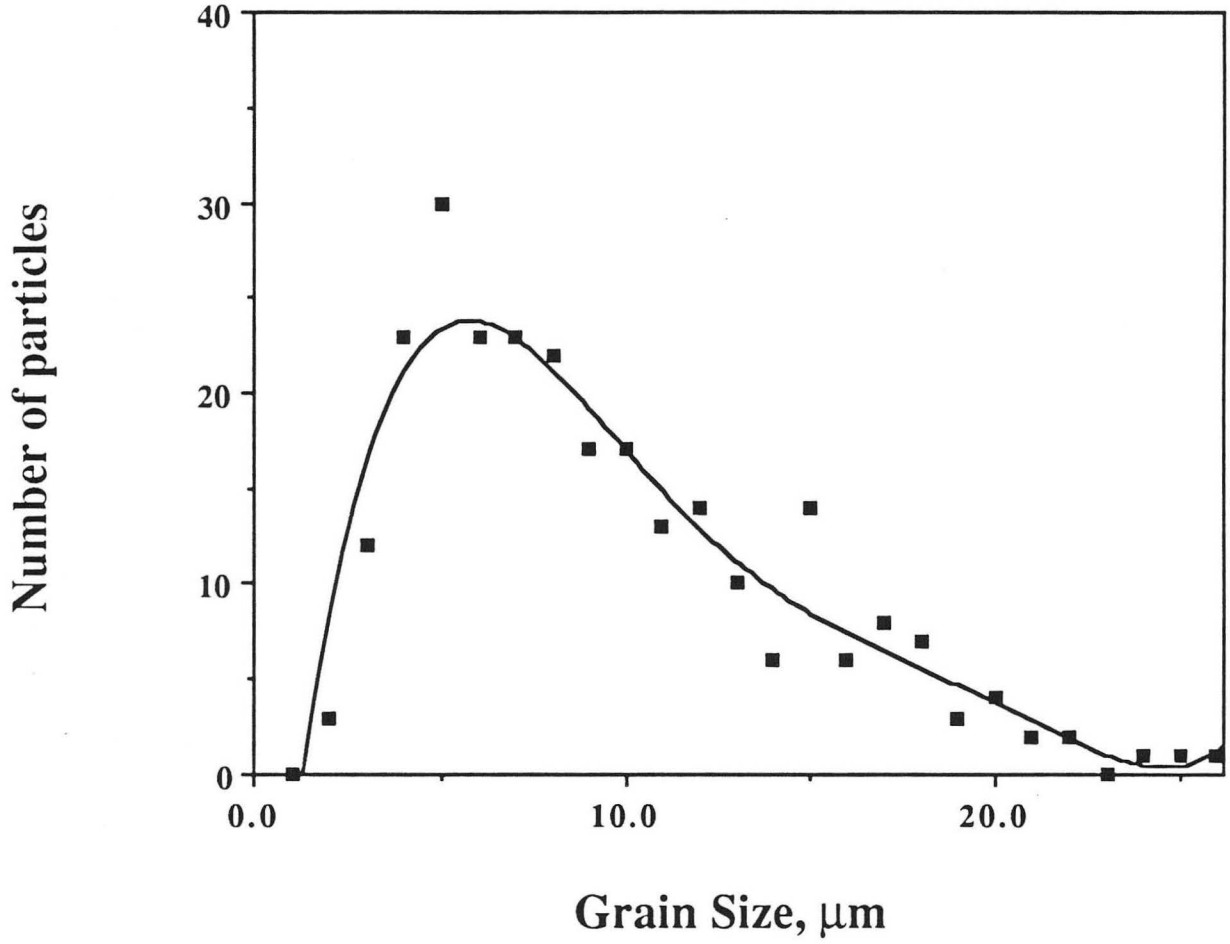

XBL 877-3382

Fig.III.48

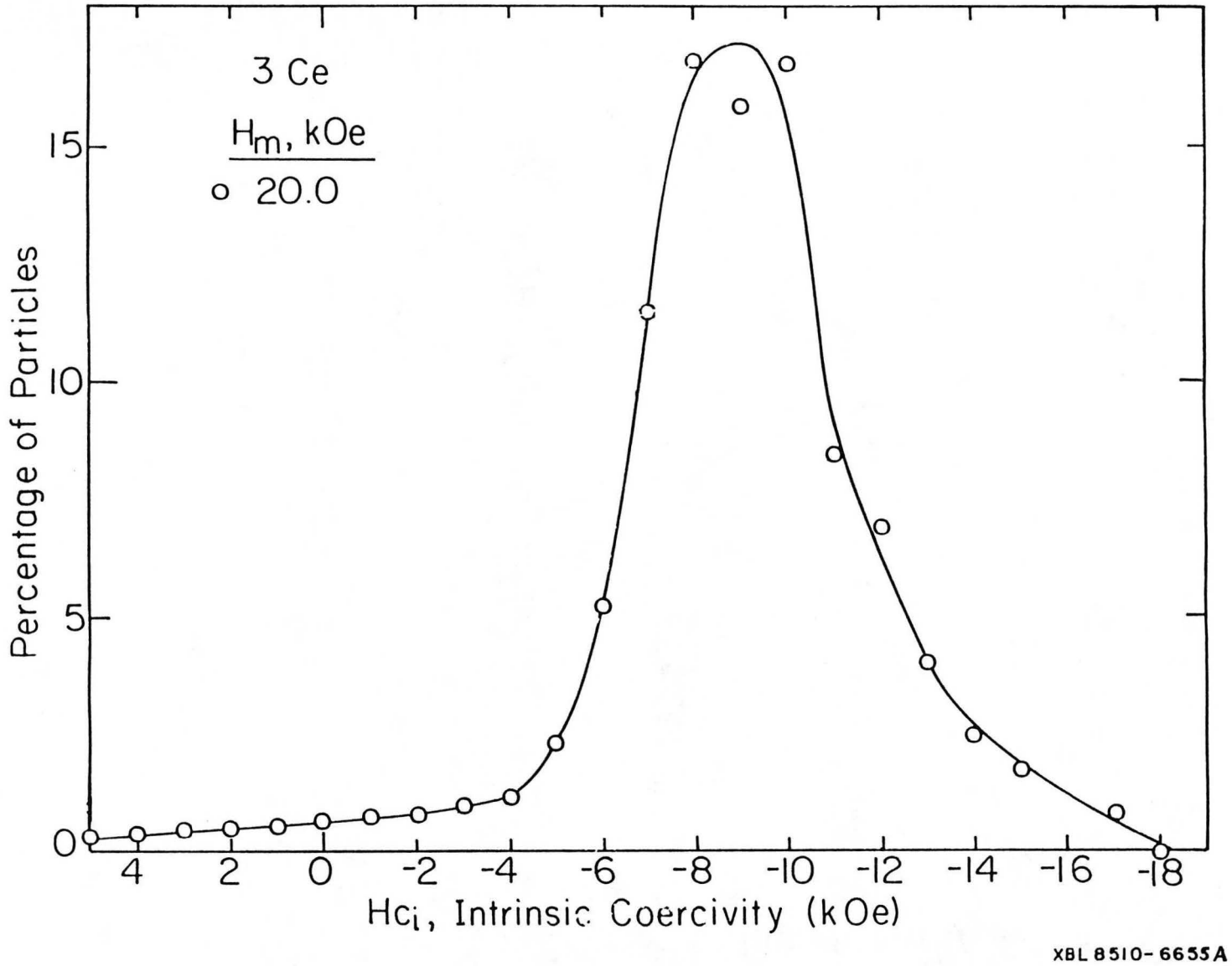
3 Ce
Hm, kOe
o 20.0
Percentage of Particles
0
5
10
15
4
2
0
-2
-4
-6
-8
-10
-12
-14
-16
-18
Hci, Intrinsic Coercivity (kOe)
XBL 8510-6655A

Fig.III.49

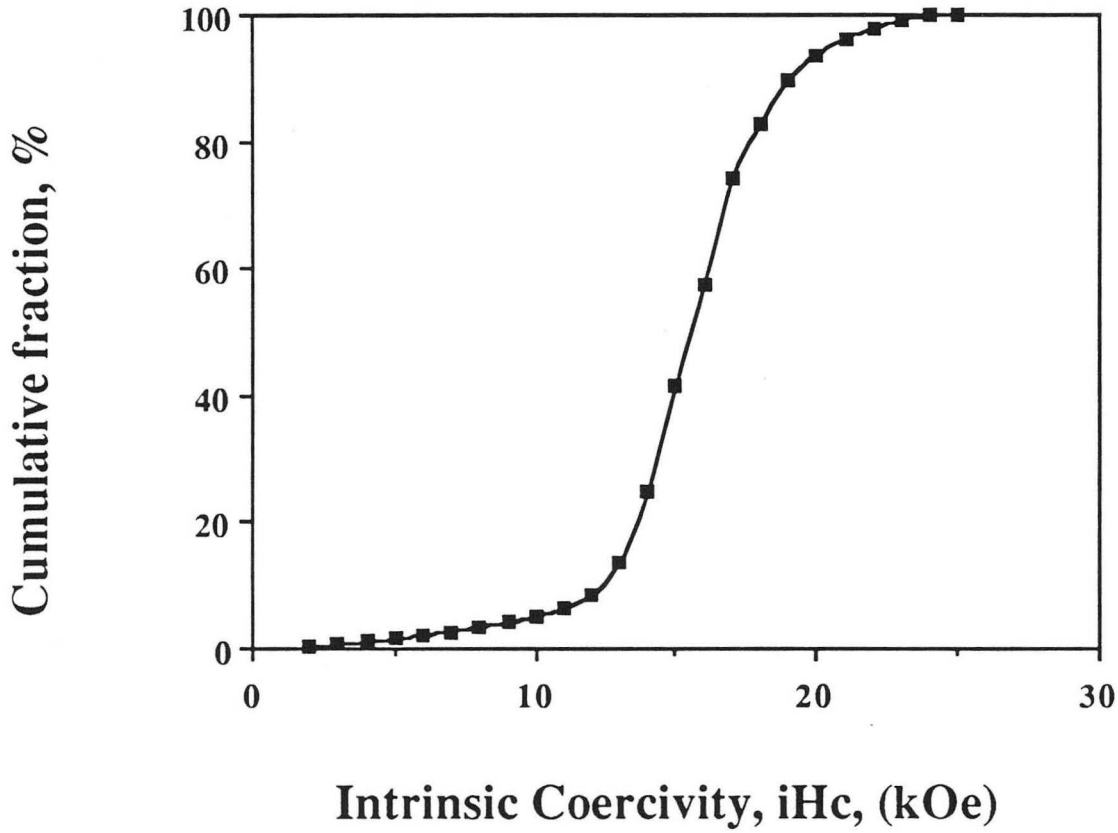

XBL 877-3360

Fig.III.50

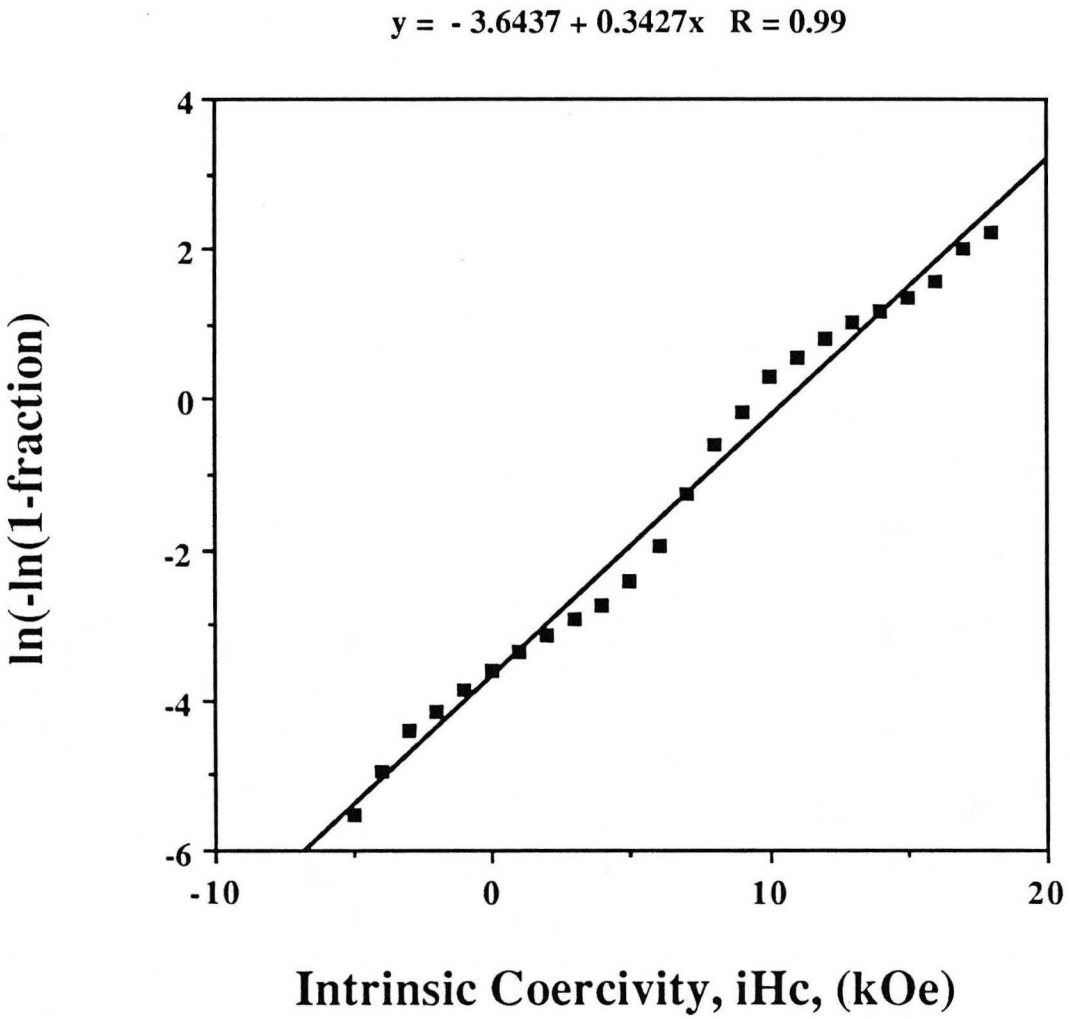

XBL 877-3359

Fig.III.51

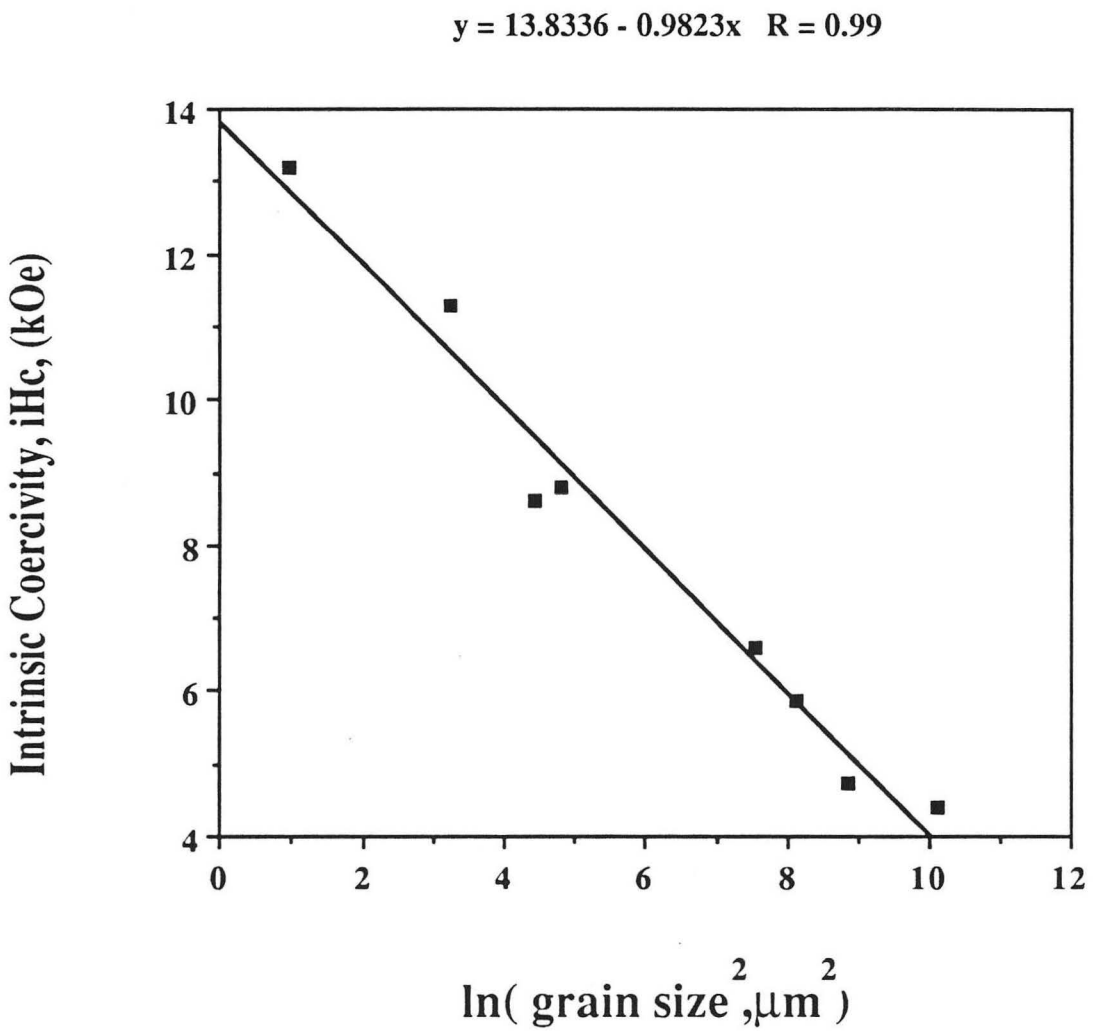

XBL 877-3385

Fig.III.52

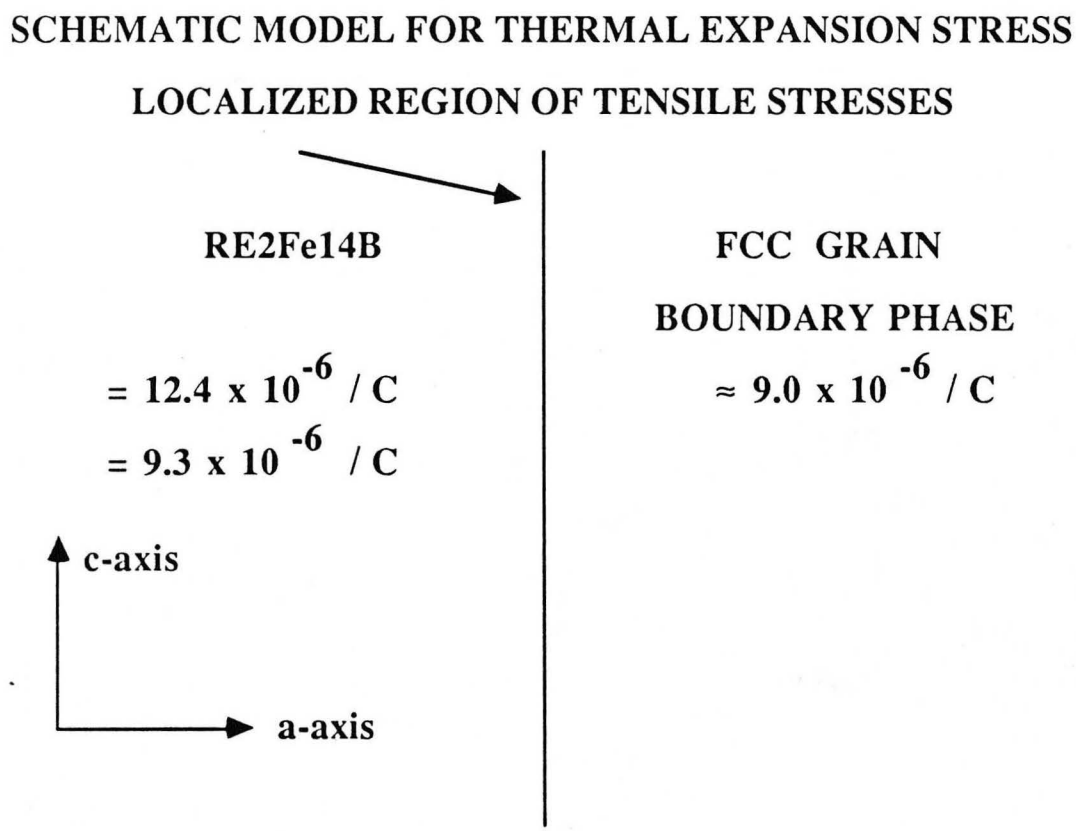

Fig.III.53

XBL 877-3386

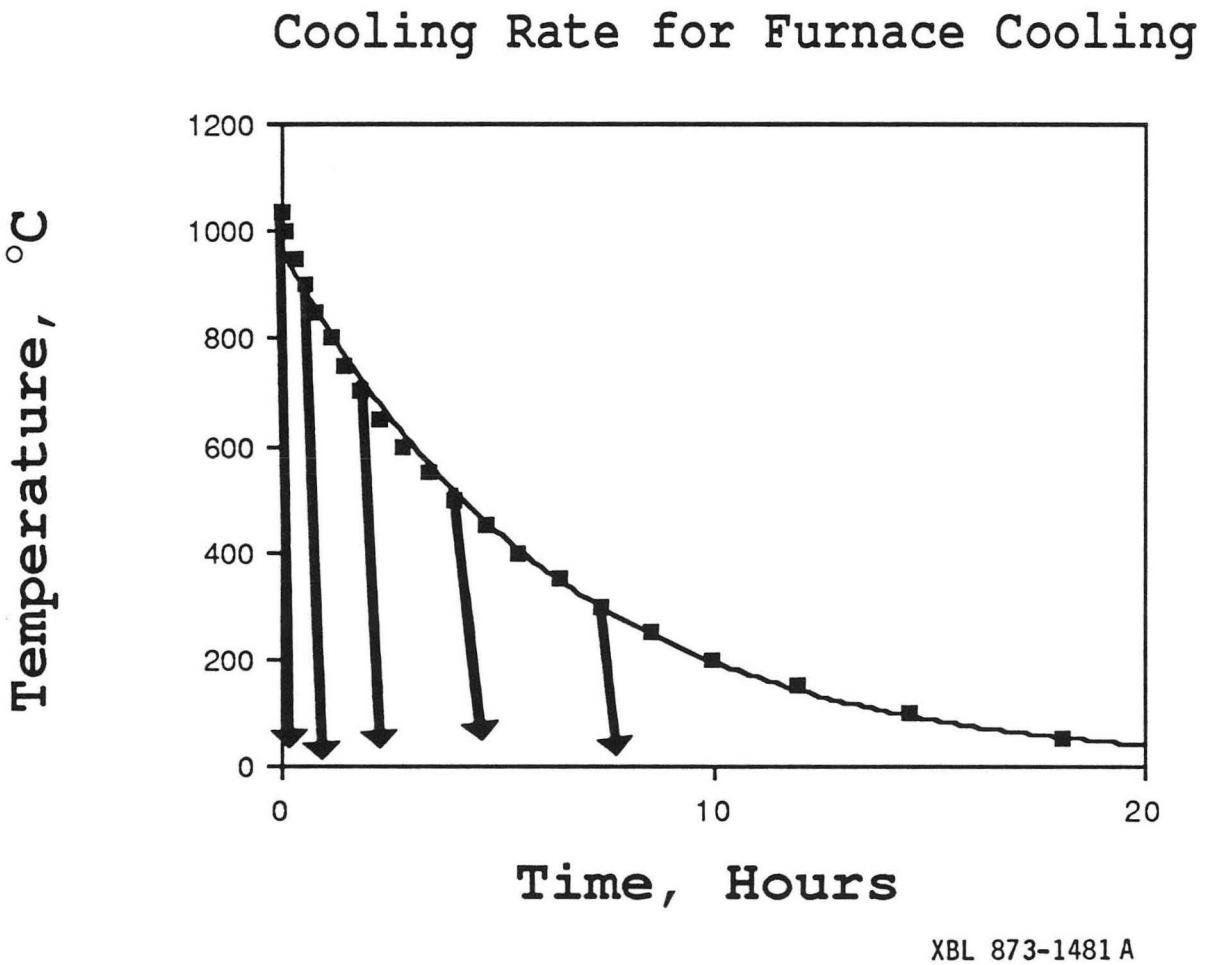
Cooling Rate for Furnace Cooling
Temperature, °C
1200
1000
800
600
400
200
0
0
10
20
Time, Hours
XBL 873-1481 A

Fig.III.54

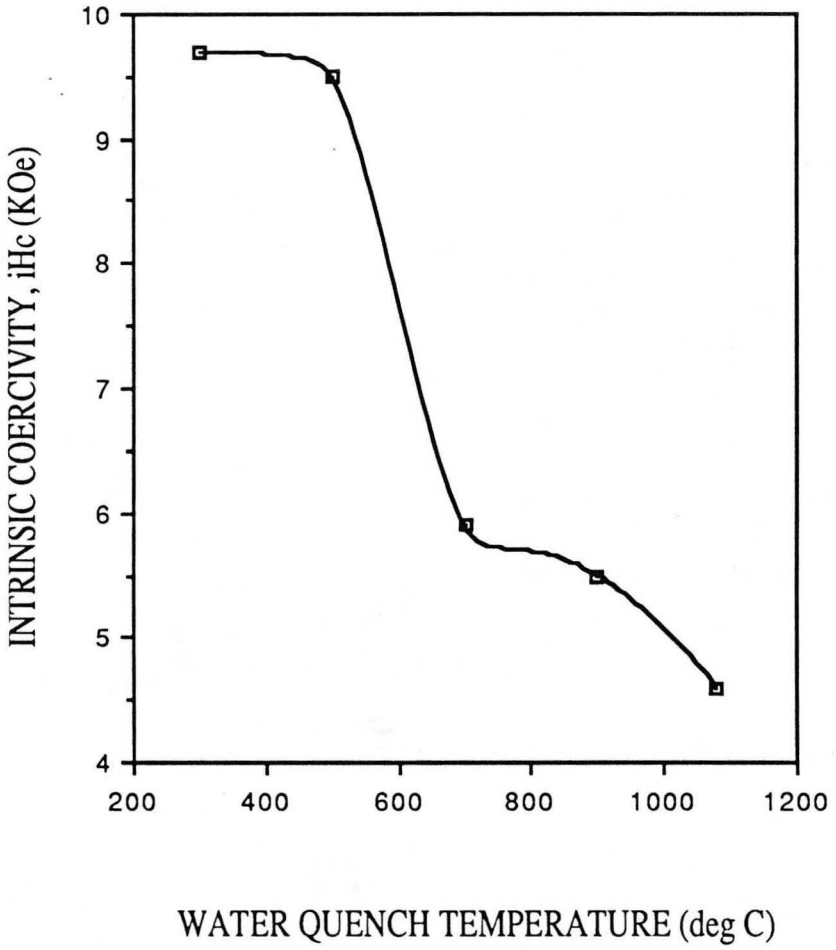

XBL 873-1406

Fig.III.55

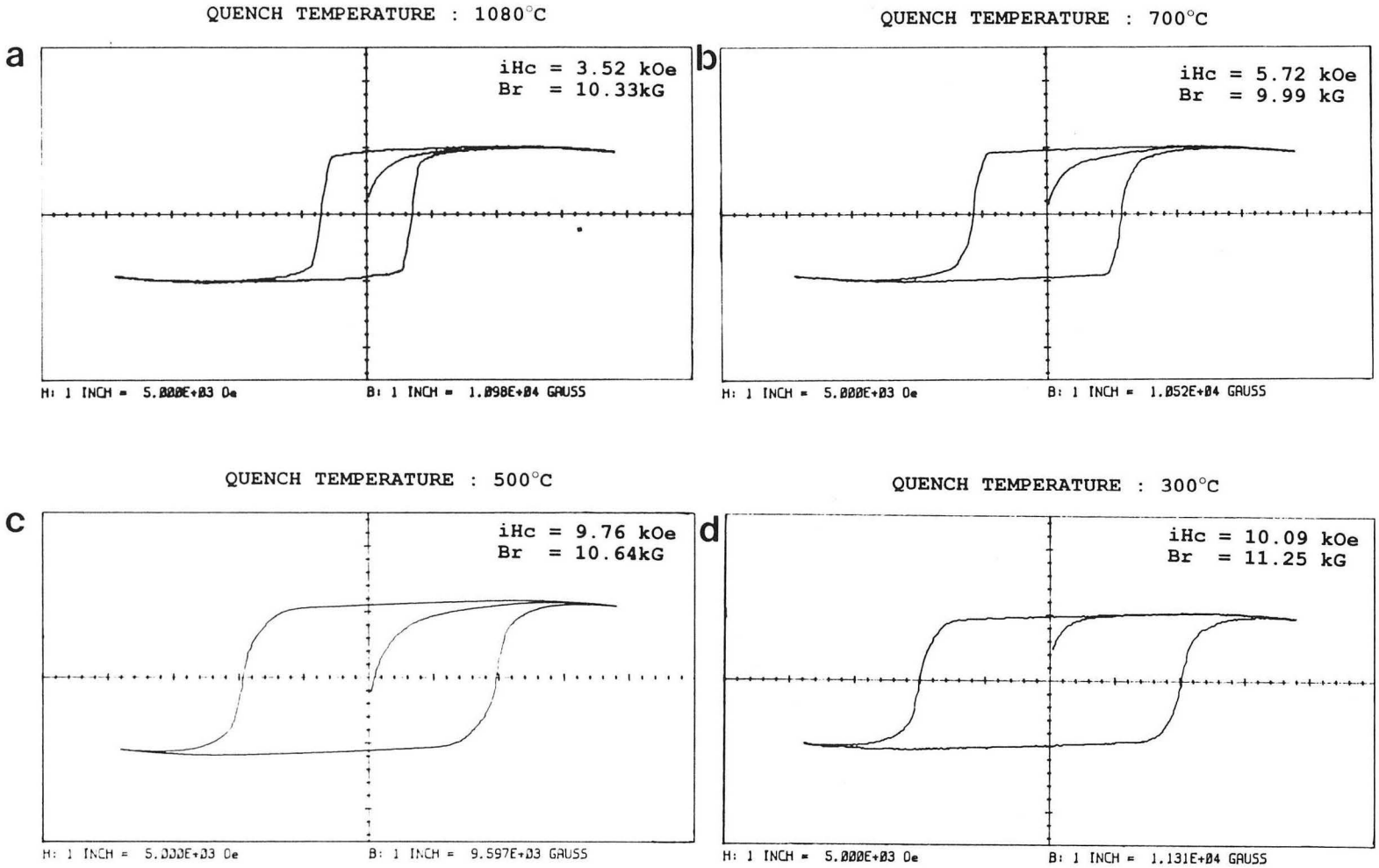

XBL 873-1487

Fig.III.56

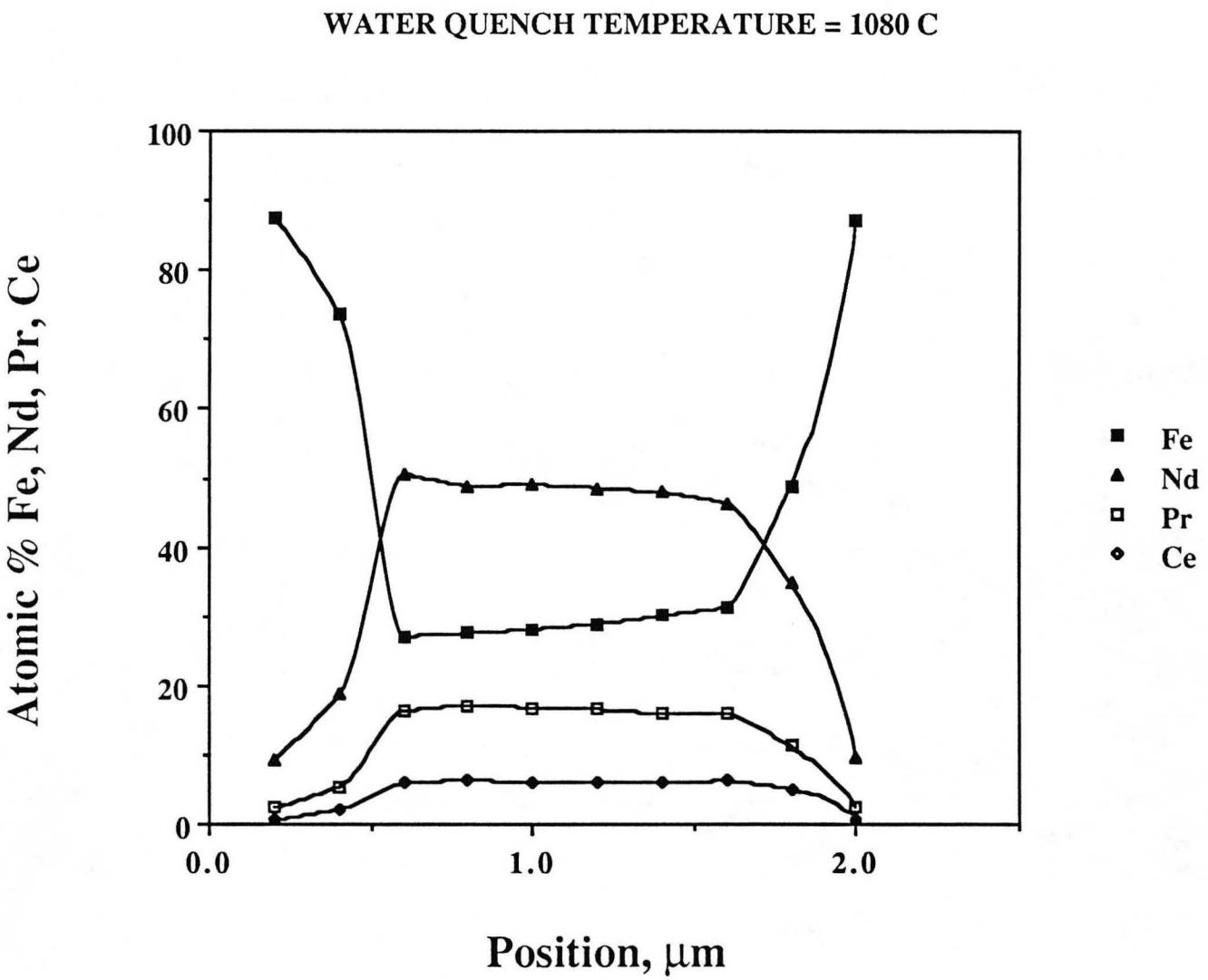

- XBL 877-3397 -

Fig.III.57(a)

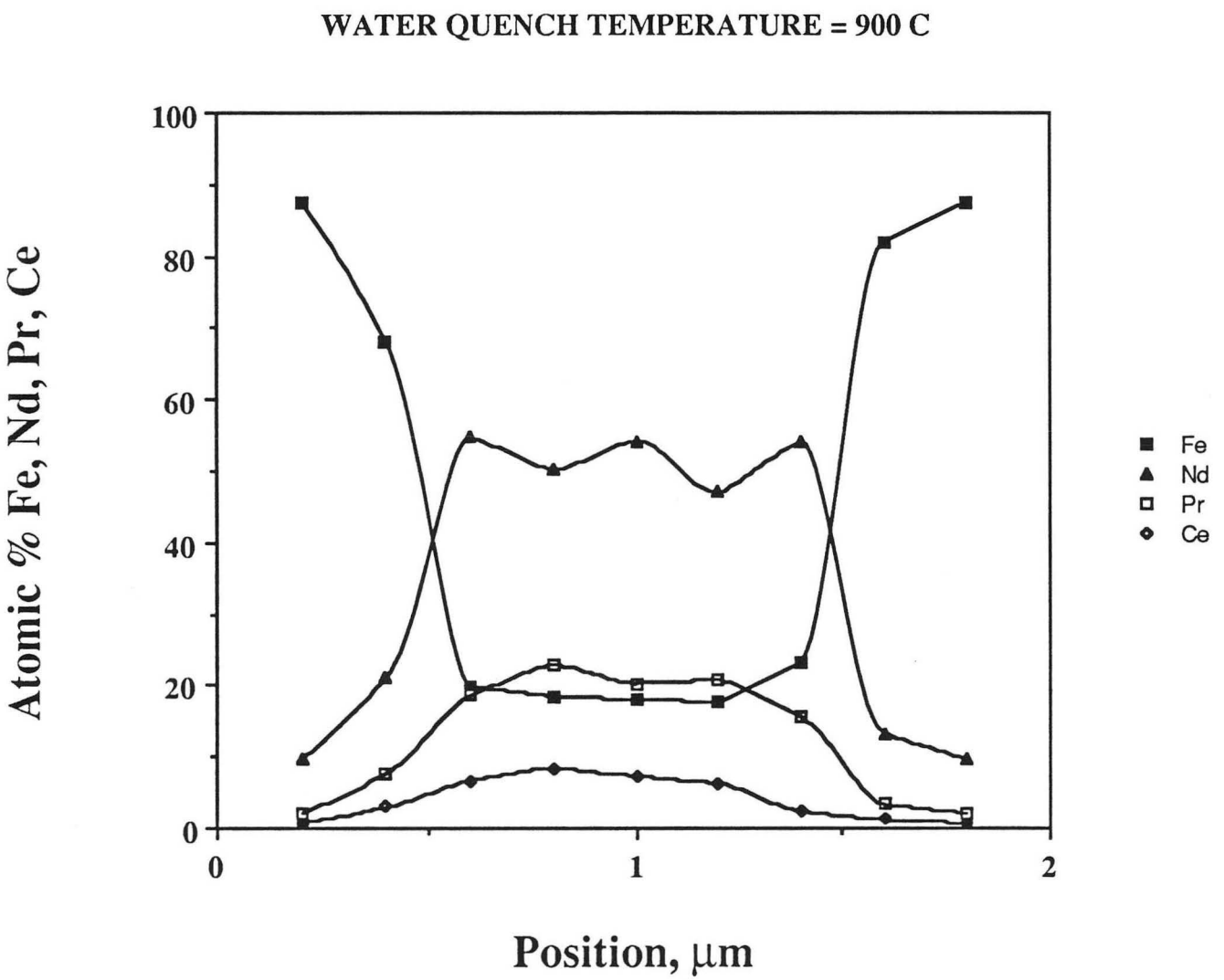

XBL 877-3394

Fig.III.57(b)

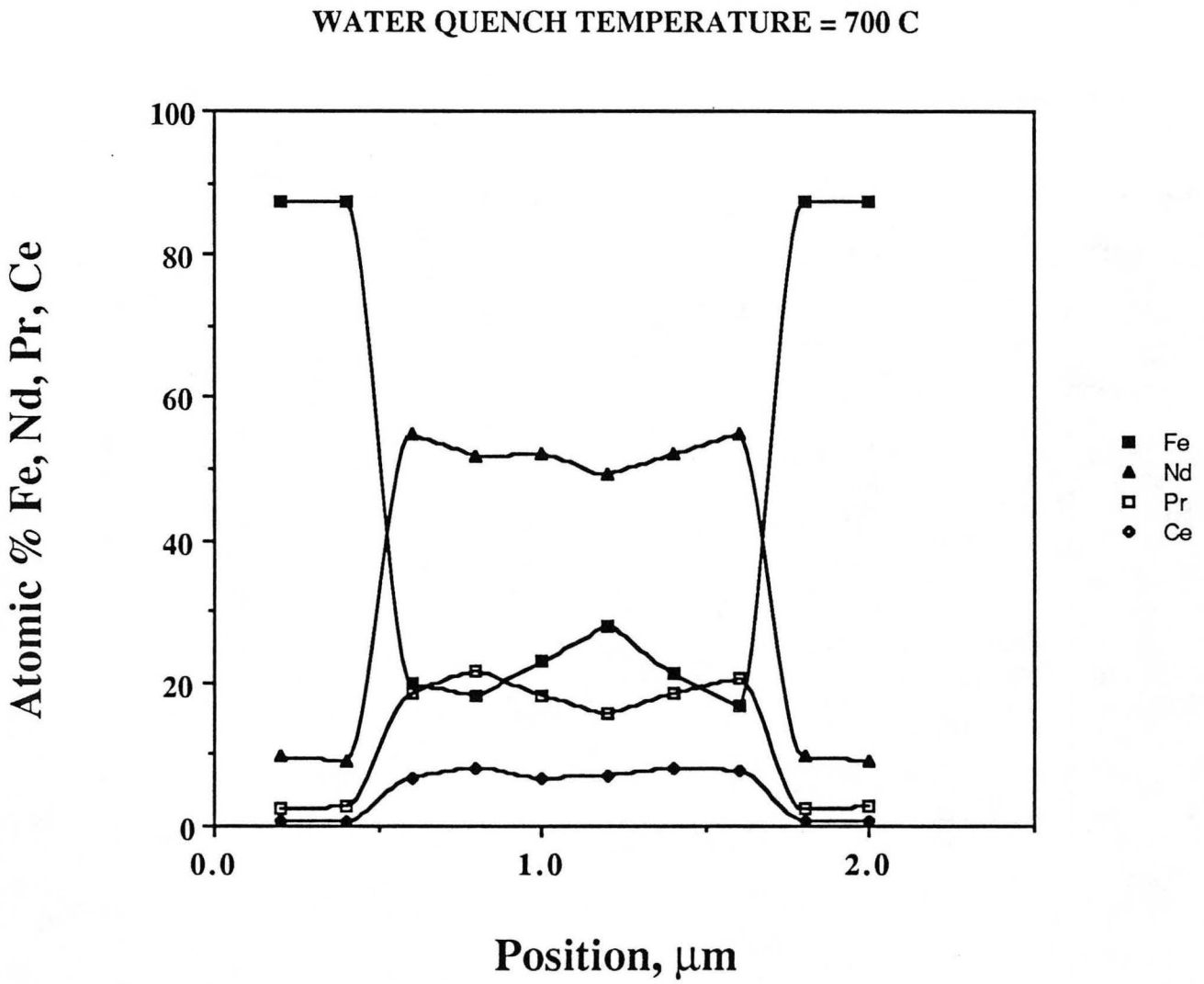

- XBL 877-3395 -

Fig.III.57(c)

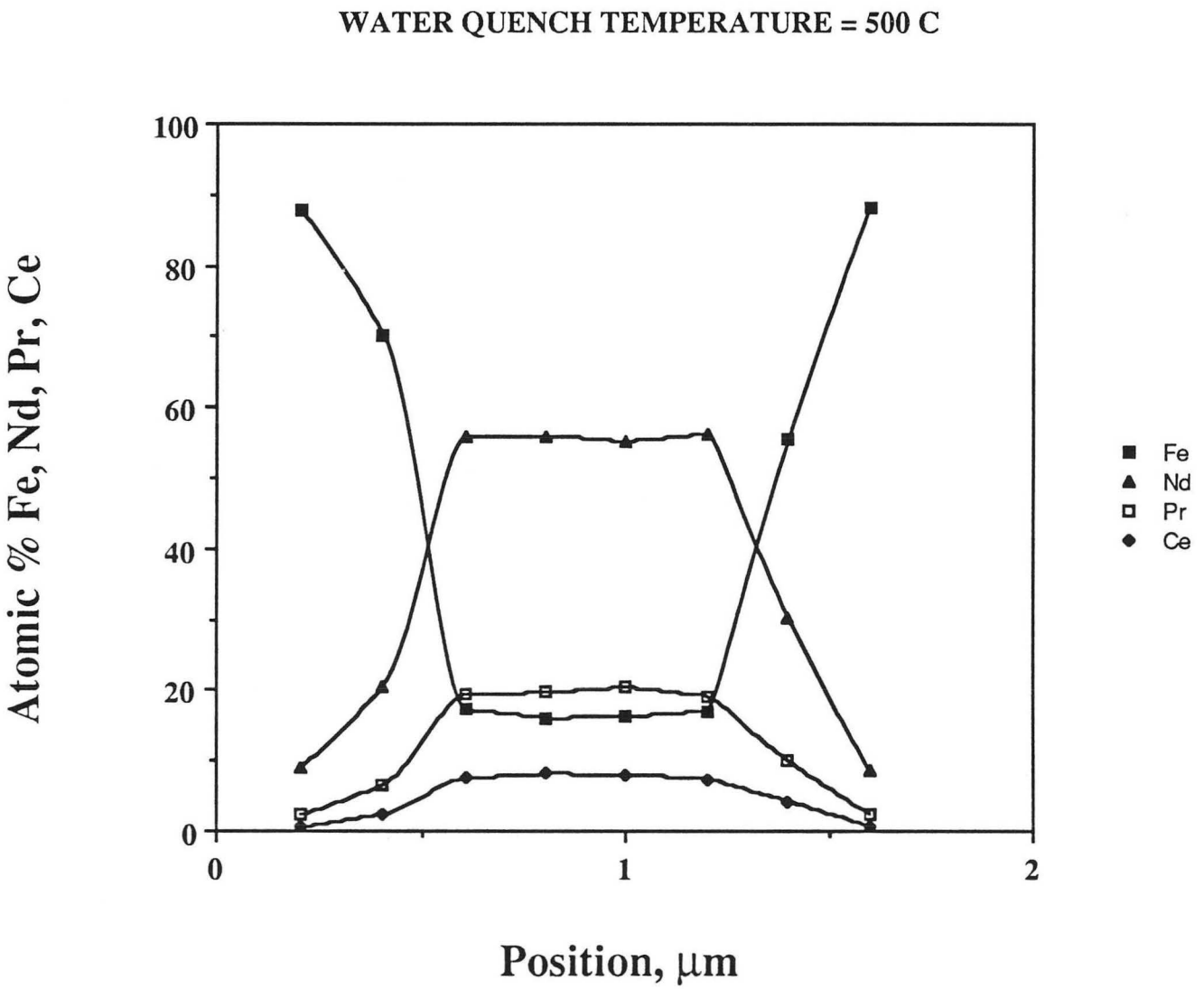

- XBL 877-3398 -

Fig.III.57(d)

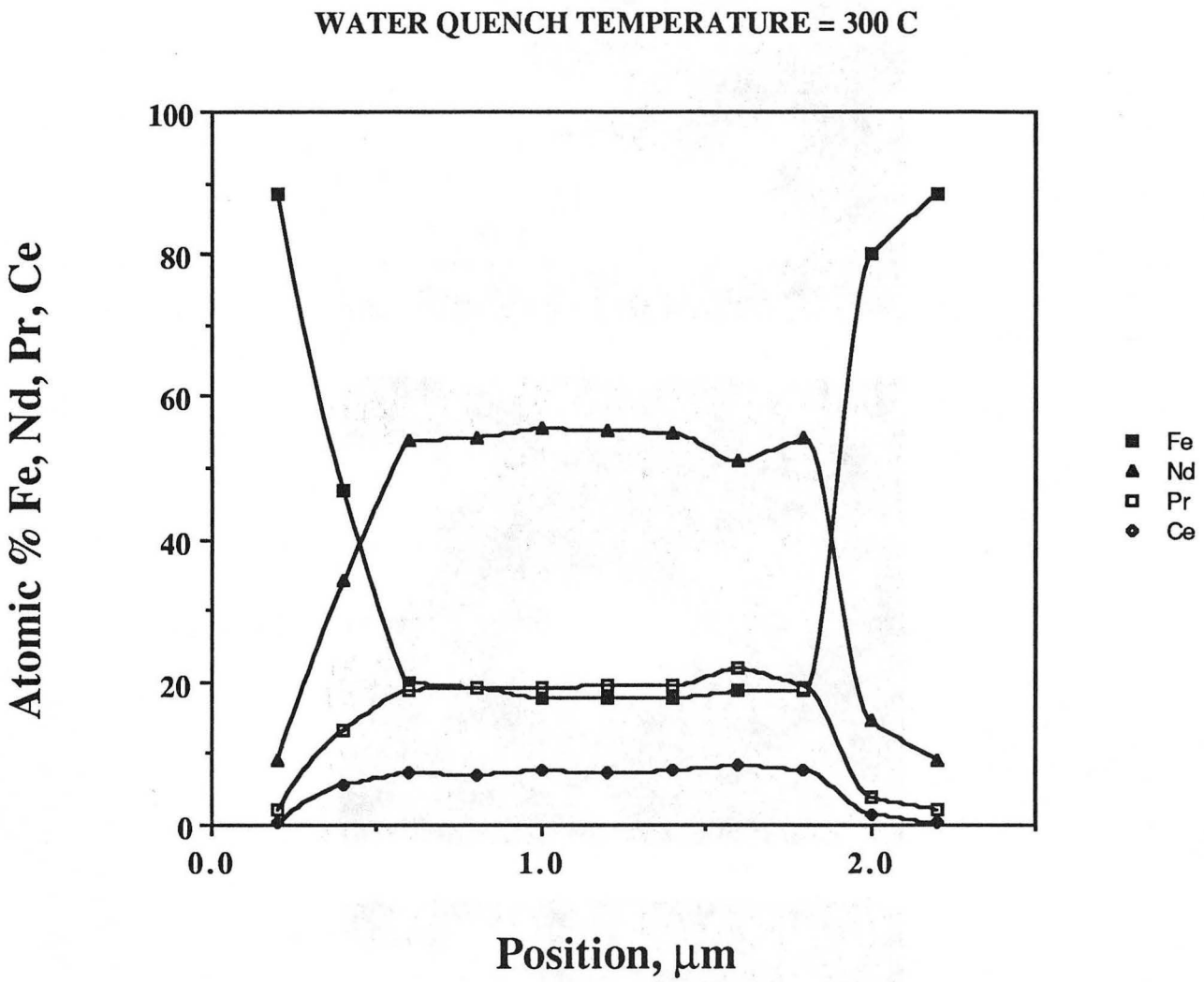

- XBL 877-3396 -

Fig.III.57(e)

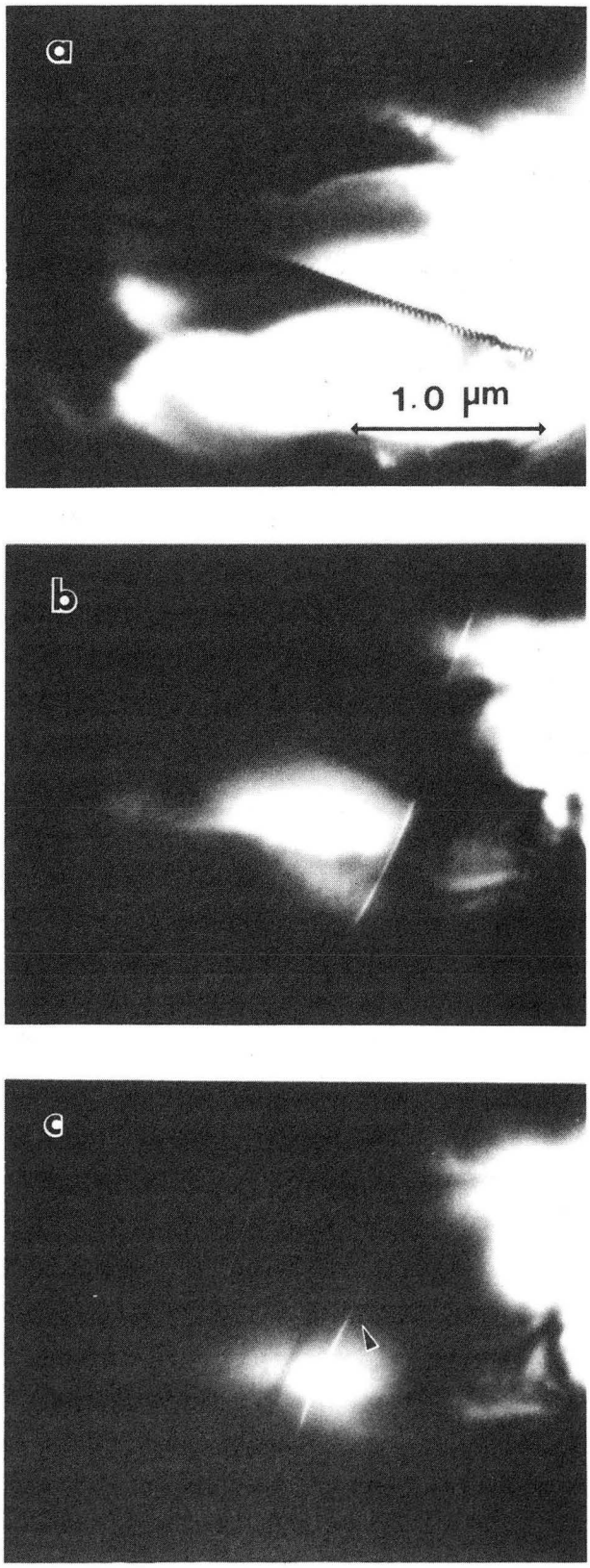

CH. 111, Fig. 58, XXB 869-7524

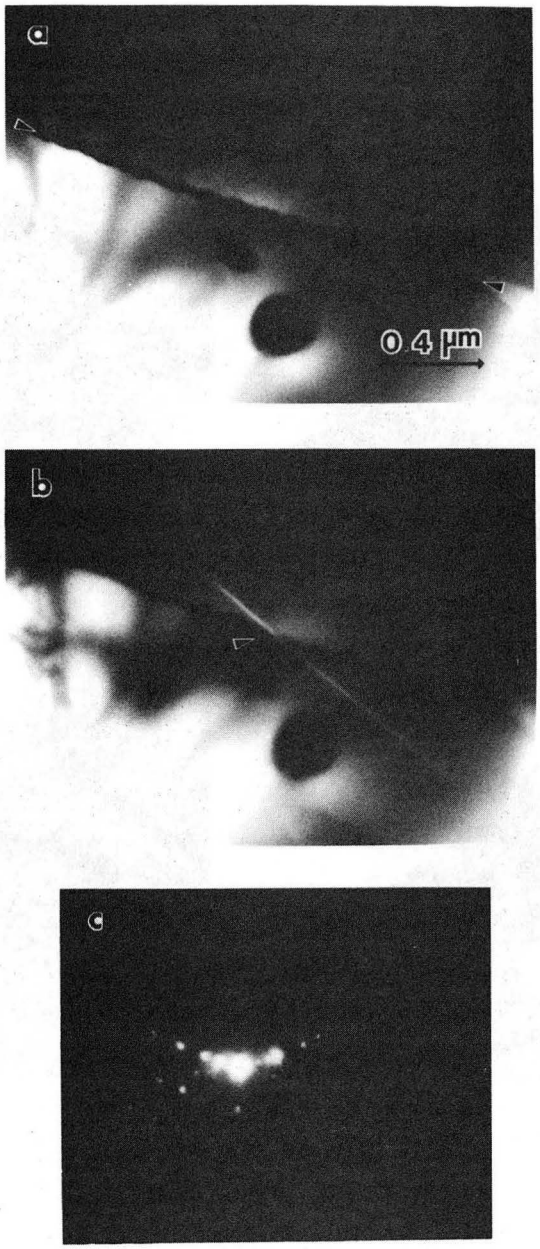

CH. 111, Fig. 59, XBB869-7530

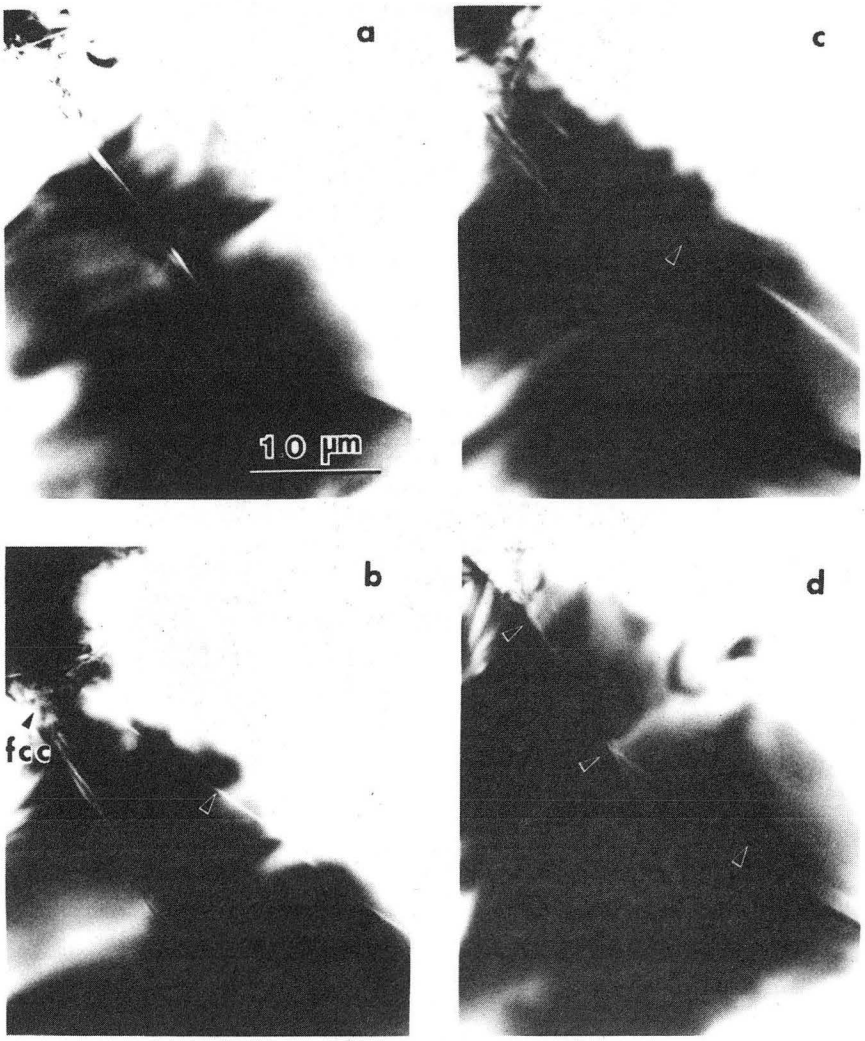

CH. 111, Fig. 60, XBB 869-7526

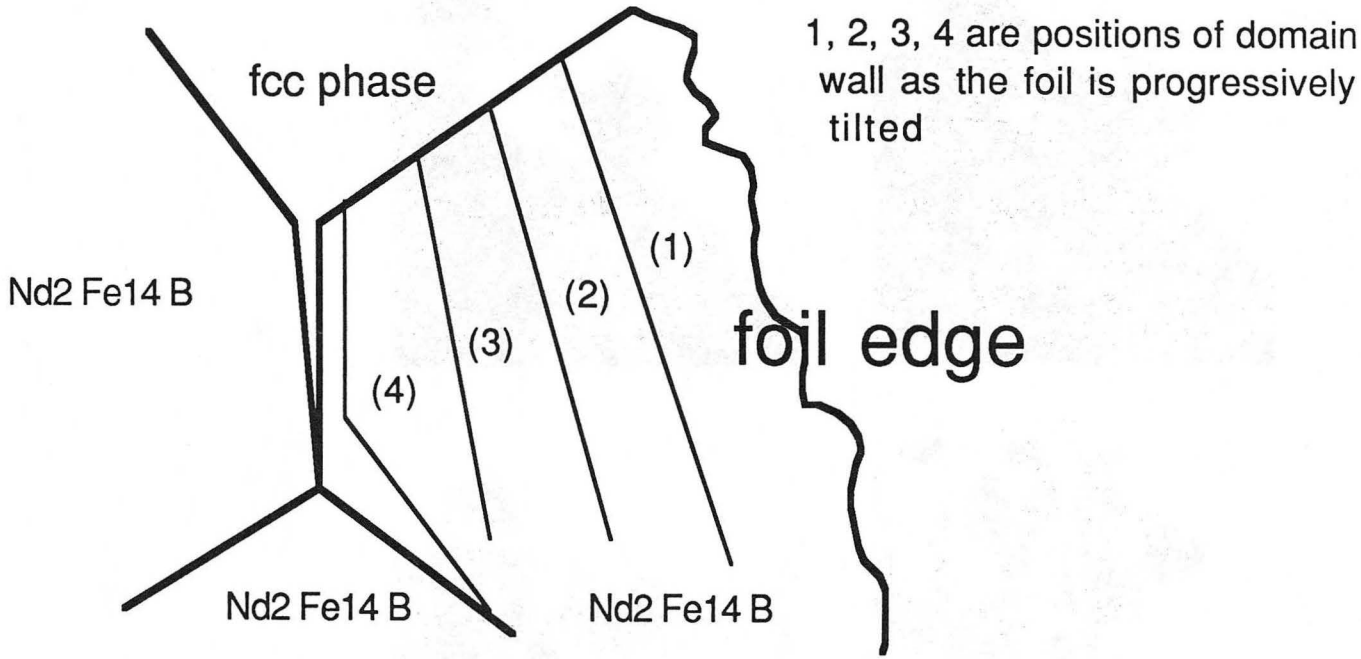

XBL 8611-4222

Fig.III.61

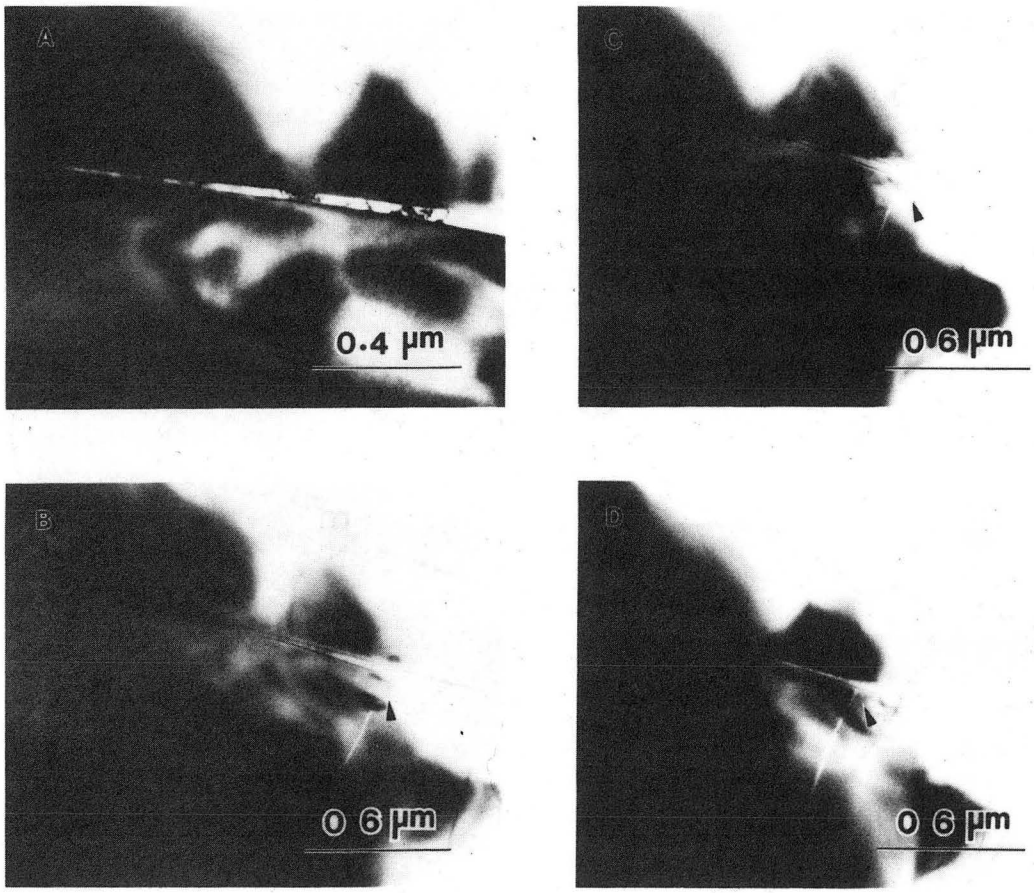

CH. 111, Fig. 62, XBB860-9222

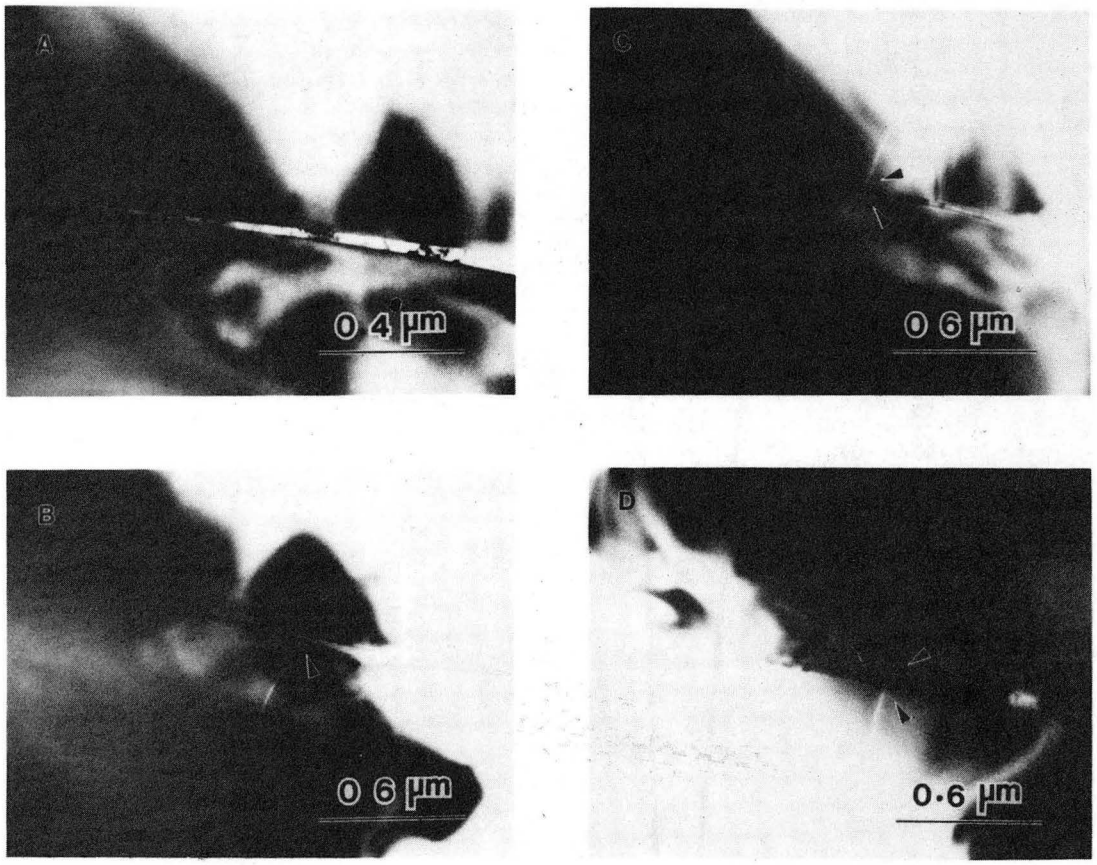

CH. 111, Fig. 63, XBB 860-9221

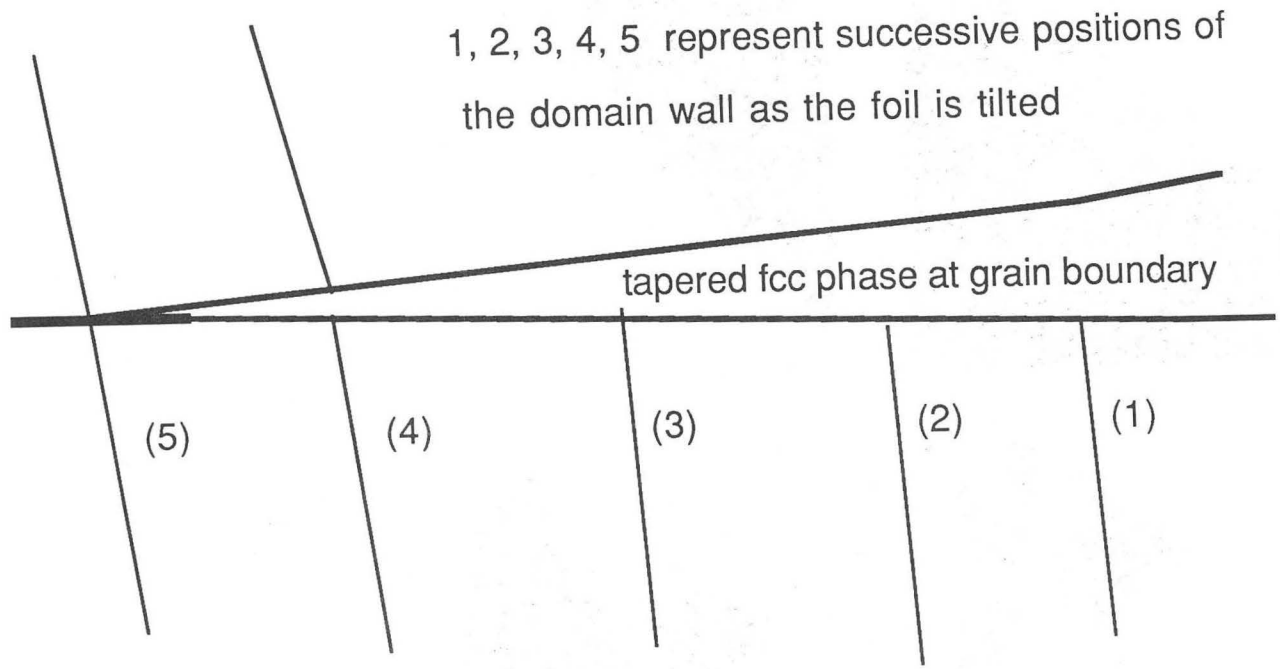

XBL 8611-4221

Fig.III.64

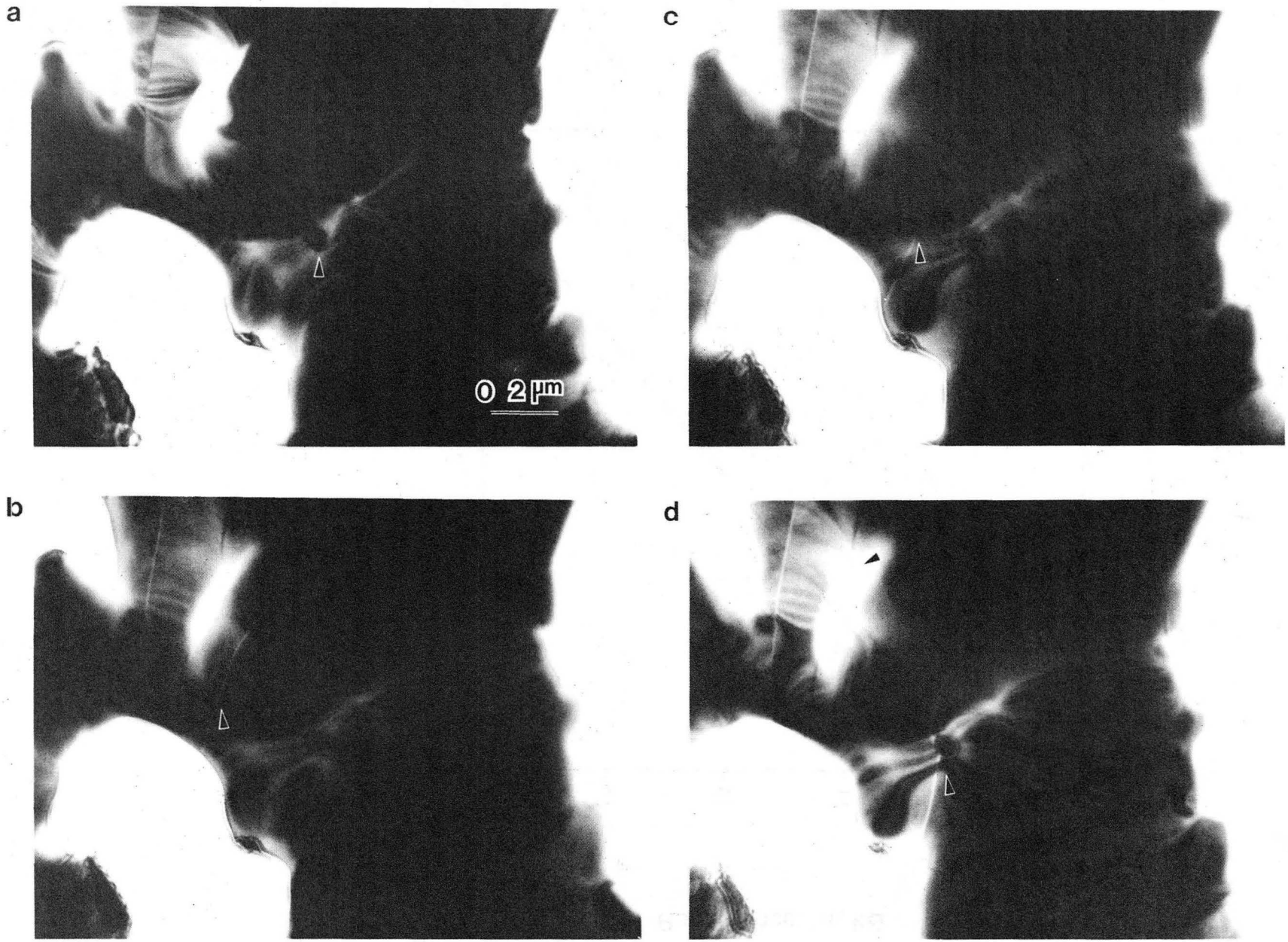

CH. 111, Fig. 65, XBB 878-6490

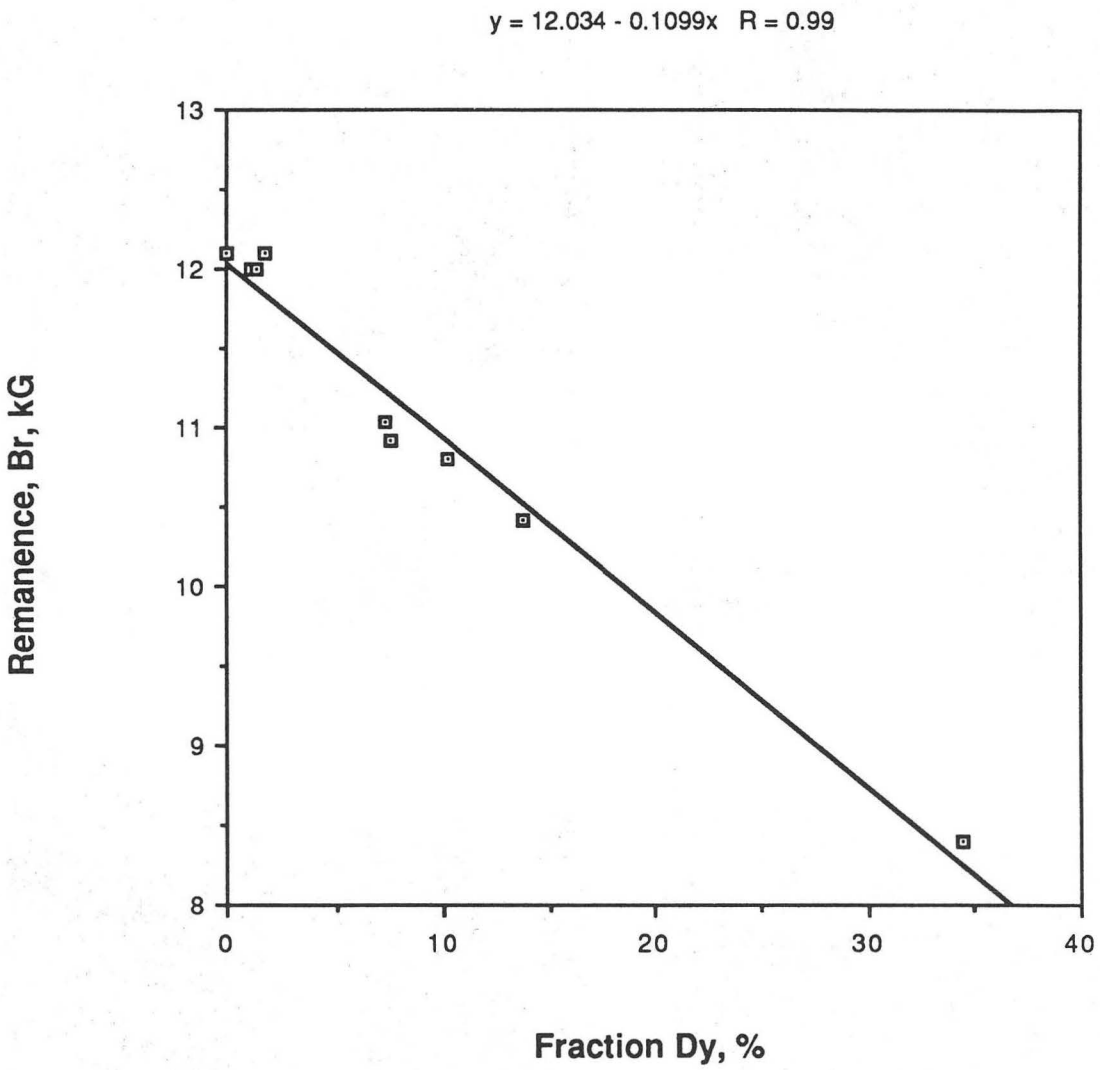

XBL 873-1414

Fig.III.66

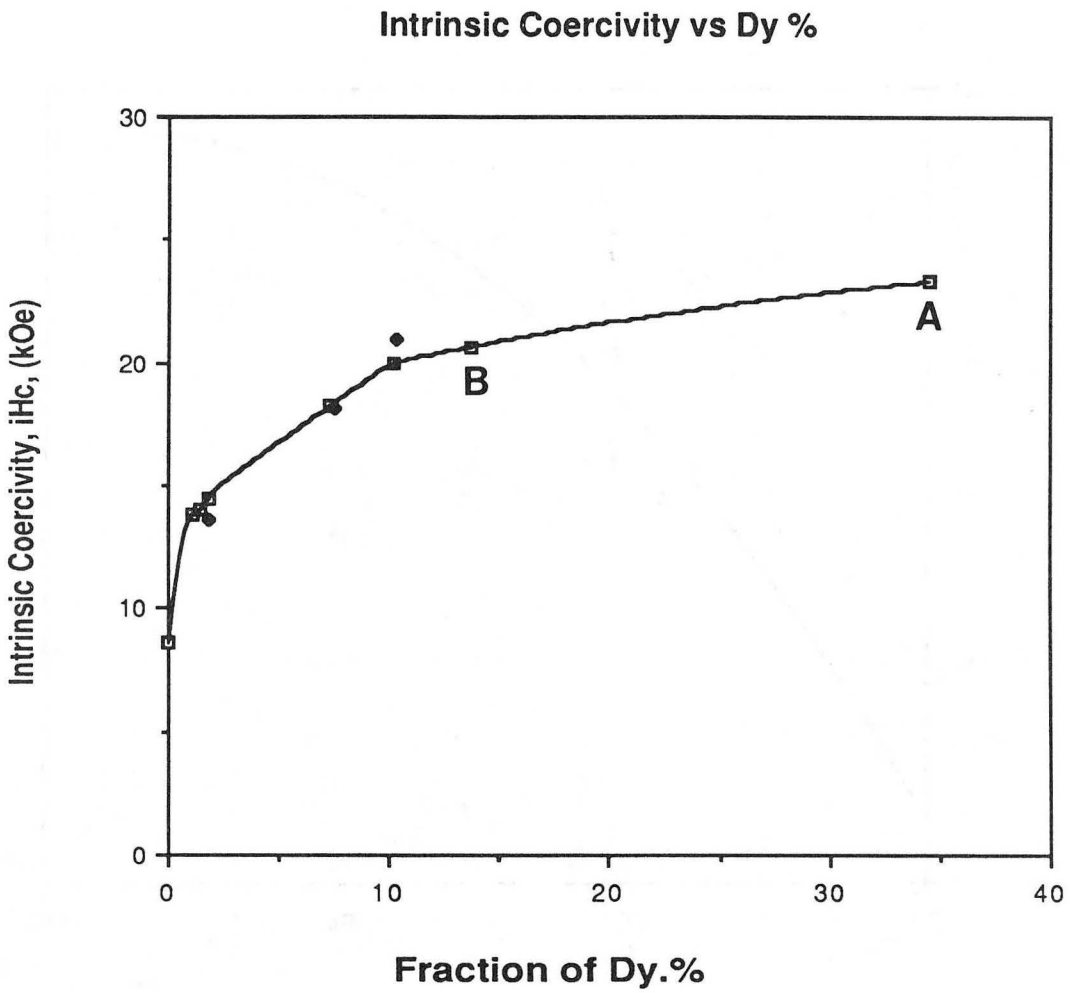

XBL 873-1415

Fig.III.67

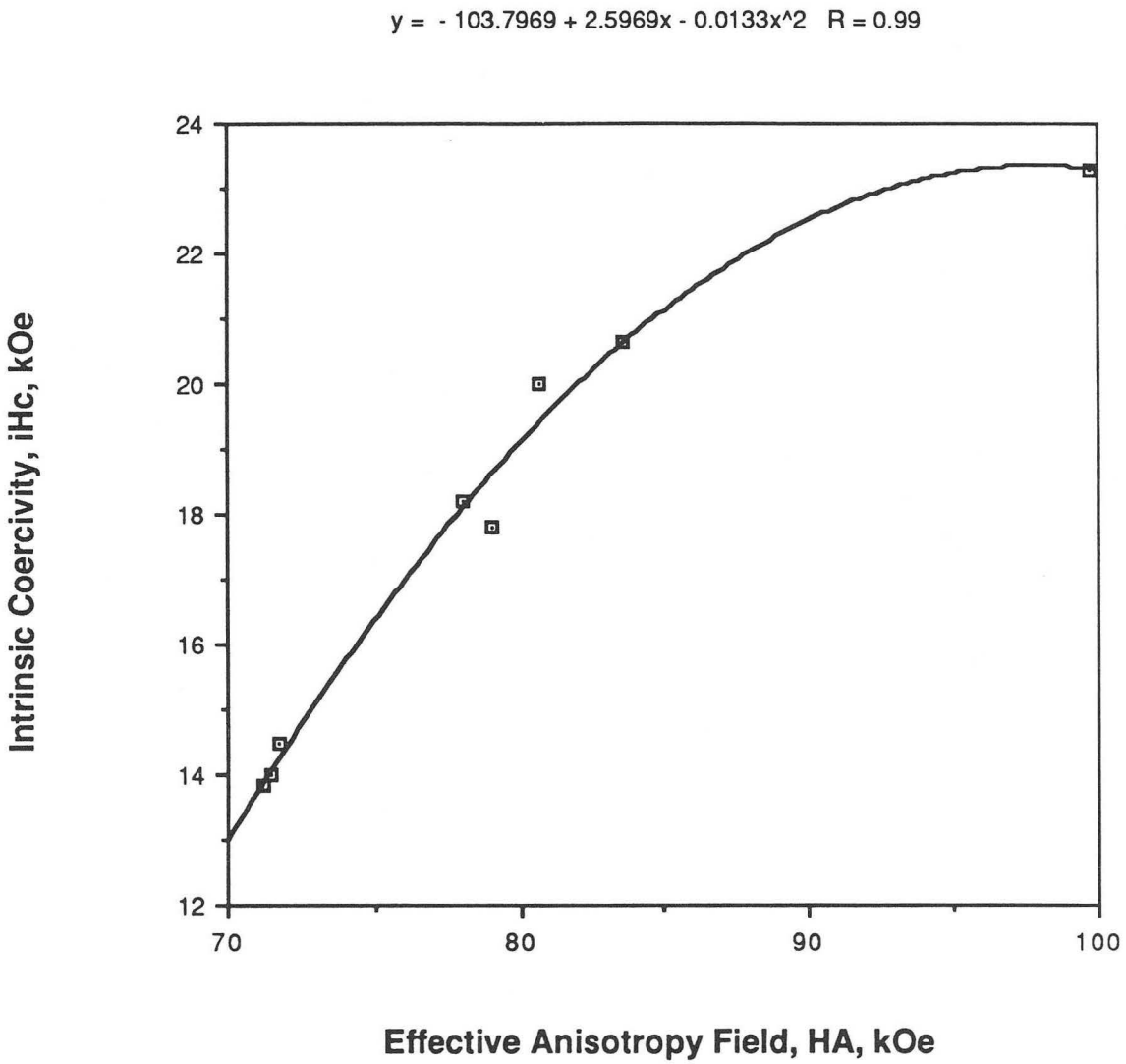

XBL 873-1411

Fig.III.68

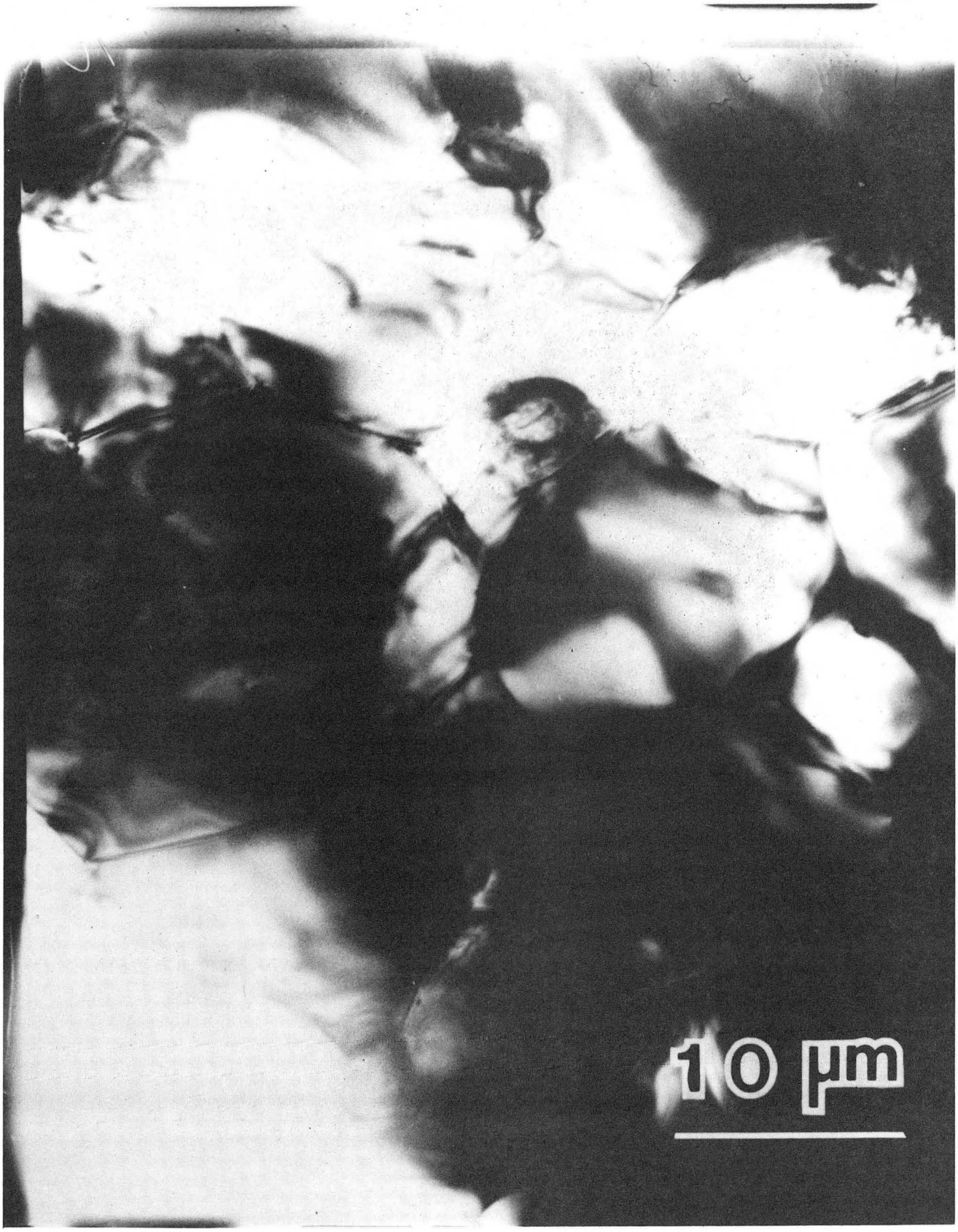

CH. 111, Fig. 69, XBB 874-2615

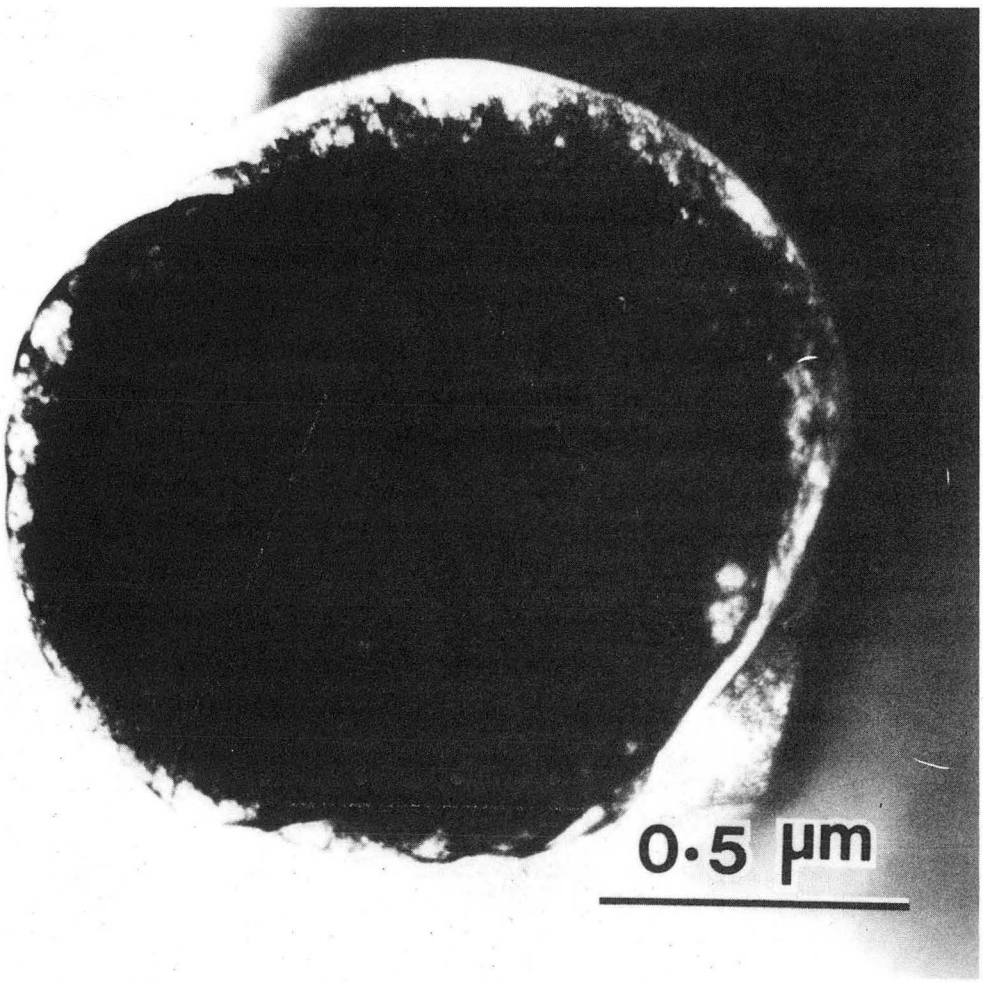

CH. 111, Fg. 70, XBB 874-2616

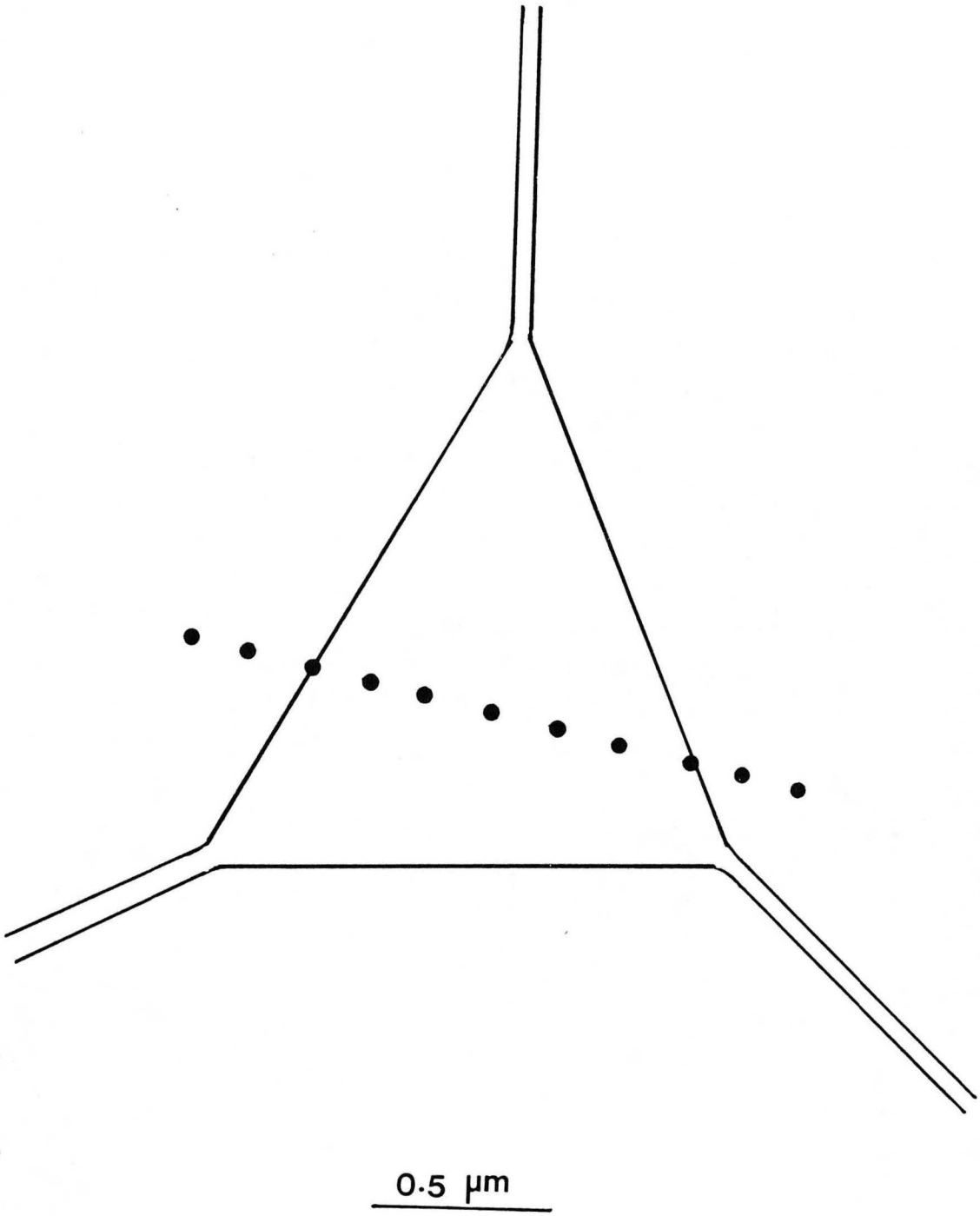

XBL 868-2980

Fig.III.71

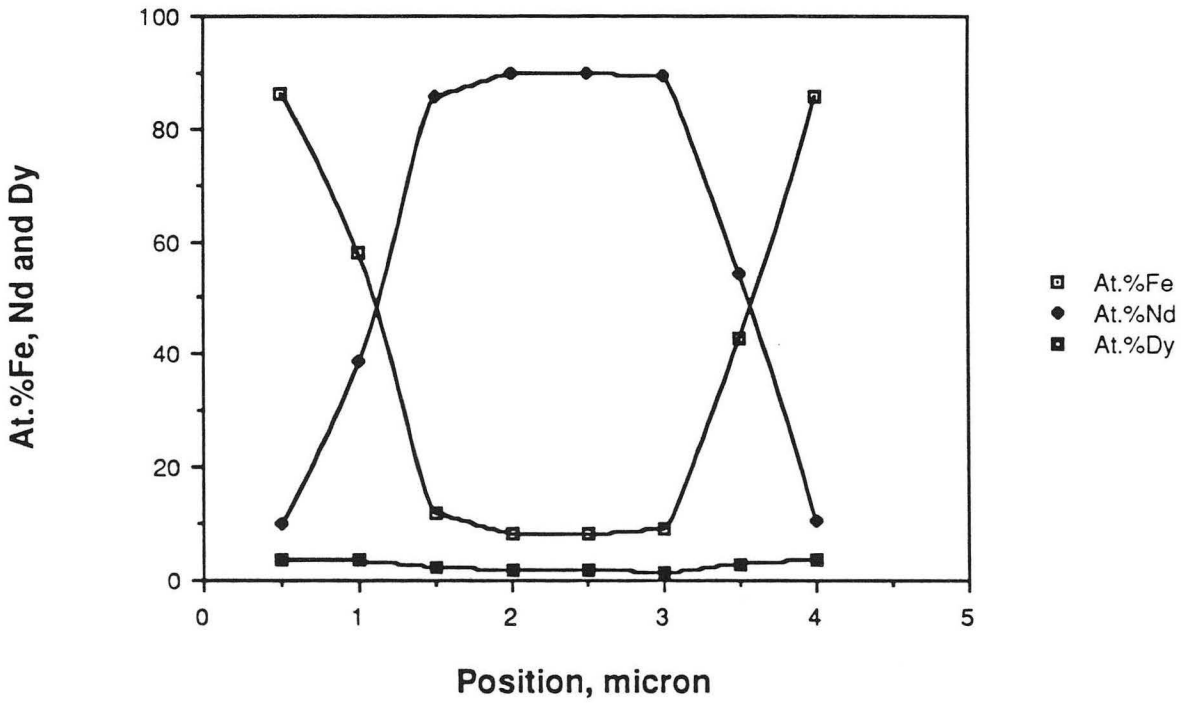

XBL 873-1410

Fig.III.72(a)

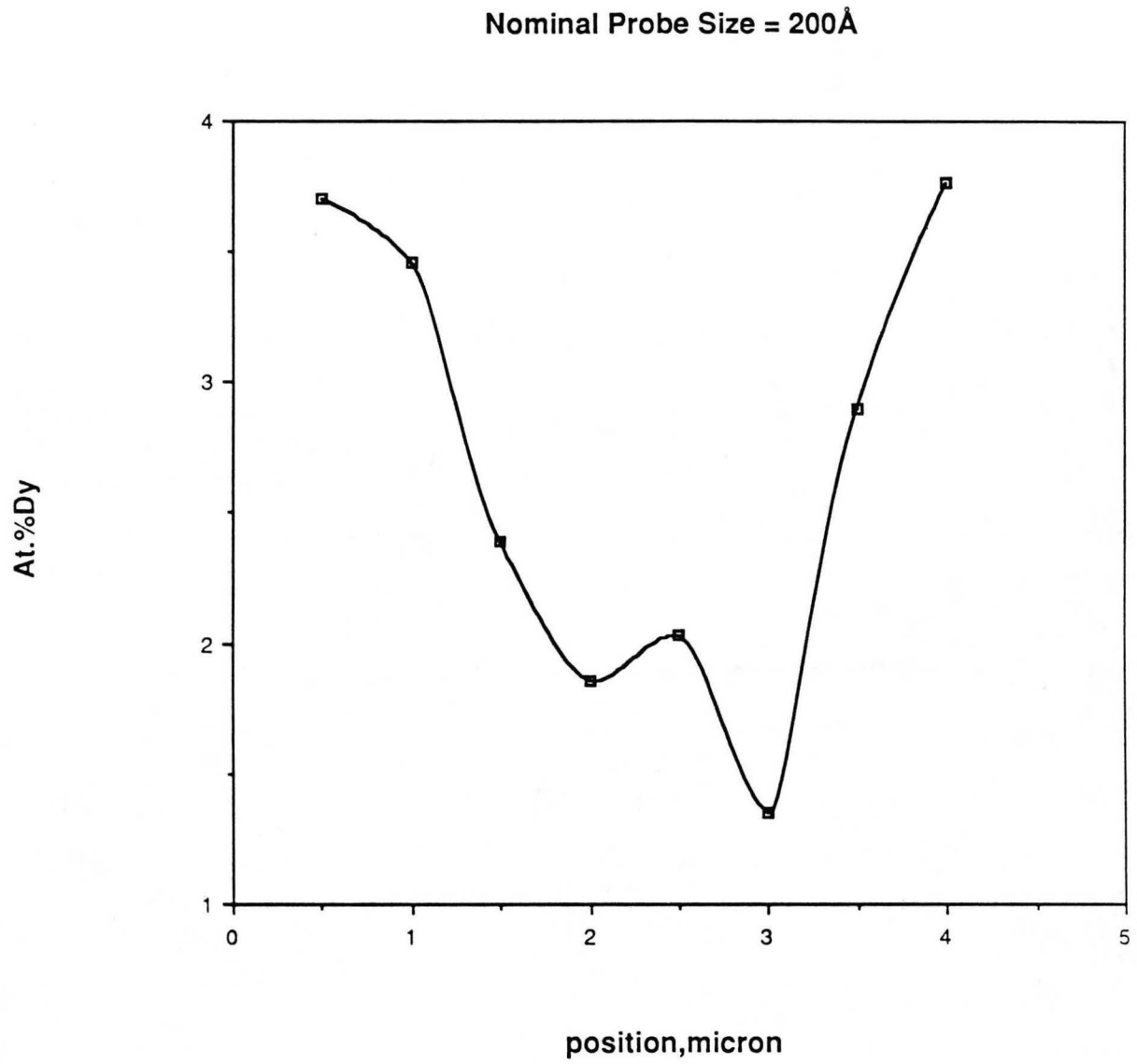

XBL 873-1409

Fig.III.72(b)

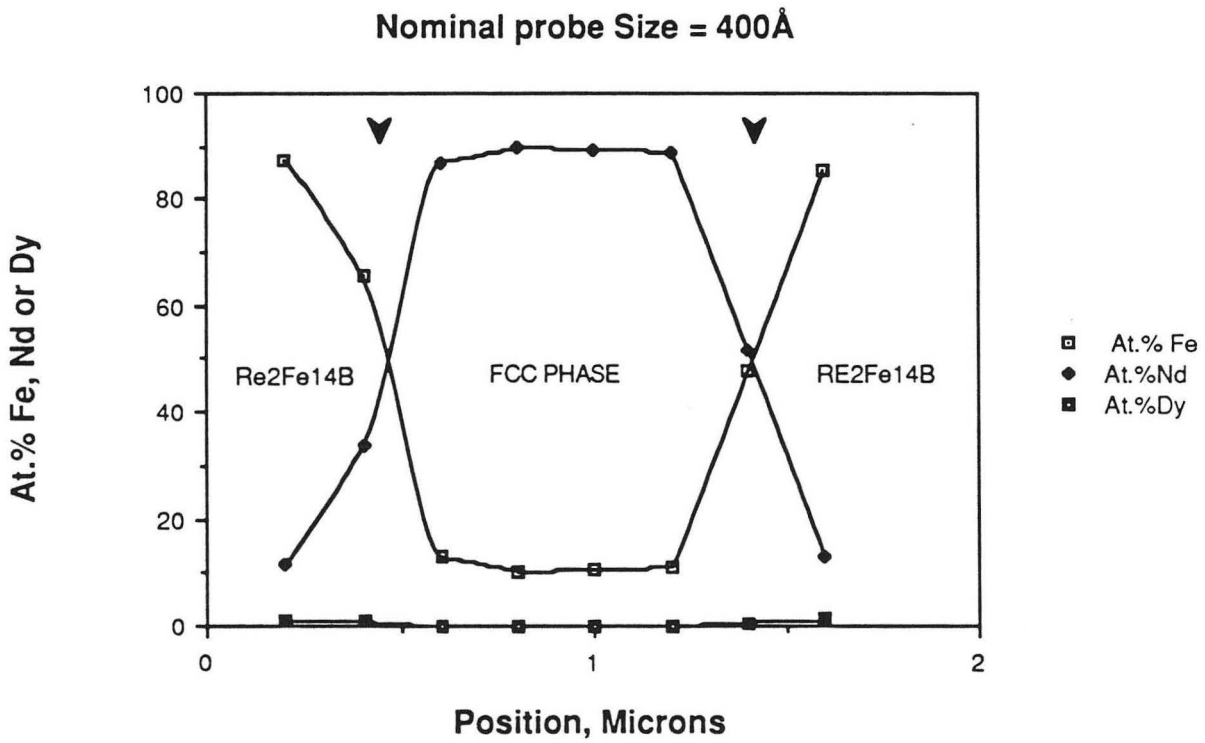

XBL 873-1408

Fig.III.73(a)

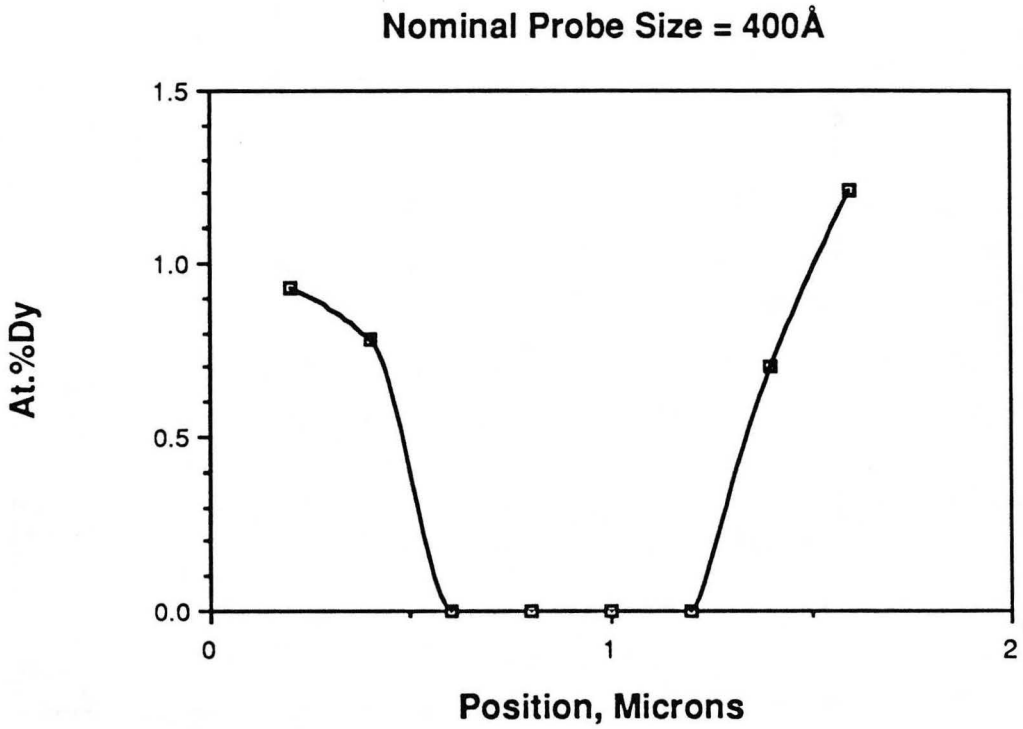

XBL 873-1407

Fig.III.73(b)

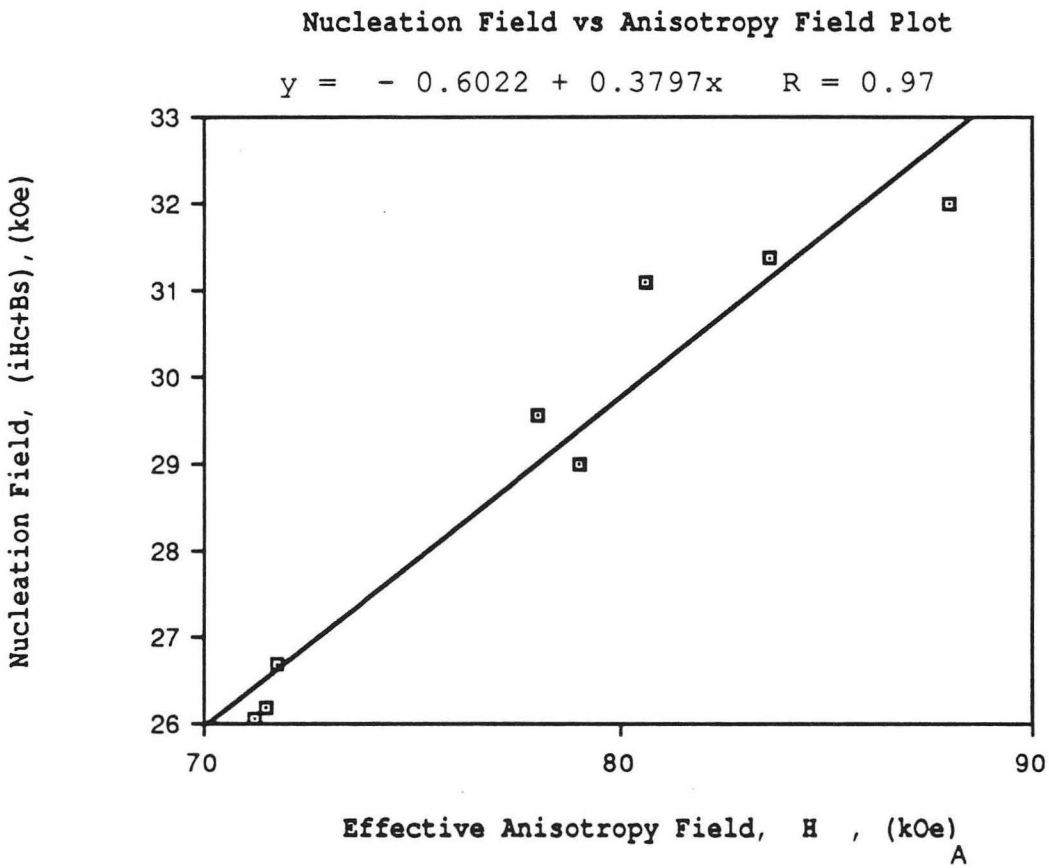

XBL 873-1413

Fig.III.74

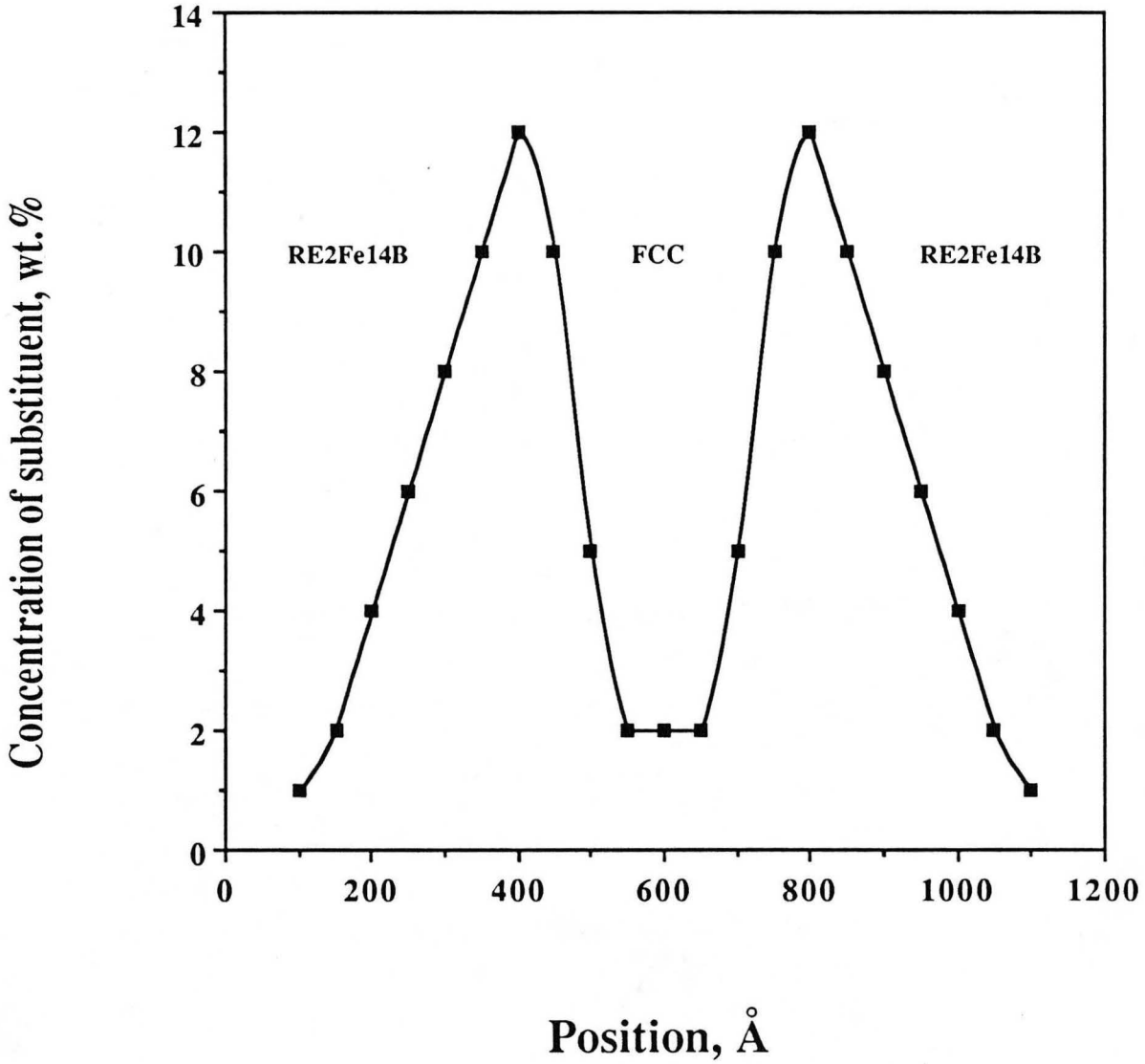

XBL 877-3361

Fig.III.75

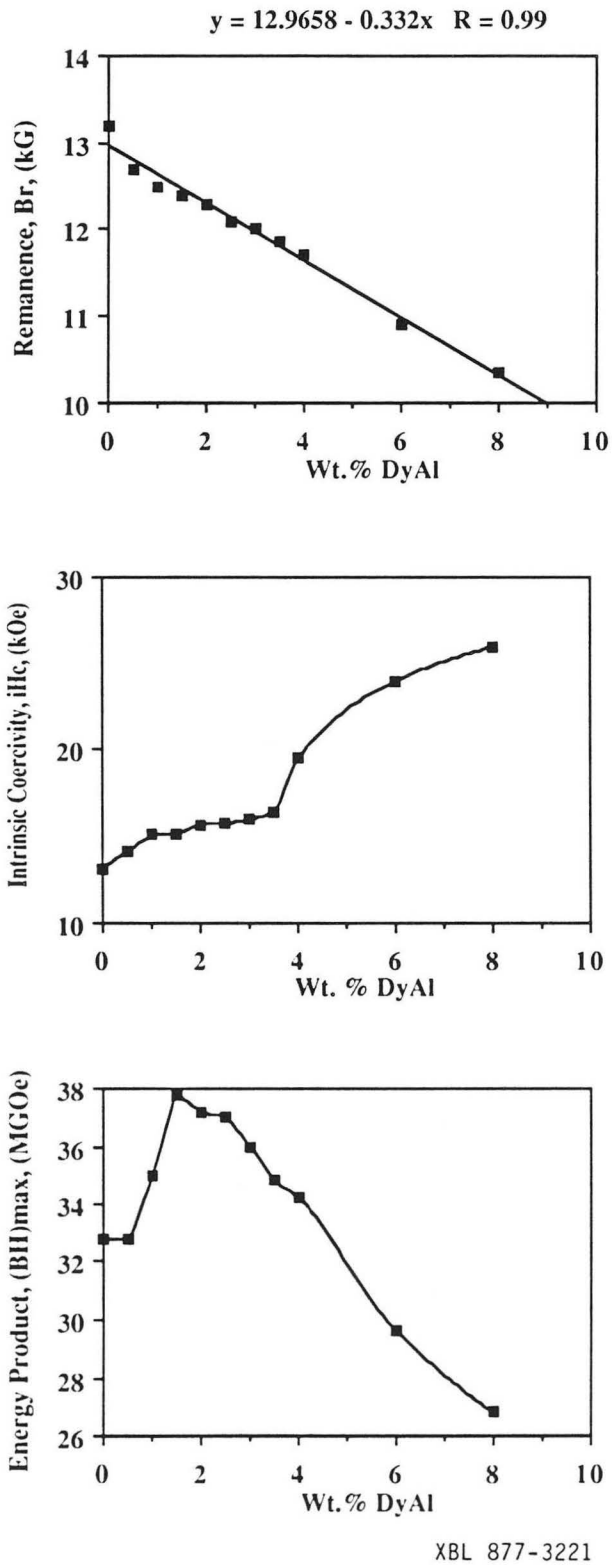
y = 12.9658 - 0.332x R = 0.99
Remanence, Br, (kG)
14
13
12
11
10
0
2
4
6
8
10
Wt.% DyAl
Intrinsic Coercivity, iHc, (kOe)
30
20
10
0
2
4
6
8
10
Wt. % DyAl
Energy Product, (BH)max, (MGOe)
38
36
34
32
30
28
26
0
2
4
6
8
10
Wt.% DyAl
XBL 877-3221

Fig.III.76

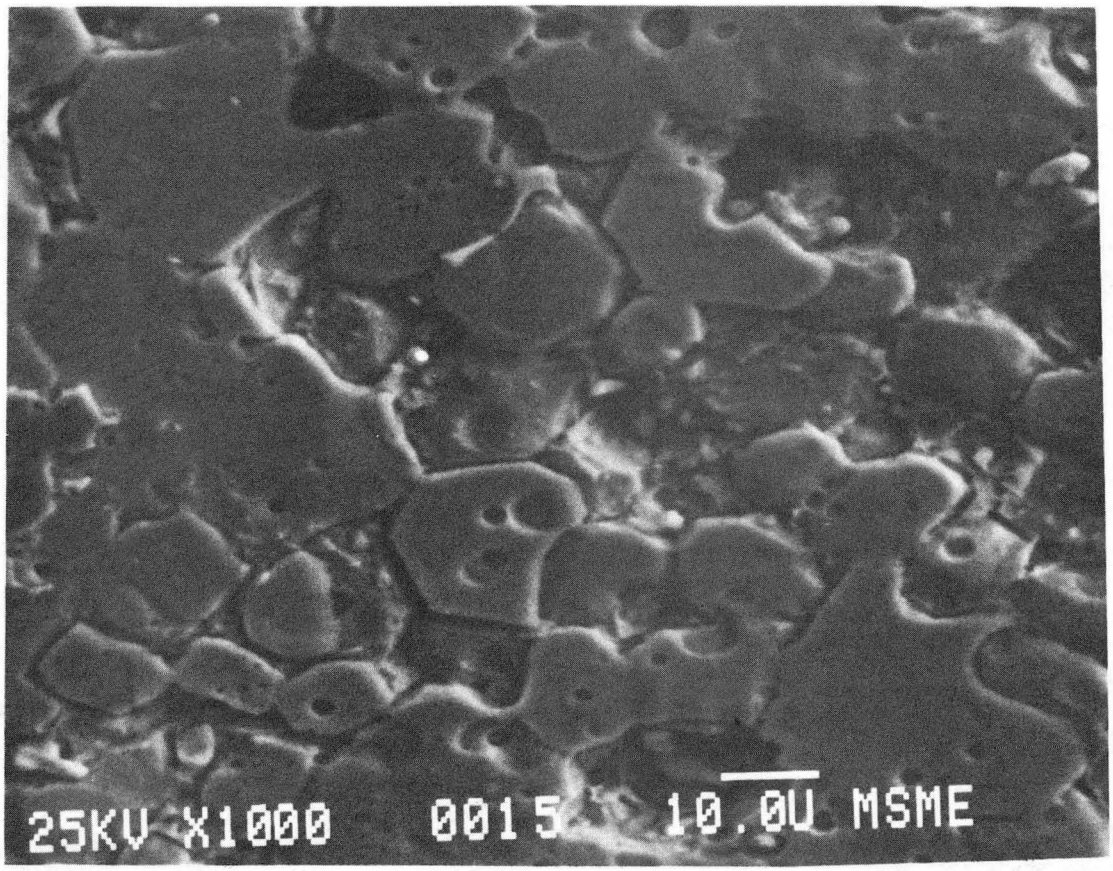

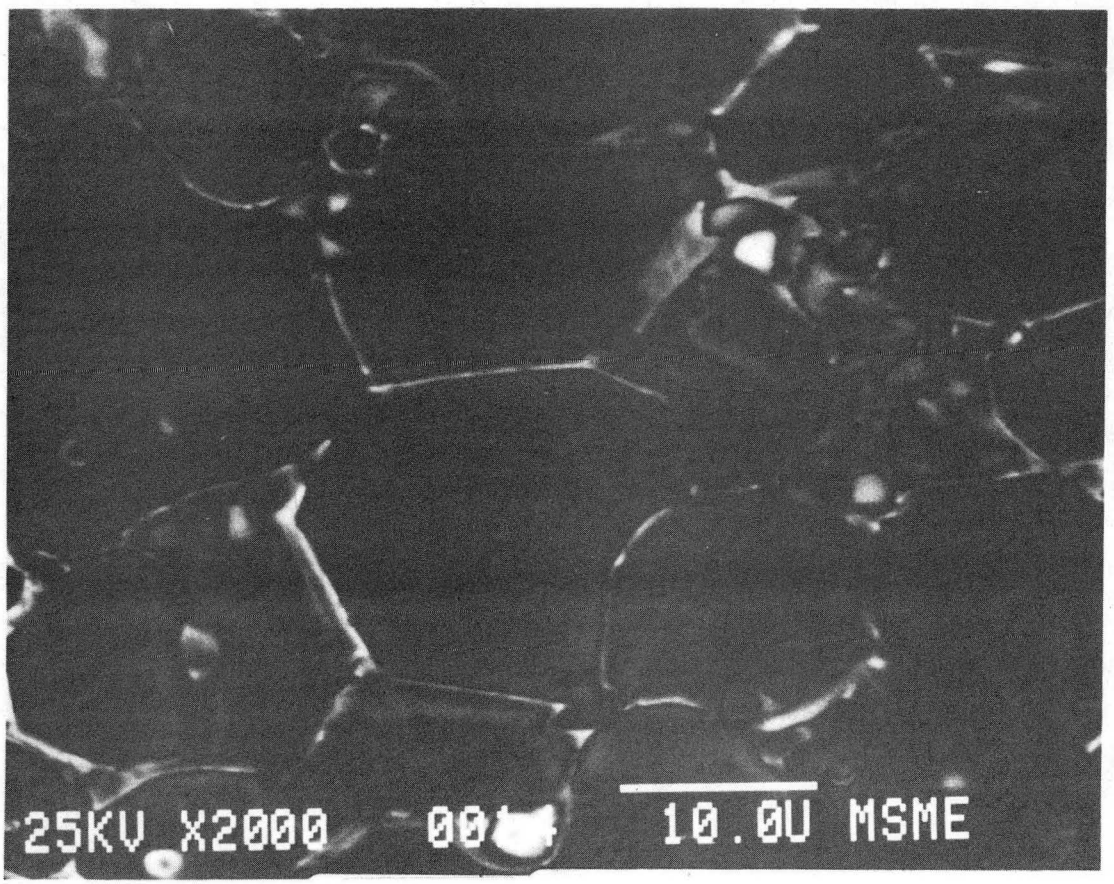

CH. 111, Fig. 77, XBB 877-5711

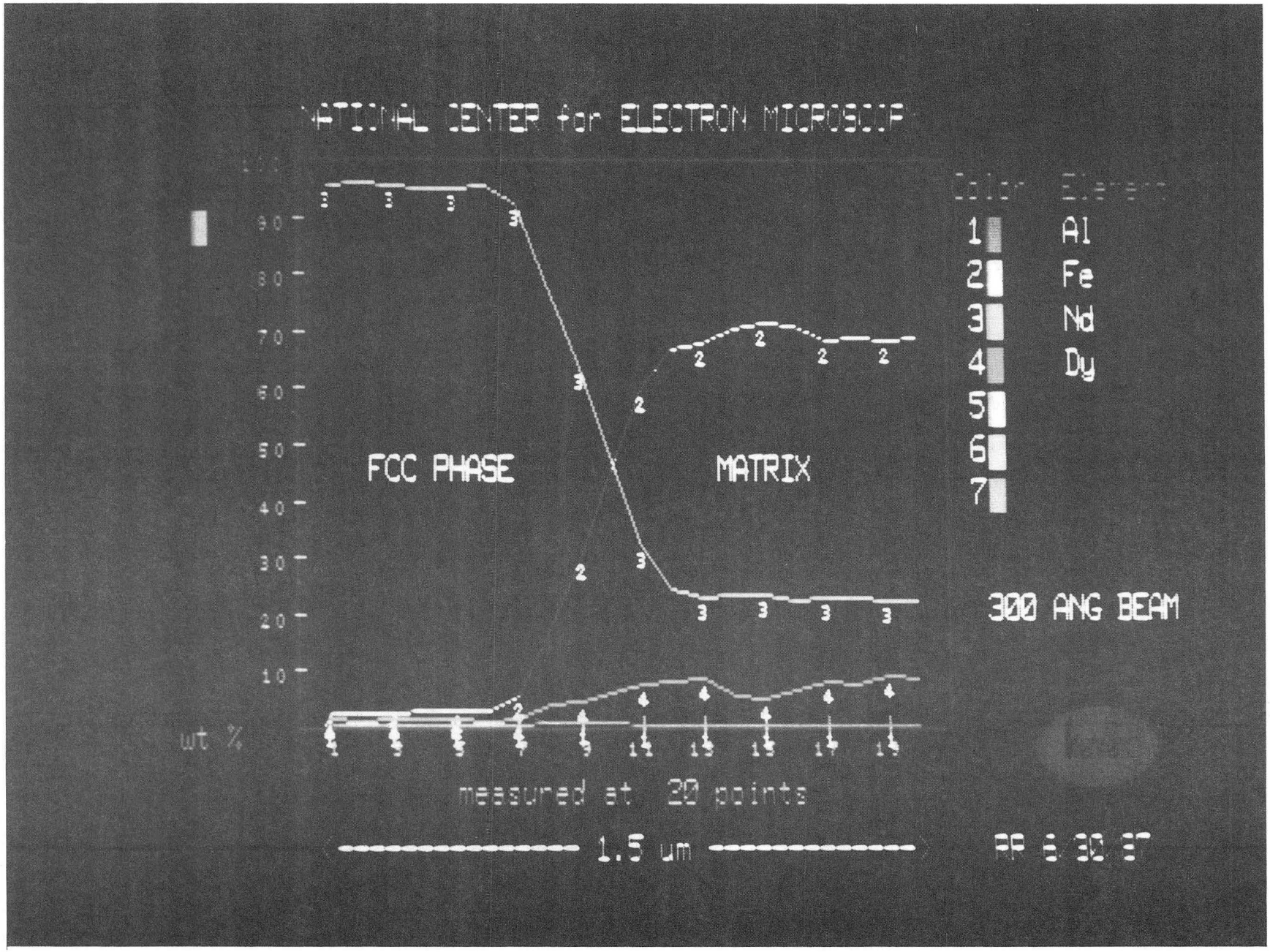

CH 111, Fig. 78(a)BBC 877-6075

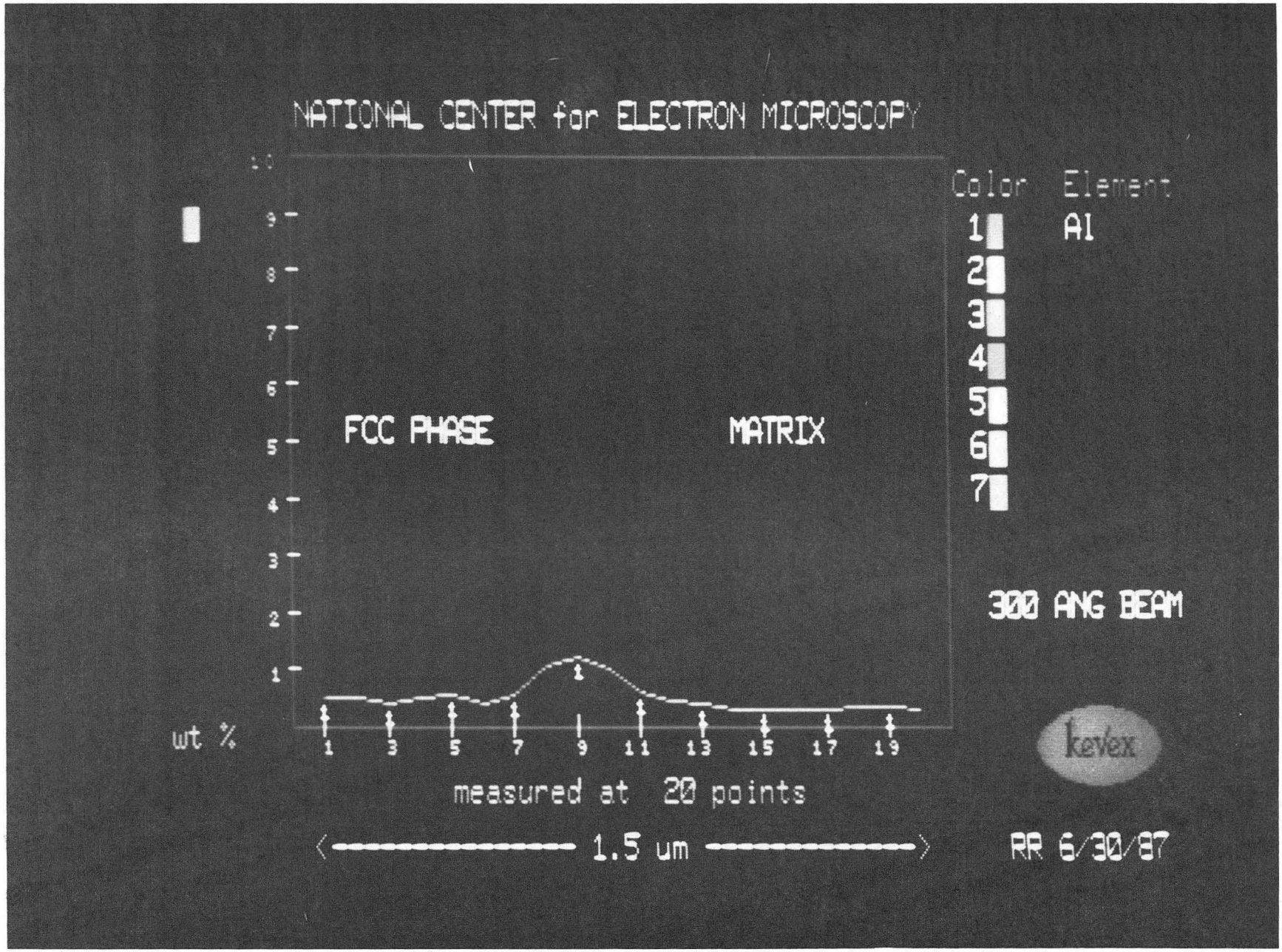

CH. 111, Fig. 78(b), BCC 877-6077

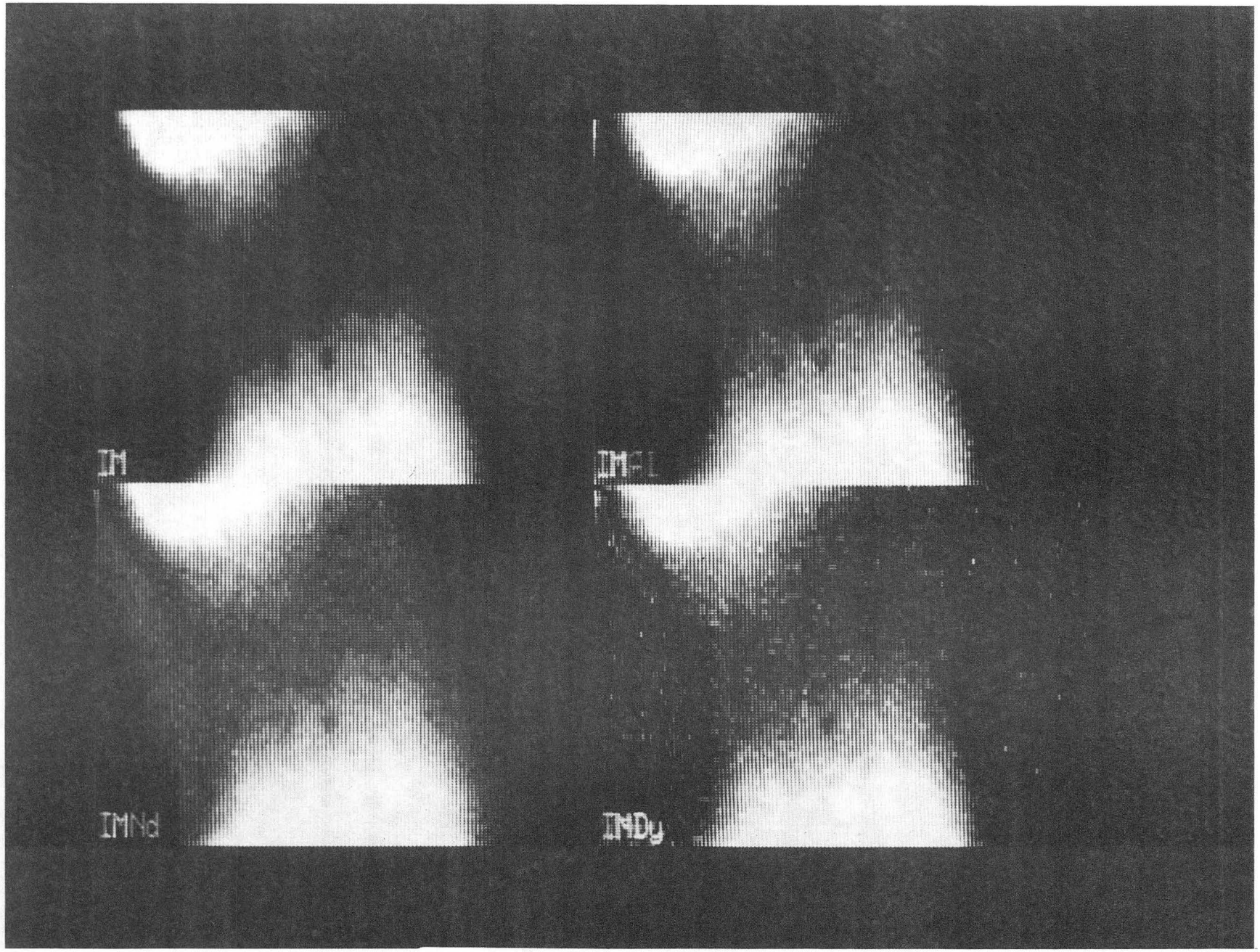

CH. 111, Fig. 79, BBC 877-6085

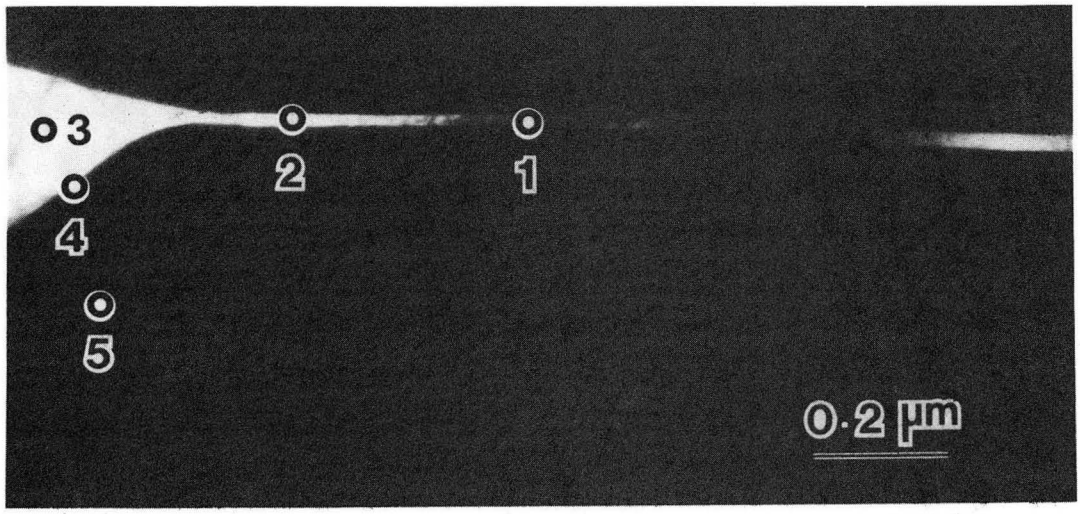

POINT ANALYSES

POSITION	At.% Fe	At.% Nd	At.% Dy	At.% Al
POINT 1	82.01	13.57	3.00	1.43
POINT 2	47.56	49.18	1.92	1.34
POINT 3	10.41	88.97	0.61	0.00
POINT 4	81.37	13.55	3.80	1.27
POINT 5	84.14	10.43	4.62	0.81

CH. 111, Fig. 80. XBB 877-6402

LAWRENCE BERKELEY LABORATORY
TECHNICAL INFORMATION DEPARTMENT
UNIVERSITY OF CALIFORNIA
BERKELEY, CALIFORNIA 94720